Durham E-Theses

RF Magnetron Sputtering of Transparent Conducting Oxides and CdTe/CdS Solar Cells

TREHARNE, ROBERT,EDWARD

How to cite:

Use policy

RF Magnetron Sputtering of Transparent Conducting Oxides and CdTe/CdS Solar Cells

Robert E. Treharne, MPhys

A thesis presented in the candidature for the degree of Doctor of Philosophy
in the University of Durham
Department of Physics
October 2011

Abstract

The applicability of radio frequency magnetron sputtering (RFMS) for the development of: a) transparent conducting oxides (TCOs) and b) fully sputtered CdTe/CdS solar cells is demonstrated.

TCO materials - In_2O_3:Sn (ITO), SnO_2:F (FTO), ZnO:Al (AZO) and ZnO:F (FZO) - were investigated with respect to key deposition parameters in an attempt to generate films with low resistivities and high transmittances. Minimum resistivity values of 1.2×10^{-4} Ω.cm and 4.7×10^{-4} Ω.cm were achieved for films of ITO and AZO respectively while maintaining transmittances of $> 80\%$. Such films are viable for incorporation into CdTe based solar cells as front contact layers. A model for the dielectric permittivity, $\varepsilon(\omega)$, for TCO materials is presented based on classical Lorentz and Drude models of bound and free electron behaviour, and a model of inter-band transitions that describes behaviour in the vicinity of a direct band-gap. The model is successfully applied to the fitting of transmittance data for TCO films and used to extract opto-electronic properties.

The results of a fully-sputtered CdTe prototype device structure are presented; a maximum conversion efficiency of 12.5% is achieved. Further investigations, via XRD, into the effect of sputter pressure on CdTe films indicates that a 10 mTorr Ar pressure is best for optimising device efficiency. J-V-T and C-V measurements show that at room temperature, current transport in the sputtered devices is dominated by Shockley-Read-Hall recombination and that the CdTe layer, under zero applied bias, is fully depleted with a carrier concentration of 4×10^{14} cm^{20}. Cross-sectional SEM and TEM show that both CdS and CdTe layers undergo significant recrystallisation during post-deposition $CdCl_2$ treatment.

A multi-layer optical model of transmittance is developed based on a transfer matrix method and using optical data acquired from spectrophotometry and ellipsometry. The model is used to predict the fraction of transmitted light received by the CdTe absorber in a fully sputtered device and it is indicated that through further thinning of the CdS layer, to below 50 nm, significant gains in transmittance, upwards of 20%, may be achieved.

It is established that the further development of sputtered CdTe/CdS solar cells requires a significant improvement in the uniformity of the current $CdCl_2$ based post-deposition treatment.

Declaration

I declare that with the exception of those procedures listed below all the work presented in this thesis was carried out by the candidate. I also declare that none of this work has been previously submitted for any degree and that it is not being submitted for any other degree.

J-V-T and C-V measurements reported in Chapter 6 were performed by Murat Bayhan, Dept. of Physics, Faculty of Art and Science, University of Muğla, Muğla, Turkey.

Focussed ion beam sample preparation, scanning electron microscopy and transmission electron microscopy of samples described in Chapter 6 was performed by Leon Bowen and Bhudika Mendes, Dept. of Physics, University of Durham, Durham, UK.

....

Dr. Douglas P. Halliday

Supervisor

....

Robert E. Treharne

Candidate

The copyright of this thesis rests with the author. No quotation from it should be published without their prior written consent and information derived from is should be acknowledged.

Acknowledgements

I would like to express my utmost thanks to my supervisor Ken Durose for all his guidance and advice throughout my Ph.D and for his extensive proof reading of this thesis. Furthermore, I am forever indebted to him for the care and consideration he has extended to both me and my wife during the group's recent relocation to Liverpool University.

My special thanks also to Jon Major, Ben Williams, Mohammed Al-Turkestani, Yuri Proskuryakov and Leon Bowen for being such a fantastic group of people to work with.

For other pockets of wisdom, advice and technical assistance I thank Claire Little, Dawn Geatches, Robyn Moorcroft, Akhtar Rind, Murat and Habibe Bayhan, Norman Thompson, David Pattinson, Duncan McCallum, Stuart Brand, Douglas Halliday, Budhika Mendis, David Lane, Chris Moore, Guillaume Zoppi, Scilla Roncallo, Kyle Hutchings, Neil McSporran, and Damian Hampshire. Without them this thesis would not have been possible.

Finally, this thesis is dedicated to my Mum and Dad, for always supporting whatever I chose to do and never once suggesting that I get a 'real' job, and to my amazing wife Suzanne, who has borne the brunt of all my bellyaching and botheration over the last year stoically. Last, but not least, thanks to Willow the cat, my sternest critic.

Contents

Chapter 1

Introduction

The current global rate of energy consumption stands at around 20 TW and is increasing by $\sim 2\%$ annually, fuelled by demand from rapidly developing countries such as China and India. With energy consumption therefore expected to double over the next 30 years [1], it is critical that the continued use of fossil fuels is limited in order to reduce greenhouse gas emissions and prevent further global warming. A full, internationally binding agreement for the reduction of emissions - to be implemented following the expiration of the Kyoto Protocol [2] in 2013 - is yet to be achieved, however some consensus has been made with the Copenhagen Accord [3], which states the long-term goal of limiting climate change to a rise in the average global temperature of no more than 2°C. The achievement of this goal is critically dependent on the development and implementation of new sources of renewable energy. Currently, the combined gamut of renewables - hydro, geothermal, biomass, wind and solar PV - contributes to approximately 16% of the total global capacity for energy production [4] and is expected to increase to around 25% by 2030.

Solar PV, while currently far from being the dominant renewable technology (contributing less than 1% to the total renewables market [5]), holds the greatest potential for long-term increases in capacity, compared to other technologies, due to the high abundance of solar energy available (the average 'on-land' solar irradiance being >100,000 TW). The total installed PV capacity, reportedly 40 GW in 2010 [5], is increasing annually by around 40% and further increases are expected as the costs of module production decrease further and as conversion efficiencies continue to rise. The biggest market for PV is within the EU which contributes to over 80% of the installed capacity - Germany alone is responsible for

1

almost half this.

The dominant PV technology, crystalline silicon, has recently received significant competition from emerging thin-film technologies such as CdTe, CIGS and amorphous Si. The key advantage of thin-film PV is the large potential for cost reduction afforded by the use of much thinner semiconductor layers (e.g. on the scale of several μm compared to hundreds of μm for crystalline Si) and relatively impure materials. To date the most successful thin-film technology is that based on CdTe with the likes of the company First Solar, the world's second largest PV manufacturer in 2011, now producing over 2 GW per annum at a cost of less than 1\$/W$_p$ [6].

One of the biggest misgivings about the widespread use of CdTe PV is the toxicity of cadmium. However, it has been shown that over the life-cycle of a CdTe module the only significant Cd emissions are those associated with the burning of fossil fuels during fabrication. Relative to crystalline Si PV the energy payback times for thin-film technologies are lower, due to the reduced processing energy requirements, and so the Cd emissions associated with Si PV is in fact higher than that for CdTe PV [7]. Furthermore, environmental assessments of the destruction of CdTe modules by fire have shown that over 99.96% of the Cd is retained within the modules by the glass encapsulation which becomes molten and prevents toxic exposure [8]. The biggest barrier to the increased uptake of CdTe PV is due to the scarcity of tellurium which is expected to limit production to around 20 GW per year by 2020 [9] unless key materials and technological challenges, namely the increase of module efficiency and the thinning of CdTe absorber layers, are met [10, 11].

CdTe PV is the main focus of this work and all investigations are performed within its context. A key theme is the use of radio frequency magnetron sputtering (RFMS) for the deposition of the transparent conducting oxide (TCO) front contact layers for CdTe devices. RFMS has some significant advantages over other techniques, such as chemical vapour deposition (CVD), for the deposition of TCOs: The technique's use of a confined plasma permits the deposition of a wide range of materials at relatively low temperatures and the nature of the deposition process permits a large degree of control over the resultant film properties. Furthermore, recent developments within the technological field of magnetron sputtering, such as the use of rotatable targets and pulsed deposition modes [12], permits the achievement of high material utilisation efficiencies compared to those for techniques

that involve liquid chemical precursors (even if these precursors are recycled).

The use of TCOs is ubiquitous across most PV technologies, but to date their largest application is in flat-panel display devices and low emissivity windows. The most widely used TCO material is Sn doped In_2O_3 (ITO) - it having a market share in 2010 of over 97% [13]. However, the long term use of ITO is considered unsustainable due to the increasing scarcity and cost of indium [14]. This work uses RFMS to develop Zn and Sn based alternatives to ITO that have comparable performance characteristics. It must be noted that while these materials are investigated with their application to CdTe PV in mind, there is great potential for their application in many other fields.

This work also focusses on the use of RFMS for the fabrication of entire CdTe device structures. Fully-sputtered CdTe solar cells have been demonstrated as having comparable efficiencies, i.e. $> 14\%$ [15, 16], to those which employ more traditional deposition techniques such as close space sublimation (CSS). The key advantage, at the laboratory scale, of using RFMS for generating complete devices is the high degree of film uniformity and run-to-run reproducibility that the technique affords. Therefore, any experiment that involves a series of devices in which a single parameter is varied, e.g. the thickness of a constituent layer, is likely to determine, with a high confidence, the effect of that parameter (if any) on the device performance. Furthermore, the uniformity of sputtered films and their sub-micron grain structures mean that they lend themselves very well to characterisation via optical techniques such as spectrophotometry and ellipsometry. These techniques are advantageous as they are non-destructive and relatively straight forward to perform, although subsequent analysis of the data can be challenging in some cases.

The development and optimisation of CdTe device structures typically adopts some systematic, experimental approach that involves the fabrication of a large number of lab-scale devices. Due to the complexity of the material interactions (optical, electrical, chemical and structural) it is very difficult to develop an all encompassing theoretical model for the resultant performance of such devices. However, the uniformity of sputtered films, and the possible achievement of abrupt interfaces between each of the constituent layers, provides an excellent opportunity for optical modelling. This work aims, through the optical characterisation of the materials involved in device design, to develop a model of the multi-layer optical response of a fully-sputtered CdTe solar cell. This model will be used

to predict optimised device structures that maximise the transmittance of incident light to the CdTe absorber layer which will result in increased photo-current generation, and higher conversion efficiencies, in real devices. It is hoped that such an approach will lead to an improved device design without the experimental need to fabricate extensive sample sets, thus providing a method by which the optical design of any sputtered device can be rapidly improved.

A more detailed overview of the contents of this work is as follows:

- **Chapter 2**: A description of how a TCO material is formed and the physics detailing the opto-electrical characteristics of a TCO is presented. Further discussions concerning the necessary requirements of TCO materials with respect to CdTe based devices is included along with a review of the research literature surrounding TCOs.

- **Chapter 3**: The fundamentals of photovoltaics - i.e the photovoltaic effect, semiconductor junction formation and current-voltage characteristics - are presented followed by a specific review of CdTe based PV which includes a literature survey of recent experimental device designs and performances.

- **Chapter 4**: A full description of radio frequency magnetron sputtering is presented with specific reference to the equipment used within this work. This is followed by a description of the optical, electrical and structural characterisation techniques applied to sputtered films and devices, and the theoretical modelling methods employed.

- **Chapter 5**: The results of investigations concerning sputtered TCO materials, namely ITO, SnO:F, ZnO:Al and ZnO:F, are presented and a detailed comparison of the performance of each material is presented.

- **Chapter 6**: Device results for fully sputtered CdTe solar cells are presented with an examination of their electrical and structural properties. A discussion is also made of the most promising routes for further device optimisation.

- **Chapter 7**: A multi-layer optical model is used to predict the effect that changes to a prototype fully-sputtered device structure, presented in chapter 6, have on the fraction of light transmitted to the CdTe absorber layer. The use of the model is also demonstrated in the design of anti-reflection coatings and Bragg reflectors.

4

- **Chapter 8**: This work is concluded by a full summary of experimental results and a discussion of potential areas of future work

1.1 References

[1] F. Birol. *IEA (International Energy Agency), Paris* (2010).

[2] M. Grubb, C. Vrolijk, D. Brack. *The Kyoto Protocol: a guide and assessment.* Earthscan (1999).

[3] D. Bodansky. *American Journal of International Law* **104**, 230 (2010).

[4] E. I. A. (US), U. E. I. Administration. *International Energy Outlook, 2010.* Energy Information Administration (2010).

[5] *Renewables 2011: Global Status Report.* REN21 (2011).

[6] *First Solar Press Release* (2009). *"First solar passes* $1 *per watt industry milestone"* http://investor.firstsolar.com/releasedetail.cfm?ReleaseID=571539 - accessed Aug 2011.

[7] V. M. Fthenakis, H. C. Kim. *Thin Solid Films* **515**, 5961 (2007).

[8] V. M. Fthenakis, M. Fuhrmann, J. Heiser, A. Lanzirotti, J. Fitts, W. Wang. *Prog. Photovolt. Res. Appl.* **13**, 713 (2005).

[9] B. Anderson. *Prog. PV* **8**, 61 (2000).

[10] K. Zweibel. The Terawatt Challenge for Thin-Film PV. Technical report, NREL/TP-520-38350 (2005).

[11] K. Zweibel. *Science* **328**, 699 (2010).

[12] W. P. Leroy, S. Mahieu, D. Depla. *J. Vac. Sci. Technol. A* **28**, 108 (2010).

[13] *Indium Tin Oxide (ITO) and Replacement Markets: Insight for End Users and Material and Equipment Suppliers.* The Information Network (2011).

[14] A. C. Tolcin. *U. S. Geological Survey* (2008).
http://minerals.usgs.gov/minerals/pubs/commodity/indium/myb1-2008-indiu.pdf - accessed Aug 2011.

[15] A. Gupta, A. Compaan. *Applied Physics Letters* **85**, 684 (2004).

[16] A. Gupta, V. Parikh, A. Compaan. *Solar Energy Materials and Solar Cells* **90**, 2263 (2006).

Chapter 2

The Physics of Transparent Conducting Oxides

2.1 Introduction

High values of electrical conductivity, typically associated with metals, are considered to be due to a high density of free carriers. These free carriers partake in optical absorption processes and prevent the optical transmission of electromagnetic radiation. Transparent insulators on the other hand possess low conductivities but typically have wide direct band gaps, E_d, such that $E_d > h\nu$ for visible wavelengths, thus making them transparent over this range. There is a well known group of materials known as transparent conducting oxides (TCOs) that possess both a high conductivity and high transparency. This class of materials was first discovered by Badekar in 1907 [1] who measured the conductivity of incompletely oxidised CdO deposited by sputtering. Today, the most commonly used TCO materials exist in the form of thin films of In_2O_3, SnO_2 and ZnO which have optical transmittances of $> 80\%$ at visible wavelengths and sheet resistances typically in the range 1-100 $\Omega/\square$. They find widespread application in solar cells, displays, electro- and photochromic windows and transparent electronics.

In this chapter the physics of TCOs is described with special reference to their application in thin film solar cells. In particular, the underlying physics of a TCO's optical and electrical properties is presented in detail with the aim of evaluating optical dispersion data of relevance to solar cell design; i.e. the determination of the wavelength dependence

of refractive index n and extinction coefficient κ from transmittance measurements.

Section 2.2 gives a qualitative overview of some important concepts relevant to TCOs and in section 2.3, the accepted models that describe the frequency dependence of the dielectric permittivity $\varepsilon(\omega)$ are reviewed in detail. Section 2.4 discusses the requirements of TCOs for use in thin film PV devices and the chapter is concluded with a review of some key TCO materials.

2.2 Energy bands and conductivity in TCOs

The properties of TCOs may be described in terms of their behaviour as wide band gap semiconductors having direct band gaps in the range $3-4$ eV. Such materials are evidently transparent to visible wavelengths ($1.8-3.1$ eV). In the absence of donor or acceptor states thermal excitation across the band gap is negligible; the Fermi level is positioned mid-gap and the material is insulating as shown in figure 2.1a.

For the case of there being a population of shallow donors (figure 2.1b) thermal excitation is sufficient to promote electrons from the donor states into the conduction band as approximated by a Fermi distribution. As a result of this population the Fermi level re-locates from mid-gap to a point just below the conduction band [2, 3]. In a metal/oxide system such shallow donor states originate from native defects, notably the oxygen vacancy V_O. In this case, an oxygen ion O^{2-} may be considered to have been removed from the lattice resulting in the loss of the covalent bond to an adjacent metal ion. The remaining metal ion donates two electron states to the lattice which are located, in terms of energy, just below the bottom of the conduction band (figure 2.1b). Note that oxygen vacancies typically occur naturally in as deposited material. It is however, possible to introduce further shallow donor states through the incorporation of extrinsic dopants that are substituted into the lattice at either the metallic (anion) sites or the oxygen (cation) sites. In the case of anion doping, a metal ion is introduced that has a different valency from that of the original host ion. For example, in the case of In_2O_3, the In^{3+} anion can be substituted with a Sn^{4+} ion. This ion again bonds covalently to the surrounding oxygen but contributes a single shallow donor state, X_M, just below the conduction band. Alternatively, a dopant with a valency of VII could be introduced to substitute at the oxygen

sites. A single shallow donor would again be introduced. Examples of commonly used cation dopants include fluorine and chlorine.

At relatively low concentrations of donor states the Fermi level remains within the band gap, but at a position very close to the bottom of the conduction band. However, as the density of these states increases they form a continuous band which continues to broaden
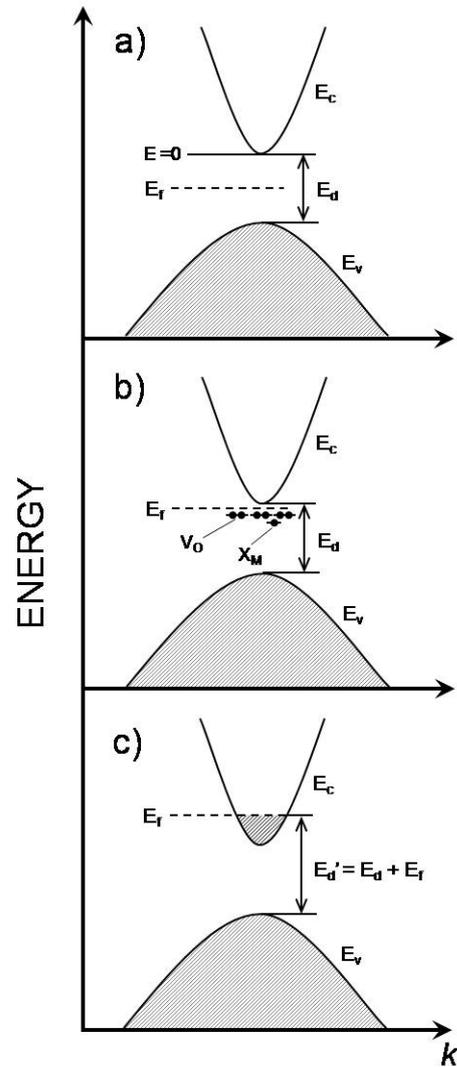
Figure 2.1: Energy band and diagrams relevant to TCO behaviour: (a) An intrinsic semiconductor for which E_f is located mid-gap. (b) A semiconductor with a population of shallow donors (oxygen vacancies, V_O, and metal ion dopants, X_M). Here E_f is positioned just below the bottom of the conduction band. (c) A heavily doped 'degenerate' semiconductor, i.e. $n_e > n_{crit}$. Here E_f is located within the conduction band.

as more states are added. At some critical density, known as the *Mott transition point* [4], the impurity band and conduction band merge to the extent that the Fermi level is effectively pushed into the conduction band, as shown in figure 2.1c. At this point the material gains a permanent (degenerate) population of free charge carriers and enters into a metallic-like conduction regime. Despite this metallic behaviour, the material's direct band gap is maintained so that it is still transparent to photons of energy less than E_d.

2.3   Models of the dielectric function relevant to TCOs

The previous section is now expanded upon by introducing a mathematical framework that describes, in detail, the effect that a population of donor states has on both the optical and electrical properties of a transparent conducting oxide. For any TCO material, all its opto-electronic properties are embodied by a single complex function, the *dielectric permittivity*,

$$\varepsilon = \varepsilon_1 - \mathrm{i}\varepsilon_2 \tag{2.1}$$

where ε_1 and ε_2 are the real and imaginary components respectively. It is these components and how they relate to measurable quantities such as carrier density and absorption coefficient that will be the main focus of the following sections. In particular, it is important to know the relation between the dielectric permittivity and the *complex refractive index*, $\tilde{n}$, the components of which can be extracted via analytical techniques from transmittance spectra (see section 4.2.4). The dielectric permittivity is related to the complex refractive index, $\tilde{n}$, according to

$$\varepsilon = \tilde{n}^2 = (n - \mathrm{i}\kappa)^2 \tag{2.2}$$

where n is the real refractive index and κ is the extinction coefficient. ε_1 and ε_2 are thus related to n and κ according to

$$\varepsilon_1 = n^2 - \kappa^2 \tag{2.3}$$

$$\varepsilon_2 = 2n\kappa \tag{2.4}$$

and conversely

$$n = \left(\frac{\sqrt{\varepsilon_1^2 + \varepsilon_2^2} + \varepsilon_1}{2} \right)^{1/2} \tag{2.5}$$

11

$$\kappa = \left(\frac{\sqrt{\varepsilon_1^2 + \varepsilon_2^2} - \varepsilon_1}{2} \right)^{1/2} \tag{2.6}$$

Throughout this thesis the frequency dependent behaviour of materials shall be referred to in terms of either ε_1 and ε_2 or n and κ as is most appropriate to the discussion.

The theoretical models used to describe the variation with frequency of ε are either classical or quantum mechanical in nature. In section 2.3.1, the classical models that account for the behaviour due to both bound and free electrons are presented. These theories require no knowledge of the band structure of the material. Secondly, the band structure and the effect of inter-band transitions across a direct band-gap are modelled explicitly according to a quantum mechanical basis as described in section 2.3.2.

2.3.1 Classical models of insulating and metallic behaviour

The Lorentz oscillator model (for insulators)

In an ideal intrinsic semiconductor system, all electrons are bound to their respective atoms within the crystal structure. The Lorentz oscillator model predicts the frequency dependence of the dielectric function for according to classical postulates: Electrons are considered bound to nuclei by Hookean springs (having orbital dependent stiffness) and respond to electromagnetic radiation by simple harmonic motion about their equilibrium positions at a resonant frequency ω_0. Such a system generates an electric dipole moment, for each electron/atom pair, of the form

$$\mathbf{p} = e\mathbf{r} \tag{2.7}$$

where e is the electronic charge and $\mathbf{r}$ is the displacement of the electron from its equilibrium position. An AC electric field, such as that associated with an incident light wave, will act to drive the electron at a frequency ω. If $\omega = \omega_0$ then energy from the light wave will be absorbed resonantly. If $\omega \neq \omega_0$ then the incident wave continues to drive the oscillator at a frequency ω but with a phase that lags behind that of the wave. The wave is therefore permitted to travel though the material, without absorption, but at a reduced velocity, i.e. the material has a refractive index > 1.

The displacement of such bound electrons in response to an incident light wave is described by the following equation of motion

$$m_e \frac{d^2\mathbf{r}}{dt^2} + m_e\gamma\frac{d\mathbf{r}}{dt} + m_e\omega_0^2\mathbf{r} = -e\mathbf{E} \qquad (2.8)$$

where m_e is the effective electron mass and γ is a damping coefficient. On the left hand side of the equation, the first term represents the acceleration generated by the external field. The second term represents the damping of the motion of the electron and may be considered to be due to electron-phonon collisions within the system. Finally the third term describes the restoring force on the electron of the spring that binds it to its nucleus.

By considering a time dependant electric field of the form $\mathbf{E} = \mathbf{E}_0\exp(-i\omega t)$, where $\mathbf{E}_0$ is the amplitude of the oscillation, equation 2.8 can be solved by looking for solutions with the same time dependence as $\mathbf{E}$ [5]. Thus,

$$\mathbf{r} = \frac{1}{m_e}\frac{-e\mathbf{E}}{\omega_0^2 - \omega^2 + i\omega\gamma} \qquad (2.9)$$

The form of the dielectric permittivity ε can be derived from the relation between the electric displacement $\mathbf{D}$ of the medium and the electric field

$$\mathbf{D} = \varepsilon_0\varepsilon\mathbf{E} = \varepsilon_0\mathbf{E} + \mathbf{P} \qquad (2.10)$$

where $\mathbf{P}$ is the macroscopic polarisation of the material defined as the number of electric dipoles per unit volume

$$\mathbf{P} = Ne\mathbf{r} = \varepsilon_0\mathbf{E}\left(\varepsilon - 1\right) \qquad (2.11)$$

in which N is the number of atoms per unit volume, assuming here that there is one electron per atom. The dielectric permittivity due to a system of bound electrons represented by Lorentz oscillators may therefore be defined by

$$\begin{aligned}
\varepsilon &= 1 + \frac{Ne\mathbf{r}}{\varepsilon_0\mathbf{E}} \\
&= 1 - \frac{e^2 N}{m_e\varepsilon_0}\left(\frac{1}{\omega_0^2 - \omega^2 + i\gamma\omega}\right) \qquad (2.12)
\end{aligned}$$

and the real and imaginary components may be separated and written as

$$\varepsilon_1 = 1 + \frac{Ne^2}{m_e\varepsilon_0}\left[\frac{(\omega_0^2 - \omega^2)}{(\omega_0^2 - \omega^2)^2 + (\gamma\omega)^2}\right] \qquad (2.13)$$

13
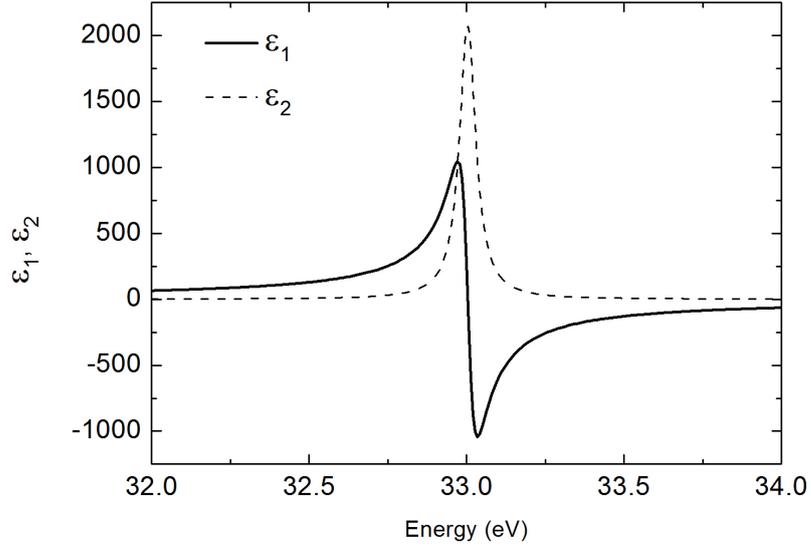
Figure 2.2: The functional form of real and imaginary components, ε_1 and ε_2, according to the Lorentz model. Values of $N = 7.8 \times 10^{22}$ cm^{-3} and $\hbar\omega_0 = 33$eV were used to calculate the component shapes. These values are associated with In$_2$O$_3$.

$$\varepsilon_2 = \frac{Ne^2}{m_e\varepsilon_0}\left[\frac{\gamma\omega}{(\omega_0^2 - \omega^2)^2 + (\gamma\omega)^2}\right] \tag{2.14}$$

For a real metal oxide system each atom will possess multiple electrons that will be arranged in a series of shells. This arrangement can be accounted for simply by assigning springs of different stiffnesses to the electrons of each shell. Therefore the resonant frequency ω_0 of each electron will depend on which orbital it occupies. Typically, the electrons in the outer shell, i.e. the valence electrons, will have the lowest ω_0 as they are the most weakly bound to the atom. It is sufficient to describe the polarisation response of the system to an external electric field in terms of these valence electrons alone. Therefore, in the case of a metal oxide, it is appropriate to multiply N in equation 2.12 by the average valency of the system.

An example of the use of the Lorentz model to describe the dielectric function and thin-film optical transmission properties is now presented: The parameters chosen for the model are representative (nominally) of In$_2$O$_3$. They are an electron density of $N = 7.8 \times 10^{22}$ cm^{-3} and a resonant energy of $\hbar\omega_0 = 33$ eV (this energy is deep in the UV). Figure 2.2 shows the variation of ε_1 and ε_2 calculated using equations 2.13 and 2.14. Both components
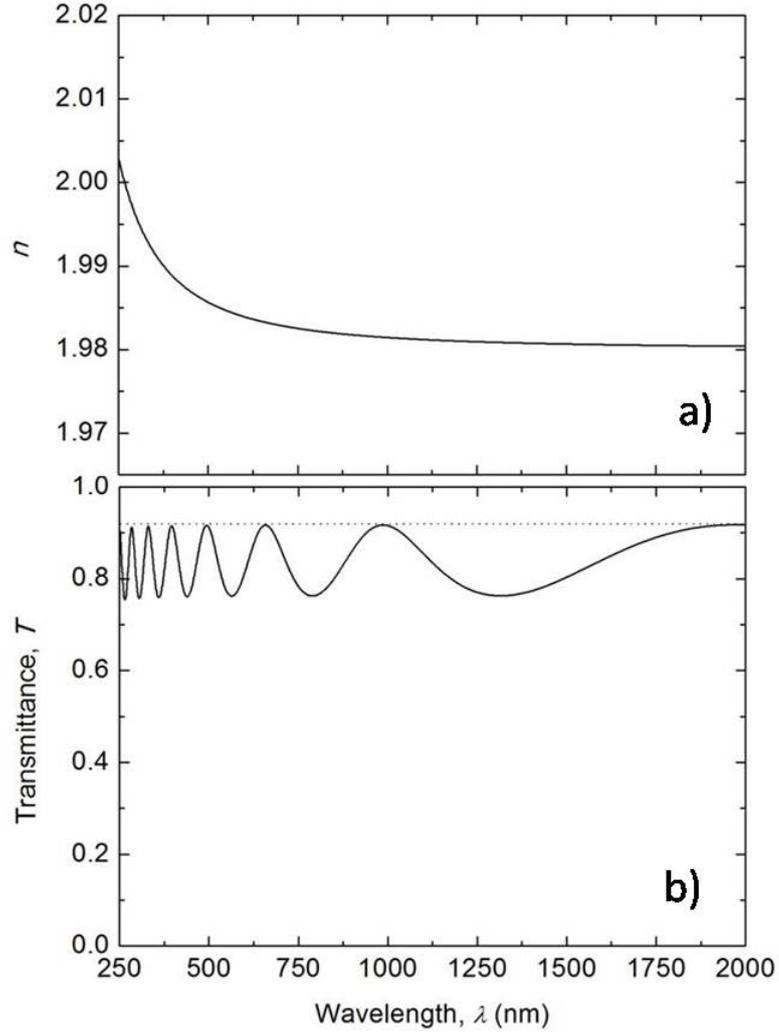
Figure 2.3: The dispersion of the refractive index and the resultant transmittance spectrum of a thin film (nominally of In_2O_3) modelled as using a single Lorentz oscillator with a resonance deep in the UV. (a) The refractive index that arises within the range shown is smoothly varying and almost constant. The extinction coefficient, κ is virtually zero. (b) The transmittance spectra for a thin film of thickness 500 nm on a non-absorbing substrate.

show resonant behaviour at the energy corresponding to the natural frequency ω_0, with ε_1 showing an overall change from positive to negative values as the energy increases through $\hbar\omega_0$, and ε_2 showing a peak at 33 eV. Figure 2.3a shows the dispersion of the refractive index calculated using equation 2.5 for the range of wavelengths most applicable to solar cell design. At wavelengths above the material's band gap (typically 330 nm, i.e. 3.75 eV,

for In_2O_3) the refractive index reaches an almost constant value of 1.98. The value of κ (not shown) is almost zero over this range. Figure 2.3b shows the corresponding transmittance spectrum for a thin film of this material having a thickness of 500 nm and being on a non-absorbing substrate that has a constant refractive index $n = 1.5$. Interference fringes in the spectra are generated by coherent and incoherent reflections from the film/air and substrate/film interfaces.

The Lorentz oscillator model is generally considered sufficient to accurately predict the magnitude of the dielectric permittivity for a system of bound electrons, such as that in a metal oxide, over the range of wavelengths associated with solar cell design.

The Drude Model

Now considerations are made of the metallic-like behaviour of a highly doped metal oxide system in which there is a population of 'free' electrons which are responsible for electrical conduction. The Drude model [6] defines these free electrons classically as solid particles that are de-localised from an assembly of large, positively charged ions. In a doped semiconductor, these positively charged ions are represented by ionized impurities (e.g. metal dopant atoms or oxygen vacancies). The free electrons are scattered, as before, by their interactions with phonons, but are now additionally scattered by the ionized impurities according to a Coulomb interaction [7–9]. Despite the underlying complexity, the Drude model approximates all electron interactions as instantaneous, elastic collisions.

The equation of motion of the free electrons in response to an external electric field is identical to that in equation 2.8 with the restoring force term removed, i.e.

$$m_e \frac{d^2\mathbf{r}}{dt^2} + \frac{m_e}{\tau}\frac{d\mathbf{r}}{dt} = -e\mathbf{E} \tag{2.15}$$

Here γ (from equation 2.8) is written as $1/\tau$, where τ is the average time between collisions, and is defined by

$$\gamma = \frac{1}{\tau} = \frac{1}{\tau_p} + \frac{1}{\tau_{ii}} \tag{2.16}$$

where the subscripts 'p' and 'ii' represent scattering due to phonons and ionized impurities respectively. It is of interest to see how the electrons respond to a constant DC electric field as this defines some useful quantities. Under an applied DC electric field equation 2.15 has a steady state solution which yields a linear relationship between the velocity $\mathbf{v}$

16

of the electrons and the magnitude of the field, i.e.

$$\frac{d\mathbf{r}}{dt} = \mathbf{v} = \frac{-e\tau}{m_e}\mathbf{E} \qquad (2.17)$$

and we define

$$\mu_e = \frac{e\tau}{m_e} \qquad (2.18)$$

as the proportionality factor between $\mathbf{v}$ and $\mathbf{E}$ known as the *electron mobility*. Equation 2.17 can also be re-written in terms of the macroscopic quantity, current density $\mathbf{j}$

$$\mathbf{j} = -n_e e\mathbf{v} = \frac{n_e e^2 \tau}{m_e}\mathbf{E} = \sigma_0 \mathbf{E} \qquad (2.19)$$

where n_e is the density of free electrons within the system and now the constant of proportionality provides the definition of the system's DC electrical conductivity σ_0

$$\sigma_0 = \frac{1}{\rho} = \frac{n_e e^2 \tau}{m_e} = n e \mu_e \qquad (2.20)$$

where ρ is the resistivity. Note that the subscript '0' indicates the fact that the electric field is static, i.e. $\omega = 0$. These quantities, μ_e and σ_0, are important because they describe the practical electrical behaviour of the system and are easily measured (see section 4.1.1). Inevitably, the behaviour of a material's DC conductivity is inextricably linked to its AC behaviour (i.e. it's optical behaviour). The effects of a time varying electric field associated with a light wave are now described.

Again, as with the Lorentz oscillator, the introduction of an AC electric field of the form $\mathbf{E} = \mathbf{E}_0 \exp(-i\omega t)$ to the system is considered. The acceleration term in 2.15 is now non-zero and so the expression for the electron velocity $\mathbf{v}$ must be re-written as

$$\mathbf{v} = \frac{e\tau}{m_e(1 - i\omega\tau)}\mathbf{E} \qquad (2.21)$$

Re-writing this in terms of $\mathbf{j}$ leads to the definition of a complex, frequency dependent conductivity, sometimes referred to as the *optical* conductivity,

$$\sigma(\omega) = \sigma_0 \left(\frac{1}{1 - i\omega\tau}\right) \qquad (2.22)$$

which, expanding to separate the real and imaginary parts becomes

$$\sigma(\omega) = \sigma_0 \left(\frac{1}{1 - \omega^2\tau^2}\right) + i\frac{\sigma_0}{\omega\varepsilon_0}\left(\frac{1}{1 + \omega^2\tau^2}\right) \qquad (2.23)$$

The form of the dielectric permittivity ε resulting from such a system of free electrons can now be derived by considering Maxwell's third equation

$$
\begin{aligned}
\nabla \times \mathbf{H} &= \varepsilon_0 \varepsilon_\infty \frac{\partial \mathbf{E}}{\partial t} + \mathbf{j} \\
&= \omega \varepsilon_0 \varepsilon_\infty \frac{\partial \mathbf{E}}{\partial t} + \frac{\sigma(\omega)}{i\omega} \frac{\partial \mathbf{E}}{\partial t} \\
&= \varepsilon_0 \left(\varepsilon_\infty + \frac{\sigma(\omega)}{i\omega\varepsilon_0} \right) \frac{\partial \mathbf{E}}{\partial t}
\end{aligned}
\tag{2.24}
$$

where $\mathbf{H}$ is the magnetic field strength and ε_∞ is defined as the high frequency dielectric constant associated with the interaction of the field with a system of bound electrons according to the previous Lorentz oscillator model. The dielectric permittivity is therefore defined as the term in brackets in equation 2.24,

$$
\varepsilon(\omega) = \varepsilon_\infty - \frac{i\sigma(\omega)}{\omega\varepsilon_0}
\tag{2.25}
$$

and expanding this in terms of its real and imaginary components yields

$$
\varepsilon(\omega) = \underbrace{\varepsilon_\infty - \frac{\sigma_0}{\varepsilon_0} \left(\frac{\tau}{1 + \omega^2\tau^2} \right)}_{\varepsilon_1} + \underbrace{\frac{i\sigma_0}{\omega\varepsilon_0} \left(\frac{1}{1 + \omega^2\tau^2} \right)}_{\varepsilon_2}
\tag{2.26}
$$

Figure 2.4a shows the functional form of ε over the wavelength range 250 - 2000 nm for a variety of carrier concentrations that are all typical of a degenerately doped TCO system (i.e. $n_e > 10^{18}$ cm^{-3}) and figure 2.4b shows the corresponding curves for n and κ. In all cases, the real component ε_1 decreases from its constant background value (attributed to the Lorentz oscillator), with increasing wavelength. Eventually, ε_1 becomes negative and it is at this point that the material enters into a highly reflective regime and wherein the transmittance, shown in figure 2.4c, drops off rapidly (The transmittance curves were calculated using dispersion data according to the methods described in section 4.3.2). The frequency at which $\varepsilon_1 = 0$ is defined as the *plasma frequency* ω_p and from 2.26 this is expressed as

$$
\omega_p = \sqrt{\frac{\sigma_0}{\varepsilon_\infty\varepsilon_0\tau} - \frac{1}{\tau^2}}
\tag{2.27}
$$

which may be approximated to

$$
\omega_p \approx \sqrt{\frac{\sigma_0}{\varepsilon_\infty\varepsilon_0\tau}} = \sqrt{\frac{n_e e^2}{m_e\varepsilon_\infty\varepsilon_0}}
\tag{2.28}
$$
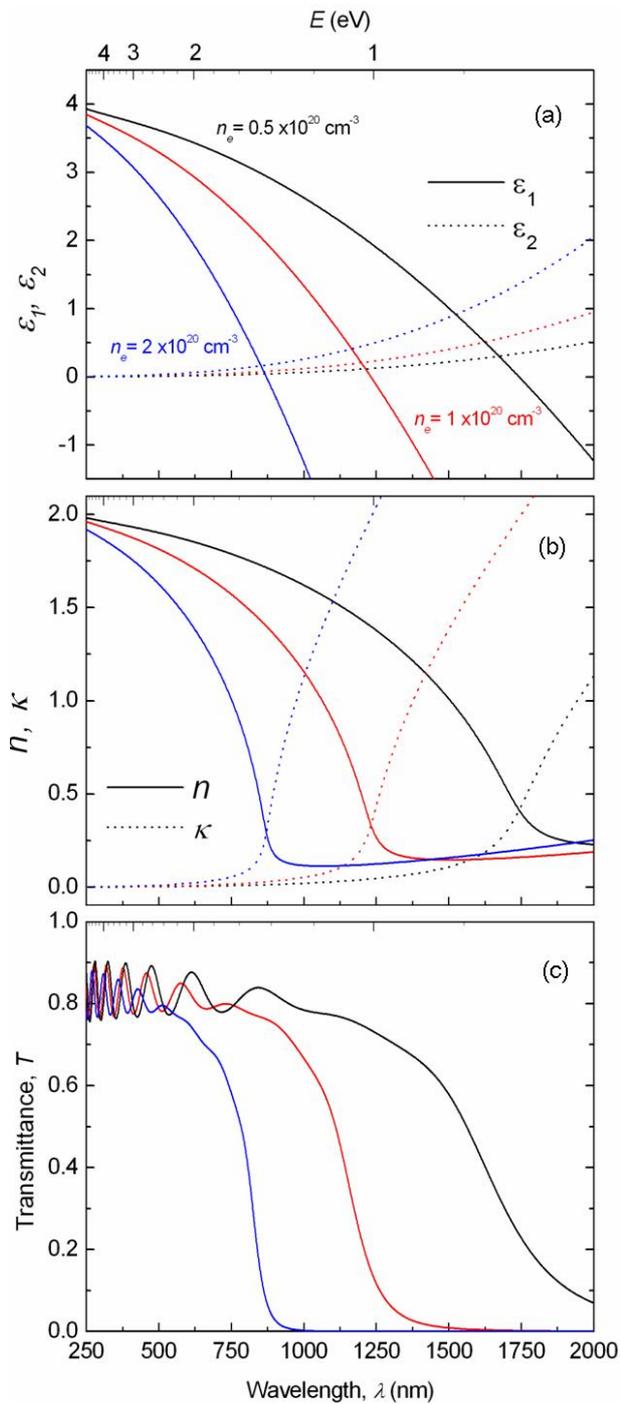
Figure 2.4: (a) The functional form of the real and imaginary components, ε_1 and ε_2, of the dielectric permittivity according to the Drude model for carrier concentrations n_e of 0.5, 1.0 and 2.0×10^{20} cm^{-3} respectively. (b) The subsequent forms of n and κ. Note that even though κ increases rapidly at wavelengths above the plasma edge $n < 1$, i.e. the film is highly reflective (metallic). (c) Transmittance spectra for corresponding doping densities. The location of the plasma edge obeys the relation $\omega_p \propto \sqrt{n}$ and at carrier concentrations $n_e > 2 \times 10^{20}$ cm^{-3}, the plasma edge encroaches into the visible wavelength range. See section 4.3.2 for details of the calculations of these curves.

The key feature of this equation is that $\omega_p \propto \sqrt{n_e}$. Thus the location of the *plasma edge* in transmittance spectra can be tailored by means of the doping level. In other words, the trade-off between the material's electrical and optical properties can be controlled exclusively by the magnitude of n_e, a process dependent parameter. The ability to control n_e experimentally for any metal oxide system is crucial and is the primary focus of Chapter 5.

The Drude model can be extended by incorporating a frequency dependent scattering time $\tau(\omega)$. This is necessary in order to describe the behaviour of a real material in which the interactions between electrons and structural defects (e.g. grain boundaries) must also be accounted for [10, 11]. The following expression is used to define $\tau(\omega)$ [12]

$$\frac{1}{\tau(\omega)} = \gamma(\omega) = \gamma_{low} - \frac{\gamma_{low} - \gamma_{high}}{\pi} \left\{ \tan^{-1} \left(\frac{\omega - \omega_{cross}}{\omega_\delta} \right) \right\} \tag{2.29}$$

where $\gamma(\omega)$ is the corresponding frequency dependent collision rate (or damping factor), γ_{low} is the collision rate as $\omega \to 0$, γ_{high} is the collision rate as $\omega \to \infty$, ω_{cross} defines the point at which the transition between γ_{high} and γ_{low} occurs and ω_δ defines the width of the transition. An example of a typical shape for $\tau(\omega)$ is shown in figure 2.5. Note that a consequence of a frequency dependent scattering time is a frequency dependent electron mobility. Therefore, in principle, the mobility of a real material determined from a DC electrical measurement (i.e. $\omega = 0$) should correspond to the value of γ_{low}.

This concludes the discussion of the use of classical models in predicting the behaviour of ε for highly doped metal oxide systems. Together, the Lorentz and Drude models, despite their very basic assumptions, can be used effectively to predict the response of bound and free electrons to both the time varying electric field (associated with a light wave) and the constant DC field associated with simple electrical measurements. However, these classical models are incapable of accounting for the behaviour in the vicinity of a material's band-gap.

2.3.2 Inter-band transition model

To describe how a TCO material responds to wavelengths of light having energies close to its direct band gap energy E_d we must consider a quantum mechanical theory of inter-band transitions between the valence and conduction bands. This requires a mathematical
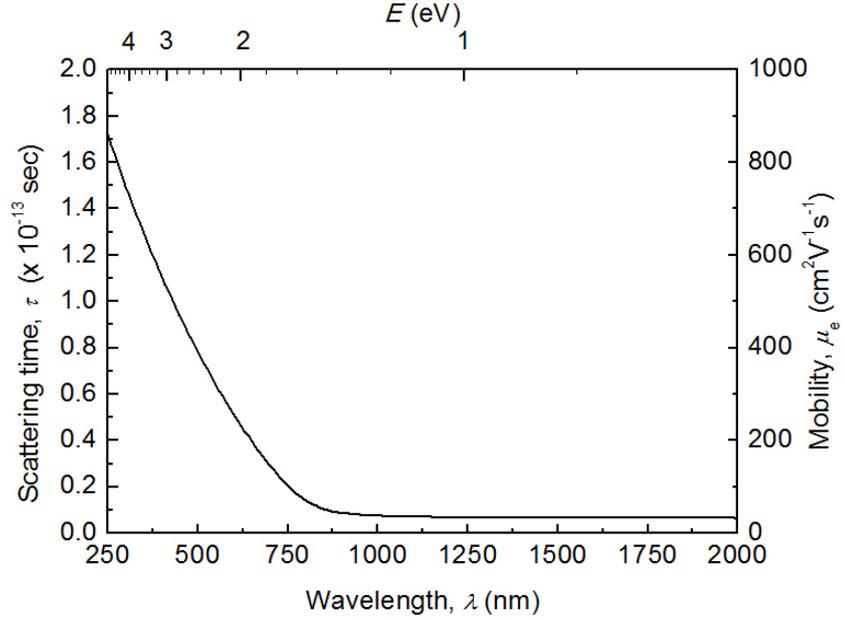
Figure 2.5: Wavelength dependence of the scattering time τ according to the extended Drude model for parameter values of $\hbar\omega_{cross} = 1.5$ eV, $\hbar\omega_\delta = 0.19$ eV, $\gamma_{low} = 1.7 \times 10^{14}$ s^{-1}, $\gamma_{high} = 3.0 \times 10^{12}$ s^{-1}. These values are typical of a TCO material. The corresponding wavelength dependence of the electron mobility is also shown. At longer wavelengths (i.e. > 1000 nm) the electron mobility is consistent with typical values determined via DC electrical measurements (e.g. Hall effect) in polycrystalline thin films.

formulation of the qualitative description provided in section 2.2. The key assumption, on which all proceeding theory is based, is that close to the band gap the shape of valence and conduction bands is parabolic and that their respective maxima and minima occur at the same momentum wave-number, $k = 0$. For simplicity the bottom of the conduction band is defined as the zero of energy (see figure 2.1). The $E - k$ relations of each of the bands can therefore be described mathematically by

$$E_c = \frac{\hbar^2 k^2}{2m_e} \tag{2.30}$$

$$E_v = -\frac{\hbar^2 k^2}{2m_h} - E_d \tag{2.31}$$

where and m_e and m_h are the effective masses of electrons within the conduction band and in the valence band bands respectively and are expressed in units of the electron rest mass

m_0 [13].

This parabolic band model is used to determine the component of the dielectric permittivity, close to the band gap, that must be added to the existing background (that has already been defined above by the classical Lorentz and Drude models) in order to fully describe the opto-electric behaviour of transparent conducting oxides. We begin with an analysis of an ideal, intrinsic semiconductor and then incorporate the effects of heavy doping and impurity states. The effects of possible indirect transitions are also discussed.

Direct Transitions

For a direct (i.e. vertical) transition to occur between the bands at a particular value of k a photon of energy

$$\hbar\omega_{cv} = E_c - E_v = \frac{\hbar^2 k^2}{2m_r} + E_d \tag{2.32}$$

is required where the subscript 'cv' denotes a transition to the conduction band from the valence band and where m_r is the *reduced* electron mass defined by

$$m_r = \frac{m_e m_h}{m_e + m_h} \tag{2.33}$$

The probability, P_{cv}, that in a given time, t, a photon will be absorbed and induce a transition is derived from time dependent first-order perturbation theory [14]

$$P_{cv} = |H_{cv}|^2 \frac{\sin^2\left[\frac{1}{2}(\omega - \omega_{cv})t\right]}{\hbar^2(\omega - \omega_{cv})^2} \tag{2.34}$$

Here, the perturbation's matrix element is defined by

$$|H_{cv}|^2 = \frac{2e^2 I(\omega)|\mathbf{p}_{cv}|^2}{3m_0^2 n \varepsilon_0 c \omega^2} \tag{2.35}$$

where $I(\omega)$ is the intensity of the incident light and $|\mathbf{p}_{cv}|^2$ is the square of the momentum matrix element, given by

$$\mathbf{p}_{cv} = -ih \int \psi_c^* \nabla \psi_v d\mathbf{r} \tag{2.36}$$

The wave functions ψ_c and ψ_v are represented by the Bloch functions

$$\psi_v = u_v(\mathbf{r}, \mathbf{k}_v) \exp i\mathbf{k}_v \cdot \mathbf{r}, \quad \psi_c = u_c(\mathbf{r}, \mathbf{k}_c) \exp i\mathbf{k}_c \cdot \mathbf{r} \tag{2.37}$$

where $\mathbf{k}_c$ and $\mathbf{k}_v$ are the corresponding momentum wave vectors of the two states and $u_c(\mathbf{r}, \mathbf{k}_c)$ and $u_v(\mathbf{r}, \mathbf{k}_v)$ that are typically trigonometric functions, the periodicity of which match that of the lattice.

To account for all the possible transitions between all pairs of states separated by $\hbar\omega_{cv}$ it is necessary to integrate equation 2.34 over all frequencies. Thus

$$P_{cv}(t) = |H_{cv}|^2 \int_0^\infty \frac{\sin^2\left[\frac{1}{2}(\omega - \omega_{cv})t\right]}{\hbar^2(\omega - \omega_{cv})^2} g(\hbar\omega_{cv})\hbar d\omega \tag{2.38}$$

gives the transition probability, where $g(\hbar\omega_{cv})$ is the *joint density of states* (JDOS) for the valence and conduction band combined. For non-infinitesimal times, the integral returns the value $\pi t/2$ and so the probability of a transition occurring in a time t is given by

$$P_{cv}(t) = \frac{e^2 I(\omega)|\mathbf{p}_{cv}|^2 g(\hbar\omega_{cv})\pi t}{3m_0^2 n\varepsilon_0 \hbar\omega^2} \tag{2.39}$$

The number of wave vector states in a shell of infinitesimal width dk is given as

$$g(k_{cv})dk = \frac{4\pi k^2}{(2\pi/L)^3}dk = \frac{Vk^2}{2\pi^2}dk \tag{2.40}$$

where L denotes the spacing between each state and V is the volume in k-space taken up by a single state (i.e. $V = L^3$). Note that each wave vector state may by occupied by two energy states according to the Pauli exclusion principle and therefore

$$g(\hbar\omega_{cv})dE = 2g(k_{cv})dk \tag{2.41}$$

Using the relation in equation 2.32 the JDOS of the system may be derived as

$$g(\hbar\omega_{cv}) = \frac{V(2m_r)^{\frac{3}{2}}}{2\pi^2\hbar}(\hbar\omega - E_d)^{\frac{1}{2}} \tag{2.42}$$

A useful, measurable quantity can now be defined that relates the intensity of the incident light to the transition probability and hence to the imaginary component of the dielectric function ε_2. The *absorption coefficient* α is defined as the fractional decrease in intensity with distance x through the material [13], expressed in units of inverse length.

$$\alpha = -\frac{1}{I(\omega)}\frac{dI(\omega)}{dx} = \frac{\hbar\omega P_{cv}}{I(\omega)Vt} \tag{2.43}$$

$$= \frac{e^2|\mathbf{p}_{cv}|^2}{6\pi m_0^2 n\varepsilon_0 c\omega}\left(\frac{2m_r}{\hbar^2}\right)^{3/2}(\hbar\omega - E_d)^{1/2} \tag{2.44}$$

α may also be related to the extinction coefficient by

$$\alpha = \frac{2\omega\kappa}{c} \tag{2.45}$$

and so using this relation along with equations 2.43 and 2.4, the form of the component ε_2 can be derived for direct inter-band transitions, i.e.

$$\varepsilon_2 = \frac{e^2|\mathbf{p}_{cv}|^2}{3\pi m_0^2 \varepsilon_0 \omega^2} \left(\frac{2m_r}{\hbar^2}\right)^{3/2} (\hbar\omega - E_d)^{1/2} \tag{2.46}$$

Figure 2.6a shows the shape of this relation for a material with a direct band gap of E_d = 3.75 eV, which is typical of a metal oxide material. At energies above the band gap, ε_2 exhibits the $(\hbar\omega - E_d)^{1/2}$ dependence associated with the JDOS of the system, whereas below the band gap, $\varepsilon_2 = 0$ and the material is non-absorbing as expected.

There is no analogous derivation for the real component of the dielectric permittivity ε_1. However, the relation between ε_1 and ε_2 is such that knowing one means that the other can be defined. This is according to the Kramers-Kronig relation [15, 16]

$$\varepsilon_1 = 1 + \frac{2}{\pi}\mathcal{P}\int_0^\infty \frac{\omega'\varepsilon_2(\omega')}{\omega'^2 - \omega^2} \tag{2.47}$$

where $\mathcal{P}$ denotes the principal value. The use of ω' is necessary as the causality of a change in ε_2 at ω' does not typically generate a change in ε_1 at the same ω' but at an another frequency ω. Applying equation 2.47, ε_1 is determined as

$$\varepsilon_1 = 1 + \frac{e^2|\mathbf{p}_{cv}|^2}{3\pi m_0^2 \varepsilon_0 \omega^2} \left(\frac{2m_r}{\hbar^2}\right)^{3/2}$$
$$\times [2E_d - E_d^{1/2}(E_d + \hbar\omega)^{1/2} - E_d^{1/2}(E_d - \hbar\omega)^{1/2}\Theta(E_d - \hbar\omega)] \tag{2.48}$$

where

$$\Theta(E_d - \hbar\omega) = \begin{cases} 1 & \text{if } E_d > \hbar\omega \\ 0 & \text{if } E_d < \hbar\omega \end{cases} \tag{2.49}$$

Knowing the form of both components of the complex dielectric permittivity due to direct transitions and superimposing their shape onto a background generated by the classical models now permits the calculation of the transmittance in the vicinity of the band gap, see figure 2.6b. The effect of a direct band gap is to produce a sharp cut-off at energies above E_d. Such a sharp transition between a transparent and absorbing region does not occur in a real semiconducting material and is usually smoothed over a wider range due to transitions involving impurity states or phonons. Also, as discussed in section 2.2, the optical band gap of intrinsic material will shift to higher energies if the doping is sufficient enough to push the Fermi level into the conduction band.
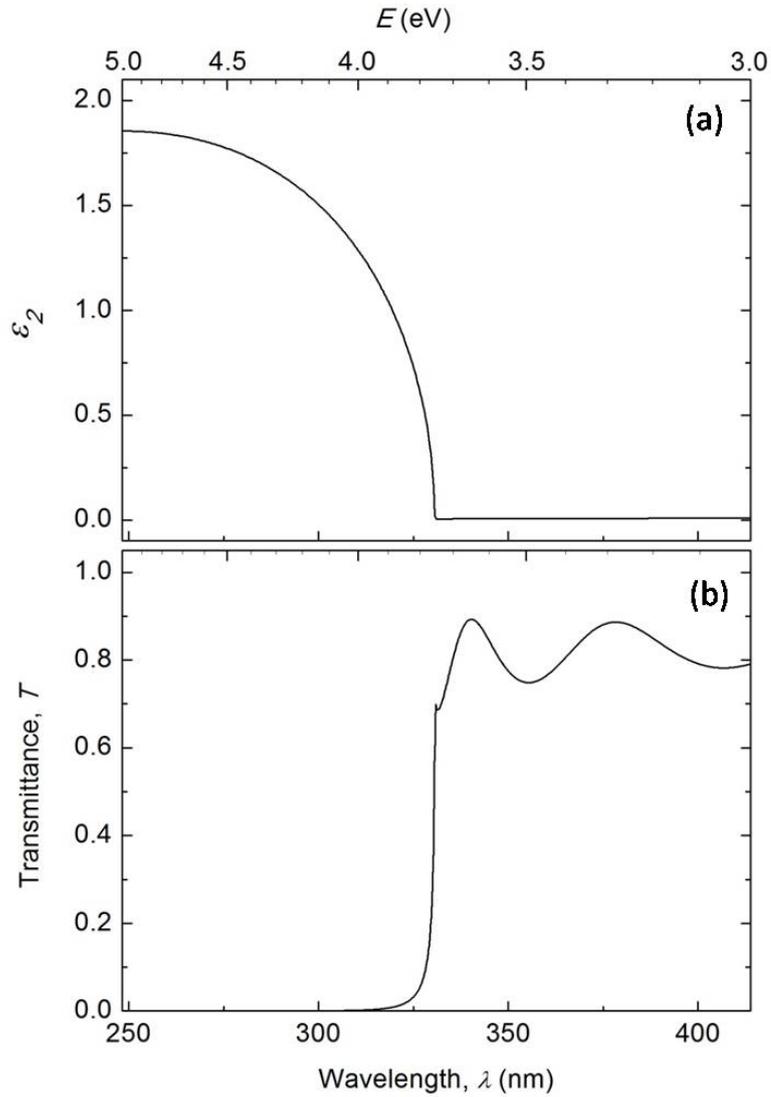
Figure 2.6: Modelling behaviour due to direct transitions. (a) The imaginary component of the dielectric permittivity ε_2 shows a $(\hbar\omega - E_d)^{1/2}$ dependence according to derivations from first order perturbation theory. The boundary, located at the band gap ($E_d = 3.75$ eV), between absorbing and non-absorbing regions is abrupt in the case of an ideal (i.e. no impurities or defects), crystalline material. (b) The corresponding transmittance is shown over the range.

Burstein-Moss shifts

The key difference between the electrical behaviour of a metal and an insulator is that at as $T \to 0$ K, the conductivity of a metal increases towards infinity whereas the conductivity of an insulator decreases to zero. It is possible to induce a transition between the insulating

and metallic state by introducing to the system a critical density of free carriers, n_c, either through intrinsic or extrinsic doping, or both. *Mott* [4] was the first to suggest such a transition and derived a semi-empirical expression for the critical density in a semiconductor material,

$$n_c^{1/3} a_H \simeq 0.2 \tag{2.50}$$

where a_H is the Bohr radius of the free electron given by

$$a_H = \frac{\varepsilon_0 \hbar^2 \varepsilon_\infty}{m_e e^2} \tag{2.51}$$

where ε_∞ again represents the background permittivity that arises from an assembly of bound valence electrons. For a typical metal oxide system $\varepsilon_\infty \sim 4$ and $m_e = 0.35\ m_0$. Thus, a typical critical density can be calculated as $n_c \sim 5 \times 10^{17}$ cm^{-3}. Such carrier densities are common in transparent conducting oxide materials.

We must now consider the effect that a population of carriers of density $n_e > n_c$ has on the imaginary component of the dielectric permittivity derived for direct transitions. As mentioned in section 2.2, for $n_e > n_c$ the Fermi level is pushed into the conduction band, and below this level all states are considered to be filled. Therefore, inter-band transitions are not permitted to states in the conduction band below the Fermi-level and the effective band gap of the material apparently shifts to higher energies (see figure 2.1c). This shift was first simultaneously observed by *Burstein* [17] and *Moss* [18] in heavily doped InSb.

The states within the conduction band are filled according to the Fermi-Dirac distribution function

$$F_e = \left[1 + \exp \frac{E_c - \Delta_{BM}}{kT} \right]^{-1} \tag{2.52}$$

$$= \left[1 + \exp \frac{\frac{1}{1 + m_e/m_h}(\hbar\omega - E_d) - \Delta_{BM}}{kT} \right]^{-1} \tag{2.53}$$

where Δ_{BM} is the Burstein-Moss shift of the system and, when the bottom of the conduction band is set at $E = 0$, is equivalent to the Fermi energy, E_f, which can be calculated from simple free-electron theory as

$$E_f = \Delta_{BM} = \frac{\hbar^2}{2m_e}(3\pi n_e)^{2/3} \tag{2.54}$$

The JDOS that may partake in inter-band transitions is therefore reduced by a factor $(1 - F_e)$ and it follows that the imaginary component ε_2 is reduced by the same factor.

Therefore, for a metal oxide system with a free carrier density $n_e > n_c$ the imaginary component of the dielectric permittivity can be expressed as

$$\varepsilon_2 = \frac{D}{\omega^2}(\hbar\omega - E_d)^{1/2}\left[1 - F_e\right] \tag{2.55}$$

where, according to equation 2.46

$$D = \frac{e^2|\mathbf{p}_{cv}|^2}{3\pi m_0^2\varepsilon_0}\left(\frac{2m_r}{\hbar^2}\right)^{3/2}$$

Figure 2.7a shows how the shape of ε_2 changes, relative to that of an intrinsic (undoped) metal oxide semiconductor, when the system is doped with carrier concentrations $> n_c$. The corresponding transmittance curve (figure 2.7b) is also shown and demonstrates the shifting of the band edge to higher energies. Note that the shape of the absorption edge in critically doped systems is not as sharp as the the abrupt cut-off associated with an intrinsic material. This is because the Fermi-Dirac distribution is blurred when $T > 0$ K.

Impurity bands: Urbach tails

The above description of the effect of direct inter-band transitions on the dielectric permittivity of a heavily doped metal oxide semiconductor is still incomplete. As mentioned in section 2.2, for a degenerately doped system the donor impurity band merges into the conduction band. However, there is a remaining density of states below the conduction band minimum that extends into the forbidden gap. In a real system it is possible for these 'tail' states to be emptied by a population of compensating acceptors that arise from defects in the lattice. It is therefore possible for these tail states to take part in direct inter-band transitions and hence contribute to the absorption coefficient at frequencies below the band gap E_d. This effect was first observed by Urbach [19] hence the tails are commonly referred to as Urbach tails. The distribution of tail states in the forbidden region can be modelled using an exponential function and their corresponding contribution to ε_2 may be expressed according to

$$\varepsilon_2 = \begin{cases} \frac{D}{\omega^2}(\hbar\omega - E_d)^{1/2}\left[1 - F_e\right] & \text{if } \hbar\omega > E_d + \Delta_{BM} \\[2ex] \exp\frac{\frac{1}{1+m_e/m_h}(\hbar\omega - E_d) - \Delta_{BM}}{\gamma_w} & \text{if } \hbar\omega < E_d + \Delta_{BM} \end{cases} \tag{2.56}$$

where γ_w represents the extent of the tail in the forbidden region. The shape of ε_2 across the boundary between the two regions is smooth and continuous, as shown in figure 2.8a.

Hence, the tail acts to reduce the sharpness of the direct band edge by extending it into the forbidden region. A corresponding reduction in the sharpness of the cut-off in transmission near the band gap is also shown in figure 2.8b. It is important to note that the exponential function used to model the shape of the Urbach tail has no physical basis, unlike the expression for behaviour above the band gap: It is simply a mathematical construct that empirically fits commonly observed behaviour in amorphous and polycrystalline
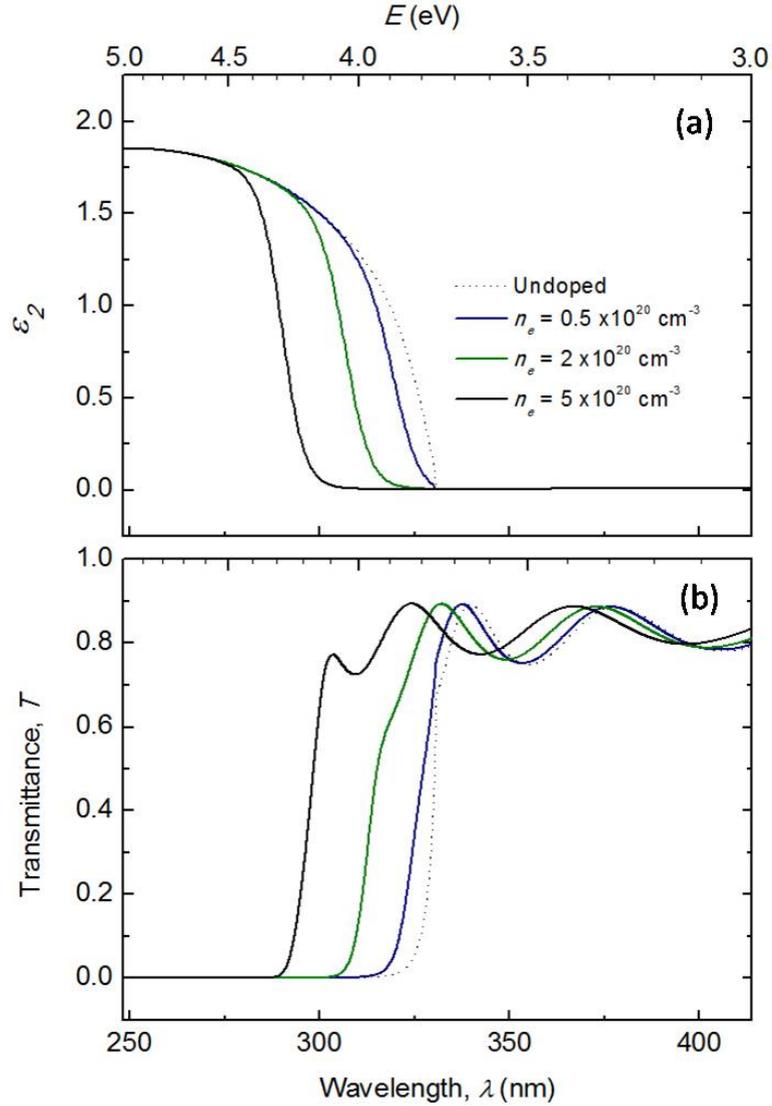
Figure 2.7: Carrier densities above the critical density n_c generate Burstein-Moss shifts according to $\Delta_{BM} \propto n_e^{2/3}$. (a) The component ε_2 for direct transitions is modified by the factor $(1 - F_e)$ which acts to shift the effective band gap, E_d', to higher energies. (b) The corresponding transmittance.
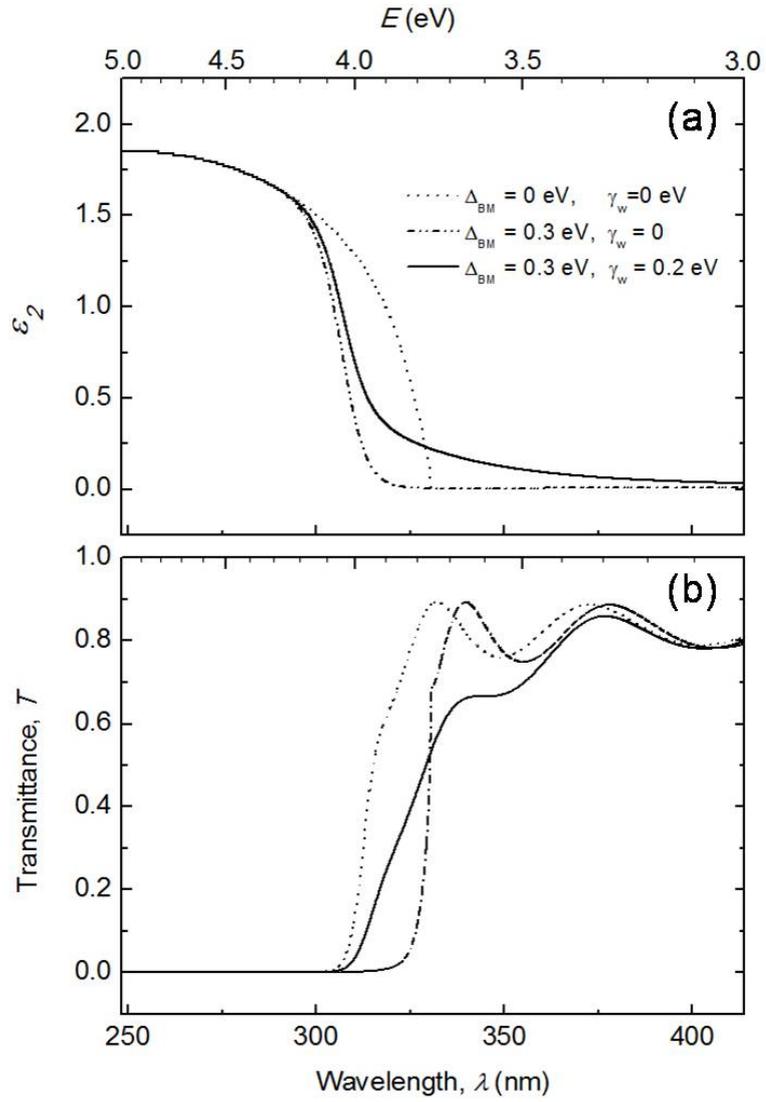
Figure 2.8: The effect of Urbach tails on direct transitions. (a) The shape of ε_2 is modified by an exponential tail parameterised by γ_w. (b) The sharpness in the cut off in the transmission is reduced by an Urbach tail as absorption is extended to lower energies.

semiconductors.

Indirect transitions

Direct transitions involve the interaction of an electron with a single photon, the momentum $\mathbf{k}_{\hbar\omega}$ of which can be considered as negligible. Therefore the momentum of the electron before (k) and after (k') the transition is assumed to be equal. However, if an interaction
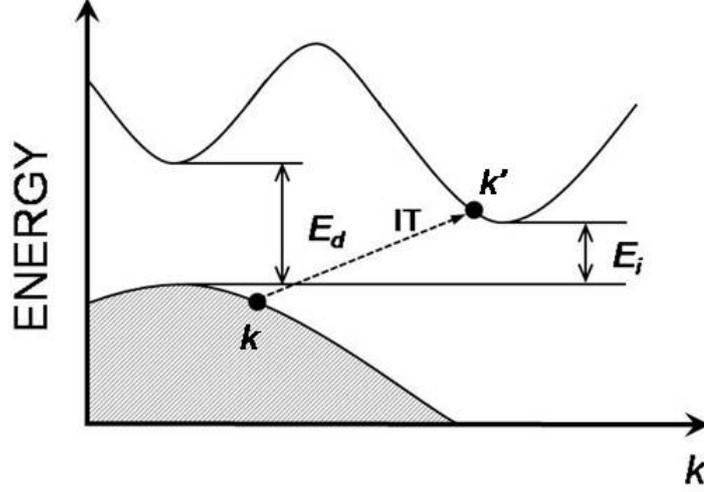
Figure 2.9: Indirect transitions: An electron is promoted to conduction band at a different momentum value, k', provided that the transition involves a phonon of energy E_p. The parabolic band approximation is still adhered to.

involves a phonon as well as a photon it is possible for $k' \neq k$. These *indirect* transitions have a much lower probability than direct transitions but nonetheless may contribute a significant component to the absorption coefficient and hence the shape of ε_2. An example of an E - k schematic representing an indirect transition is shown in figure 2.9. The conservation of momentum for an indirect transition may be expressed as

$$\mathbf{k'} = \mathbf{k} \pm \mathbf{K}_p \tag{2.57}$$

where $\mathbf{K}_p$ is the momentum of the photon. The sign $\pm$ indicates that the interaction may involve either the absorption or emission of a phonon. The corresponding relationship for the energies involved in the interaction is expresses as

$$E_c(k') = E_v(k) + \hbar\omega \pm E_p \tag{2.58}$$

Note that it is still possible to use the parabolic band model if it is assumed that transitions occur to regions close to a minimum in the conduction band. The contribution to ε_2 is derived from second order perturbation theory [20]

$$\varepsilon_2 = \frac{D'}{\omega^2} \left\{ \frac{(\hbar\omega + E_p - E_i)^2}{\exp(E_p/kT) - 1} + \frac{(\hbar\omega - E_p - E_i)^2}{1 - \exp(-E_p/kT)} \right\} \tag{2.59}$$

30
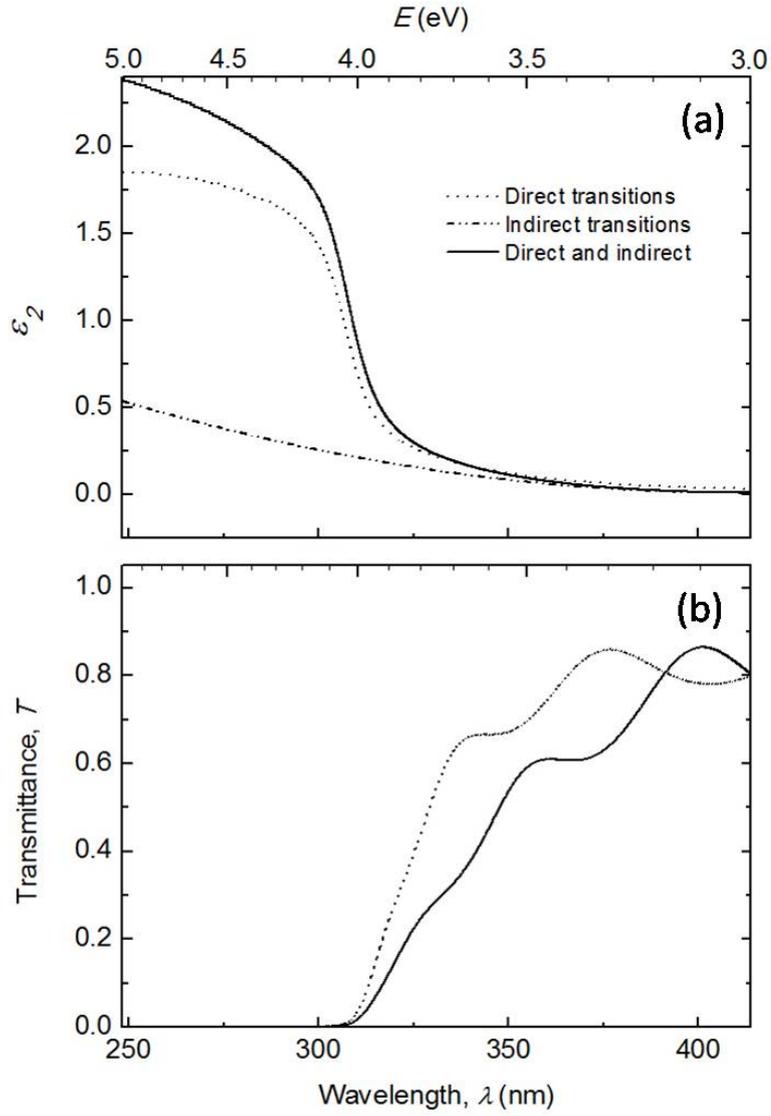
Figure 2.10: The contribution of indirect transitions. (a) The line $-\cdot-\cdot\cdot$ shows the shape of the component of ε_2 due to indirect transitions according to $\varepsilon_2 \propto (\hbar\omega - E_i \pm E_p)^2$, where $E_i = 3.0$ eV, $E_p = 3$ meV. The line $\cdots$ shows the contributions of direct transitions (including a BM shift and an Urbach tail), and $-$ shows the combined contribution of direct and indirect transitions. (b) The transmittance curves for a system that permits only direct transitions and a system that permits both direct and indirect transitions.

where E_i is the indirect band gap and represents the difference in energy between the top of the valence band and the adjacent minimum in the conduction band.

Figure 2.10 shows the contribution to ε_2 and the corresponding transmittance curve

generated by indirect transitions accross a gap of $E_i = 3.0$ eV and involving phonons of energy 3 meV. The contribution of indirect transitions acts to broaden the cut-off in transmittance at the direct band gap edge.

This concludes the description of the relevant theory for describing the dielectric permittivity of transparent conducting oxide materials. The theory presented in this chapter is key to understanding the profiles of experimentally determined transmittance spectra and will be used extensively in the following chapters, particularly Chapter 5, to extract optical and electrical parameters from real materials.

2.4   TCO requirements for thin film PV

Within this thesis, transparent conducting oxide materials will be discussed almost exclusively within the context of thin film photovoltaics, particularly CdTe based devices. It is therefore necessary to specify, for TCOs, the ranges of optical and electrical behaviour most appropriate for solar cell design. They key *optical* parameter of a TCO film is its transmittance, $T(\lambda)$, which may be defined approximately as

$$T(\lambda) = T_{sub} \exp(-\alpha(\lambda)d) \tag{2.60}$$

where d is the film thickness and T_{sub} is the substrate transmittance. The linear absorption coefficient $\alpha(\lambda)$ is defined as

$$\alpha(\lambda) = \frac{4\pi k}{\lambda} \tag{2.61}$$

When quoting the transmittance of a TCO film according to equation 2.60 the convention throughout this thesis shall be that the combined transmittance of both the material and the substrate is stated. Furthermore, it is useful to assess the transmittance over the range of wavelengths relevant to solar cell design by defining the parameter $\tilde{T}$, the *integrated transmittance*

$$\tilde{T} = \frac{1}{b-a} \int_a^b T(\lambda)d\lambda \approx T_{sub} \exp(-\tilde{\alpha}d) \tag{2.62}$$

where a and b are the lower and upper limits of the wavelength range respectively and the parameter $\tilde{\alpha}$ is the equivalent integrated absorption coefficient over the range $a \to b$. For CdTe based solar cells a suitable value of a is 400 nm which represents a value close to the onset of the UV cut-off in the solar spectrum while a value of $b = 850$ nm represents the

band gap of CdTe. Wavelengths outside the range 400-850 nm are unable to contribute towards the generation of a photo-current within a CdTe device and are therefore not to be considered when determining the optical performance of a TCO.

It is clear from equation 2.62 that the maximum value of $\tilde{T}$ (even for a film with $\tilde{\alpha} = 0$) is determined by the substrate transmittance T_{sub}. A typical soda-lime glass substrate has an almost constant value of $T_{sub} \sim 0.9$ over the range of interest and so the optical performance of a TCO can be determined by how close $\tilde{T}$ is to this value. In general, any TCO film with a $\tilde{T} > 0.8$ is considered as having a 'good' optical performance.

The key *electrical* parameter of a TCO film is its *sheet resistance* defined by

$$R_\square = \frac{\rho}{d} \tag{2.63}$$

where ρ is the bulk resistivity, as defined previously and typically is expressed in units of Ω.cm. The unit of sheet resistance is therefore Ω, which is more commonly expressed as $\Omega/\square$ (Ohms per square), the $\square$ unit representing the fact that the value of $R_\square$ will remain constant provided it is measured over any square area of the film's surface. Generally, for a TCO film to be incorporated into a solar cell device a sheet resistance of $R_\square < 10$ $\Omega/\square$ is required, however sheet resistances as high as 15 $\Omega/\square$ are commonly employed in commercial solar modules.

The overall quality of a TCO film must be assessed in terms of both its optical and electrical performance. A figure of merit, originally proposed by *Haacke* [21, 22], is defined that embodies both a film's optical and electrical properties according to

$$\phi = \frac{(\tilde{T}/T_{sub})^{10}}{R_\square} \approx \frac{d}{\rho} \exp(-10\tilde{\alpha}d) \tag{2.64}$$

The exponent '10' acts to weight the significance of the transmittance so that ϕ is maximised at a value of $\tilde{T} \sim 0.8$. An estimate for the film thickness (d_{max}) that maximises the value ϕ can be calculated according to

$$\frac{\partial \phi}{\partial d_{max}} = 0 = \frac{1}{\rho} \exp(-10\tilde{\alpha}d_{max})(1 - 10\tilde{\alpha}d_{max}) \tag{2.65}$$

the solution to which gives

$$d_{max} = \frac{1}{10\tilde{\alpha}} \tag{2.66}$$

Figure 2.11 shows the relationship between ϕ and d for a variety of films having different values of $\tilde{\alpha}$ and ρ. It is clear that the films that have lower $\tilde{\alpha}$, and correspondingly higher
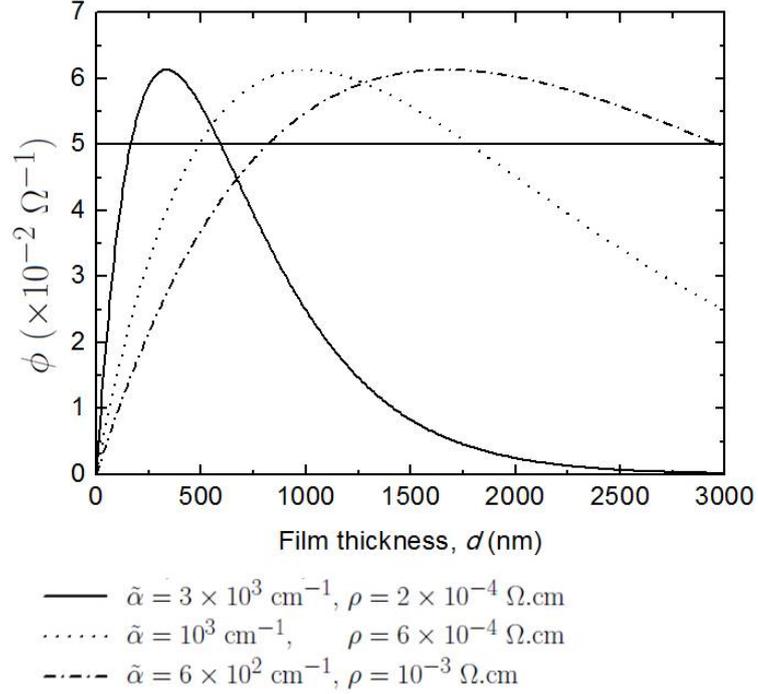
Figure 2.11: The figures of merit, over a range of film thicknesses, for several hypothetical TCO materials defined by their values of $\tilde{\alpha}$ and ρ. A line of constant ϕ is shown at $\sim 5 \times 10^{-2}$ Ω^{-1} and is consistent with the criteria $\tilde{T} = 0.85$, $R_\square = 10$ $\Omega/\square$. Films with values of ϕ above the line are considered as good candidates for front contact layers in CdTe thin film solar cells.

ρ values, require a greater film thickness for ϕ to be maximised. Nonetheless, all the films represented in figure 2.11 surpass the value of $\phi = 5 \times 10^{-2}$ Ω^{-1}, consistent with the criteria $\tilde{T} = 0.85$ and $R_\square = 10$ $\Omega/\square$, for a range of film thicknesses.

The figure of merit, ϕ, is only ever to be used as a rough guide as to whether a TCO material is suitable for use as a front contact layer in a CdTe solar cell. There are other material properties that determine a TCO's applicability, such as morphology (i.e. grain size, structure) and temperature stability, which will determine it's overall performance. Also, the determination of d_{max} for a material, depends on a linear relationship between sheet resistance and thickness. This may not be the case for a real material as it is possible for the bulk resistivity to also have a thickness dependence, i.e. $R_\square = \rho(d)/d$. Nonetheless, the optical and electrical properties of a TCO are the most significant and the figure of merit ϕ will serve as a good indicator as to whether a material is suitable for solar cell

design.

2.5 TCO literature review

To date, the most commonly researched n-type TCO materials are doped forms of In_2O_3, SnO_2 and ZnO. Tin doped In_2O_3 in particular has received extensive investigation, via a wide range of deposition techniques [23, 24], and today is produced industrially to meet the ever growing demand for flat-panel and touch screen devices. However, the high relative cost and scarcity of indium makes the continued use of In_2O_3:Sn unsustainable and in recent years there has been a concerted effort to find a TCO material that is In free.

Fluorine doped SnO_2 has been employed extremely successfully within the float glass industry as a low emissivity coating for architectural applications. It is deposited almost exclusively using chemical vapour deposition techniques [25] which are highly compatible with the float glass fabrication process [26]. SnO_2:F is therefore able to meet large scale production demands and achieve excellent economies of scale through "in-line" fabrication procedures, as well as eliminating the need for In. However, CVD deposited SnO_2:F, while suitable for window coatings, does not achieve the high visible transmittances required for thin-film solar cell design. This is due to the large grain sizes, a product of the CVD technique, which increases the haze factor of the films and reduces their specular transmittance. Nonetheless, commercial glass substrates that have a CVD deposited SnO_2:F layer have been used experimentally to achieve high quality CdTe devices that have conversion efficiencies greater than 15% [27, 28]. An excellent review of doped SnO_2 is given in [29].

ZnO based TCOs show the most promise for the reduction of large scale production costs due to the very low price of Zn (see table 2.1). The use of Al doped ZnO is now widespread in thin film PV, particularly for CIGS based devices [30], where magnetron sputtering is the favoured deposition technique. Sputtering has two advantages over CVD: Firstly, lower substrate temperatures are necessary, making sputtered materials more compatible with cell fabrication procedures. Secondly, sputtering allows for a much broader range of deposition parameters and hence film compositions. This provides the opportunity for the properties (optical, electrical and structural) of doped ZnO films to be fully optimised for their application. However, sputtering is yet to match the throughput capa-

bility of CVD and any industrial production of doped ZnO films must take place "off-line". Nonetheless, with continued research into new sputtering approaches [31, 32], the technnique's producability is sure to match that of CVD in the near future. A full review of doped ZnO films deposited by magnetron sputtering is given in [33, 34]. The technique of radio frequency magnetron sputtering (RFMS) is discussed in greater detail in Chapter 4.

Recently, successful attempts have been made to fabricate high performance TCOs based on cadmium stannate (Cd_2SnO_4) and incorporate them into record efficiency CdTe devices [35]. This material demonstrates very high electron mobilities and in turn low sheet resistances while maintaining a superior optical transmittance compared with other TCOs. Sn_2O_4 is therefore an excellent alternative to In_2O_3:Sn for use in solar cell design. However, the fabrication of high quality Cd_2SnO_4 films typically requires an additional annealing step, involving temperatures $> 550°C$. Furthermore, the fabrication of Cd_2SnO_4 on cheap soda-lime glass substrates, an important requirement for CdTe based PV in particular, has yet to be demonstrated.

Table 2.1 shows the physical properties of the undoped forms of the TCO materials discussed above as well as the annual production and cost of each of their constituent metals. Table 2.2 reviews in detail the most significant research contributions, according to their optical and electrical properties, for each TCO material.

Table 2.1: Physical properties, production and cost of the most common TCO materials

Property	In_2O_3	SnO_2	ZnO	Cd_2SnO_4
Direct band gap, E_d (eV)	3.75 [36]	3.70 [37]	3.30 [38]	2.06 - 3.30 [39, 40]
Effective electron mass (m_e/m_0)	0.5^a, 0.3^b [41, 42]	0.4^a, 0.2^b [43, 44]	0.24^a, 0.3^c [45, 46]	0.14 - 0.3 [47]
Density (g/cm^3)	7.12	6.99	5.67	–
Dopants	Sn, Ga, Zn, F, Cl	Sb, Mo, F, Cl	B, Al, Ga, Si, F, Cl	In, Sb, Pb, Y
Structure	cubic	tetragonal, rutile	hexagonal, wurtzite	orthorhombic, spinel
Lattice parameters (Å)	a: 10.1 [24]	a: 4.74 [48]	a: 3.25 [49]	a: 9.14 [50]
		c: 3.19	c: 5.21	
World production of metal (tons/year)^d	573 [51]	> 600,000 [52]	> 11,000,000 [53]	19,600 (Cd metal) [54]
Metal cost ($/kg)^e	650 [55]	21.50 [56]	1.9 [57]	3.00 [58]

[a]Single crystal
[b]Polycrystalline film
[c]Theoretical value for polycrystalline film
[d]Figures for 2008
[e]Figures for Nov 2011

Table 2.2: A summary of the opto-electronic properties of the most common TCO materials as reported in the literature

Material: dopant	Deposition technique[b]	T_{sub}[a] (°C)	n_e (10^{20} cm^{-3})	μ_e (cm^{2}V^{-1}s^{-1})	ρ (10^{-4} Ω.cm)	E'_d (eV)	$R_\square$ (Ω/□)	$\tilde{T}$	d (nm)	ϕ (Ω^{-2})	Ref.
In$_2$O$_3$:V$_O$	RE	390	0.4	56.0	27.0	–	90	0.75	300	0.2	[59]
In$_2$O$_3$:In	TE	350	4.7	74.0	1.8	3.88	7	0.85	270	8.3	[60]
In$_2$O$_3$:V$_O$	TE	420	3.0	72.0	2.9	–	64	0.65	45	0.6	[61]
In$_2$O$_3$:Sn	TE	400	3.8	43.0	3.7	–	15	0.85	250	3.7	[61]
In$_2$O$_3$:Sn	SP	450	–	–	6.0	3.95	–	0.83	–	–	[62]
In$_2$O$_3$:Sn	CVD	400	9.0	43.0	1.6	–	2	0.81	950	20.5	[63]
In$_2$O$_3$:Sn	SGSC	550	6.95	14.2	6.3	–	105	0.85	60	0.9	[64]
In$_2$O$_3$:Sn	SGDC	>400	1.2	7.0	12.0	3.4	40	0.85	300*	1.4	[65]
In$_2$O$_3$:Sn	PLD	300	10.8	29.0	2.0	4.20	12	0.82	170	3.2	[66]
In$_2$O$_3$:Sn	EBE	350	9.23	54.1	1.3	–	4	–	301	–	[67]
In$_2$O$_3$:Sn	RFMS	370	27.0	36.0	4.4	4.40	5	0.85	150	12.1	[68]
In$_2$O$_3$:Sn	RFMS	400	–	–	–	–	2	0.83	–	22	[69]
In$_2$O$_3$:Sn	RFMS	350	–	–	1.3	–	4	0.87	300	16.6	[70]
In$_2$O$_3$:Sn	DCMS	400	10.5	42.9	1.3	–	10	–	137	–	[67]
In$_2$O$_3$:Zn	DCMS	500	5.3	35.0	3.4	–	11	0.80	300*	2.8	[71]
In$_2$O$_3$:F	DCMS	500	1.5	28.0	0.2	–	50	0.75	300*	0.3	[72]

Continued on next page . . .

Table 2.2 – Continued

Material: dopant	Deposition technique	T_{sub} (°C)	n_e (10^{20} cm^{-3})	μ_e (cm^{2}V^{-1}s^{-1})	ρ (10^{-4} Ω.cm)	E'_d (eV)	$R_\square$ (Ω/□)	$\tilde{T}$	d (nm)	ϕ (Ω^{-2})	Ref.
SnO$_2$:V$_O$	SP	560	1.0	13.0	50.1	–	85	0.85	590	0.7	[73, 74]
SnO$_2$:V$_O$	CVD	450	2.0	29.0	10.7	–	21	–	500	–	[75]
SnO$_2$:Sb	RFMS	530	1.5	5.8	13.0	–	37	0.63	347	< 0.1	[29]
SnO$_2$:Sb	RE	350	–	–	0.8	–	2	0.77	500	14.0	[76]
SnO$_2$:Sb	SGDC	500	2.8	5.0	45.0	3.85	90	0.86	500	0.7	[77]
SnO$_2$:(Sb, F)	RFMS	530	2.3	18.9	12.8	4.07	41	0.83	283	1.1	[29]
SnO$_2$:F	SP	560	10.5	10.6	5.6	–	11	0.85	530	5.3	[73, 74]
SnO$_2$:F	SP	425	34.7	30.0	0.6	–	4	–	165	–	[78]
SnO$_2$:F	PLD	300	8.3	15.0	5.0	–	11	0.85	450	5.3	[79]
SnO$_2$:F	RFMS	450	7.0	25.0	3.6	3.8	18	0.81	200	1.9	[80]
SnO$_2$:F	RFMS	530	1.5	13.8	28.0	4.14	86	0.80	330	0.4	[29]
SnO$_2$:F	CVD	400	10.6	10.0	5.9	–	5	–	200	–	[81]
SnO$_2$:Mo	CVD	450	–	–	20.0	4.25	50	0.80	400	0.6	[82]

Table 2.2 – Continued

Material: dopant	Deposition technique	T_{sub} (°C)	n_e (10^{20} cm^{-3})	μ_e (cm²V^{-1}s^{-1})	ρ (10^{-4} Ω.cm)	E'_d (eV)	$R_{\square}$ (Ω/□)	$\tilde{T}$	d (nm)	ϕ (Ω^{-2})	Ref.
ZnO:V$_O$	RFMS	40	1.2	16.0	32.5	–	65	–	500	–	[83]
ZnO:B	ALD	136	8.2	11.0	6.9	–	23	–	300	–	[84]
ZnO:B	ALD	160	5.0	19.5	6.4	–	32	–	200	–	[85]
ZnO:B	CVD	150	2.0	15.6	20.0	–	10	0.75	2000	1.6	[86]
ZnO:Ga	DCMS	400	5.7	22.0	5.0	–	15	0.82	330	2.6	[87]
ZnO:Ga	PLD	300	24.8	31.0	0.8	3.51	3	0.85	300	18.8	[88]
ZnO:Ga	RFMS	30	15.0	7.1	5.9	3.69	20	0.83	300	2.2	[89]
ZnO:Si	RFMS	170	7.5	23.0	3.6	–	–	–	–	–	[90]
ZnO:Al	SGDC	400	6.5	13.7	7.0	–	140	0.90	50	0.7	[91]
ZnO:Al	RFMS	150	13.0	34.0	1.4	–	5	0.89	300	17.8	[92]
ZnO:Al	RFMS	150	7.5	17.7	4.7	3.54	31	0.86	150	2.0	[93]
ZnO:Al	DCMS	250	12.7	27.4	1.8	–	2	0.85	837	28.2	[94]
ZnO:(Al, F)	RFMS	300	4.0	33.2	4.7	–	24	0.85	200	2.3	[95]
ZnO:F	RFMS	500	19.5	4.8	6.7	3.46	34	0.81	200	1.0	[96]
ZnO:F	RFMS	300	1.0	43.0	14.5	3.33	41	0.85	350	1.3	[97]
ZnO:F	RFMS	300	1.1	26.4	20.9	3.40	105	0.86	200	0.6	[98]
ZnO:Cl	MOCVD	425	1.8	9.6	36.0	–	51	0.80	700	0.6	[99]

Table 2.2 – Continued

Material: dopant	Deposition technique	T_{sub} (°C)	n_e (10^{20} cm^{-3})	μ_e (cm^{2}V^{-1}s^{-1})	ρ (10^{-4} Ω.cm)	E'_d (eV)	$R_{\square}$ ($\Omega/\square$)	$\tilde{T}$	d (nm)	ϕ (Ω^{-2})	Ref.
Cd$_2$SnO$_4$	RFMS	425	–	–	7.5	2.51	2	–	3300	–	[39]
Cd$_2$SnO$_4$	RFMS	570	8.9	54.5	1.3	3.10	3	0.86	510	21.1	[47, 100]
Cd$_2$SnO$_4$	RFMS	600	8.5	29.2	2.0	3.15	10	0.85	200	5.6	[101]
Cd$_2$SnO$_4$	MOCVD	550	2.5	50.0	5.0	3.30	50	0.85	100	1.1	[40]
Cd$_2$SnO$_4$	RFMS	600	–	–	1.8	2.90	1	0.87	1287	71.2	[102]
CdIn$_2$O$_4$	DCMS	400	4.0	57.0	2.7	3.24	5	0.80	540	6.2	[103]
CdIn$_2$O$_4$	RFMS	285	1.8	34.2	10.1	–	20	–	500	–	[104]
CdIn$_2$O$_4$	DCMS	400	3.5	60.3	3.0	–	10	–	300*	–	[105]

*Nominal thickness value used to estimate $R_{\square}$

[a]Indicates maximum substrate temperature reached during processing

[b]**RE** - Reactive evaporation

TE - Thermal evaporation

SP - Spray pyrolysis

CVD - Chemical vapour deposition

SGSC - Sol gel + spin coat

SGDC - Sol gel + dip coat

PLD - Pulsed laser deposition

EBE - Electron beam evaporation

RFMS - Radio frequency magnetron sputtering

DCMS - Direct current magnetron sputtering

ALD - Atomic layer deposition

MOCVD - Metal organic CVD

T_{sub} - substrate temperature

n_e - carrier density (eqn 2.28)

ρ - resistivity

E'_d - effective direct band gap

$R_{\square}$ - sheet resistance (eqn 2.63)

$\tilde{T}$ - integrated transmittance (eqn 2.62)

d - film thickness

ϕ - figure of merit (eqn 2.64)

2.6 References

[1] K. Badekar. *Ann. Phys.* **22**, 749 (1907).

[2] J. Fan, J. Goodenough. *J. Appl. Phys.* **48**, 3524 (1977).

[3] P. P. Edwards, A. Porch, M. O. Jones, D. V. Morgan, R. M. Perks. *Dalton T.* 2995 (2004).

[4] N. Mott. *Metal-Insulator Transitions.* Taylor and Francis (1974).

[5] M. Fox. *Optical properties of solids.* Oxford Univ Press (2010).

[6] P. Drude. *Ann. Phys.* **306**, 566 (1900).

[7] H. Brooks. *Phys. Rev.* **83**, 879 (1951).

[8] F. J. Blatt. *J. Phys. Chem. Solids.* **1**, 262 (1957).

[9] D. Chattopadhyay, H. Queisser. *Rev. Mod. Phys.* **53**, 745 (1981).

[10] S. Brehme, F. Fenske, W. Fuhs, E. Nebauer, M. Poschenrieder, B. Selle, I. Sieber. *Thin Solid Films* **342**, 167 (1999).

[11] F. Ruske, A. Pflug, V. Sittinger, B. Szyszka, D. Greiner, B. Rech. *Thin Solid Films* **518**, 1289 (2009).

[12] W. Theiss. Scout 3.0. Aachen, Germany (2002).

[13] F. Wooten. *Optical Properties of Solids*, volume 41. Academic Press (1972).

[14] A. I. M. Rae. *Quantum Mechanics.* IoP, Bristol (1992).

[15] H. A. Kramers. *Trans. Vol. Cen. Cong.* **2**, 545 (1927).

[16] R. Kronig. *J. Opt. Soc. Am.* **12**, 547 (1926).

[17] E. Burstein. *Phys. Rev.* **93**, 632 (1954).

[18] T. S. Moss. *Phys. Soc. B* **67**, 775 (1954).

[19] F. Urbach. *Phys. Rev.* **92**, 1324 (1953).

[20] R. A. Smith. *Wave Mechanics of Crystalline Solids.* Chapman and Hall (1961).

[21] G. Haacke. *J. Appl. Phys.* **47**, 4086 (1976).

[22] G. Haacke. *Ann. Rev. Mater. Sci.* **7**, 73 (1977).

[23] R. B. H. Tahar, T. Ban, Y. Ohya, Y. Takahashi. *J. App. Phys.* **83**, 2631 (1998).

[24] I. Hamberg, C. Granqvist. *J. Appl. Phys.* **60**, R123 (1986).

[25] A. Jones, M. Hitchman. *Chemical Vapour Deposition: Precursors, Processes and Applications.* Royal Society of Chemistry (2009).

[26] Pilkington Brothers Ltd. *Proc. R. Soc. Lond. A* **314**, 1 (1969).

[27] C. S. Ferekides, U. Balasubramanian, R. Mamazza, V. Viswanathan, H. Zhao, D. L. Morel. *Solar Energy* **77**, 823 (2004).

[28] A. Gupta, A. Compaan. *Applied Physics Letters* **85**, 684 (2004).

[29] B. Stjerna, E. Olsson, C. Granqvist. *J. Appl. Phys.* **76**, 3797 (1994).

[30] K. Ramanathan, M. A. Contreras, C. L. Perkins, S. Asher, F. S. Hasoon, J. Keane, D. Young, M. Romero, W. Metzger, R. Noufi, J. Ward, A. Duda. *Prog. Photovoltaics* **11**, 225 (2003).

[31] R. Kukla. *Surface and Coatings Technology* **93**, 1 (1997).

[32] S. P. Bugaev, A. N. Zakharov, K. V. Oskomov, N. S. Sochugov, A. A. Solovjev. *Plasma Physics* **669**, 373 (2003).

[33] K. Ellmer. *J. Phys. D: Appl. Phys* **33**, R17 (2000).

[34] K. Ellmer. *J. Phys. D: Appl. Phys.* **34**, 3097 (2001).

[35] X. Wu, J. C. Keane, R. G. Dhere, C. DeHart, D. S. Albin, A. Dudam, T. A. Gessert, S. Asher, D. H. Levi, P. Sheldon. *Proc. of 17th European PVSEC* (2001).

[36] R. Weiher, R. Ley. *J. Appl. Phys.* **37**, 299 (1966).

[37] J. Manifacier, M. D. Murcia, J. Fillard, E. Vicario. *Thin Solid Films* **41**, 127 (1977).

[38] V. Srikant, D. R. Clarke. *J. Appl. Phys.* **83**, 5447 (1998).

[39] A. J. Nozik. *Phys. Rev. B* **6**, 453 (1972).

[40] X. Li, T. A. Gessert, T. Coutts. *Appl. Surf. Sci.* **223**, 138 (2004).

[41] R. L. Weiher. *J. Appl. Phys.* **33**, 2834 (1962).

[42] H. K. Muller. *Phys. Status Solidi* **27**, 723 (1968).

[43] M. Nagasawa, S. Shionoya, M. S. *J. Phys. Soc. Jpn.* **20**, 1093 (1965).

[44] K. Ishiguro, T. Sasaki, T. Arai, I. Imai. *J. Phys. Soc. Jpn.* **13**, 296 (1958).

[45] W. S. Baer. *Phys. Rev.* **154**, 785 (1967).

[46] B. Enright, D. Fitzmaurice. *J. Phys. Chem.* **100**, 1027 (1996).

[47] T. Coutts, D. Young, X. Li, W. Mulligan, X. Wu. *J. Vac. Sci. Technol. A* **18**, 2646 (2000).

[48] B. Thangaraju. *Thin Solid Films* **402**, 71 (2002).

[49] C. Bunn. *Proc. Phys. Soc.* **47**, 835 (1935).

[50] L. A. Siegel. *Journal of Applied Crystallography* **11**, 284 (1978).

[51] A. C. Tolcin. *U. S. Geological Survey* (2008). http://minerals.usgs.gov/minerals/pubs/commodity/indium/myb1-2008-indiu.pdf - accessed Aug 2011.

[52] J. F. Carlin. *U. S. Geological Survey* (2008).
http://minerals.usgs.gov/minerals/pubs/commodity/tin/myb1-2008-tin.pdf -
accessed Aug 2011.

[53] A. C. Tolcin. *U. S. Geological Survey* (2008).
http://minerals.usgs.gov/minerals/pubs/commodity/zinc/myb1-2008-zinc.pdf -
accessed Aug 2011.

[54] A. C. Tolcin. *U. S. Geological Survey* (2008).
http://minerals.usgs.gov/minerals/pubs/commodity/cadmium/myb1-2008-
cadmi.pdf - accessed Aug 2011.

[55] http://www.metal-pages.com/metalprices/indium/ - Accessed Nov 2011.

[56] http://www.metalprices.com/pubcharts/Public/TinPriceCharts.asp?WeightSelec
t=KG&SizeSelect=M&ccs=5&cid=0 - Accessed Nov 2011.

[57] http://www.metalprices.com/pubcharts/Public/ZincPriceCharts.asp?WeightSelect
=KG&SizeSelect=M&ccs=5&cid=0 - Accessed Nov 2011.

[58] http://www.metalprices.com/pubcharts/Public/CadmiumPriceCharts.asp?WeightSelec
t=KG&SizeSelect=M&ccs=5&cid=0 - Accessed Nov 2011.

[59] S. Noguchi, H. Sakata. *J. Phys. D: Appl. Phys* **13**, 1129 (1980).

[60] C. A. T. P. Pan, T. P. Ma. *Appl. Phys. Lett.* **37**, 163 (1980).

[61] M. Mizuhashi. *Thin Solid Films* **70**, 91 (1980).

[62] R. Riveros, E. Romero, G. Gordillo. *Braz. J. Phys.* **36**, 1042 (2006).

[63] L. A. Ryabova, V. S. Salun, I. A. Serbinov. *Thin Solid Films* **92**, 327 (1982).

[64] A. Solieman, M. Aegerter. *Thin Solid Films* **502**, 205 (2006).

[65] K. Nishio, T. Sei, T. Tsuchiya. *J. Mater. Sci.* **31**, 1761 (1996).

[66] H. Kim, C. M. Gilmore, A. Pique, J. S. Horwitz, H. Mattoussi, H. Murata, Z. H.
Kafafi, D. B. Chrisey. *J. Appl. Phys.* **86**, 6451 (1999).

[67] Y. Shigesato, S. Takaki, T. Haranoh. *J. Appl. Phys.* **71**, 3356 (1992).

[68] S. Ray, R. Banerjee, N. Basu, A. K. Batabyal, A. K. Barua. *J. Appl. Phys.* **54**, 3497 (1983).

[69] A. Gheidari, E. Soleimani, M. Mansorhoseini, S. Mohajerzadeh, N. Madani, W. Shams-Kolahi. *MRS Bull.* **40**, 1303 (2005).

[70] R. N. Joshi, V. P. Singh, J. C. McClure. *Thin Solid Films* **257**, 32 (1995).

[71] N. Ito, Y. Sato, P. K. Song, A. Kaijio, K. Inoue, Y. Shigesato. *Thin Solid Films* **496**, 99 (2006).

[72] Z. Y. Ning, S. H. Cheng, F. Huang, Y. B. Bian, X. H. Luo. *Mater. Sci. Eng. B-Adv* **90**, 196 (2002).

[73] J. C. Manifacier, L. Szepessy, J. F. Bresse, M. Perotin, R. stuck. *MRS Bull.* **14**, 109 (1979).

[74] J. C. Manifacier, L. Szepessy, J. F. Bresse, M. Perotin, R. stuck. *MRS Bull.* **14**, 163 (1979).

[75] M. Kojima, H. Kato, A. Imai, A. Yoshida. *J. Appl. Phys.* **64**, 1902 (1988).

[76] H. Randhawa, M. Matthews, R. Bunshah. *Thin Solid Films* **83**, 267 (1981).

[77] C. Terrier, J. Chatelon, J. Roger. *Thin Solid Films* **295**, 95 (1997).

[78] C. Agashe, B. Marathe, M. Takwale, V. Bhide. *Thin Solid Films* **164**, 261 (1988).

[79] H. Kim, R. C. Y. Auyeung, A. Pique. *Thin Solid Films* **516**, 5052 (2008).

[80] C. Geoffroy, G. Campet, F. Menil, J. Portier, J. Salardenne, G. Couturier. *Act. Pass. Electron. Compon.* **14**, 111 (1991).

[81] T. Maruyama, K. Tabata. *J. Appl. Phys.* **68**, 4282 (1990).

[82] S. C. Ray, M. K. Karanjai, D. Dasgupta. *Thin Solid Films* **307**, 221 (1997).

[83] J. B. Webb, D. F. Williams, M. Buchanan. *App. Phys. Lett.* **39**, 640 (1981).

[84] Y. Yamamoto, K. Saito, K. Takahashi, M. Konagai. *Sol. Energy Mater. Sol. Cells* **65**, 125 (2001).

[85] B. Sang, A. Yamada, M. Konagai. *Sol. Energy Mater. Sol. Cells* **49**, 19 (1997).

[86] W. W. Wenas, A. Yamada, K. Takahashi, M. Yoshino, M. Konagai. *J. Appl. Phys.* **70**, 7119 (1991).

[87] P. K. Song, M. Watanabe, M. Kon, A. Mitsui, Y. Shigesato. *Thin Solid Films* **411**, 82 (2002).

[88] S. M. Park, T. Ikegami, K. Ebihara. *Thin Solid Films* **513**, 90 (2006).

[89] B. H. Choi, H. B. Im, J. S. Song, K. H. Yoon. *Thin Solid Films* **193-194**, 712 (1990).

[90] T. Minami, H. Sato, T. Sonoda, H. Nanto, S. Takata. *Thin Solid Films* **171**, 307 (1989).

[91] W. Tang, D. Cameron. *Thin Solid Films* **238**, 83 (1994).

[92] Y. Igasaki, H. Saiton. *J. Appl. Phys.* **70**, 3613 (1991).

[93] K. H. Kim, K. C. Park, D. Y. Ma. *J. Appl. Phys.* **81**, 7764 (1997).

[94] W. Wang, X. Diao, Z. Wang, M. Yang, T. Wang, Z. Wu. *Thin Solid Films* **491**, 54 (2005).

[95] B. G. Choi, I. H. Kim, D. H. Kim, K. S. Lee, T. S. Lee, B. Cheong, Y. J. Baik, W. M. Kim. *J. Eur. Ceram. Soc.* **25**, 2161 (2005).

[96] Y. Tsai, N. Wang, C. Tsai. *Materials Letters* (2009).

[97] H. Yoon, K. Lee, T. Lee, B. Cheong, D. Choi, D. Kim, W. Kim. *Sol. Energy Mater. Sol. Cells* **92**, 1366 (2008).

[98] D. Ku, Y. Kim, K. Lee, T. Lee, B. Cheong, T. Seong, W. Kim. *J. Electroceramics* **23**, 415 (2009).

[99] E. Chikoidze, M. Nolan, M. Modreanu, V. Sallet, P. Galtier. *Thin Solid Films* **516**, 8146 (2008).

[100] X. Wu, W. P. Mulligan, T. J. Coutts. *Thin Solid Films* **286**, 274 (1996).

[101] R. Mamazza, D. L. Morel, C. S. Ferekides. *Thin Solid Films* **484**, 26 (2005).

[102] G. Haacke, W. Mealmaker, L. Siegel. *Thin Solid Films* **55**, 67 (1978).

[103] K. Budzynska, E. Leja, S. Skrzypek. *Solar Energy Materials* **12**, 57 (1985).

[104] B. Li, L. Zeng, F. S. Zhang. *Phys. Status Solidi A* **201**, 960 (2004).

[105] F. Yang, L. Fang, S. Zhang, J. Sun, Q. Xu, S. Wu, J. Dong, C. Kong. *App. Surf. Sci.* **254**, 5481 (2008).

Chapter 3

Solar Cell Characteristics and CdTe Devices

3.1 Introduction

Photovoltaic (PV), or solar cell, devices convert solar radiation directly into electrical current through the use of semiconductor materials that exploit the photovoltaic effect (see section 3.2.1). Over the last decade the demand for terrestrial PV has increased considerably, motivated by the desire to increase the contribution of renewables to the global energy capacity and combat global warming. In 2001 the total global installed PV capacity was $\sim$ 1.6 GW (equivalent to the output of a single typical UK coal-fired power station). This capacity has increased annually by an average of 40%, standing today (2011) at just over 40 GW. It is predicted to increase in this manner, breaking the Terawatt barrier in around 2020 [1]. The dominant PV technology to date has been that based on bulk crystalline silicon. However, new thin-film PV platforms, e.g. CdTe, CIGS and amorphous Si, continue to increase their market share and have made significant advances in the reduction of module production costs. In the case of CdTe in particular, production cost has already been reduced to below $1/W_p$ by the company First Solar [2, 3]. Further advances in cost reduction, the most crucial objective within the PV industry, will make the use of thin-film PV more attractive for domestic use, particularly in the current climate of ever increasing gas and oil prices. In this chapter the necessary physics describing a solar cell's opto-electric behaviour is presented in section 3.2 which includes: A discussion of

the photovoltaic effect, the formation of an n-p heterojunction and its corresponding J-V response and the factors that contribute to losses in device conversion efficiencies. This is followed, in section 3.3, by a specific review of CdTe based PV which includes a discussion of all component layers and a literature survey of recent experimental device designs and performances.

3.2   Solar cell characteristics

3.2.1   The photovoltaic effect

The key physical phenomenon responsible for the operation of a solar cell is the photovoltaic effect, whereby two materials in close contact, at least one of which is a semiconductor, generate a voltage on exposure to light. A manifestation of the effect (the 'photogalvanic' effect), observed during experiments involving electrolytic cells, was reported as early as 1839 by Becquerel [4] but it was not until 1873, following the observation of the effect in selenium [5], that initial attempts were made to exploit the phenomenon and convert light into useful electrical energy [6].

The photovoltaic effect is a direct consequence of a semiconductor's band structure (see Chapter 2) and the potential for the promotion of bound electrons within the valence band to higher energy states in the conduction band where they are free to partake in electrical conduction. The outcome of the interaction between a single incident photon and a semiconductor has three different possibilities depending on the energy of the photon, $h\nu$, and the inherent band gap, E_g of the material. Firstly, if $h\nu < E_g$ then the photon is not absorbed as there is insufficient energy to generate a transition. The material is said to be 'transparent' to photons in this energy range. Secondly, if $E_g < h\nu < 2E_g$ then the photon is absorbed and a single electron is promoted to the conduction band, leaving behind it a hole in the valence band. Thirdly, if $h\nu > 2E_g$ the photon is again absorbed but promotes an electron with enough kinetic energy to generate further transitions through impact ionization.

Should these interactions occur in a lone piece of semiconductor material the promoted electrons and the corresponding holes would naturally recombine, thus ensuring the cancellation of any generated photo-voltage. However, the electron-hole pairs generated in a

semiconductor that is in close contact with some other material may be separated by the internal electric field that arises at the interface between the two. The separation of these carriers mean that the photo-voltage can be sustained. Making a connection to either side of the interface through some external load will therefore permit a 'photo-current' to flow and work to be done. There are three distinct types of semiconductor junction that may be used to exploit the photovoltaic effect. They are:

- Schottky junction - a semiconductor is contacted to a metal

- Homo-junction - the junction formed between two layers of the same semiconductor material that have different majority carrier types, i.e n-type and p-type

- Hetero-junction - the junction formed between two different semiconductor materials of different carrier types

For a full description of the behaviour of the Schottky junction and homo-junction the reader is referred to key texts by Sze [7] and Fahrenbruch [8]. The n-p hetero-junction, being of specific relevance to the field of thin-film photovoltaics, and the themes within this work, is described in detail below with reference to its formation and electrical response.

3.2.2   Formation of an n-p hetero-junction

Figure 3.1a shows the energy band diagrams for two isolated semiconductor materials, one being n-type and the other p-type. The two materials are characterised by their values for the band gap, E_g, electron affinity, χ, work function, ϕ and Fermi level, E_f, and for each material these values are distinguished by the subscripts n and p. These materials may be brought into intimate contact with each other through a wide range deposition techniques (e.g. thermal evaporation, spray pyrolysis, sputtering, MOCVD, PLD etc.) to form an n-p hetero-junction.

The junction forms according to the key condition that the Fermi levels of each material must re-align to coincide with each other. This requires a transfer of some electrons, via diffusion, from the n-type material into the p-type material where they annihilate with holes (or equivalently, the transfer of holes from the p to the n-type material and their annihilation with electrons). The result of this transfer and annihilation is the formation

of a region close to the interface between the two materials where ionised atoms together with very few carriers exist. This region is called the *depletion zone.*
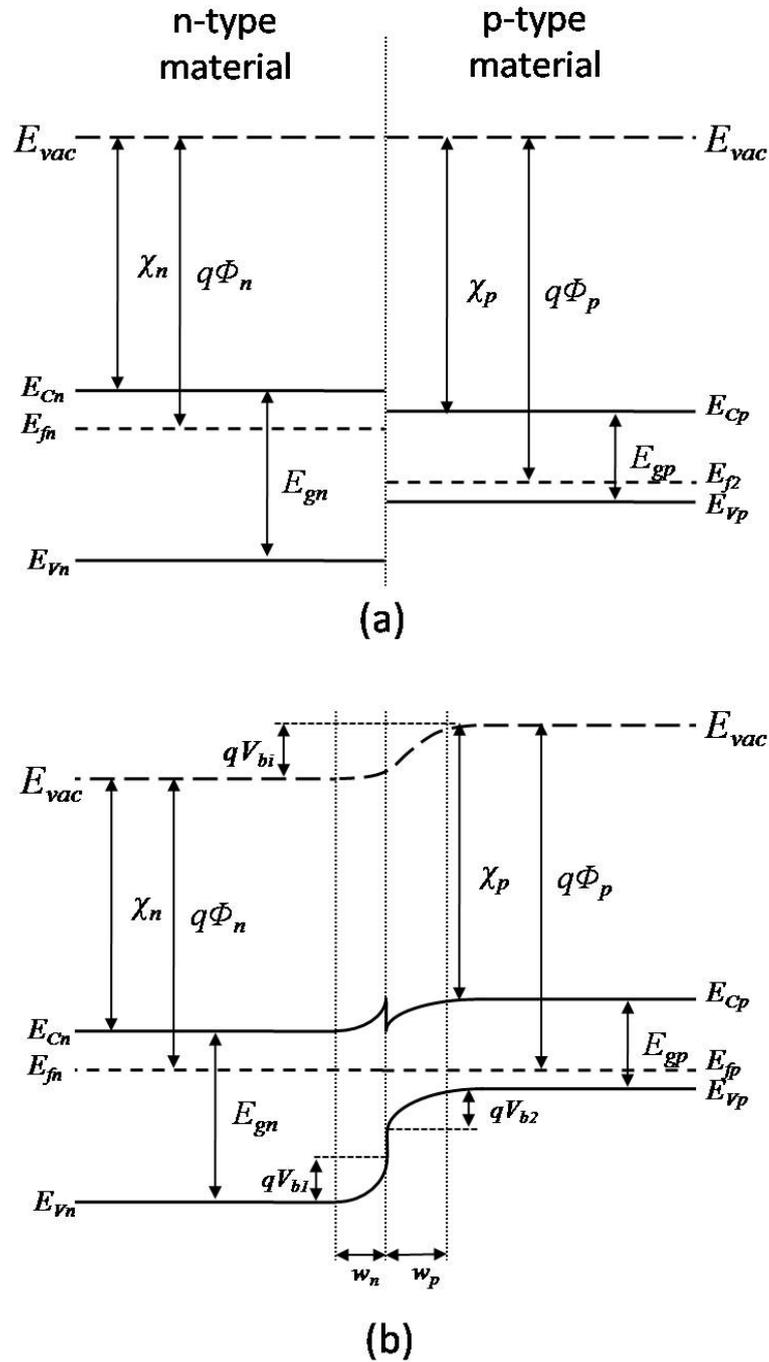

Figure 3.1: Formation of an n-p junction: (a) Band structure of two isolated semiconductors, one being n-type and the other p-type. (b) The resultant band structure at the interface between the two semiconductors on formation of a hetero-junction.

Figure 3.1b shows the resultant changes in the band structure of the two materials in the vicinity of the interface. This energy band model for the formation of an abrupt, ideal hetero-junction was fist proposed by Anderson [9]. A consequence of the transfer and annihilation of carriers during junction formation and the generation of a depletion zone is the bending of the conduction and valence bands. In the case of an n-p homo-junction (i.e where the n-type and p-type layers are of the same semiconductor material), the bending of the bands is continuous across the point $x = 0$. However, in a hetero-junction, because of the initial offsets in the band positions, i.e. $\Delta E_C = |E_{Cn} - E_{Cp}|$ and $\Delta E_V = |E_{Vn} - E_{Vp}|$, the resultant band profiles are discontinuous at the interface ($x = 0$). A spike is therefore formed in the conduction band at $x = 0$ which will oppose the flow of carriers.

The total built in potential V_{bi} is equal to the sum of the partial voltages V_{b1} and V_{b2} that arise due to band bending at the interface. As in the case of a homo-junction this V_{bi} corresponds to the difference in work function of each material, i.e.

$$V_{bi} = V_{b1} + V_{b2} = q(\phi_p - \phi_n) \tag{3.1}$$

It is assumed that the junction is abrupt, i.e. the boundary between the n and p materials is sharp, and that the carrier concentrations decrease rapidly from the bulk values, N_D and N_A, at the edges of the depletion zone. It is therefore possible to calculate the extent of the depletion zone into each material, w_n and w_p, by solving Poisson's equation, which relates the potential $\phi(x)$ to the charge density $\rho(x)$. The reader is referred to the detailed derivation provided in reference [10]. The calculation is dependant on the condition that both the potential and electric field are continuous at the interface ($x = 0$), i.e. $\varepsilon_n E_n = \varepsilon_p E_p$, where ε refers to the dielectric permittivity of each material. The extent of the depletion zone may therefore be expressed as

$$w_n = \left[\frac{2N_A \varepsilon_n \varepsilon_p \varepsilon_0 V_{bi}}{eN_D(\varepsilon_n N_D + \varepsilon_p N_A)} \right]^{1/2} \tag{3.2}$$

$$w_p = \left[\frac{2N_D \varepsilon_n \varepsilon_p \varepsilon_0 V_{bi}}{eN_A(\varepsilon_n N_D + \varepsilon_p N_A)} \right]^{1/2} \tag{3.3}$$

$$\tag{3.4}$$

and the total width, W, of the depletion zone may be expressed as

$$W = w_n + w_p = \left[\frac{2\varepsilon_0 \varepsilon_p V_{bi}(\varepsilon_n N_D + \varepsilon_p N_A)}{e\varepsilon_n N_A N_D} \right]^{1/2} \tag{3.5}$$

In many real situations it is often the case that the carrier concentration in one material is much greater than the other. For example, in CdTe/CdS the carrier concentration in the n-type CdS layer is several orders of magnitude higher than that in the p-type CdTe layer. In this case the extent of the depletion zone into the low doped layer will be far greater and it is possible to apply a one sided junction approximation whereby the junction extends solely in the direction of the low doped material from $x = 0$. Equation 3.5 can therefore be re-written as

$$W = \left[\frac{2\varepsilon_p \varepsilon_n V_{bi}}{eN_A}\right]^{1/2} \qquad \text{if} \quad N_D \gg N_A \tag{3.6}$$

If the external faces of the two semiconductors are contacted and a bias voltage, V, is applied then this bias acts as if it is applied directly across the junction. This is because of the relatively high resistivity of the depletion zone which is free of carriers. The width of the depletion zone will therefore change as a function of applied bias according to

$$W = \left[\frac{2\varepsilon_p \varepsilon_n (V_{bi} - V)}{eN_A}\right]^{1/2} \tag{3.7}$$

From this it is clear that under forward bias the width of the junction will decrease and under reverse bias, increase. The corresponding junction capacitance per unit area may be calculated according to

$$C = \frac{\varepsilon_p}{W} = \left[\frac{eN_A \varepsilon_p \varepsilon_0}{2(V_{bi} - V)}\right]^{1/2} \tag{3.8}$$

Respective plots of W and C as a function of bias, calculated from equations 3.7 and 3.8, are shown in figure 3.2 for an n-p junction characterised by the value $eV_{bi} = 1.4$ eV, constructed from p-type material having a carrier concentration of $N_A \approx 10^{15}$ cm^{-3}. Such values are typical of those found in CdTe based devices.

Experimentally, it is possible to determine values of V_{bi} and N_A by measuring C as a function of applied bias and then plotting the linear relation $1/C^2$ vs V. Any resultant straight line trend in the data will yield a gradient that is equivalent to N_A and a V-axis intercept equivalent to V_{bi}. This approach is applied in section 6.3.3 for a CdTe device.

3.2.3 J-V characteristics of ideal devices

The current-voltage (J-V) response of an n-p junction as derived by Shockley [11, 12] can be written as

$$J = J_0 \left[\exp\left(\frac{qV}{Ak_BT}\right) - 1\right] \tag{3.9}$$
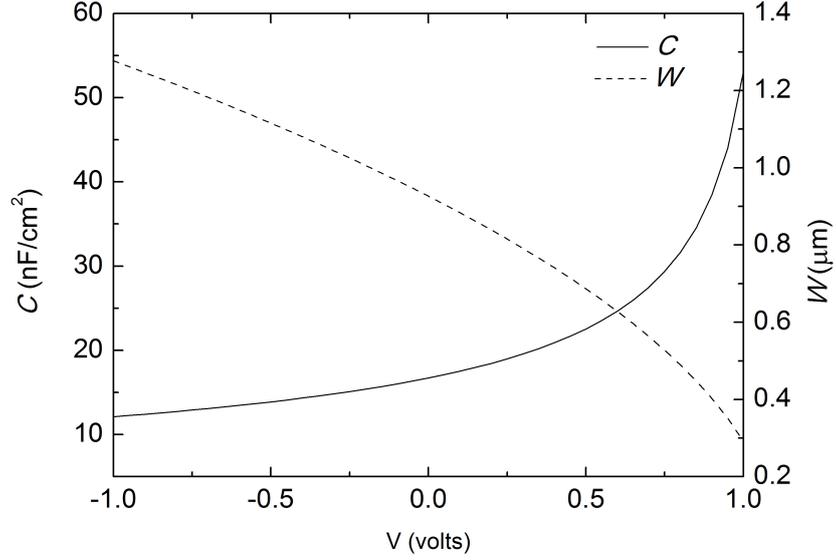
Figure 3.2: Simulated curves and depletion zone width plotted as a function of applied bias. The plots were constructed using equations 3.7 and 3.8 and are for an abrupt, one-sided n-p junction having $eV_{bi} = 1.4$ eV and $N_A = 10^{15}$ cm^{-3}.

where J_0 is the reverse saturation current, k_B is Boltzmann's constant, T is the temperature in Kelvin and V is the applied bias in volts. A is a constant called the *diode ideality factor* and has a value of 1 for an ideal device in which the current transport across the junction is not limited by recombination. For real junctions A typically takes values between 1 and 2.

As discussed in section 3.1, any semiconductor junction under illumination will exhibit the photovoltaic effect and in the case of an n-p junction any e-h pairs generated by light induced transitions within the depletion zone will be separated by the internal potential V_{bi}. Therefore, under illumination, equation 3.9 must be re-written as

$$J = J_0 \left[\exp\left(\frac{qV}{Ak_BT} \right) - 1 \right] - J_L \tag{3.10}$$

where J_L is the corresponding photo-current generated by the photo-voltaic effect. Note that J_L acts in the opposite direction to the current flow through the junction when under forward bias.

Such an n-p junction may be represented by the equivalent circuit diagram shown in figure 3.3. The n-p junction itself is represented by a single diode and the origin of the
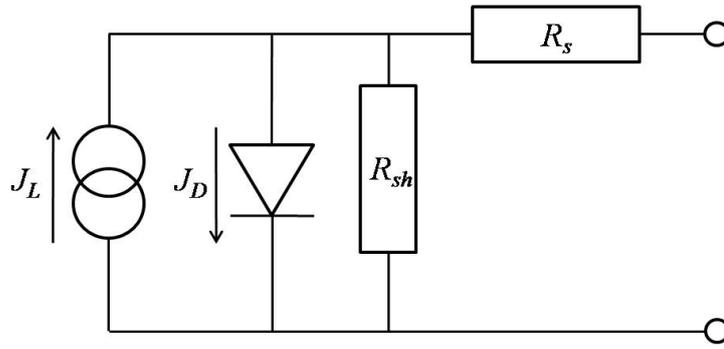
Figure 3.3: Equivalent circuit diagram for a hetero-junction under illumination. Note that the ideal case is represented by values of $R_s = 0$ $\Omega.cm^2$ and $R_{sh} = \infty$ $\Omega.cm^2$.
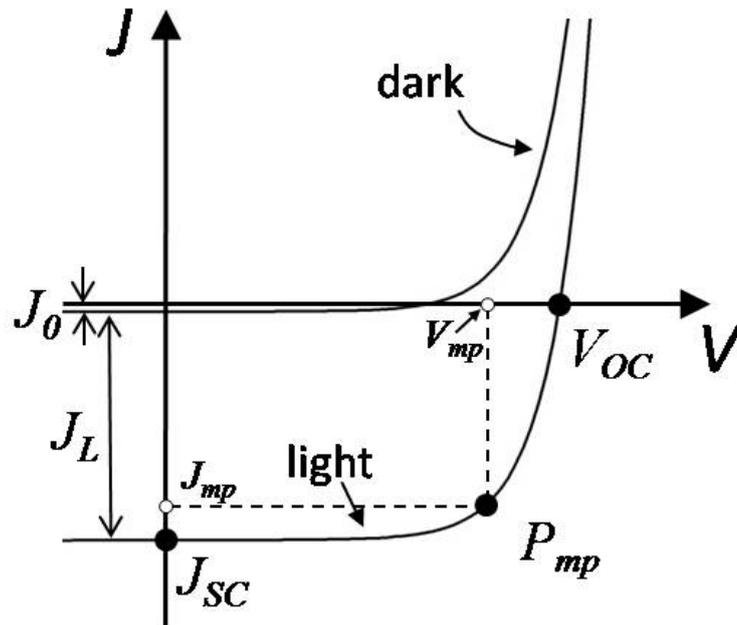
Figure 3.4: J-V response of an ideal hetero-junction in dark and under illumination.

photo-current is represented by a current source in parallel to this diode. Two resistances R_s and R_{sh}, connected in series and parallel respectively, represent effects typically present in real devices and will be discussed in detail in section 3.2.4. For an ideal device however, these resistances take values of $R_s = 0$ $\Omega.cm^2$ and $R_{sh} = \infty$ $\Omega.cm^2$.

Figure 3.4 shows the J-V response of an ideal device in the dark and under illumination. The dark curve shows the expected behaviour of a diode. Under illumination however this curve is shifted downwards by an amount J_L. From this light curve, some important

parameters may be extracted that characterise the junction's ability to convert light energy into electrical power. They are the short circuit current, J_{SC}, the open circuit voltage, V_{OC} and the fill factor, FF.

Short circuit current J_{SC}

The J_{SC} is defined as the current that would flow under illumination with a zero applied bias, and in an ideal device is equivalent to the total generated photo-current, J_L.

Open circuit voltage V_{OC}

The V$_{OC}$ corresponds to the voltage maintained across the junction, under illumination, when it is not connected to anything, or is connected to an infinite load i.e. zero current is permitted to flow out of the junction. By re-arranging equation 3.10 the V_{OC} can be expressed in terms of the photo-current J_L.

$$V_{OC} = \frac{Ak_BT}{q} \left[\ln\left(\frac{J_L}{J_0}\right) + 1 \right] \approx \frac{Ak_BT}{q} \ln\left(\frac{J_L}{J_0}\right) \tag{3.11}$$

Note that the size of the V_{OC} is inevitably limited by the built in voltage V_{bi} and in real devices, $V_{OC} \sim 0.7V_{bi}$, due to shunt and series resistances described below.

Fill factor FF

The fill factor defines the "squareness" of the J-V response and is calculated with reference to the maximum power rectangle (shown in figure 3.4) defined by the pair of values J_{mp} and V_{mp} the product of which corresponds to the maximum power point P_m. The FF factor can thus be expressed as

$$FF = \frac{J_{mp}V_{mp}}{J_{SC}V_{OC}} \times 100\% \tag{3.12}$$

Device efficiency η

The efficiency of an illuminated junction, η, is defined simply as the ratio of the incident radiant power, P_{in}, to the electrical power generated, P_{mp}, i.e

$$\eta = \frac{P_{mp}}{P_{in}} \times 100\% = \frac{J_{SC}V_{OC}FF}{P_{in}} \tag{3.13}$$

thus giving the key parameter by which a comparison of all solar cell devices can be readily made.

3.2.4 Losses in real devices

The above discussions are limited to the case of ideal devices, the performance of which is maximised with respect to some arbitrary, wavelength independent input power, P_{in}. However, real devices must be designed in response to the incident light received from the Sun, the spectral behaviour of which is by no means wavelength independent. The shape of the spectrum is equivalent to that of a black body emission spectra at a temperature of ~ 5780 K, as shown in figure 3.5. Furthermore, the effects of atmospheric absorption must be considered when designing terrestrial PV. Therefore it is conventional to design devices with respect to the radiation received from the Sun following its path through an air mass of 1.5 (AM1.5), i.e at an angle of 48.2° to a plane normal the the Earth's surface (AM1.0 representing the path at the equator). The AM1.5 spectrum is also shown in figure 3.5 [13].

The limitation that the AM1.5 spectrum imposes on device performance is twofold: Firstly, the use of a semiconductor material with a large band gap, e.g. $E_g > 2$ eV, means that a significant fraction of the solar spectrum will pass through the material without being absorbed and therefore the potential for photo-current generation will be reduced. Secondly, the use of a semiconductor with a relatively low band gap, e.g. $E_g < 1$ eV, permits the absorption of the majority of the spectrum at the cost of a reduced V_{bi} and
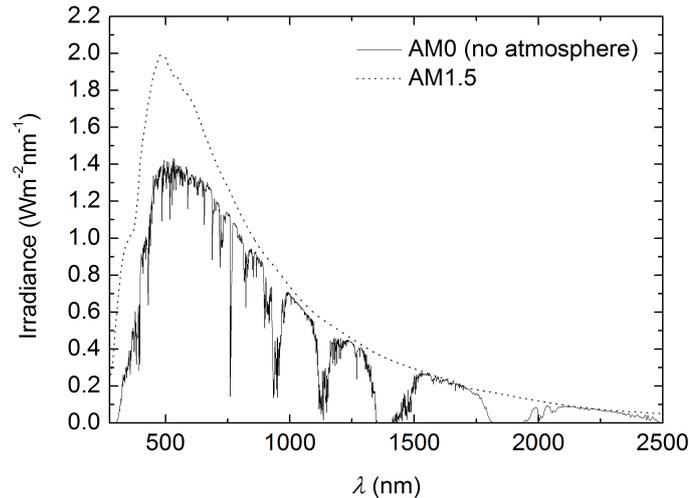

Figure 3.5: The solar spectrum at air mass indexes of AM0 (i.e outside Earth's atmosphere) and AM1.5.

hence a reduced V_{mp}. Figure 3.6 shows the theoretical maximum conversion efficiency as a function of band gap. A maximum conversion efficiency of $\sim 30\%$ is achieved for a material with a band gap of ~ 1.5 eV [14, 15]. The energy gaps of some commonly used PV materials are superimposed onto this curve. Note that one of the best candidate materials for the maximisation of conversion efficiency is CdTe, having a band gap of 1.45 eV.

Further losses to device efficiency relate to the series and shunt resistances alluded to in section 3.2.3 that are present in real devices. Their origin and effect on device performance is now discussed.

Series resistance R_s

Series resistances may arise at interfaces, e.g. between the semiconductor materials and their metallic contacts, due to the formation of non-Ohmic contacts. However, the most significant contribution to R_s is generally made by a device's TCO front contact layer (see Chapter 2), the resistivity of which is relatively high compared to metals. The reduction in resistivity of these TCO materials, while maintaining a high optical transmittance, is key to reducing R_s and maximising device performance. The minimisation of the resistivity of TCO materials is the main objective of the work presented in chapter 5.

The effect of R_s on the J-V characteristics of a device is shown in figure 3.7a. The
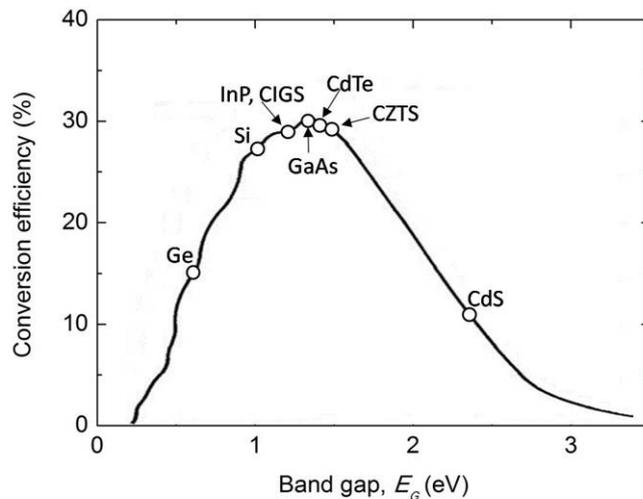

Figure 3.6:   Theoretical maximum conversion efficiency as a function of band gap in response to an AM1.5 spectrum

gradient of the forward bias section of the curve becomes less steep with increasing R_s and generates a reduction in the fill factor thus generating a corresponding loss in efficiency. Experimentally, it is possible to estimate the size of a device's series resistance from the linear part of the illuminated J-V curve under forward bias, which is approximately $1/R_s$.

Shunt resistance R_{sh}

Shunt resistances originate from the formation of leakage paths through the semiconductor materials, via pin-holes or grain boundaries, that permit the flow of current to bypass the n-p junction. The corresponding effect of such resistances are shown in figure 3.7b. A positive increase in the gradient of the reverse bias section of the curve is observed with a decrease in R_{sh}. This again generates a reduction in the FF. Experimentally, a value of R_{sh} can be estimated from the gradient of reverse bias part the J-V curve which is proportional to $1/R_{sh}$.

Equation 3.10 can be modified to account for these series and shunt resistances according to

$$J = J_0 \left[\exp \left(\frac{q(V - JR_s)}{Ak_BT} \right) - 1 \right] + \frac{V - JR_s}{R_{sh}} - J_L \qquad (3.14)$$

Potential for further losses in real devices, other than those described above, include a reduction in the photo-current due to the reflection of incident light at material interfaces [16]. For example, the combined reflection loss due to the air/glass and glass/TCO inter-
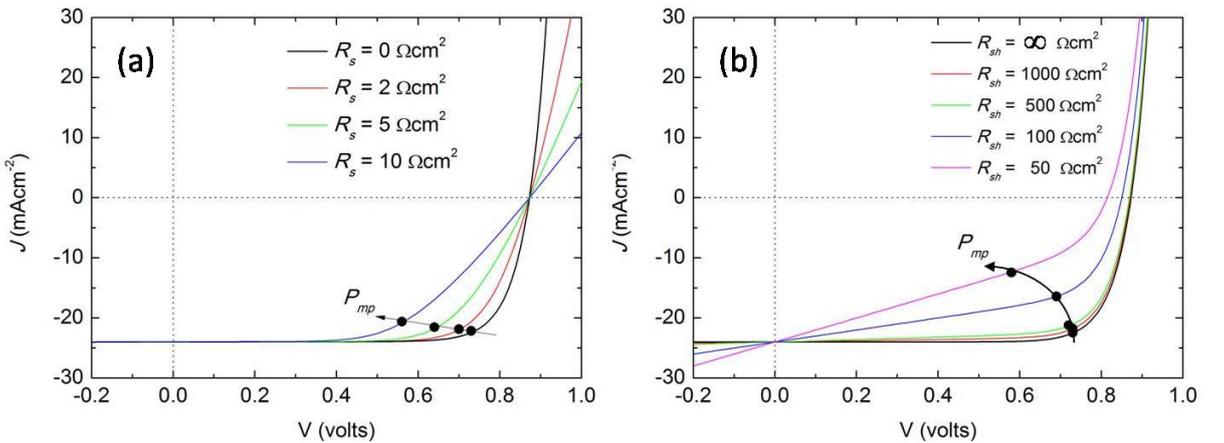

Figure 3.7: Calculated curves showing (a) series resistance and (b) shunt resistance on the J-V response of an n-p hetero-junction device under illumination.

60

faces in a typical CdTe device can be as high as 10%. The reduction of these reflection losses presents an excellent opportunity for performance improvements and is the subject of Chapter 7.

3.3 CdTe devices

As mentioned in section 3.2.4, CdTe is an ideal candidate material for solar cell design. Theoretical estimates for idealised CdTe devices show that conversion efficiencies up to $\sim 27\%$ may be achieved [14]. Furthermore, the linear absorption coefficient of CdTe is very high at wavelengths above the band gap, $\alpha > 10^4$ cm^{-1}, meaning that a relatively thin layer of CdTe is required for maximum absorption, a film thickness of ~ 2 μm being sufficient to absorb over 99 % of incident light.

The most common CdTe based PV devices are those that consist of an n-type CdS window (i.e transparent) layer and a p-type CdTe absorber layer. The fist demonstration of such a device was reported by Bonnet and Rabenhorst [17]. From here onwards, the term *CdTe based device* will refer to this specific n-type/p-type material combination. To date, these devices have been constructed almost exclusively in the *superstrate* configuration, i.e the CdTe layer is deposited following the deposition of a TCO front contact and CdS window layer onto a rigid, transparent substrate (typically glass). However, it has been shown that devices constructed in the *substrate* configuration, i.e. the CdTe being deposited prior to the CdS and TCO layers directly onto some metallic substrate, can achieve reasonable efficiencies of up to 8% [18]. The advantages offered by substrate device designs and their potential for the further reduction of performance losses are discussed in Chapter 8.

The following section discusses the role of each component layer within a CdTe device and the subsequent post-deposition treatment that is required to generate devices with high performances.

3.3.1 Device structure

Figure 3.8 shows the most common CdTe device structure consisting of a glass substrate, a transparent conducting oxide (TCO) front contact, a highly resistive transparent (HRT) oxide intermediate layer, n-type CdS and p-type CdTe semiconductor layers and a metallic

back contact. The current record for such a device stands at 16.5% ($J_{SC} = 25.88$ mAcm^{-2}, $V_{OC} = 845$ mV, $FF = 75.51\%$) over a 1 cm^2 contact [19]. However, recent press releases from First Solar report that the company has achieved a new record efficiency of 17.3% [20].

Glass substrate

A transparent substrate is a requirement of any superstrate solar cell design. Glass is an ideal candidate as it is robust, readily available and has a very low absorption coefficient ($< 10^{-1}$ cm^{-1}) over the range of wavelengths important to cell design. The most common type of glass used for module production is soda-lime (SL) glass, large volumes of which can be easily manufactured using the float glass process [21]. However, the use of SL glass limits any subsequent device fabrication procedures to maximum substrate temperatures of $\sim 550°$C, beyond which SL glass begins to soften. Cell fabrication procedures that require substrate temperatures higher than this must use aluminosilicate or borosilicate glasses which are stable up to $\sim 800°$C and $\sim 700°$C respectively. However, while both the temperature stability and purity of these glasses are better than SL glass they are significantly higher in cost and are not considered viable for large scale module production.
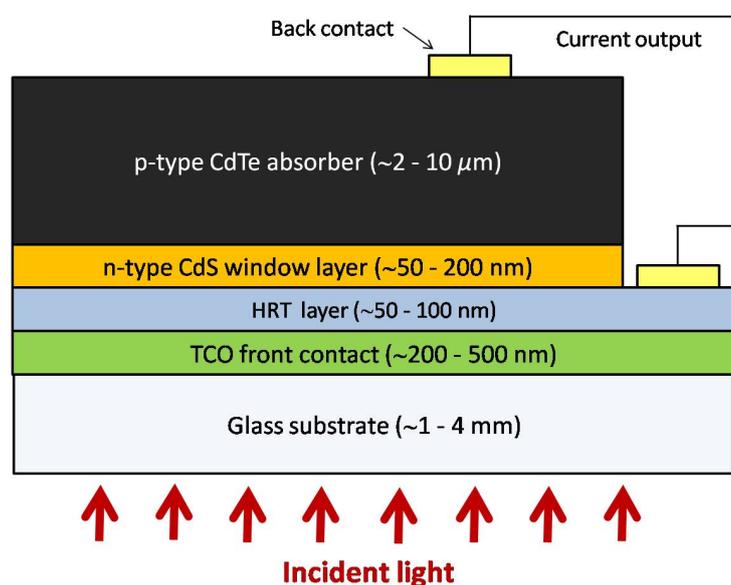

Figure 3.8: Common design for a CdTe solar cell in the superstrate configuration, i.e. where light enters through a the glass substrate.

One of the key photo-current losses in a superstrate device is due to the reflection of light from the front surface of the glass (i.e the air/glass interface), with up to 5% of the incident light being lost over the range of useful wavelengths. This may be reduced to $\sim 2\%$ through the application of an anti-reflection coating to this front surface. Such anti-reflective coatings and their contribution to device efficiency are discussed in section 7.5.2.

TCO front contact

An n-type front contact is required to contact the CdS layer. The requirements of an n-type TCO material with respect to solar cell design are discussed in detail in the previous chapter (Section 2.4) but to summarise they are:

- A sheet resistance of $R_s < 10\ \Omega/\square$.

- An integrated optical transmittance of $\tilde{T} > 85\%$ over the range 400-850 nm.

The development of new TCO materials that meet and improve upon these criteria is a critical objective for thin-film solar cell design. It is the resistance of this layer that makes the greatest contribution to a device's series resistance, R_s. A reduction in the TCO's sheet resistance will therefore generate gains in device fill factors.

Highly resistive and transparent (HRT) layer

It has been shown that the insertion of a highly resistive ($10^1 - 10^4$ Ω.cm) oxide layer between the TCO front contact and n-type CdS window layer can significantly improve device performance [22]. It is widely accepted that the key reason for this improvement is through the layer's ability to limit the negative effect that pin-holes in the CdS layer have on device performance. Typically pin-holes in the CdS give rise to shunt paths that form between the CdTe and TCO layer which can cause reductions in both the fill factor and the shunt resistance, R_{sh}. Both these parameters may be stabilised through the incorporation of a HRT layer. It has also been shown that the incorporation of a HRT layer reduces the reverse saturation current, J_0, leading to improved J-V characteristics [23, 24]. The extra stability that this layer affords permits the subsequent CdS layer to be thinned, resulting

in an increase in the transmittance through to the CdTe layer of wavelengths below the CdS band gap providing an extra contribution to a photo-current.

Further improvements to device performance, through incorporation of a HRT layer are believed to arise due to the prevention of the diffusion of electrically active impurities, from the glass substrate or TCO layer, into the CdS and CdTe layers that may have a negative impact on device performance (Na, In and Al for example are all n-type dopants in CdTe) [25]. Also, it is suggested that a HRT layer may act as an electrical barrier, preventing the formation of complete pin-holes though the CdS or further shunt paths along grain boundaries following post deposition processing procedures.

The most common materials used for HRT layers are SnO_2, ZnO and Zn_2SnO_4 which are typically deposited by either CVD or sputtering methods. The use of Zn-based layers are thought to be of particular benefit due to the potential for inter-diffusion of Zn into the CdS layer during post-deposition annealing treatments. Such inter-diffusion may generate an increase in the CdS band gap, thus permitting a higher fraction of the solar spectrum to be transmitted to the CdTe layer [26].

CdS window layer

In the case of a CdTe device an n-type CdS window layer, having a typical thickness in the range 100 - 300 nm, is most commonly used. Note that a CdTe homo-junction device (i.e. consisting of both n-type and p-type CdTe) would be of little use as a PV device due to the fact that a significant fraction of light would be absorbed before it reached the depletion zone. The band gap of CdS is $\sim 2.3 - 2.5$ eV for polycrystalline material and films are therefore transparent at wavelengths above $\sim 500 - 540$ nm. Although absorption due to direct-transitions increases rapidly below these wavelengths, a significant transmittance is observed (i.e $> 40\%$) for film thicknesses below 100 nm. A key aim of CdTe device design is to reduce the thickness of the CdS layer as much as possible in order to maximise the transmitted light at wavelengths below the band gap of CdS and hence further increase the photo-current, J_L. However, there are problems associated with CdS thinning due to the increased density of pin-holes within the layer and the assosiated shunt path formation through these pin-holes between the CdTe absorber and TCO layers. These shunt paths generate a decrease in the shunt resistance, R_{sh}, which in turn gives rise to a decrease in the

fill factor. While the introduction of a HRT layer may prevent a decrease in R_{sh} it is not possible to reduce the thickness of CdS indefinitely as eventually there will form a significant number of HRT/CdTe microjunctions. Although this junction is still a heterojunction and may contribute to the device performance it will generally operate with a reduced V_{OC} (e.g. for ZnO/CdTe, $V_{OC} \sim 500$ mV) [27].

The extent to which the CdS can be thinned without incurring losses depends primarily on the density and uniformity of the film, the control of which depend largely on the choice of deposition technique. Common deposition techniques for CdS include CSS [28], MOCVD [29–31], CBD [32, 33] and RFMS [34–36] all of which have been used to fabricate high efficiency (i.e. $\eta > 10\%$) CdTe devices, however the greatest potential for controlling these physical characteristics of the film are afforded by RFMS.

CdTe absorber layer

The p-type CdTe layer is referred to as the *absorber* as it is within this layer that all incident light is absorbed and the total photo-current generated. Note that any e-h pairs generated by absorption in the CdS window layer makes a negligible contribution to the photo-current. To date, the best performing CdTe devices consist of CdTe layers deposited by CSS [19, 37]. These devices typically have a CdTe thicknesses of between $5 - 10$ μm, significanly more than required to absorb all incident light (~ 2 μm). Such thicknesses are required to ensure the reduction of the density of pin-holes and other leakage paths (e.g. along grain boundaries) that arise from post-deposition processes such as acid etching (see section 3.3.3). However, it has been shown that performance can be maintained for films deposited by RFMS down to thicknesses of ~ 800 nm [38], due to high quality of sputtered films. This is significant because it presents an opportunity to dramatically reduce the amount of CdTe used in module production, a key objective due to the increasing scarcity of Te [1, 39]. Other deposition techniques include electro-deposition [40], evaporation [41], PLD [42] and MOCVD [43].

CdTe films deposited by all of the above techniques are polycrystalline. They are also typically weakly p-type due to the high population of intrinsic electrically active centres that arise from a difference in the vapour pressures between Cd and Te. Films typically grow with an excess of Te generating both singly and double ionised cadmium vacancies,

V_{Cd}^- and V_{Cd}^{2-}, which act as acceptors [44, 45]. The concentration of these vacancies is of the order $10^{17} - 10^{19}$ cm^{-3} [46, 47] but their contribution to the conductivity of the material is limited by the formation of neutral or singly ionized donor complexes of the form $V_{Cd}Te_{Cd}$ [48]. The level of compensation increases in line with increases in the V_{Cd} concentration meaning that a net p-type carrier concentration greater than $10^{14} - 10^{15}$ cm^{-3} is difficult to achieve [49]. A detailed review of intrinsic defects is given by Zoppi [30].

The resultant grain structure of the CdTe films is related to device performance, with features such as grain boundaries, twins, dislocations and voids all potentially acting as recombination centres within the layer and having a negative effect on performance. Grain boundaries in particular give rise to a significant level of recombination and therefore it is desirable that CdTe films have large grain sizes, > 1 μm, so that the total density of grain boundaries is reduced. Indeed, the best performing devices that have been reported consist of CdTe films that are composed of grains the size of the entire film width, i.e with no grain boundaries lying in a plane (i.e. columnar grains) that might oppose the flow of current through the device. Such grain structures are generally only achieved through the re-crystallisation of as-deposited layers during post-deposition treatments.

3.3.2   Post-deposition treatment

In general, it is not possible to generate high efficiency CdTe solar cells without some form of post-deposition treatment. Ubiquitous to all such treatments is the use of some Cl containing compound to which the as-grown device is exposed. Furthermore, most treatments involve annealing the as-grown device in either an oxygen rich or air ambient at a temperature between $350 - 450°$C and for a typical duration of $20 - 30$ mins [50]. An optimised treatment procedure will result in the complete formation of a heterojunction, such as that described in section 3.2.2, where the electrical junction coincides with the position of the CdTe/CdS interface (i.e the metallurgical junction).

There are several effects that the post-deposition treatment have on the CdTe absorber layer: Firstly, the introduction of Cl to the layer during annealing creates $V_{Cd}Cl_{Te}^{2-}$ acceptor complexes [51] which make the film more p-type and significantly reduces the resistivity of the layer [52]. Note that on the introduction of a very large concentration of Cl, compensation occurs through the formation of Cl_{Te} donors. Secondly, small grained (i.e < 1 μm)

as deposited CdTe films undergo significant re-crystallisation [53] which generates a high degree of grain growth through the coalescence and consumption of smaller grains [54]. Also, films with a high degree of orientation, typically in the (111) direction, become more randomised following recrystallisation during treatment. As-grown films will undergo re-crystallisation naturally during annealing in an air ambient with no Cl present. However, the introduction of Cl dramatically increases the rate at which re-crystallisation occurs [55].

Thirdly, the post-deposition treatment promotes the intermixing of the CdS and CdTe layers [56]. This is beneficial as it removes defect states at the interface between the layers that are created due to the strain arising from a 10 % lattice mis-match between CdS and CdTe. An improvement in V_{OC} is generally observed as a result of inter-mixing [26] and also a reduction in the reverse saturation current J_0 [57]. Lastly, in as-grown CdTe layers a high concentration of defect states located at grain boundaries present a barrier to current flow. It has been shown that following the introduction of Cl during annealing, the grain boundaries are no longer electrically active, i.e they are passivated [58–60].

Many post-deposition treatment approaches have been reported, however the most common approach is the deposition of a thin $(50 - 200$ nm) film of $CdCl_2$ via thermal evaporation followed by an air anneal at $\sim 390°C$ for ~ 20 min [19, 54, 61]. Other approaches include the in-situ incorporation of Cl (e.g. during CdTe deposition) [62, 63], dipping the back CdTe surface in a methanol solution of $CdCl_2$ and allowing a $CdCl_2$ deposit to form on evaporation [64], or annealing in a chlorine containing gas, typically a freon. Of all these post-deposition treatments that involving the evaporation of $CdCl_2$ prior to annealing has produced devices with the highest efficiencies.

It has recently been demonstrated that annealing a device in the presence of Cl containing freons can also generate devices with efficiencies up to 15.8% [37, 65, 66]. This route is advantageous as it eliminates the use of toxic $CdCl_2$. It also presents an opportunity to increase the rate of module production by removing the extra evaporation step associated with the use of $CdCl_2$. A key disadvantage of the technique is the use of gases that contribute to ozone depletion, however this effect can be minimised through the recycling or pyrolisation of process gas.

3.3.3 The back contact

An Ohmic metal contact to the back surface of the CdTe is required. However, this is difficult to achieve due to the high electron affinity, $\phi_p \sim 5.7$ eV [67], of CdTe which is higher than most metals. Therefore, in most cases a Schottky junction is formed at the interface between the CdTe back surface and the metal contact (which, in research lab tests, is most commonly gold). Figure 3.9 shows an energy level diagram for such a junction. The junction possesses a potential barrier V_{bi} that opposes the flow of photo-current generated by the heterojunction at the CdTe/CdS interface.

To overcome this problem the back surface of the CdTe may be doped highly p-type, i.e. p^+, prior to contact deposition. This will reduce the width of the potential barrier. There are several approaches that have been adopted to achieve this doping: Most common, is the introduction of Cu, a p-type dopant in CdTe, to the back surface via either the direct deposition of a copper film [68] or the application of a copper containing graphite paste [69]. Subsequent annealing is required for doping to be achieved and the formation of a thin, highly conductive $Cu_x Te$ phase (where $x < 1.4$) at the back surface. However, the use of copper can be disadvantageous due to it diffusing freely throughout the rest of the device structure. The segregation of Cu at grain boundaries, forming shunt paths [70], and
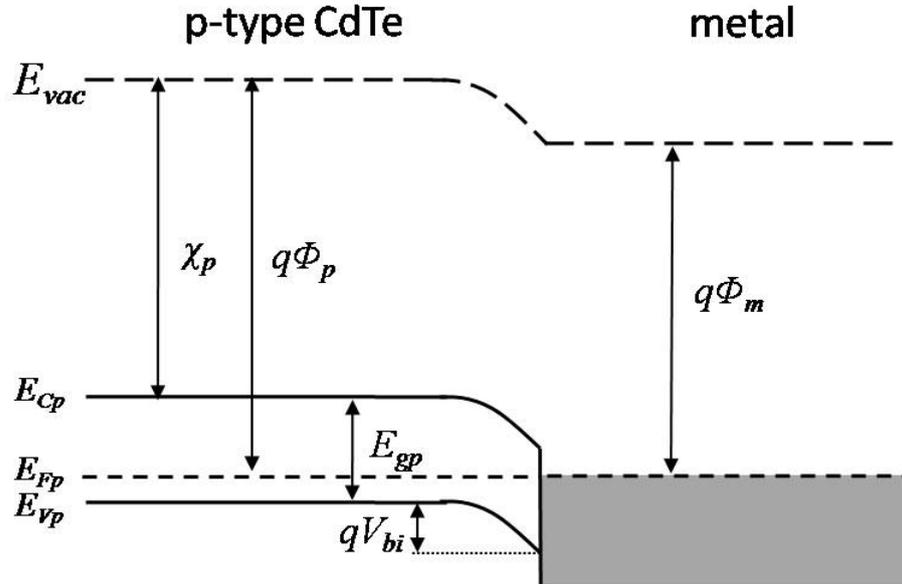

Figure 3.9: Formation of a Schottky junction at p-type CdTe/metal contact interface. ϕ_p and ϕ_m represent the work functions of the CdTe and metal respectively.

its diffusion into the CdS where it acts acts as a p-type dopant [71], generate losses in the fill factor and V_{OC}. Note that it has been shown that copper diffusivity can be controlled to an extent by limiting the thickness of a deposited Cu layer to ~ 4 nm [72]. Aresenic doping has also been shown to create a sufficient p^+ layer at the CdTe back surface [30, 73]. It has also been shown that the use of copper doped intermediate layers such as ZnTe:Cu [74] and HgCdTe:Cu [75] can help stabilise devices by preventing an excess Cu diffusing into the device. It has also been demonstrated that the used of materials such as $NiTe_2$ [76] and Sb_2Te_3 [77, 78] can eliminate the need for Cu altogether.

In most cases the formation of a p^+ layer is aided by chemically etching the CdTe back surface using bromine methanol (BM) [79] or nitrophosphoric (NP) acid [80] prior to doping and contact deposition. Etching removes Cd from the back surface of the film, leaving it Te rich and more p-type, reducing the width of any subsequent Schottky junction Hence, the transport of current via tunnelling is encouraged. However, etching is often more pronounced at the grain boundaries and therefore the likeliness of shunt paths forming through the film is increased. Thicker layers of CdTe are required to overcome this problem. Note that for fully sputtered devices it has been shown that etching is unnecessary [72]. This is significant as the elimination of an etching step is likely to reduce module production costs.

3.4 Concluding Remarks

The market position of thin-film PV continues to strengthen year on year. This is particularly so for CdTe based PV with First Solar now producing over 2 GW per annum at an average module cost of less than $1/W_p$. However, in order to ensure the future success of the CdTe platform further reductions in processing costs and increases in module efficiencies are necessary. Some of the key areas of new research within the field of CdTe solar cells are:

- **Design of high performance TCOs**: The achievement of sheet resistances below 5 $\Omega/\square$, while maintaining high transmittance ($> 85\%$), is key to the reduction of device series resistance and the improvement of fill factors. The development of TCO materials via RF magnetron sputtering is the subject of Chapter 5.

- **Reduction of optical losses**: The device J_{SC} may be further improved by minimising the reflection from material interfaces. In the case of superstrate designs an immediate 4% reduction can be achieved through development and application of an efficient anti-reflection (AR) coating the front glass surface. Further reductions may be achieved by finding optimum device configurations through a consideration of the constituent film dispersion properties. The modelling of AR coatings and optimised device structures is the subject of Chapter 7.

- **Reduction of CdTe thickness**: The biggest concern regarding the sustainability of CdTe solar cells is the availability of Te. The thinning of the CdTe absorber layer while maintaining high device efficiencies is therefore a key objective within the field.

- **HRT layers**: Investigations that lead to a full understanding of the effects that HRT layers have on cell stability are desired. This will aid the design of existing and new HRT materials and improve their performance within device configurations. Such layers are key for maintaining stability under the reduction of both CdS and CdTe film thicknesses.

- **Substrate devices**: The development of efficient solar cells orientated in the substrate configuration immediate eliminates the reflection losses associated with the air/glass interface. Furthermore, the potential for the use of metal foils or possibly even polymers as substrates instead of glass presents an excellent opportunity for module cost reduction.

3.5 References

[1] K. Zweibel. Technical report, NREL (2005). TP-520-38350.

[2] R. Stevenson. *Spectrum, IEEE* **45(8)**, 26 (2008).

[3] *First Solar Press Release* (2009). *"First solar passes* $1 *per Watt industry milestone"* http://investor.firstsolar.com/releasedetail.cfm?ReleaseID=571539. Accessed Aug 2011 -
accessed Aug 2011.

[4] E. Becquerel. *C. R. Hebd. Acad. Sci.* **9**, 561 (1839).

[5] W. Smith. *Nature* **7**, 303 (1873).

[6] E. Weston (1888). US Patent 389,125.

[7] S. M. Sze. *Physics of Semiconductor Devices*. Wiley (1981). 2nd Ed.

[8] A. Fahrenbruch, R. Bube. *Fundamentals of Solar Cells*. Academic Press, Orlando USA (1983).

[9] R. L. Anderson. *Solid State Electron.* **5**, 341 (1962).

[10] J. R. Hook, H. E. Hall. *Solid State Physics*. Wiley (2003). Pp172-173.

[11] W. Shockley. *Bell Syst. Tech. J* **28**, 435 (1949).

[12] W. Shockley. *Electrons and Holes in Semiconductors*. Van Nostrand, Princeton (1950).

[13] Data online at http://rredc. nrel. gov/solar/spectra/am1.5 - accessed Aug 2011.

[14] J. J. Loferski. *J. Appl. Phys.* **27**, 777 (1956).

[15] C. H. Henry. *J. Appl. Phys.* **51**, 4494 (1980).

[16] J. R. Sites. *Sol. Energy Mater. Sol. Cells* **75**, 243 (2003).

[17] D. Bonnet, H. Rabenhorst. *Proc. of 9th European PVSEC*, 129 (1972).

[18] X. Mathew, J. P. Enrique, A. Romeo, A. N. Tiwari. *Solar Energy* **77**, 831 (2004). Thin Film PV.

[19] X. Wu, J. C. Keane, R. G. Dhere, C. DeHart, D. S. Albin, A. Dudam, T. A. Gessert, S. Asher, D. H. Levi, P. Sheldon. *Proc. of 17th European PVSEC* (2001).

[20] Press Release (2011). *"First Solar sets the world record for CdTe solar PV efficiency"* http://investor.firstsolar.com/releasedetail.cfm?ReleaseID=593994 - accessed Aug 2011.

[21] Pilkington Brothers Ltd. *Proc. R. Soc. Lond. A* **314**, 1 (1969).

[22] C. S. Ferekides, R. Mamazza, U. Balasubramanian, D. L. Morel. *Thin Solid Films* **480**, 224 (2005).

[23] W. Li, R. Ribelin, Y. Mahathongdy, D. Albin, R. Dhere, D. Rose, S. Asher, H. Moutinho, P. Dheldon. The effect of high-resistance SnO_2 on CdS/CdTe device performance. Technical report, NREL (1998). CP-520-25607.

[24] Q. Chen, G. Zeng, H. Song, J. Zheng, L. Feng. *J. Mater. Sci: Mater. Electron.* **20**, 661 (2009).

[25] E. Watson, D. Shaw. *J. Phys. C Solid State* **16**, 515 (1983).

[26] X. Wu, S. Asher, D. H. Levi, D. E. King, Y. Yan, T. A. Gessert, P. Sheldon. *J. Appl. Phys.* **89**, 4564 (2001).

[27] J. A. Aranovich, D. Golmayo, A. L. Fahrenbruch, R. H. Bube. *J. Appl. Phys.* **51**, 4260 (1980).

[28] D. Bonnet. *Thin Solid Films* **361**, 547 (2000).

[29] A. Tetsuya, S. Kumazawa, H. Higuchi, T. Arita, S. Shibutani, T. Nishio, J. Nakjima, M. Tsuji, A. Hanafusa, T. Hibino, K. Omura, H. Ohyama, M. Murozono, T. Aramato. *J. J. App. Phys.* **36**, 6304 (1997).

[30] G. Zoppi. *Studies of CdTe thin films and solar cells grown by MOCVD*. Ph.D. thesis, Durham University (2005).

[31] E. W. Jones, V. Barrioz, S. J. C. Irvine, D. Lamb. *Thin Solid FIlms* **517**, 226 (2009).

[32] A. K. Turner, J. M. Woodcock, M. E. Ozsan, D. W. Cunningham, R. J. Johnson, D. R. Marshall, N. B. Mason, S. Oktik, M. H. Patterson, S. J. Ransome, S. Roberts, M. Sadeghi, J. M. Sherborne, D. Sivapathasundaram, I. A. Walls. *Sol. Energy Mater. Sol. Cells* **35**, 263 (1994).

[33] M. D. Archbold, D. P. Halliday, K. Durose, T. P. A. Hase, D. S. Boyle, S. Mazzamuto, N. Romeo, A. Bosio. *Thin Solid Films* **515**, 2954 (2007).

[34] A. Bosio, N. Romeo, S. Mazzamuto, V. Canevari. *Prog. Cryst. Growth* **52**, 247 (2006).

[35] A. Compaan, R. Collins, V. Karpov, D. Giolando. Fabrication and physics of cdte devices by sputtering. Technical report, NREL (2008). www.nrel.gov/docs/fy09osti/45398.pdf - accessed Aug 2011.

[36] R. E. Treharne, A. Seymour-Pierce, K. Durose. *J. Phys. Conf. Ser.* **286** (2011).

[37] N. Romeo, A. Bosio, A. Romeo, M. S, C. V. *Proc. 21st EPSEC* 1857 (2006).

[38] A. Gupta, V. Parikh, A. Compaan. *Sol. Energy Mater. Sol. Cells* **90**, 2263 (2006).

[39] B. A. Andersson, C. Azar, J. Holmberg, S. Karlsson. *Energy* **23**, 407 (1998).

[40] B. M. Basol. *Solar Cells* **23**, 69 (1988).

[41] R. W. Birkmire, B. McCandless, W. N. Shafarman. *Solar Cells* **23**, 115 (1988).

[42] J. Ramiro, A. Perea, J. F. Trigo, E. G. Camarero. *Thin Solid Films* **361**, 65 (2000).

[43] R. A. Berrigan, N. Maung, S. J. C. Irvine, D. J. Cole-Hamilton, D. Ellis. *J. Cryst. Growth* **195**, 718 (1998).

[44] F. A. Abulfotuh, A. Balcioglu, T. Wangensteen, H. R. Moutinho, F. Hassoon, A. Douri, A. Alnajjar, L. L. Kazmerski. *Proc. 26th IEEE PVSEC*, 47 (1997).

[45] P. Emanuelsson, P. Omling, B. K. Meyer, M. Wienecke, M. Shenk. *Phys. Rev. B* **47**, 15578 (1993).

[46] M. A. Berding. *Phys. Rev. B* **60**, 8943 (1999).

[47] M. Wienecke, M. Shchenk, H. Berger. *Semicond. Sci. Technol* **8**, 299 (1993).

[48] K. Krsmanovic, K. G. Lynn, M. H. Weber, R. Tjossem, T. Gessmann, C. Szeles, E. E. Eissler, J. P. Flint, H. L. Glass. *Phys. Rev. B* **60**, 8950 (2000).

[49] J. Sites. Technical report, NREL (1999). SR-520-26315.

[50] C. S. Ferekides, U. Balasubramanian, R. Mamazza, V. Viswanathan, H. Zhao, D. L. Morel. *Solar Energy* **77**, 823 (2004).

[51] P. Hoschl, R. Grill, J. Franc, P. Moravec, E. Belas. *Mater. Sci. Eng. B* **16**, 215 (1993).

[52] H. Bayhan, C. Ercelebi. *Semi. Sci. Technol.* **12**, 600 (1997).

[53] B. E. McCandless, L. V. Moulton, R. W. Birkmire. *Prog. PV* **5**, 249 (1997).

[54] H. Moutinho, M. Al-Jassim, F. Abulfotuh, D. Levi, P. Dippo, R. Dhere, L. Kazmerski. *Proc. 26th IEEE PVSC*, 431 (1997).

[55] D. H. Levi, H. R. Moutinho, F. S. Hasoon, B. M. Keyes, R. K. Ahrenkiel, M. Al-Jassim, L. L. Kazmerski, R. W. Birkmire. *Sol. Energy Mater. Sol. Cells* **41**, 381 (1996).

[56] D. G. Jensen, B. E. McCandless, R. W. Birkmire. *Proc. 25th IEEE PVSC*, 773 (1996).

[57] D. M. Oman, K. M. Dugan, J. L. Killian, V. Ceekala, C. S. Ferekides, D. L. Morel. *App. Phys. Lett.* **67**, 1896 (1995).

[58] P. R. Edwards, D. P. Halliday, K. Durose, H. Richter, D. Bonnet. *Proc. 14th PVSEC* 2083 (1997).

[59] P. R. Edwards, K. Durose, s. Galloway, D. Bonnet, H. Richter. *Proc. 2nd World Conf. PVSE* 472 (1998).

[60] L. M. Woods, G. Y. Robinson. *Proc. 28th IEEE PVSC* 603 (2000).

[61] X. Wu. *Solar Energy* **77**, 803 (2004).

[62] P. D. Paulson, V. Dutta. *Thin Solid Films* **370**, 299 (2000).

[63] V. Barrioz, S. Irvine, E. Jones, R. Rowlands, D. Lamb. *Thin Solid Films* **515**, 5808 (2007).

[64] B. McCandless, R. Birkmire. *Solar Cells* **31**, 527 (1991).

[65] S. Mazzamuto, L. Vaillant, A. Bosio, N. Romeo, N. Armani, G. Salviati. *Thin Solid Films* 7079–7083 (2008).

[66] N. Romeo, A. Bosio, A. Romeo. *Sol. Energy Mater. Sol. Cells* **94**, 2 (2010).

[67] S. Banerjee, B. Streetman. *Solid State Electronic Devices 5th Ed.* New Delhi, PHI Learning Private Ltd. (2005).

[68] M. Shao, A. Fischer, D. Grecu, U. Jayamaha, E. Bykov, G. Contreras-Puente, R. G. Bohn, A. D. Compaan. *Appl. Phys. Lett.* **69**, 3045 (1996).

[69] R. Dhere, D. Rose, D. Albin, S. Asher, M. Al-Jassim, H. Cheong, A. Swartzlander, H. Moutinho, T. Coutts, R. Ribelin, *et al. Proc. 26th IEEE PVSC*, 435 (1997).

[70] D. Bätzner, R. Wendt, A. Romeo, H. Zogg, A. Tiwari. *Thin Solid Films* **361**, 463 (2000).

[71] D. Petre, I. Pintilie, E. Pentia, T. Botila. *Mater. Sci. Eng. B* **58**, 238 (1999).

[72] A. Compaan, A. Gupta, S. Lee, S. Wang, J. Drayton. *Solar Energy* **77**, 815 (2004).

[73] V. Barrioz, Y. Y. Proskuryakov, E. W. Jones, J. D. Major, S. J. C. Irvine, K. Durose, D. A. Lamb. *MRS Res. Symp. Proc.*, 367 (2007).

[74] S. H. Kim, J. H. Ahn, S. H. Kim, H. M. lee, D. H. Kim. *Curr. Appl. Phys.* **10**, S484 (2010).

[75] K. D. Dobson, I. Visoly-Fisher, G. Hodes, D. Cahen. *Sol. Energy Mater. Sol. Cells* **62**, 295 (2000).

[76] O. Rotlevi, K. D. Dobson, D. Rose, G. Hodes. *Thin Solid Films* **387**, 155 (2001).

[77] A. Abken. *Sol. Energy Mater. Sol. Cells* **73**, 391 (2002).

[78] N. Romeo, A. Bosio, R. Tedeschi, V. Canevari. *Thin Solid Films* **361**, 327 (2000).

[79] B. McCandless, K. Dobson. *Solar Energy* **77**, 839 (2004).

[80] J. Sarlund, M. Ritala, M. Leskelä, E. Siponmaa, R. Zilliacus. *Sol. Energy Mater. Sol. Cells* **44**, 177 (1996).

Chapter 4

Experimental Methods

4.1 Introduction

A variety of growth and characterisation techniques were used within this work. The following description of these techniques is divided into three sections. Firstly, the key growth technique (i.e radio frequency magnetron magnetron sputtering) is discussed with regards to the deposition of single layers and multi-layered structures and this is followed by a summary of the procedures used in the processing of CdTe PV devices. Secondly, the measurement techniques employed in the electrical, optical and structural characterisation of single films is discussed. Lastly, the techniques used in the electrical and structural characterisation of completed CdTe devices are presented.

4.2 Film deposition and device fabrication

In this section the technique of magnetron sputtering and the subsequent processing steps used in device fabrication are described in detail. Common features of the deposition and processing are presented but a discussion of conditions and parameters associated with specific materials or experiments are deferred until the relevant points in subsequent chapters.

4.2.1 Radio frequency magnetron sputtering

Radio frequency magnetron sputtering (RFMS) is a thin-film deposition technique that can be used to deposit a wide range of dielectric and semiconductor materials. Figure 4.1 shows schematic of the magnetron/substrate arrangement used within this work. The magnetrons contain a symmetrical configuration of permanent magnets to which a disc of the desired target material is fixed. They are water cooled to prevent the targets from overheating. A summarised description of the sputtering process, from a single target, is as follows:

- The vacuum chamber is filled with a pressure (1 - 20 mTorr) of argon.

- An RF voltage (13.56 MHz) is applied accross the substrate holder and the magnetron.

- Residual electrons, within the vacuum chamber, are accelerated by the voltage and confined to spiral paths around the magnetic field lines at the target surface.

- The Ar atoms within the region of the target surface are ionized by electrons, forming a plasma, and are accelerated towards the target. The motion of the Ar^+ ions is not influenced by the magnetic field because of their large mass, relative to electrons.
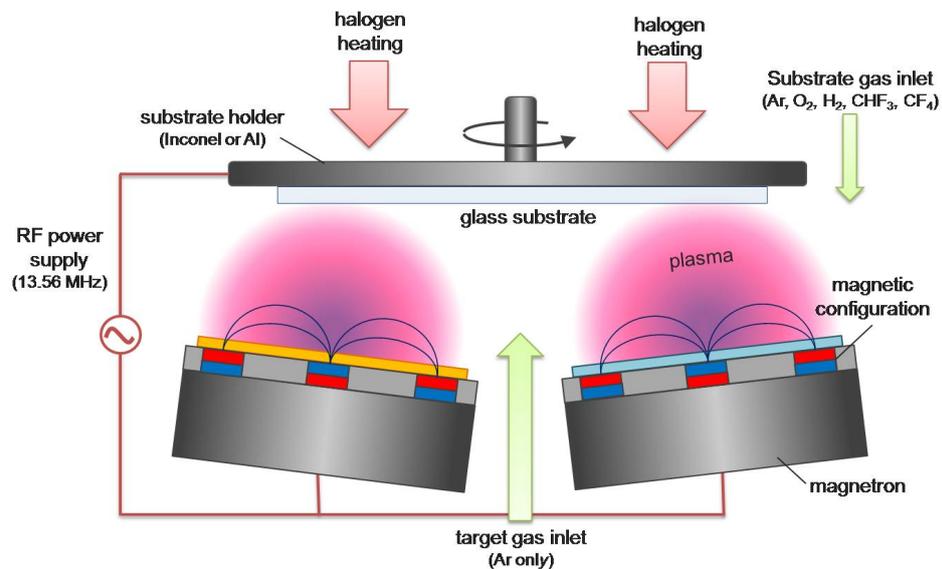

Figure 4.1: Schematic of sputtering chamber.
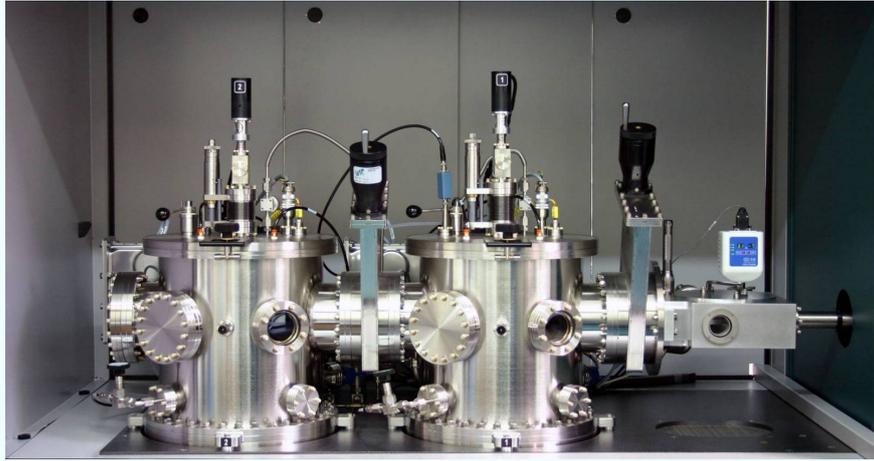
Figure 4.2: AJA Orion Phase II-J dual chamber sputtering kit.

- Ar^+ ions that impact upon the target surface knock out neutrally charged species of target material which travel, with long mean free paths, until they encounter the substrate.

For a more detailed description of the principles behind the sputtering process and technical reviews of the current state of the art the reader is referred to references [1–5].

The use of an RF voltage is necessary for dielectric materials in order to overcome the build-up of positive charge at the target surface. Because of this, the growth rates associated with RFMS are typically half those of direct current magnetron sputtering (DCMS) as the Ar^+ ions spend as much time travelling away from the target as travelling towards it. In general, it is only possible to use DCMS to deposit from metallic targets where the high conductivity of the materials prevent a charge build-up. In this work, RFMS was performed using an AJA Orion Phase II-J dual chamber kit (figure 4.2). Chamber 1 was used in the deposition of metal-oxides (i.e. In_2O_3, SnO_2, ZnO, TiO_2, SiO_2) and chamber 2 was used to deposit semiconductor films required for PV devices (i.e. CdS and CdTe). Features of the kit include:

- Substrate heating: halogen lamps located behind the substrate holder were used to heat substrates to a maximum of 800°C.

- Growth monitoring: A quartz crystal oscillator, located in the vicinity of the substrate, could be used to monitor the change in film thickness during deposition. However, it was necessary to calibrate this oscillator against a physical measurement, e.g.

surface profilometry (section 4.3.3).

- Reactive gases: incorporation of H_2, O_2, CHF_3 and CF_4 gases to the chamber during deposition permitted reactive sputtering, achieving reduction, oxidation and doping of resultant films respectively. Gas flow rates were controlled by mass flow controllers (MFCs) that permitted flows in the range 0.15 - 10 sccm.

- Co-sputtering: the arrangement of multiple magnetrons within each chamber (four in chamber 1 and two in chamber 2) permitted materials from different targets to be deposited simultaneously and the growth rates from each to be controlled independently.

- DC bias: The application of a DC voltage between the substrate and chamber generated a plasma that was confineable to the substrate surface and used to back-sputter from the substrate surface. This feature was used exclusively prior to deposition to clean the glass substrates.

- Load lock: substrates were loaded into chambers via a load lock so that the chambers did not have to be opened after each run. This helped to preserve the conditioning of the targets and dramatically reduced the pumping time required.

- Chamber transfer: the substrates were transferred between chambers 1 and 2 without breaking vacuum.

- Computer control: All runs could be programmed and completely automated using a LabView based program. This was particularly useful for the deposition of complicated multi-layer structures and eliminated the potential for human error during growth. The use of datalogging software during growth also ensured that if a run was aborted then it was possible to determine why.

The three key deposition parameters of RFMS are RF power, pressure and substrate temperature. Some general characteristics relating to the effect on the growth rate of varying these three parameters include:

- A linear increase in the growth rate of a material with RF power.

- An increase in growth rate with a reduction in pressure.

- A relatively small decrease in growth rate with increasing substrate temperature.

4.2.2 Device fabrication and processing

The following is a brief description of how CdTe devices were prepared from start to finish. In general all devices were deposited onto 10 cm × 10 cm × 3.2 mm low Fe soda-lime glass (SLG) substrates provided by Pilkington (OptiWhite). The thickness uniformity of layers deposited on this scale was deemed excellent with a typical variation of < 5% accross each layer. Following deposition, via RFMS, the 10 cm × 10 cm samples were cut into either four 5 cm × 5cm or sixteen 2.5 cm × 2.5 cm pieces. Doing this permitted investigations into the effect of multiple post growth treatments, the details of which are deferred to section 6.3.2.

Glass cleaning

Prior to deposition the substrates underwent the following cleaning regime:

- EX SITU

    - Scrub with nylon brush and de-ionized (DI) water.

    - Ultrasonication in boiling DI water + 2% Decon90 detergent.

    - Rinse with DI water followed by rinse with isopropanol alcohol.

    - Nitrogen blow dry.

- IN SITU

    - 10 - 15 min DC bias plasma etch: RF power = 50 W, pressure = 5 mTorr (Ar only)

RFMS of device structures

Each target was pre-sputtered, under the conditions of the subsequent film deposition, for a minimum of 10 mins prior to the opening of the shutter (located directly above target surface). This helped to ensure that any contaminants were removed from the target surface before deposition. The TCO (ITO) and buffer (ZnO) layers were deposited firstly

in chamber 1 (see section 4.3.1) and then the sample was transferred, under vacuum, to chamber 2 where films of CdS and CdTe were deposited. The sample underwent natural cooling to room temperature (typically taking ~ 1 hour) before being removed via the load lock.

Post growth treatment with CdCl$_2$

The 10 cm^2 samples were quartered into 5 cm^2 pieces and films of CdCl$_2$ were deposited onto the CdTe surfaces of each piece via vacuum evaporation using a custom built evaporator unit. A CdCl$_2$ thickness of 200 nm, determined by a callibrated oscillator crystal, was maintained for all samples within this work. Each piece was then quartered again into 2.5 cm^2 pieces and annealed, one by one, in a tube furnace in air. A range of annealing temperatures (375 - 420°C) and times (5 - 35 min) were used, the specific details of which are described at the relevant points in Chapter 7. Following annealing, each piece was rinsed in warm DI water and dried with nitrogen prior to contacting. Note that no chemical etch, commonly used for such devices, was performed prior to contacting.

Contacting

Back contacts were formed by vacuum deposition of Au (99.999% purity) in a Leybold Univex 300 evaporator system. The contacts, deposited using a mask array, were square and 5 mm × 5 mm in size. It was possible to deposit nine such contacts onto each 2.5 cm^2 piece. A front contact was made by using a scalpel blade to scratch away part of the CdTe film at the edge of each piece. A cotton bud swab of a dilute hydrochloric acid was used to remove the CdS beneath this and reveal the ZnO layer to which a direct contact could be made during electrical characterisation of the device (see section 4.4).

4.3   Characterisation of single films

The characterisation of single films refers almost exclusively to TCO materials within this work and it is principally the electrical and optical properties of these materials that are of interest. The key properties that can be determined directly from electrical methods described below are the sheet resistance, $R_\square$, and the sheet carrier concentration $n_\square$. From

these measurements further electrical characteristics can be calculated, namely the resistivity, ρ, bulk carrier concentration, n_e, and the carrier mobility, μ_e, provided that the thickness, d, of the film is known. Note that the subscripts 'e' denote that the origin of the conductivity is due to electron donors (i.e. 'n-type' conductivity) and this is the case for all TCO materials studied within this work. The key optical properties of single films that are of interest are the direct band gap, E_d, the integrated transmittance, $\tilde{T}$, and the dispersion (i.e. refractive index, n, and extinction coefficient, κ). These can be determined using the optical methods described below. It is also possible to determine values for the electrical properties from these optical methods however these do not necessarily provide absolute values, unlike those provided by the electrical methods.

4.3.1 Electrical methods

Van der Pauw

The van der Pauw technique [6, 7] allows the sheet resistance of a square sample to be measured. Two characteristic resistances, R_A and R_B, are measured using a square contact geometry such as that shown in figure 4.3, where

$$R_A = \frac{R_A^+ + R_A^-}{2} = \frac{V_{43}/I_{12} + V_{34}/I_{21}}{2} \tag{4.1}$$

$$R_B = \frac{R_B^+ + R_B^-}{2} = \frac{V_{23}/I_{14} + V_{32}/I_{41}}{2} \tag{4.2}$$

The subscripts for I denote the contacts into which current is injected into, e.g. for I_{12} the current flows into contact 1 and out of contact 2. Similarly, the subscripts for V denote the contacts across which the corresponding (positive) voltage is measured. Two Kiethley 2400 source meters were used seperatly to apply a current to the sample and measure the corresponding voltage. The subscripts '+' and '-' denote the resistances measured when the current was applied in positive and negative directions respectively. The sheet resistance was calculated by iteratively solving the following relation for $R_\square$:

$$\exp^{\frac{-\pi R_A}{R_\square}} + \exp^{\frac{-\pi R_B}{R_\square}} = 1 \tag{4.3}$$

The error associated with this sheet resistance value was calculated as the standard deviation between a minimum of three repeated measurements. For further reviews on resistance

measurements using the van der Pauw technique the reader is directed to the folllowing references, [8, 9]

All measurements were made using custom built equipment and software. A contact relay was used to automatically swap the orientation of the contacts for each measurement. This eliminated the need to manually disconnect and reconnect the contacts. Also, by ensuring that contacts were not moved throughout the measurement the systematic error associated with changes in contact position were avoided. Note that for the measurement of R_A and R_B to be reliable an Ohmic contact was required otherwise equations 4.1 and 4.2 were not applicable. Prior to measurement, a simple I-V curve was taken for each contact geometry and an appropriate current (typically in the region of between 1 - 100 mA) was applied that corresponded to an ohmic response corresponding to the linear region of this I-V curve. For samples with reasonably low sheet resistance values (i.e. $< 200 \ \Omega/\square$) suitable contacts were made by applying spring loaded gold probes directly to the sample surface. For films with larger $R_\square$ values the quality of the contacts was improved by applying a small amount of silver paste to the sample corners.

To ensure that the equipment measured correctly, a sheet resistance measurement was regularly performed on a calibration sample of TEC15 SnO_2:F coated glass (Pilkington), it having a known sheet resistance, $R_\square = 13.2 \pm 0.1 \ \Omega/\square$.

Hall effect measurements

Hall measurements were made using the same contact geometry as that used in the van der Pauw measurement (i.e corner contacts on a square sample) but the injected current and
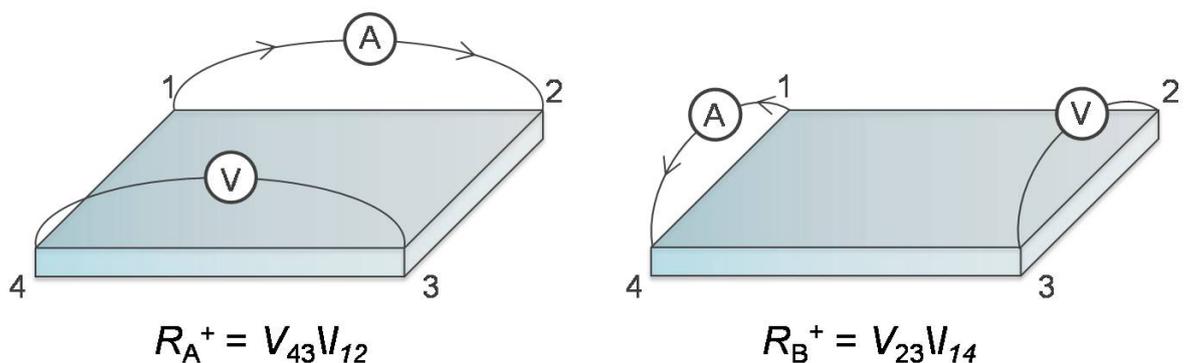

Figure 4.3: Contact configuration for van der Pauw resistivity measurement.

measured voltages were made across the diagonals of the sample as shown in figure 4.4. Additionally, the method requires a uniform magnetic field directed orthogonally to the sample surface. The technique involved the direct measurement of eight separate voltages. The first four are denoted by V_{24p}, V_{42p}, V_{13p} and V_{31p}, where the subscript '24' corresponds to the voltage measured across corners 2 and 4 when a current flows from 1 to 3 and the subscript '42' corresponds to the voltage measured when the current is reversed (i.e flow from 3 to 1). The subscripts '13' and '31' correspond to voltages that are similarly defined. The '+' subscript denotes that these voltages were measured when the magnetic field was in a positive direction. The same four voltages were measured for a reversal of the magnetic field and denoted by the subscript '-'.

Following the measurement of these eight voltages the following characteristic differences were calculated:

$$V_A = V_{24+} - V_{24-} \tag{4.4}$$

$$V_B = V_{42+} - V_{42-} \tag{4.5}$$

$$V_C = V_{13+} - V_{13-} \tag{4.6}$$

$$V_D = V_{31+} - V_{31-} \tag{4.7}$$

and using the sum of these differences it was possible to calculate the sheet carrier density $n_\square$ according to [10]

$$n_\square = \left| \frac{8.1 \times 10^{-8} IB}{e(V_A + V_B + V_C + V_D)} \right| \tag{4.8}$$

where I is the current injected into the sample and B is the magnetic field strength (in Gauss). By combining results from both the van der Pauw and Hall methods the carrier mobility μ_e can be calculated from

$$\mu_e = \frac{1}{q n_\square R_\square} \tag{4.9}$$

The same equipment was used for the Hall measurement as that described above for the van der Pauw measurement. A bench top permanent magnet, with a field strength of 3850 G (0.385 Tesla), was also used. Samples were placed centrally between the two poles of the magnet, the diameter of which were 7 cm. A comparison between voltages measured for different sample sizes of the same material, ranging from 1 cm^2 to 5 cm^2, showed an excellent consistency indicating that the uniformity of the field between the
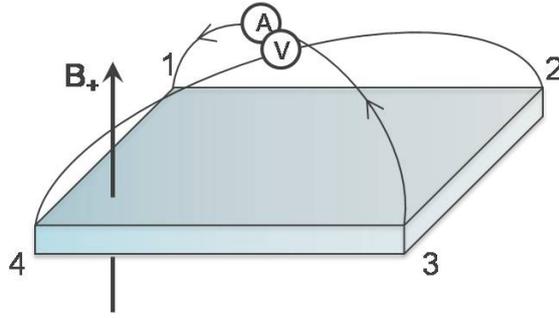
Figure 4.4: Example of single contact permutation for Hall measurement of a single thin-film sample.

poles was very good. Again a calibration sample of TEC15, having a known sheet carrier density of $n_\square = 1.46 \pm 0.02 \times 10^{15}$ cm^{-2}, was measured regularly to ensure that the Hall method was reliably accurate.

4.3.2 Optical methods

Spectrophotometry (SP)

A Shimadzu SolidSpec-3700DUV dual beam spectrophotometer was used to measure the specular transmittance of single films. Features of this equipment include:

- An integrating sphere with three separate detectors to cover the wavelength range 165 - 2600 nm. The limits of the detectors are as follows,

    - Photomultiplier (PMT): 165 - 1000 nm.

    - InGaAs detector: 700 - 1800 nm.

    - PbS detector: 1600 - 3000 nm.

- A computer controlled X-Y stage for measuring multiple points on large samples (maximum sample size = 310 mm^2).

- Automated scanning capability.

- 5° reflectance attachment for measuring reflectance spectra in conjunction with X-Y stage.

Figure 4.5 shows a schematic ray diagram that summarises the configuration for a transmittance measurement. The sample beam and reference beams are split from the same source and the reference beam is used to correct for fluctuations in the signal generated by the light source and the detectors. For all samples, measurements were made in the range 250 - 2000 nm using a slit widths between 2 - 8 nm and resolutions of between 0.5 - 1 nm. Samples were orientated 'face-up' during the measurements, i.e with the sample beam entering through the glass substrate and leaving through the film.

Following a transmittance measurement the data was exported to the program SCOUT3.0 [11]. This program was used to model the dielectric permittivity of the measured material, according to the theory described in Chapter 2, and fit the transmittance data. Figure 4.6 shows a flow chart of the algorithm that was implemented during the fitting. Prior to fitting, rough estimates for the parameters of each of the model components (e.g. Drude, Lorentz, Inter-band), including the film thickness, were input. A downhill simplex method [12] was then used to increment the parameters until a value for the mean squared error (MSE), calculated as the standard deviation between experimental and theoretical spectra, of < 0.0001 was achieved. The key parameters (e.g. d, E_d, ω_p, γ_{low}) were then extracted from the model. Also, the fitted model was used to calculate the dispersion spectra (n and κ) which were then exported to a library of optical data for use in subsequent multi-layer models (Chapter 6). The fitting method described above is in later chapters referred to as the SP method.
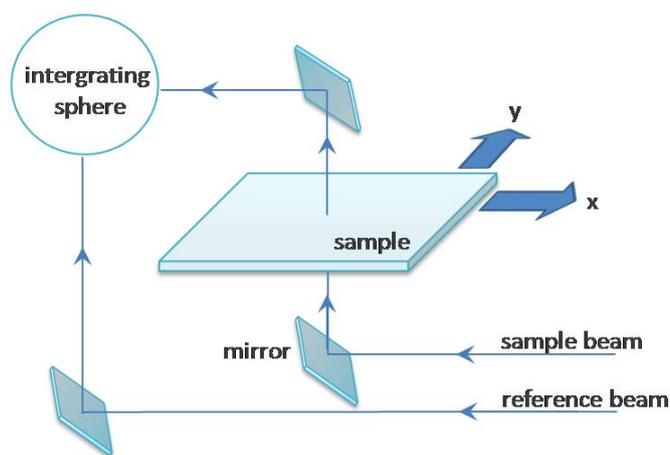

Figure 4.5:   Schematic of beam and sample configuration for spectrophotometry measurement.
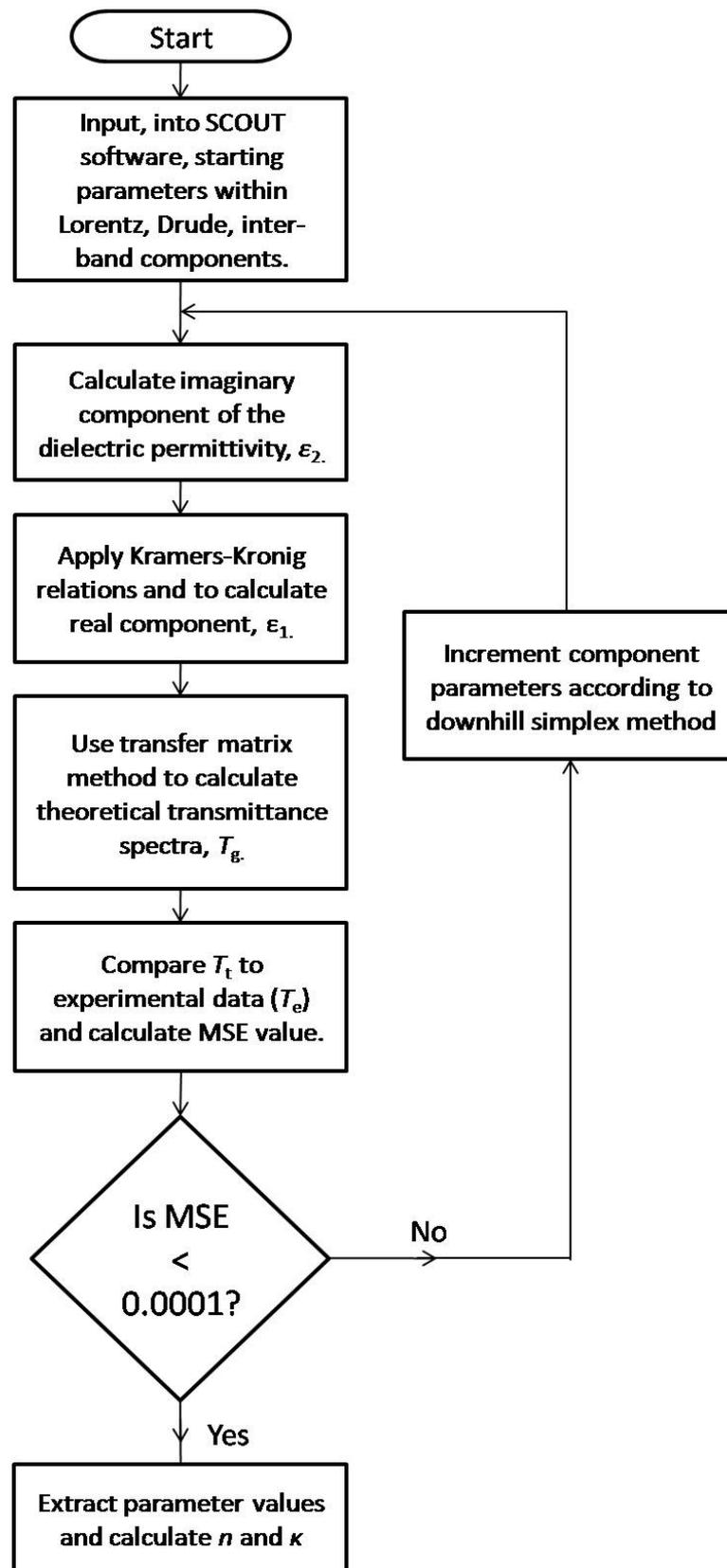
Figure 4.6: Flow chart algorithm describing extraction of dispersion data according to the spectrophotometry (SP) method. See text for further details.

Spectroscopic ellipsometry (SE)

Ellipsometry was also used to determine similar parameters for single films as those described above in the SP method. The key difference in the principle behind each of techniques is that spectrophotometry is simply used to measure the transmitted intensity of light through a sample whereas ellipsometry measures the changes in polarisation states of an incident beam of light following its reflection from a sample's surface. A Woollam M2000UI variable angle spectroscopic ellipsometer and CompleteEASE™ software [13] (located at Cranfield University, UK) was used for the measurement and analysis of single films. Figure 4.7 shows a schematic representation of the equipment. The incident beam, emitted by a white light source was linearly polarized before undergoing a reflection from the sample surface. A rotating compensator, analyser and CCD were then used to measure the plane polarized, r_p, and vertically polarized, r_s, components of the beam's electric field over the range in wavelengths 250 - 1500 nm. The phase difference, Δ, and the amplitude ratio, Ψ, between the two components was then calculated, as a function of wavelength, according to

$$\frac{r_p}{r_s} = \tan(\Psi) \exp^{(i\Delta)} \tag{4.10}$$

Each film was scanned at multiple incident beam angles of 50°, 60° and 70°. To eliminate reflections from the back surface of the glass substrate the surface was lightly brushed with a fine sandpaper and covered with PTFE tape [14]. The set of six optical spectra (i.e. Δ
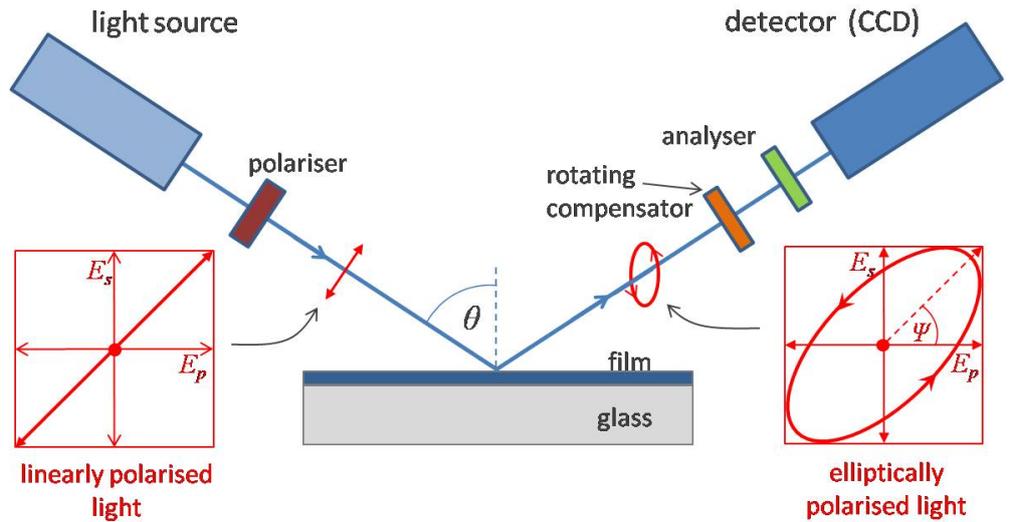

Figure 4.7: Schematic of ellipsometry measurement of a thin-film sample.
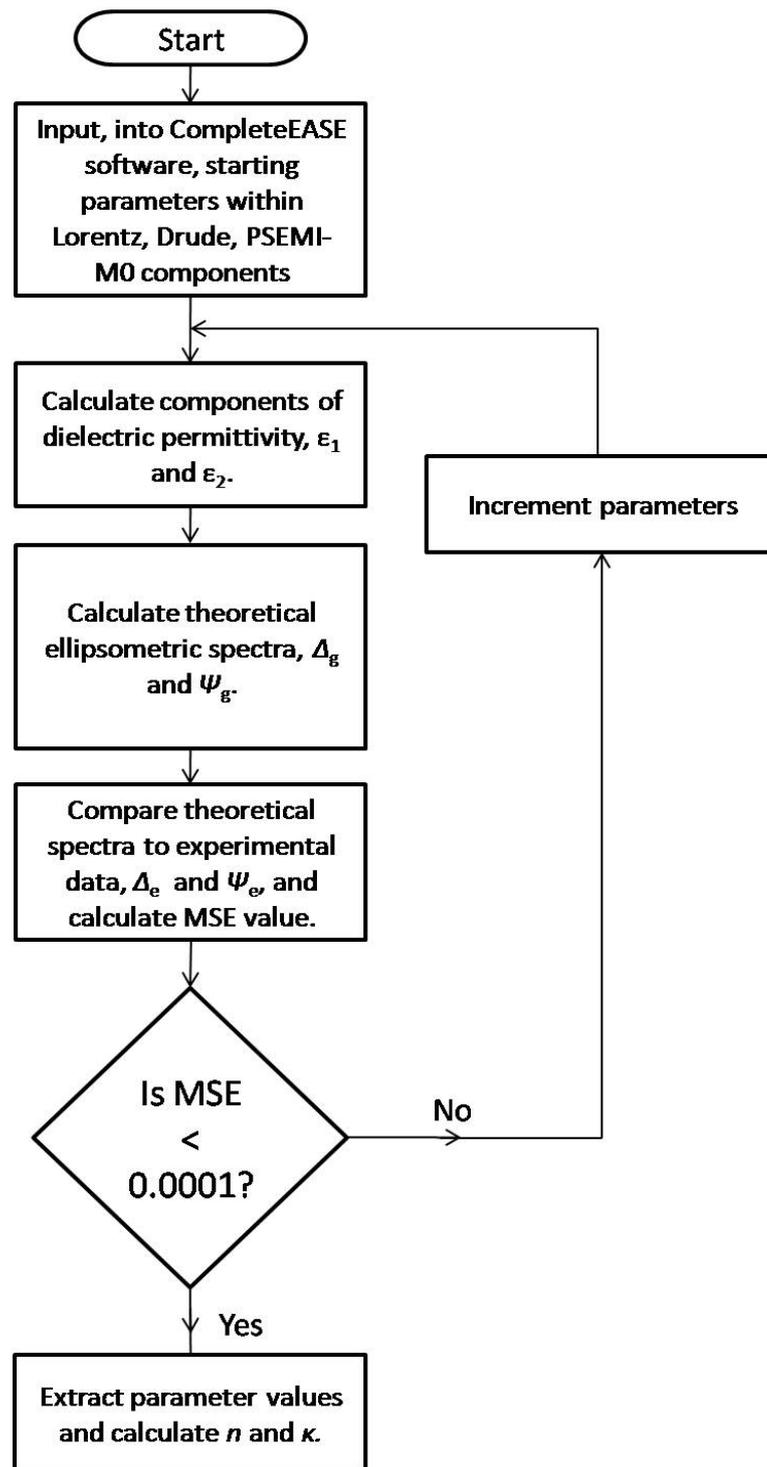
Figure 4.8: Flow chart algorithm describing extraction of dispersion data according to the spectroscopic ellipsometry (SE) method. see text for further details.

and Ψ measured at the three separate angles) were then input into the CompleEASE software and fit simultaneously according the the algorithm represented by the flow chart in figure 4.8. The fit algorithm is very similar to that described for the SP method. However, the inter-band transition component of the model is represented by a stand alone PSEMI-M0 oscillator [15, 16] which was parameterised by values for the direct band gap, E_d, and amplitude, A_{PSEMI}. The parameters of the combined model components were varied until a value for the mean squared error of MSE < 0.0001, or lower, was achieved. In this case the MSE value was calculated as

$$\text{MSE} = \times \sqrt{\frac{1}{3l - m} \sum_{i=1}^{l} [N_{e_i} - N_{g_i}]^2 + [C_{e_i} - C_{g_i}]^2 + [S_{e_i} - S_{g_i}]^2} \qquad (4.11)$$

where l is the number of wavelengths, m is the number of fit parameters within the model, $N = \cos(2\Psi)$, $C = \sin(2\Psi)\cos(\Delta)$ and $S = \sin(\Psi)\sin(\Delta)$. Subscripts e and g are ascribed to experimental and generated parameters respectively. The method for fitting ellipsometry data is referred to in the remainder of this work as the SE method. For a detailed review of spectroscopic elliposometry the reader is referred to [17].

4.3.3 Other methods

Surface profilometry

An AMBIOS XP 200 surface profiler was used to measure the thickness of single films. In the case of soft films, e.g. CdTe, a scalpel was used to scratch away a small region of the sample surface at the point of measurement. The needle of the profiler (figure 4.9) was then scanned accross the step at the edge of this region. For harder films, e.g. oxides, a mask was used during deposition to generate such a step or silver paste was applied to a small area of the substrate before deposition and then removed with acetone post growth, creating a distinct step edge between film and substrate. In the case of CdS films it was necessary to remove the film using a dilute hydrochloric acid solution. For each measurement an estimated error was calculated from the standard deviation of multiple (at least three) repeat readings. In general, the minimum limit to the measurable thickness of the profiler was ~ 20 nm and film thickness could be determined to an accuracy of $\sim 5\%$.
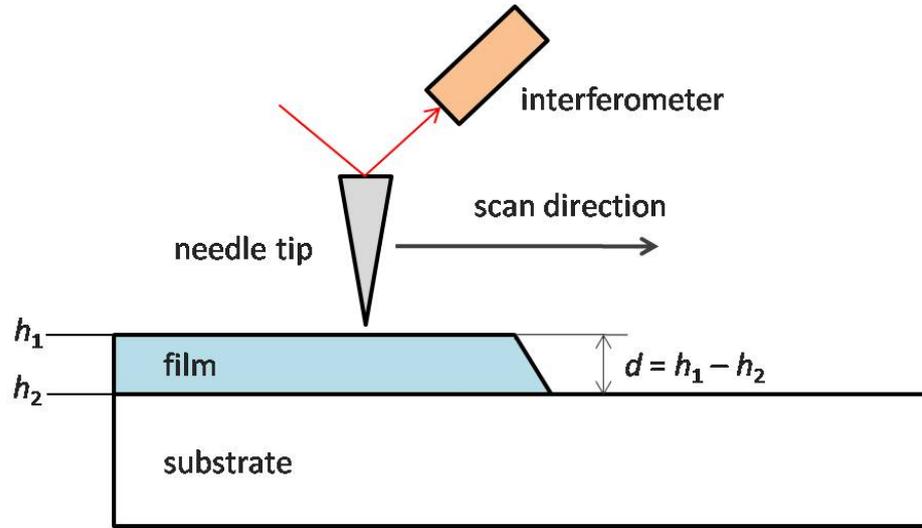
Figure 4.9: Schematic of profilometry measurement.

X-Ray diffraction

X-Ray diffraction (XRD) was used to characterise the crystal structure of single films of CdTe deposited onto OptiWhite substrates. The technique permitted the preferred orientation of the grains within the films and also the lattice parameter, a, to be determined. Samples were measured in the Bragg-Brentano geometry [18, 19] as shown in figure 4.10. Incident X-rays, provided by a monochromatic X-ray tube source, underwent diffraction from the sample and their intensity was measured as a function of angle, θ, using a photomultiplier tube. Peaks in the intensity spectra were observed when the Bragg condition was met according to

$$m\lambda = 2d_{hkl}\sin\theta \qquad (4.12)$$

where m is the order of reflection (assumed to be $m = 1$) and d_{hkl} corresponds to the spacing between the lattice planes defined by the Miller indices h, k and l. For a cubic structure (i.e CdTe) the lattice parameter can be calculated according to the equation

$$d_{hkl} = \sqrt{\frac{a}{h^2 + k^2 + l^2}} \qquad (4.13)$$

Measurements were made with a Siemens D5000 diffractometer (located at Northumbria University, UK) and samples were scanned using a CuK$_{\alpha_{1,2}}$ emmision line (1.5406 $\mathring{A}$) and over the range $20° - 90°$, in 2θ.
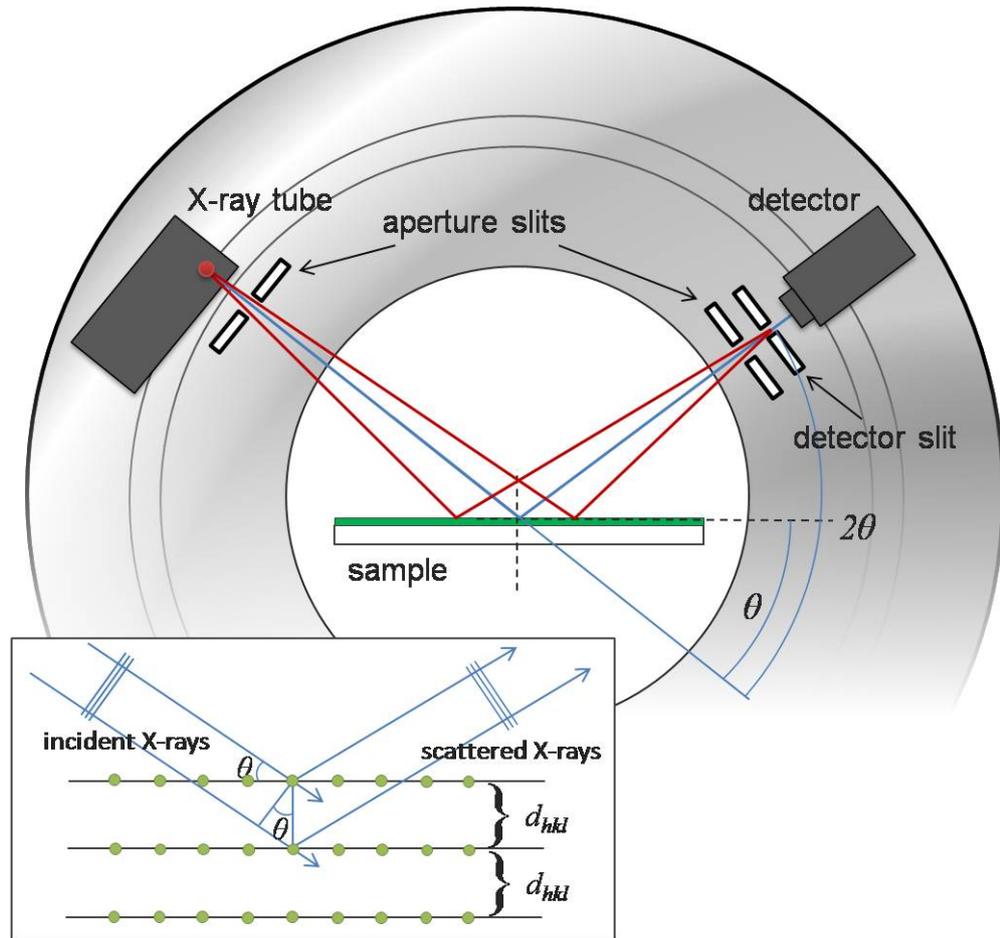
Figure 4.10: The Bragg-Brentano (θ-2θ) geometry for XRD measurement.

4.4 Device characterisation

4.4.1 Current - voltage measurements

Current - voltage (J-V) measurements were made on completed CdTe devices to determine their performance parameters, i.e. η, FF, J_{SC} and V_{OC}. Devices were illuminated under a 100 mW/cm² (AM1.5) source, provided by an Oriel 81160 solar simulator calibrated using a reference Si cell, and the current was measured as a function of applied bias voltage. The voltage was sourced and the current measured using a single Kiethley 2400 source meter. The measurement was automated using a custom built LabView program [20] that interfaced with the Kiethley source meter via a GPIB connection. The resultant J-V curves were used to extract the performance parameters according to the theory described

in Chapter 3. All measurements were made at room temperature (21 ± 2°C) and over a range in bias of -1V to +1V. Care was taken to ensure that the temperature of the sample remained approximately constant throughout.

4.4.2 Current - voltage - temperature measurements

A selection of samples were also contacted and mounted inside a cryostat chamber (CTI cryogen refrigerator, Helix Technology Corporation) to make J-V measurements as a function of temperature (i.e J-V-T). The measurement involved the same experimental setup as that described above. All measurements were made under dark conditions over a range in temperature 120 - 330 K.

4.4.3 External quantum efficiency measurements

The external quantum efficiency (EQE) of a solar cell device is defined as the ratio of incident photons to the number of electrons generated, measured as a function of wavelength. In this work, EQE spectra were measured for CdTe devices using custom built equipment, a full description of which is presented in [21]. Measurements were made over the wavelength range 350 - 900 nm and at room temperature.

4.4.4 Electron microscopy

Electron microscopy was used to probe the resultant micro-structure of completed multi-layer devices. While little quantitative information was determined using the microscopy techniques a great deal of qualitative information concerning grain structure and morphology, film adhesion, recrystallisation and inter-diffusion was observed. Analysis of cross-sectional imaging also permitted the confirmation of layer thicknesses thus providing another method by which the growth rate of the films could be calibrated. Three key microscopy techniques were applied to a selection of multi-layer samples within this work: Scanning electron microscopy (SEM), scanning transmission microscopy (TEM), and electron beam induced current (EBIC).

Scanning electron microscopy

This technique involves the injection of a highly focussed beam of electrons into a sample surface and the collection of subsequent electrons that are re-emitted from the sample. The detection of these electrons as the e-beam is scanned across an area of the sample permits the build up of an image of the sample surface. A schematic for the interaction of the incident e-beam with a sample is shown in figure 4.11a. Depending on where in the generation volume electrons are re-emitted from corresponds to different interaction mechanisms. Each set of electrons (e.g. secondary, backscattered or Auger) can provide information on different material properties. For example, the detection of secondary electrons provides a high resolution image contrast that allows key features of the film, such as voids, grain boundaries etc., to be investigated. Backscattered electrons however provide compositional information and permits the distinction of separate material phases. The detector geometries for imaging of secondary and backscattered electrons is shown in fig 4.11b.

Cross-sectional samples were prepared and secondary electron imaging performed using a FEI Helios Nanolab 600. A focussed beam of Ga^+ was used to mill away material from the sample to form a cross-section. A layer of platinum was deposited onto the sample
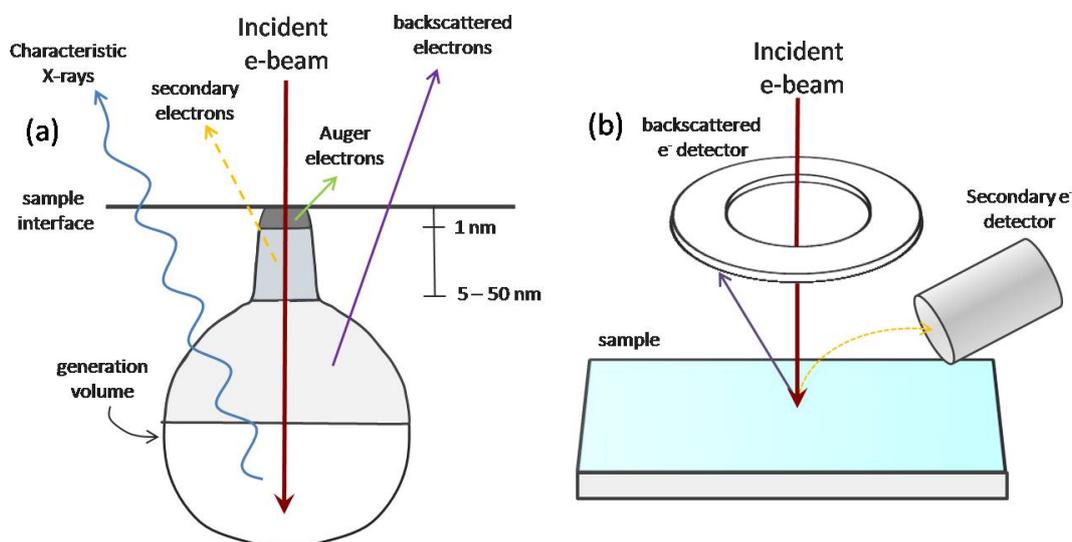

Figure 4.11: Principles of scanning electron microscopy. (a) The characteristic generation volume associated with an incident electron beam. (b) Secondary and backscattered detector configurations.

surface prior to milling to ensure that a uniform polishing of the cross-section was achieved. Backscattered imaging was performed using a Hitachi SU-70 FEG SEM.

Further book length reviews of scanning electron microscopy are provided in references [22, 23].

Scanning transmission electron microscopy

Higher resolution images of device cross-sections were achieved using scanning transmission electron microscopy. The principles of image formation using TEM is distinctly different to that of SEM, and an excellent reviews of this technique is provided by [24]. Thinly polished (< 100 nm) cross-sections were prepared, again using the focussed ion beam, and transferred using an in-situ Omniprobe system to a TEM sample grid. The samples were then transferred to a JEOL 2100 FEG TEM microscope for imaging.

Electron beam induced current (EBIC) measurements

This technique was used to provide qualitative analysis of the electrical response of CdTe device cross-sections and performed simultaneously to SEM imaging using the Hitachi SU-70. A single contact on a completed device, following FIB preparation, was connected via back and front contacts to an amplifier. The signal generated as a function of position from the injected e-beam was then measured and provided information concerning the location of the junction within the cross-section (i.e whether it was at the CdTe/CdS or buried elsewhere within the CdTe layer). The results were indicative of the efficacy of the $CdCl_2$ post treatment process. Extensive reviews on the EBIC technique and its use in the characterisation of CdTe solar cells are provided by [25, 26].

4.5   References

[1] B. Chapman. *Glow Discharge Processes: Sputtering and Plasma Etching*. Wiley, New York (1980).

[2] K. Wasa, S. Hayakawa. *Handbook of Sputter Deposition Technology: Principles, Technology, and Applications*. William Andrew Publishing (1992).

[3] K. Wasa, M. Kitabatake, H. Adachi. *Thin Film Materials Technology: Sputtering of Compound Materials*. Springer (2004).

[4] R. Kukla. *Surface and Coatings Technology* **93**, 1 (1997).

[5] M. Lieberman, A. Lichtenberg. *Principles of Plasma Discharges and Materials Processing*. Wiley Online Library (2005).

[6] L. van der Pauw. *Philips Res. Rep* **13**, 1 (1958).

[7] L. van der Pauw. *Philips Technical Review* **20**, 220 (1958).

[8] G. Rietveld, C. Koijmans, L. Henderson, M. Hall, S. Harmon, P. Warnecke, B. Schumacher. *IEEE T Instrum Meas* **52**, 449 (2003).

[9] D. K. Schroder. *Semiconductor Material and Device Characterization*. John Wiley & Sons, New York (1998).

[10] E. H. Putley. *The Hall Effect and Related Phenomena*. Butterworths, London (1960).

[11] W. Theiss. Scout 3.0. Aachen, Germany (2002).

[12] J. Nelder, R. Mead. *The computer journal* **7**, 308 (1965).

[13] J. A. Woollam Co., Inc. *Easy-to-Use Acquisition/Analysis Software for Spectroscopic Ellipsometry (EASE^{TM})* (2009). Version 4.05.

[14] R. Synowicki. *Wollam Co. News* **11**, 10 (2010).

[15] B. Johs, C. Herzinger, J. Dinan, A. Cornfeld, J. Benson. *Thin Solid Films* **313**, 137 (1998).

[16] T. Tiwald. *Wollam Co. News* **7**, 6 (2006).

[17] W. McGahan, B. Johs, J. Woollam. *Thin Solid Films* **234**, 443 (1993).

[18] R. L. Snyder. *X-ray Characterization of Materials*. Wiley-VCH, Weinheim (1999).

[19] C. Hammond. *The Basics of Crystallography and Diffraction*. Oxford Univ Press (2009).

[20] M. D. Archbold. *Polycrystalline CdS Thin Films and Their Role in CdTe/CdS Photovoltaic Devices*. Ph.D. thesis, University of Durham (2007).

[21] J. D. Major. *CdTe Solar Cells: Growth Phenomena and Device Performance*. Ph.D. thesis, Durham University (2008).

[22] L. Reimer, P. W. Hawkes. *Scanning Electron Microscopy: Physics of Image Formation and Microanalysis*. Springer, Berlin (1998).

[23] J. Goldstein. *Scanning Electron Microscopy and X-Ray Microanalysis*. Springer (2003).

[24] S. J. Pennycook, P. D. Nellist. *Scanning Transmission Electron Microscopy: Imaging and Analysis*. Springer (2011).

[25] S. Galloway. *Sol. Energy Mater. Sol. Cells* **57**, 61 (1999).

[26] K. Durose, S. Asher, W. Jaegermann, D. Levi, B. McCandless, W. Metzger, H. Moutinho, P. Paulson, C. Perkins, J. Sites. *Progress in Photovoltaics Research and Applications* **12**, 177 (2004).

Chapter 5

Deposition and Characterisation of TCOs

5.1 Introduction

This chapter presents an experimental study of several TCO materials, namely In_2O_3, SnO_2 and ZnO. The key aim of the work was to achieve and quantify the best optical and electrical performance for each material with respect to the design criteria set for CdTe based PV and to generate films that can potentially be incorporated into completed device structures (Chapter 7). The use of RF magnetron sputtering presented an excellent opportunity to develop and optimize each material by providing a high degree of control over deposition parameters and maintaining an excellent run to run consistency in film properties once the optimum parameters had been found.

A further aim of the work was to develop an optical technique, based upon simple transmittance measurements and the theory laid out in Chapter 2, for the rapid and accurate characterisation of TCO films. A non-contact method of materials characterisation is highly desirable for routine use given the high sample throughput that is achievable with magnetron sputtering. Reliance on contact based electrical measurements (e.g. van der Pauw and Hall) reduces the speed with which new materials can be developed. Furthermore, the optical technique permits the extraction of fundamental parameters such as $n(\lambda)$ and $\kappa(\lambda)$ which can be incorporated into models for the behaviour of multi-layer structures (Chapter 6). Throughout this chapter, such an optical technique is repeatedly applied and

assessed with respect to each of the TCO materials studied.

Section 5.2 presents a short study of Sn doped In_2O_3 films and provides an initial benchmark with which subsequent films can be compared. Section 5.3 explores, in detail, alternative doping routes to F doped SnO_2, which include the use of reactive sputtering in the presence of trifluoromethane (CHF_3) and tetrafluoromethane (CF_4), sputtering from a mixed composition SnO_2:SnF_2 target and co-sputtering from independent SnO_2 and SnF_2 targets. Section 5.4 investigates the properties of intrinsic, highly resistive ZnO as well as Al and F doped ZnO films. The chapter is concluded with a comparison of the performance of each of the materials described and also includes two commercial TCO materials, namely Pilkington TEC8 and TEC15 which have both been used extensively by several groups as substrates for CdTe solar cells [1–5].

5.1.1   Experimental and analytical methodology

The general methodology of RF magnetron sputtering has been outlined in Chapter 3 and in this chapter any specific description of growth conditions are deferred to the appropriate subsections. All materials were deposited onto 3 mm thick, low Fe OptiWhite soda-lime glass substrates (Pilkington NSG group). Fabrication of wedge shaped or combinatorial samples involved the use of an aluminium substrate holder which ensured that uniform heating of the substrate during deposition. A target-substrate separation of 10 cm was maintained throughout all experiments.

Electrical measurements were made using the custom built equipment described in Chapter 3 and were performed on square samples of sizes 5×5 cm^2 or 2×2 cm^2. They were contacted at the four corners by gold pins and in general, samples were conductive enough for the contact resistance to be ignored. However, in cases of highly resistive films silver paste was used to ensure that a stable contact was achieved. The experimental errors associated with each resistivity or Hall measurement were determined from the standard deviation in multiple (at least 3) measurements. In general, the reproducibility of electrical results using the electrical set-up was very good with repeat readings typically being withn 5% of each other.

Optical transmittance spectra in the range 250 to 2000 nm were recorded using a Shimadzu Solid Spec 3600 spectrophotometer (see Chapter 3). These spectra were then

fitted according to a physical model for the dielectric permittivity which was constructed from the theory described in chapter 2 and consisted of Lorentz, Drude (and extended Drude), and inter-band transition components. Fitting was achieved using commercial software (SCOUT [6] - see section 4.3.2) which implemented a downhill simplex iteration to model parameters (i.e ω_p, τ, Δ_{BM} etc). After each iteration the parameters were used to calculate the components ε_1 and ε_2 over full range of the spectrum. These components were then passed to a transfer matrix algorithm [7] to calculate a model transmittance spectrum that was then compared directly with the measured data. The iteration continued until the mean squared error, MSE, between the experimental and model spectra was minimised. The final MSE value indicated the quality of the resultant fit. MSE values below 1×10^{-4} indicated that the resultant model parameters yielded a good fit to the transmittance spectra. The procedure is illustrated by a flow chart in figure 4.6.

5.2 In$_2$O$_3$:Sn

As discussed in Chapter 2, Sn doped In$_2$O$_3$ (ITO) is currently the most ubiquitous TCO, but the increasing scarcity of In means that it is unlikely to remain so. A key focus of this chapter was therefore to investigate alternative materials based upon Sn and Zn, the relative costs of which are significantly lower than In. Nonetheless, the fabrication of In$_2$O$_3$:Sn films served as an exercise in which the experimental capabilities of the deposition equipment, in terms of reproducing results reported by others (see table 2.2), could be assessed. Furthermore, the films served as a reference with which subsequent SnO$_2$ and ZnO based TCOs could be compared.

Films were deposited from a standard In$_2$O$_3$:SnO$_2$ (10% wt.) target (99.99% purity, Pi-Kem Ltd.) the use of which is widely reported. Initial attempts to sputter from the target were complicated by an unusual type of circular arcing confined to the surface of the target. A high density plasma discharge was observed precessing around the circumference of the target and within minutes of applying an RF power a circular trench, approximately 2mm in depth and 1 mm in diameter had been carved from the target surface. The phenomenon occurred repeatedly at powers greater than 50 W. To overcome the arcing problem, the target was conditioned at a very low RF power (20 W) for a period of 5 hours

following which the arcing did not reoccur. Similar occurrences have since been observed following the installation of other target materials; most notably CdTe, in which the arcing is particularly violent and damaging to the target. In all cases, the arcing can be overcome by low power conditioning of the target surface.

The optimum deposition parameters for films of In_2O_3:Sn (ITO) were established as being an RF power of 60 W, a substrate temperature of 400°C and an Ar pressure of 1 mTorr. The separation between target and substrate was approximately 10 cm. Under these conditions the electrical resistivity of the films reached a reproducible minimum of 1.2×10^{-4} Ω.cm. These parameters were arrived at via an empirical approach and no systematic investigation into the effect of the sputtering parameters on film properties was made. This was partly due to the fact that all films were generally of a very good quality (i.e. good uniformity and adhesion, with typical resistivites below 1×10^{-3}) regardless of the deposition parameters, provided that a substrate temperature above 300°C was employed. In general, however films deposited at Ar pressures below 2 mTorr were electrically superior and had considerably higher carrier densities of the order $n_e > \times 10^{20}$ cm^{-3}. This is explained by the fact that at lower pressures, Ar ions undergo less scattering as they
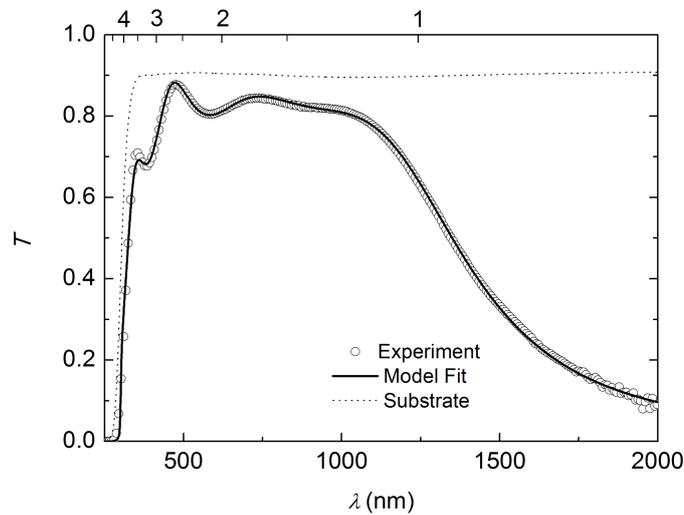

Figure 5.1: Direct transmittance of Sn doped In_2O_3 (ITO) film deposited from an In_2O_3:Sn (10% wt.) target. The film was deposited onto an OptiWhite soda-lime glass substrate under the following conditions: RF Power = 60 W, pressure = 1 mTorr, T_{sub} = 400°C, deposition time = 120 mins.

are accelerated toward the target. The impact energy of ion bombardment is therefore much higher and both In_2O_3 and SnO_2 present in the target are more likely to completely dissociate into their constituent elements as they are ejected from the target. More free Sn atoms are available to take part in doping processes at the surface of the substrate as a result.

Figure 5.1 shows transmittance data of the baseline In_2O_3:Sn film deposited under optimum conditions. A model for the dielectric permittivity of TCO materials, consisting of Lorentz, Drude and inter-band transition components (see Chapter 2) was used to fit the transmittance data. The fit was achieved using the SCOUT software [6] according to a downhill simplex method. The only fixed input to the model was the direct band gap which was set at the value of $E_d = 3.75$ eV generally found in the literature [8]. All other initial parameter values were input using physically reasonable estimates. The fitting process, which typically lasted no longer than 20 seconds, was allowed to continue until an MSE value of $< 1 \times 10^{-4}$ was achieved. The parameter values yielded from the fit are shown in table 5.1. Note that while the parameters from both Drude and extended Drude components are shown together within the table, they were not used within the model simultaneously.

Table 5.2 compares the experimentally determined electrical properties of the ITO baseline sample, determined by van der Pauw and Hall measurements, with those values calculated from the parameters extracted from the models. Both types of Drude components generated well matched values for the carrier density but only the extended Drude component accurately predicted the value of the electron mobility. The assumption that the scattering is frequency dependant (extended Drude) is therefore better than that of a constant scattering parameter (Drude) which leads to much higher predicted values of electron mobility. Subsequent values for $R_\square$ and ρ are therefore incorrect according to the Drude component but match extremely well if the extended Drude component is used.

The effective electron mass was calculated in both instances using the plasma frequencies determined from the model and the experimentally determined carrier density (in accordance with equation 2.28). A value of $m_e = 0.4\ m_0$ was determined in both cases which is slightly higher than the value of $0.3\ m_e$ quoted in the literature for intrinsic In_2O_3 [9]. This is expected as it has been shown by Ruske *et al.* [10] that in the case of heavily

doped TCO films the effective mass is generally increased. It was also possible to estimate the size of the effective electron mass from the Burstein-Moss shift, Δ_{BM}, extracted from the inter-band transition component of the model, according to equation 2.54. A value of 0.39 m_0 is in good agreement with the other values.

Table 5.1: Parameters extracted from fitting the model to the optical transmittance spectrum of the baseline ITO sample. The symbols used are explained in Chapter 2.

Model Component	Parameter	Value
Lorentz Oscillator	A_0 (eV)	196.9
	$\hbar\omega_0$ (eV)	19.67
	τ (eV)	0
Drude	$\hbar\omega_p$ (eV)	1.73
	γ ($\times 10^{13}$ s^{-1})	1.68
Extended Drude	$\hbar\omega_p$ (eV)	1.72
	γ_{low} ($\times 10^{13}$ s^{-1})	8.68
	γ_{high} ($\times 10^{13}$ s^{-1})	1.40
	ω_{cross} (eV)	0.21
	ω_δ (s^{-1})	0.13
Direct Transitions	E_d (eV)	3.75
	E_d' (eV)	4.15
	Δ_{BM} (meV)	394
	D (eV$^{3/2}$)	29.93
	γ_w (eV)	0.54
Indirect Transitions	E_i (eV)	2.58
	E_p (meV)	7.9
	D'	0.21
	d (nm)	249.8
	MSE ($\times 10^{-5}$)	7.5
	$\tilde{T}$	0.83
	$\tilde{\alpha}$ (cm^{-1})	3419

Table 5.2: A comparison between electrical properties of the ITO baseline sample determined by experiment and by fitting to optical data.

	$R_\square$ ($\Omega/\square$)	$n_\square$ ($\times 10^{16}$ cm^{-2})	n_e ($\times 10^{20}$ cm^{-3})	μ_e (cm^{2}V^{-1}s^{-1})	ρ ($\times 10^{-4}$ Ω.cm)	m_e (m_0)
Experiment[a]	5.1	2.1	8.9	58.4	1.2[b]	–
Drude	1.1	2.2	8.6	261.7	0.3	0.40[c]
Extended Drude	5.2	2.1	8.5	56.9	1.3	0.40[c]
B-M shift	–	–	–	–	–	0.39[d]

[a] van der Pauw and Hall measurements

[b] Calculated using $d = 249.8$ nm value extracted from model

[c] Calculated according to equation 2.28

[d] Calculated according to equation 2.54 and using values determined by extended Drude component
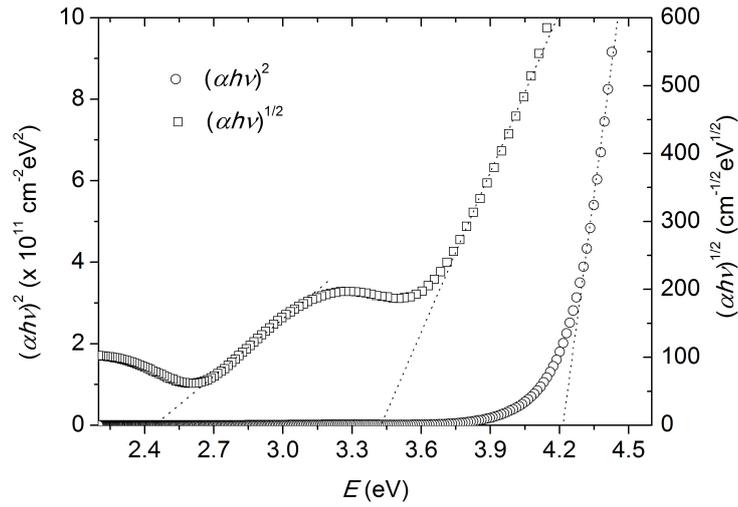

Figure 5.2: Determination of effective direct and indirect band gaps of ITO baseline sample via extrapolation of linear regions of $(\alpha h\nu)^2$ and $(\alpha h\nu)^{1/2}$ plots. α was calculated according to $\alpha = -\frac{1}{d} \ln \frac{T}{T_{sub}}$. Values of $E_d = 4.2 \pm 0.2$ eV and $E_i = 3.4 \pm 0.2$ eV were determined from the plots.

Figure 5.2 shows $(\alpha h\nu)^2$ and $(\alpha h\nu)^{1/2}$ vs E plots for the ITO baseline sample. A value of the effective direct band gap of the film was extrapolated as $E_d' = 4.2 \pm 0.2$ eV which compares favourably to the value of 4.15 eV (i.e. $E_d + \Delta_{BM}$) given by the model. This again suggests that equation 2.54 is correct and that the only reason for a shift in the

effective band gap is due to a BM effect. There was, however, a considerable discrepancy between the extrapolated and model determined values of the indirect band gap, the values being 3.4 ± 0.2 eV and 2.58 eV respectively. Without a third means of investigating the indirect band gap it is hard to say which method gives a reliable value, or indeed if either is correct. All that can be certain is that there is a relatively small component to the absorption coefficient that is generated by indirect transitions at energies above ~ 2.5 eV.

The full optical behaviour (complex dielectric function, refractive index and absorption), shown as a function of wavelength, determined by the model's fit to the transmittance spectrum, is presented in figure 5.3. The shapes of the plots include all the features expected of a heavily doped semiconductor, as described in Chapter 2. Knowledge of the film's wavelength dependent properties permit the simulation of transmittance spectra at any chosen film thickness, which is of great use in the theoretical design of optical stack structures.

To further test the model's ability to accurately extract electrical and optical behaviour it was applied to 72 separate transmittance spectra taken over a single wedge shaped film of In_2O_3:Sn deposited under the optimum conditions but with the substrate rotation turned off. The resultant thickness profile, determined by repeated model fits, is shown in figure 5.4. The profile varies smoothly as a function of position, with no anomalous spikes in thickness indicating that the fitting procedure is self consistent. The carrier concentration across the sample remained roughly constant at $1.01 \pm 0.04 \times 10^{21}$ cm^{-3}, as did the effective band gap at 4.27 ± 0.03 eV. However, a small variation in mobility was observed as a function of thickness, as shown in figure 5.5. Values of mobility increased from around 33 cm^{2}V^{-1}s^{-1} at thicknesses close to 100 nm, to around 40 cm^{2}V^{-1}s^{-1}, as the film thickness increased beyond 400 nm.
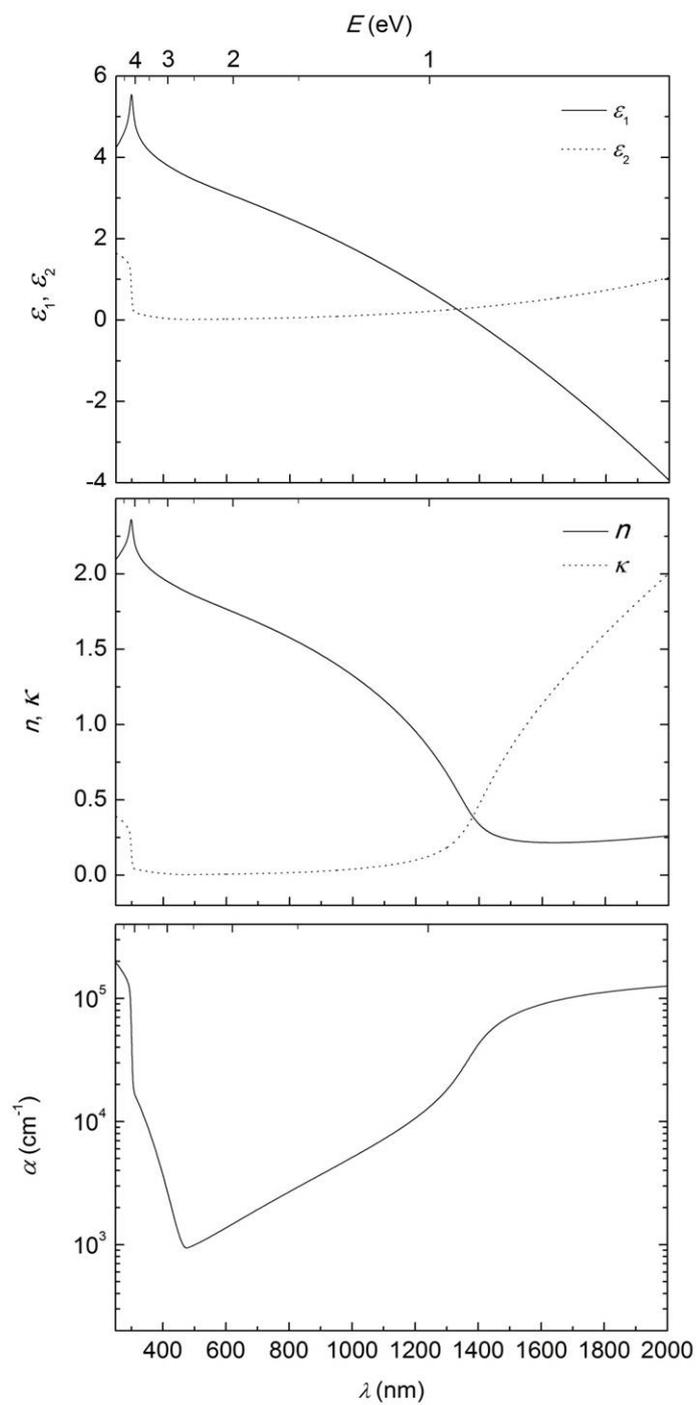
Figure 5.3: Optical behaviour of the baseline ITO sample as determined from fitting the model to the experimental transmittance spectrum: a) Components of complex dielectric permittivity. b) Corresponding n and κ spectra. c) Absorption coefficient.
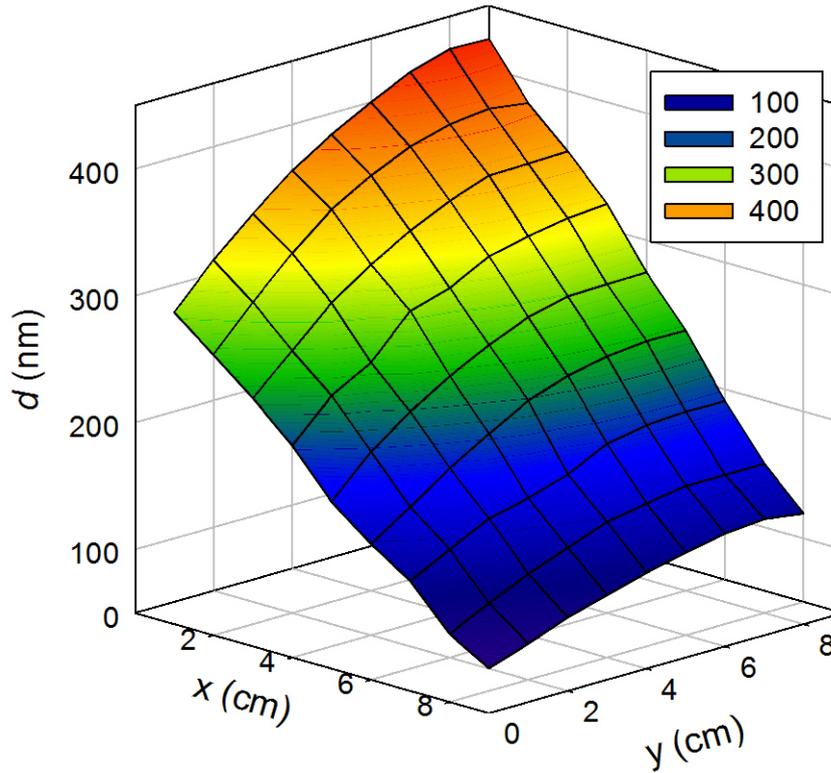
Figure 5.4: The thickness profile of a wedge shaped ITO sample (deposited under the same conditions as the ITO standard). The profile was determined by fitting 72 transmittance spectra taken from points separated by intervals of 1 cm over a 10 cm^2 sample.

The reason for this variation is likely to be a consequence of the polycrystalline structure of the film. A component of the scattering of free carriers can be attributed to grain boundaries, the density of which decreases as grain size increases with film thickness. Therefore, the electron scattering is reduced and in turn electron mobility increased in thicker regions of the film. This indicates some potential for reducing the resistivity further through tailoring the grain size. This might be achieved through further variation of the sputtering parameters.

To summarise, Sn doped In$_2$O$_3$ was a reasonably easy material to sputter and very little effort was required to discover a set of deposition parameters that yielded high quality films. In fact the lowest achievable resistivity of 1.2×10^{-4} Ω.cm equals the best values quoted in the extensive literature regarding ITO (see table 2.2). The sputtered ITO films provide an excellent bench-mark to which other TCO materials can be compared. They are also
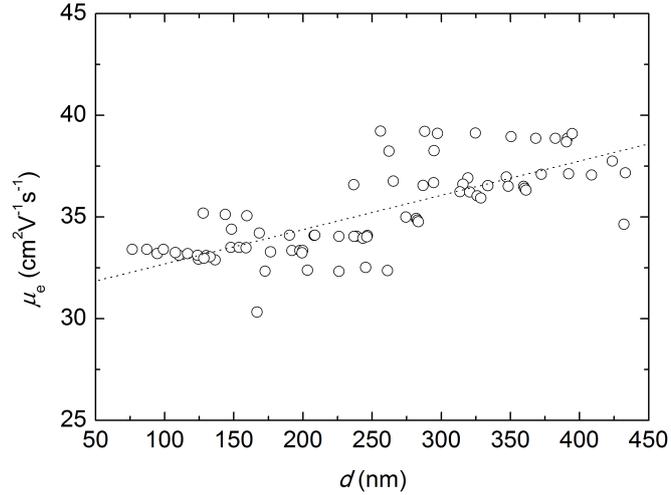
Figure 5.5: The mobility values over the wedge shaped sample of ITO were seen to increase with thickness. It may be speculated that the increase can be attributed to changes in micro-structure (e.g. grain size and texture) as the film thickens.

highly reproducible, with properties varying very little on a run to run basis, and the films are potentially compatible with a CdTe device structure (Chapter 7).

5.3 SnO$_2$

The most common deposition technique for SnO$_2$ based TCOs, in particular fluorine doped SnO$_2$, is chemical vapour deposition (CVD) [11–13]. Relatively few attempts have been made to create such materials using magnetron sputtering and the technique is generally unable to reproduce the quality of CVD deposited films which typically have sheet resistances reported to be below 20 $\Omega/\square$ and transmittances above 0.8. In this section, a range of alternative doping routes for SnO$_2$:F are explored and the limitations of RF magnetron sputtering for this material system firmly established. The range of different doping routes used were:

- Reactive sputtering from a SnO$_2$ target in Ar with partial pressures of CHF$_3$ or CF$_4$ gases.

- Sputtering from a mixed composition, SnO$_2$:SnF$_2$ (10% wt.), target.

- Co-sputtering from separate SnO_2 and SnF_2 targets.

However, prior to these investigations a brief assessment of the effect of deposition parameters on the properties of undoped SnO_2 films is presented.

5.3.1   Undoped SnO_2

All SnO_2 films were deposited from a SnO_2 ceramic target (99.99 % purity, Pi-Kem Ltd.) under a constant total chamber pressure of 5 mTorr. Initially, the effect of the substrate temperature on resultant film properties was investigated over the range 17 - 450°C, while maintaining a constant RF power of 100 W. Figure 5.6 shows the effect on growth rate, resis-
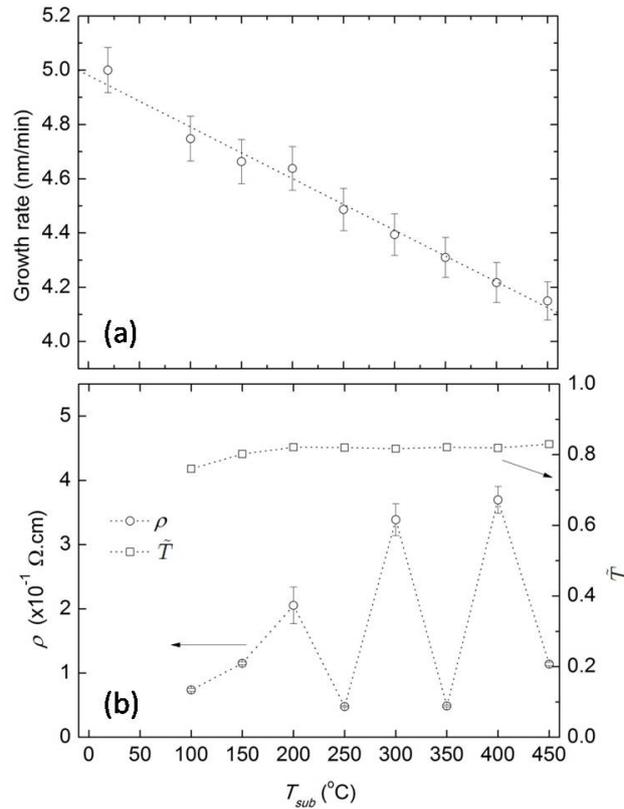

Figure 5.6: The effect of T_{sub} on (a) growth rate, (b) resistivity and transmittance for films of undoped SnO_2 films deposited from a ceramic SnO_2 target at a fixed RF power of 100 W and a 5 mTorr pressure of Ar (The resistivity values obtained are subject to run-to-run variability that gives scatter greater than indicated by the measurement error bars).
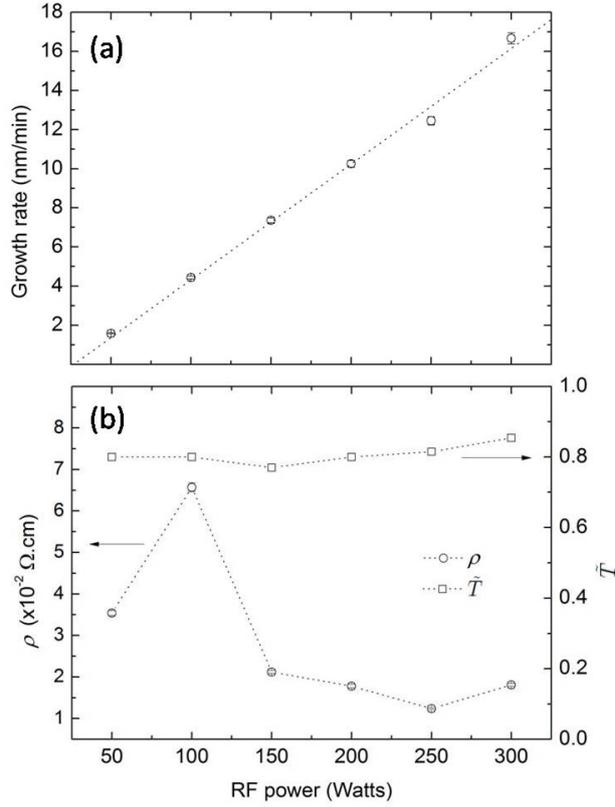
Figure 5.7: The effect of RF power on (a) growth rate, (b) resistivity and transmittance for films of undoped SnO_2 films deposited from a ceramic SnO_2 target at a fixed substrate temperature of 250°C.

tivity and transmittance. A modest reduction in growth rate from 5 nm/min to 4.2 nm/min was observed, decreasing linearly over the temperature range. The integrated transmittance, $\tilde{T}$, remained independent of substrate temperature and in general maintained a value above 0.8. On the other hand, the film resistivity fluctuated between 0.5×10^{-1} Ω.cm and 4×10^{-1} Ω.cm, with the lowest resistivity being achieved at a temperature of 250°C. Substrate temperatures of $> 250°$ were chosen for all subsequent experiments involving SnO_2. and it is thought, based on work by Stjerna et $al.$ [14], that this is sufficient to promote the effects of extrinsic doping following the incorporation of a fluorine containing gas.

Figure 5.7 shows the variation in growth rate, resistivity and transmittance with RF power, over the range 50 - 300 W, for films deposited at a constant substrate temperature of 250°C. A linear increase in the growth rate, from 2 to 16 nm/min, is observed with

increasing power. Again, $\tilde{T}$ is maintained at values of ~ 0.8 over the range. In general the resistivity was seen to decrease with increasing sputter power with a minimum value of 2.1×10^{-2} Ω.cm achieved at an RF power of 250 W. This power was therefore chosen for all subsequent doping experiments as it would be expected to promote further reductions in resistivity whilst allowing practical growth rates (i.e. films of thickness > 100 nm could be grown within ~ 1 hour). Note that while there were no attempts to introduce extrinsic dopants to the SnO_2 films represented in figures 5.6 and 5.7, they were far from being intrinsic (i.e. non-conducting) and possessed measurable sheet resistances, probably due to native oxygen vacancies, V_o.

An attempt to manipulate the level of oxygen vacancies was made by introducing partial pressures of oxygen $(0 - 8\%)$ into the chamber during deposition. Figure 5.8 shows that the film resistivity increased with O_2 partial pressure as expected, there being an order of magnitude increase in ρ upon increasing it from 0 to 8%, at an RF power of 250 W and a substrate temperature of 250°C. Further analysis was performed on a film sputtered in a 1% partial pressure of oxygen through application of the optical model. The fit to the transmittance spectrum, shown in figure 5.9, used the parameters listed in table 5.3
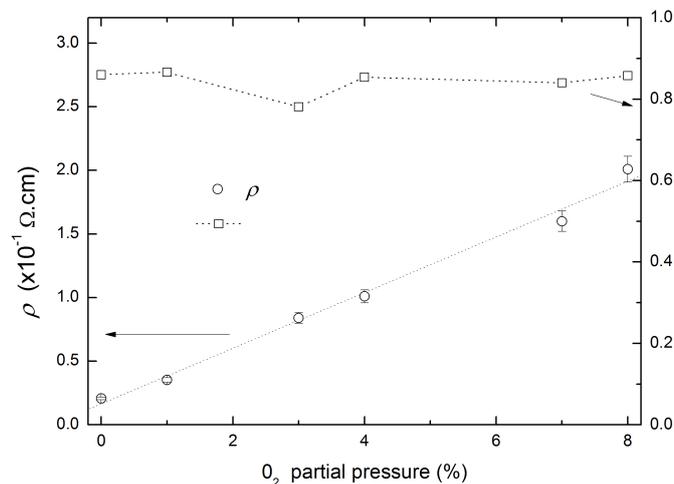
Figure 5.8: Reactive sputtering of SnO_2 from a SnO_2 ceramic target with Ar and oxygen. The variation in resistivity as a function of oxygen partial pressure is shown. Films were sputtered at a constant RF power and substrate temperature of 250 W and 250°C respectively.
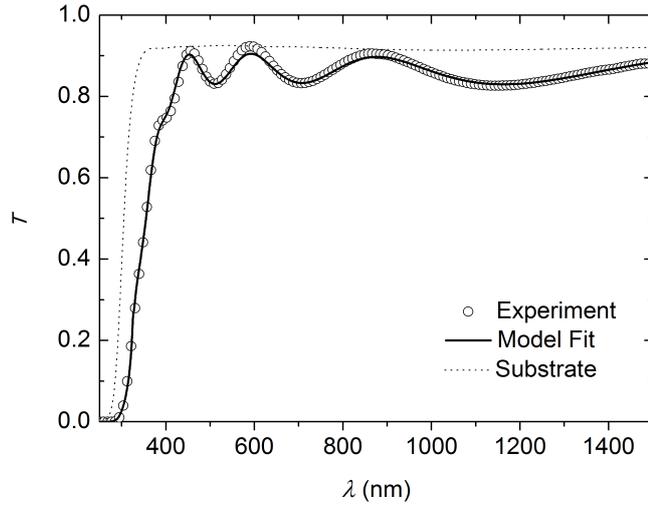
Figure 5.9: Direct transmittance of SnO_2 deposited under the following conditions: RF power = 250 W, pressure = 5 mTorr (+ 1% O_2 pp.), T_{sub} = 250°C. The thick line shows the model fit and the dotted line the substrate transmittance.
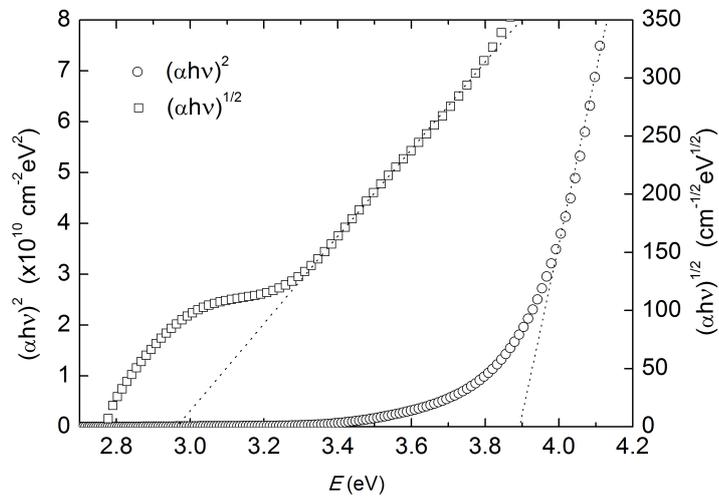
Figure 5.10: Determination of direct and indirect band gaps for a SnO_2 film sputtered in a 1% partial pressure of O_2. Values of $E_d = 3.9 \pm 0.2$ eV and $E_i = 2.96 \pm 0.08$ eV were estimated from the intercepts.

Table 5.3: Parameter values extracted from model fit to transmittance spectrum of an undoped SnO_2 film sputtered in a 1% partial pressure of O_2 (Figure 5.9). The symbols used are defined in Chapter 2

Model Component	Parameter	Value
Lorentz Oscillator	A_0 (eV)	90.52
	$\hbar\omega_0$ (eV)	52.51
	$\frac{1}{\tau}$ (eV)	0.42
Direct Transitions	E_d (eV)	3.94
	Δ_{BM} (meV)	0^a
	D (eV$^{3/2}$)	17.3
	γ_w (eV)	0.35
Indirect Transitions	E_i (eV)	2.85
	E_p (meV)	5.75
	D'	0.35
	d (nm)	502.4
	MSE ($\times 10^{-5}$)	7.9
	$\tilde{T}$	0.87
	$\tilde{\alpha}$ (cm^{-1})	820

[a] Fixed value and not used as a fitting parameter.

and yielded an MSE value of 7.9×10^{-5}.

Throughout the fitting procedure a value for the Burstein-Moss shift of $\Delta_{BM} = 0$ was maintained as it was assumed that the shift was negligible, the carrier density most likely being below the critical density, n_c required for a degenerate population of carriers. Instead, E_d (usually a fixed parameter) was allowed to vary in order to find the material's effective band gap. A value of $E_d = 3.94$ eV was determined using the model and corroborated through extraction from an $(\alpha h\nu)^2$ plot (figure 5.10).

This value is significantly higher (+0.2 eV) than the expected value of around 3.7 eV given in the literature for undoped SnO_2. The assumption that the BM shift is negligible is justified since to induce a shift, a carrier concentration of $n_e \sim 10^{20}$ cm^{-3} is required.

This would correspond to a resistivity of the order 10^{-3} Ω.cm (assuming a mobility of ~ 30 cm^{2}V^{-1}s^{-1}) which is an order of magnitude lower than the value actually measured. The shift in the effective band gap must therefore be explained by another mechanism, e.g. through quantum confinement effects caused by a small, < 10 nm, grain size [15–20].

Note that due to the low level of doping in the sample, no Drude component was required for the fitting of the transmittance spectra. The expected carrier density of $< 10^{19}$ cm^{-3}, determined from fitting, would correspond with a plasma frequency greater than $\hbar\omega_p = 0.3$ eV (i.e. 4 μm) which is far beyond the range of measurement for transmittance spectrum, making a Drude component redundant for fitting in the range studied.

5.3.2   F doped SnO$_2$

Reactive sputtering with Ar and CHF$_3$ or CF$_4$

i) CHF$_3$:   A series of films was grown in an Ar/CHF$_3$ ambient at a total pressure of 5 mTorr and with the partial pressure of CHF$_3$ being adjusted in the range 0 - 15%. Figure 5.11 shows the variation of the film properties obtained. Generally the resistivities fell in the range 1 - 4 $\times 10^{-2}$ Ω.cm (there being some anomalous points with high resistivity that were attributed to run to run variation rather than a systematic effect). The lowest achievable resistivity was found at a CHF$_3$ partial pressure of 8% and was 1×10^{-2} Ω.cm. Over the range investigated the integrated optical transmittance remained approximately constant at 0.85. Table 5.4 shows the parameters used in a model of the optical transmittance of the film sputtered in 8% CHF$_3$. Note that in this case, E_d was set at the literature value of 3.7 eV and Δ_{BM} was used as a fitting parameter. The value for the resultant BM shift, $\Delta_{BM} = 0.19$ eV, is bigger than expected when considering the film's resistivity. As for the undoped SnO$_2$ (5.3.1) the extended shift is likely due to a small grain structure, but the effect is less pronounced than for films sputtered in oxygen.

ii) CF$_4$:   A second sequence of gas doping trials was conducted under identical conditions but using CF$_4$, with partial pressures being in the range 0 - 15 %. For these samples the resistivity was high compared to the previous set of samples: For 1% CF$_4$ the resistivity was 11.5 Ω.cm for a 450 nm thick film ($R_\square = 250$ kΩ/$\square$). Higher partial pressures generated films with resistances that were immeasurably high using the van der Pauw method (i.e.
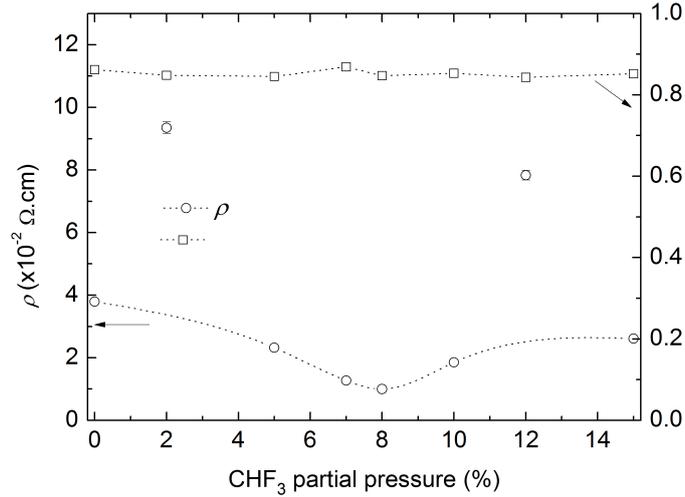
Figure 5.11: Reactive sputtering of SnO_2:F in CHF_3. The variation of ρ and $\tilde{T}$ as a function of CHF_3 partial pressure is shown. A constant RF power and T_{sub} of 250 W and 300°C respectively was maintained throughout. The minimum resistivity was achieved at a CHF_3 partial pressure of 8%.

$R_\square > 10$ M$\Omega/\square$). Again, all films in the series had a transmittance of ~ 0.85.

Whereas the use of CHF_3 served to reduce the resistivity of undoped SnO_2 from 2.1×10^{-2} Ω.cm to 1×10^{-2} Ω.cm, the use of CF_4 caused a significant increase in resistivity to $\rho > 10$ Ω.cm. It may be concluded that CHF_3 imparts doping to SnO_2 but the effect cannot be extended to give higher doping simply by the use of a more fluorine rich species. It may therefore be speculated that either H· or CH· radicals contribute to the doping mechanism, possibly by influencing the population of V_o (or V_F). On the other hand CF_4 may act to introduce a compensating centre.

Doping with SnF_2

SnF_2 is a white solid with a melting point of 215°C [21]. While recognising that it may be considerably less stable than SnO_2 as a sputtering target, the use of SnF_2 has nevertheless been investigated here for use in doping by sputtering from both a mixed target and by co-sputtering.

Table 5.4: Parameter values extracted from model used to fit the optical transmittance spectrum of the F doped SnO_2 film sputtered in an 8% partial pressure of CHF_3

Model Component	Parameter	Value
Lorentz Oscillator	A_0 (eV)	124.21
	$\hbar\omega_0$ (eV)	70.57
	$\frac{1}{\tau}$ (eV)	0.33
Direct Transitions	E_d (eV)	3.7^a
	Δ_{BM} (meV)	190
	D (eV$^{3/2}$)	6.63
	γ_w (eV)	0.42
Indirect Transitions	E_i (eV)	2.90
	E_p (meV)	4.90
	D'	0.47
	d (nm)	487.1
	MSE ($\times 10^{-5}$)	8.3
	$\tilde{T}$	0.85
	$\tilde{\alpha}$ (cm^{-1})	1265

[a] Set at value and not used as a fit parameter.

i) Sputtering from a mixed SnO_2/SnF_2 (10% wt.) target: Film growth using the mixed SnO_2/SnF_2 target was attempted using the following deposition parameters: An RF power of 250 W, substrate temperature of 250°C, and an Ar pressure of 5 mTorr. However, the use of this RF power caused severe differential sputtering of the mixed target. SnF_2-rich regions of the target, $\sim$ 1 mm in diameter, were rapidly denuded of material over very few runs leading to the formation of voids in the target. Hence, the target became unusable for doping experiments under these sputtering conditions and further investigations were abandoned. In principle it may be possible to find conditions having more equal sputtering rates (at low RF power) but this was not attempted in this work.

ii) Co-sputtering of SnO$_2$/SnF$_2$: Since it was demonstrated that SnO$_2$ and SnF$_2$ have disparate sputtering rates, co-sputtering was investigated as an alternative doping route that involved the use of two separate SnO$_2$ and SnF$_2$ targets, to which the power could be varied independently. In order to make a rapid assessment of the composition ratios likely to effect optimised doping, a combinatorial approach was adopted in which a compositional gradient - over the width of a 10 cm^2 substrate - was generated by sputtering simultaneously from each of the targets without substrate rotation. In preliminary experiments, each of the targets was used separately to generate a sample with a wedge shaped thickness distribution. The profile of these wedges were measured, via fitting to optical transmittance spectra, as a function of position (x) through a centered cross section for both SnO$_2$ deposited at 300°C and SnF$_2$ deposited at room temperature with RF powers of 100 W and 50 W respectively. The SnF$_2$ target was stable at a power of 50 W. A co-sputtered sample was fabricated at a substrate temperature of 300°C and at the same values of RF power. The thickness profile through a centered cross-section was again determined optically. The resultant film profiles are shown in figure 5.12. Note that the resultant profile of a co-sputtered film is not given exactly by the superposition of thickness profiles from the seperate targets. This is because of the interference effects that both plasmas,
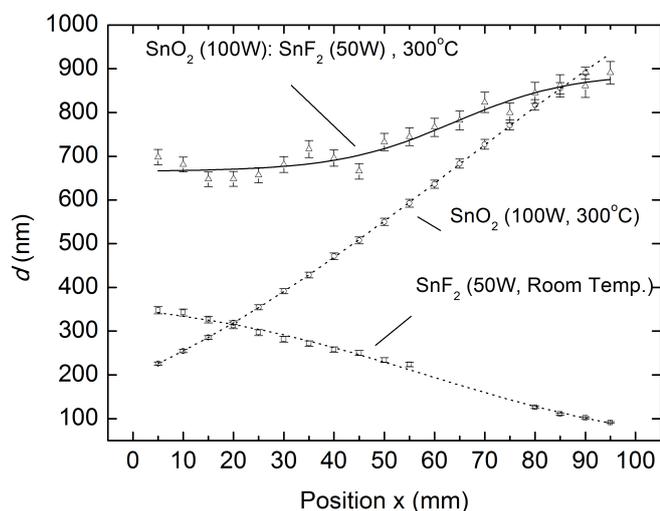

Figure 5.12: Thickness profile through films of separately sputtered SnO$_2$ and SnF$_2$ and resultant profile for a co-sputtered SnO$_2$:SnF$_2$ film. In all cases, films were deposited with the substrate rotation switched off.
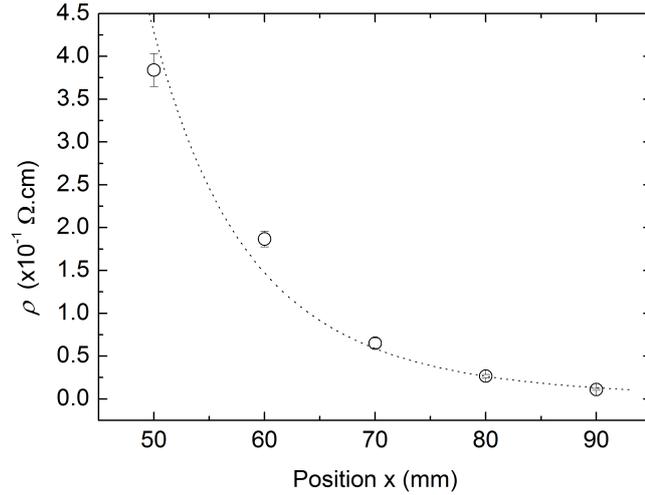
Figure 5.13:   Variation in resistivity as a function of position in a co-sputtered SnO_2:SnF_2 sample. Resistivity values at positions below 50 mm were too high for measurement.

located over the target surfaces, have on each other when running simultaneously.

Figure 5.13 shows the corresponding variation in resistivity across the co-sputtered sample as a function of position. Van der Pauw measurements were made on 1 cm^2 pieces cut from the middle segment of the sample, the resistivity values are therefore averaged over these areas. At positions below 50 mm, i.e the parts of the sample closest to the SnF_2 target, the resistivities were very high and hence figure 5.13 only shows data for positions above this. The composition of the film at these points was likely to have contained phases of both SnO_2 and SnF_2. However, at positions beyond 50 mm a rapid decrease in resistivity was observed indicating a compositional change in the film to SnO_2:F rather than a mixture of phases. The most conductive part of the film ($\rho \sim 1.2 \times 10^{-2}$ Ω.cm) was located at a position furthest away from the SnF_2 target at $x = 90$ mm. It is therefore likely that further exploration of this low-doped region, achievable by increasing the relative difference between the powers applied to each target, will yield films with lower resistivities than the best value obtained here.

Table 5.5 shows a summary of results for SnO_2 and the properties for the best SnO_2 films from each doping study. It was not possible using RF magnetron sputtering to match the opto-electrical properties of films deposited via CVD whose resistivities tend to be

Table 5.5: A summary of sputtering parameters for films that exhibited the lowest achievable resistivity for each doping route.

Target	Reactive gas	pp. (%)	Power (W)	T_{sub} (°C)	Pressure (mTorr)	d (nm)	$R_\square$ (Ω/□)	ρ (Ω.cm)	$\tilde{T}$	$\tilde{\alpha}$ (cm^{-1})
SnO_2	–	–	250	250	5	380	550	2.0×10^{-2}	0.81	1996
SnO_2	CHF_3	8	250	300	5	430	232	1.0×10^{-2}	0.85	1432
SnO_2	CF_4	1	50	350	1	250	460 k	11.5	0.85	2464
SnO_2:SnF_2[a]	–	–	100:50	300	5	900	154	1.2×10^{-2}	0.74	13000

[a] Co-sputtered from separate targets.

at least two order of magnitude lower. However, some potential for further reduction in resistivity for sputtered films has been identified either by incorporating hydrogen into the deposition or investigating the co-sputtering route further by reducing the fractional composition of SnF_2.

5.4   ZnO

There is increasing interest in doped ZnO films, particularly for application in thin-film solar cells. The use of ZnO is desirable for two key reasons: Firstly, the relative cost of Zn compared with both In and Sn is significantly lower, providing excellent opportunity for large scale cost reduction. Secondly, unlike SnO_2 based TCOs, which favour deposition via CVD and spray pyrolysis techniques, magnetron sputtering seems particularly well suited for the deposition of ZnO. This is advantageous in the case of thin-film PV where sputtering is considered more compatible with the need in some cases for lower substrate temperature and a high degree of control over deposition parameters. In the case of CdTe based devices, the use of ZnO:Al has already been demonstrated as an effective front contact TCO material [22].

In this section, the use of radio frequency magnetron in the deposition of high quality Al and F doped ZnO TCOs is investigated according to two distinct growth strategies:

- **ZnO:Al:** Deposition from a mixed composition target (section 5.4.2).

- **ZnO:F:** Reactive sputtering of a ceramic ZnO target in an $Ar/H_2/CHF_3$ ambient (5.4.3).

Prior to these investigations however, a study is made of the deposition and resultant properties of undoped ZnO films from a single ZnO target.

5.4.1   Undoped ZnO films

Initially, the influence of RF power on the growth and properties of ZnO films was investigated. Films were deposited from a ZnO (99.999%, Pi-Kem Ltd.) target at room temperature and a pressure of 5 mTorr over a range of powers from 50 W to 175 W. RF powers above 175 W were not applied to the target following previous trials where, at these powers, ZnO targets suffered cracking and deformation which rendered them unusable without potential damage to the magnetron guns. Figure 5.14 shows the effect of power on the growth rate, E_d and $\tilde{T}$. Resistivity could not be investigated as a function of power because all the films deposited in this study possessed sheet resistances greater than 1 M$\Omega/\square$ (i.e. beyond the measurement capability of the van der Pauw system). Growth rate was seen to increase linearly with increasing RF power as expected, from ~ 0.8 nm/min at 50 W up to 4 nm/min at 175 W. Note that at all RF powers, growth rates were approximately half those observed when sputtering from a SnO_2 target. Over the range, values of E_d and $\tilde{T}$ remained constant at 3.2 ± 0.02 eV (consistent with published values for undoped films [23]) and 0.85 respectively. This indicates an excellent run to run consistency in film properties, despite changes in RF power, which was helpful in the determination of any key trends in opto-electric parameters in later reactive sputtering experiments.

Figure 5.15 shows the refractive index the undoped ZnO (deposited at 150 W) determined using the optical method described earlier in section 4.3.2 and outlined in figure 4.6. This is compared to data extracted using the Swanepoel envelope method [24, 25] which permitted the extraction of n at wavelengths corresponding to maxima and minima in the fringe profile of the transmittance spectrum in the region of high transmittance only (i.e. at wavelengths above the band gap). The data points in figure 5.15 therefore represent a collective analysis of all films shown in figure 5.14. The data points were fitted using a
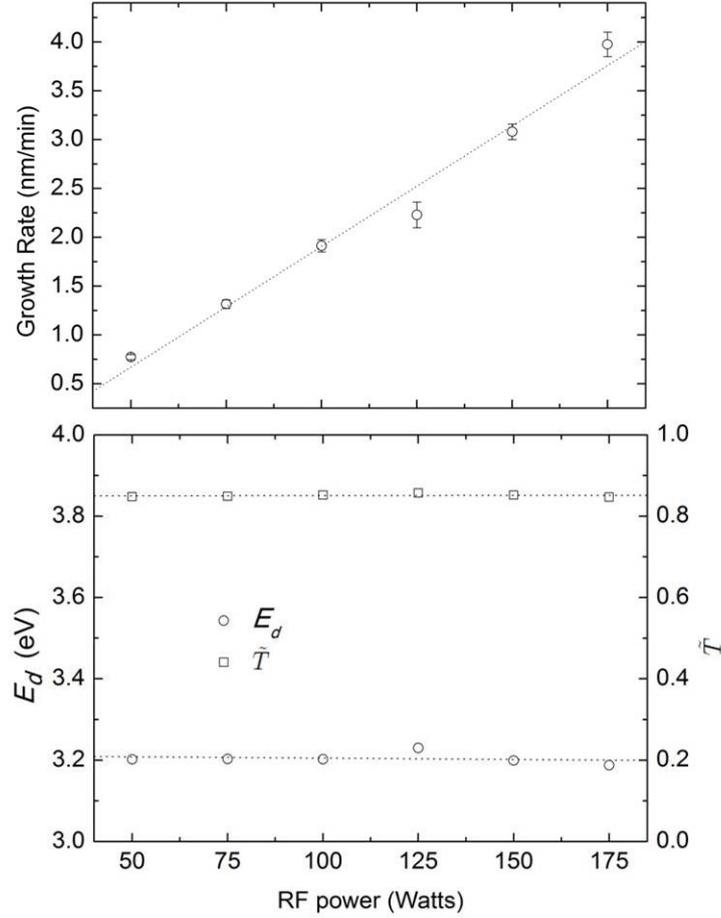
Figure 5.14: The effect of RF power on (a) growth rate, (b) direct band gap and transmittance for films of undoped ZnO films deposited from a ceramic ZnO target at a fixed substrate temperature of 17°C. For all films, the resistivity was too high for measurement (i.e $R_\square$ >1 MΩ). An average band gap for all films was determined as 3.2 ± 0.02 eV.

Sellmeir function of the form

$$n(\lambda) = \frac{a_1^2 \lambda^2}{\lambda^2 - b_1^2} + \frac{a_2^2 \lambda^2}{\lambda^2 - b_2^2} \qquad (5.1)$$

where a_1, a_2, b_1 and b_2 are constants. The two curves are not in complete agreement, the Swanepoel analysis yielding slightly higher values, but a difference of no more than 0.1 (i.e $\sim 5\%$) is observed over the measurement range. Indeed, the shapes of the curves are very similar with an increase in n observed in both cases at wavelengths close to the band edge and a levelling out of the curves at wavelengths beyond 1000 nm. This flat tail in

122
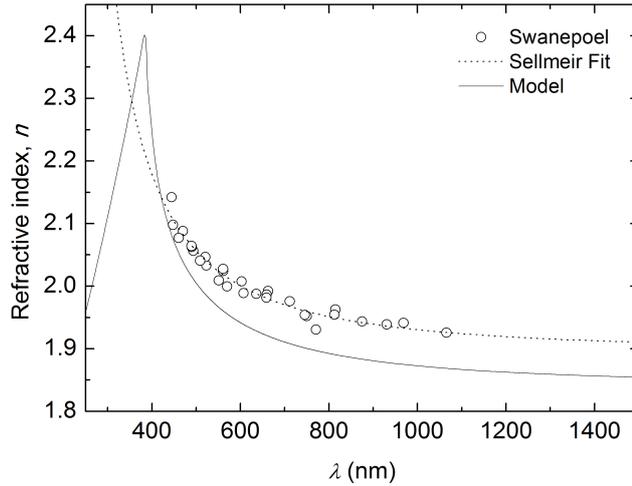
Figure 5.15: Refractive index of undoped ZnO films sputtered from a ZnO target under 5 mTorr Ar and at room temperature. Data points have been extracted from transmittance curves of multiple films using the Swanepoel envelope method. The functional form of $n(\lambda)$ is determined using a Sellmeir fit ($\cdots\cdots$). The shape of the dispersion is also calculated by fitting a single transmittance curve according to the SP method (——).

n indicates that the doping level within the films is low ($< n_c$) and is consistent with the fact that the films are highly resistive.

Of the two methods, the SP method is considered to be the more reliable in extracting the dispersion as it makes use of every data point within a transmittance spectrum during its fitting procedure. The Swanepoel method only makes use of data points located at the maxima and minima for fringes located in the region of the transmittance spectra located at wavelengths above the band edge and relies upon a "zero-absorption" approximation which is not completely accurate. A large number of samples, deposited under identical conditions but of different thicknesses, are required to generate a reliable Sellmeir fit whereas the SP method can extract continuous relations for n and κ from a single transmittance curve. Furthermore, the SP method is regarded as being of particular use in extracting n at wavelengths below the band edge. This is not possible using the Swanepoel method.

5.4.2 Al doped ZnO

Films of ZnO:Al (AZO) were deposited from a mixed composition, ZnO:Al$_2$O$_3$ (2% wt.) target. Again, as for the deposition of In$_2$O$_3$:Sn films, the optimum sputtering parameters were found by an empirical approach. It was found that any combination of RF power and chamber pressure, in the ranges 50-180 W and 150-300°C, generally yielded films with resistivities below 1×10^{-3} Ω.cm provided that substrate temperatures above 150°C were used. The most significant deposition parameter was again found to be the pressure, with lower pressures ($<$ 2 mTorr) giving rise to superior electrical properties. The best films were generated at the lowest achievable pressure of 0.5 mTorr, below which the plasma could not be sustained with enough stability to ensure continuous deposition from the target.

Figure 5.16 shows the transmittance of a film deposited under 150 W, 0.5 mTorr Ar and at a substrate temperature of 150°C. A deposition time of 120 mins was used to establish a film with an approximate thickness of 500 nm. The model fits using either a Drude
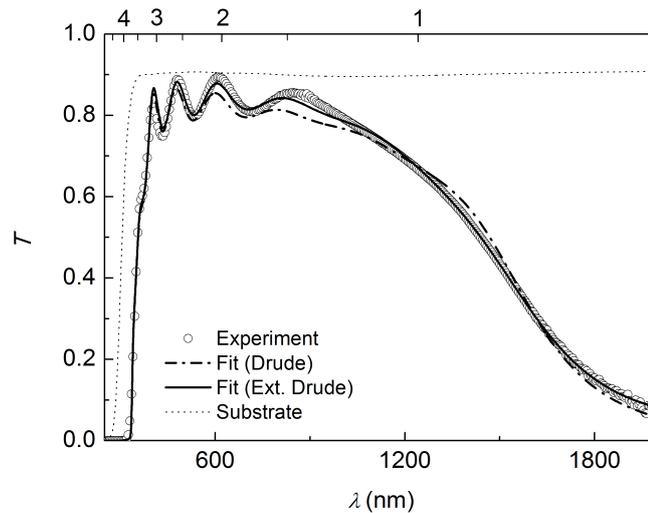

Figure 5.16: Direct transmittance of an Al doped ZnO (AZO) film deposited from ZnO:Al$_2$O$_3$ (2% wt.) target. The film was deposited onto an OptiWhite soda-lime glass substrate under the following conditions: RF Power = 150 W, pressure = 0.5 mTorr, T_{sub} = 150°C, deposition time = 120 mins.

Table 5.6: Parameter values extracted from model fit to AZO standard transmittance spectra (Figure 5.16). The symbols used are defined in Chapter 2.

Model Component	Parameter	Value
Lorentz Oscillator	A_0 (eV)	108.6
	$\hbar\omega_0$ (eV)	46.4
	τ (eV)	0
Drude	$\hbar\omega_p$ (eV)	1.33
	γ ($\times 10^{13}$ s^{-1})	1.85
Extended Drude	$\hbar\omega_p$ (eV)	1.22
	γ_{low} (s^{-1})	16.31×10^{13}
	γ_{high} (s^{-1})	0.30×10^{13}
	ω_{cross} (eV)	0.55
	ω_δ (s^{-1})	0.20
Direct Transitions	E_d (eV)	3.20[a]
	Δ_{BM} (meV)	519
	D (eV$^{3/2}$)	16.3
	γ_w (eV)	0.52
Indirect Transitions	E_i (eV)	3.02
	E_p (meV)	2.6
	$D^{'}$	0.31
	d (nm)	516.7
	MSE $\times 10^{-5}$	5.1
	$\tilde{T}$	0.84
	$\tilde{\alpha}$ (cm^{-1})	1371

[a] Fixed value and not used as a fitting parameter.

Table 5.7: A comparison between electrical properties of the AZO standard determined by experiment and model fit.

	$R_\square$ ($\Omega/\square$)	$n_\square$ ($\times 10^{16}$ cm^{-2})	n_e ($\times 10^{20}$ cm^{-3})	μ_e (cm^{2}V^{-1}s^{-1})	ρ ($\times 10^{-4}$ Ω.cm)	m_e (m_0)
Experiment[a]	9.1	2.2	4.3	30.8	4.7[b]	–
Drude	1.0	2.2	5.1	237.5	0.5	0.35[c]
Extended Drude	10.5	2.0	3.8	30.8	5.4	0.35[c]
B-M shift	–	–	–	–	–	0.17[d]

[a] van der Pauw and Hall measurement

[b] Calculated using $d = 249.8$ nm value extracted from model

[c] Calculated according to equation 2.28

[d] Calculated according to equation 2.54 and using values determined by extended drude component

or extended Drude component, in conjunction with Lorentz, direct inter-band and indirect inter-band components, are also shown in the figure. The corresponding model parameter values for the fits are shown in table 5.6. The fit that uses the extended Drude component clearly achieves a better fit, particularly at wavelengths above the plasma edge.

Table 5.7 compares the experimentally determined electrical properties of the AZO film with those calculated from the parameters extracted from the Drude and extended Drude model components. Neither model component was able to accurately predict the experimentally determined value for the carrier concentration, however the value of 3.8×10^{20} cm^{-3} given by the extended Drude component (according to equation 2.28) is significantly closer to the experimental value of 4.3×10^{20} cm^{-3}. In the case of the carrier mobility, the Drude component, based upon a constant electron scattering factor, again fails to predict the mobility determined by the Hall measurement and actually gives a value that is almost an order of magnitude higher. This renders subsequent estimates for ρ and $R_\square$ wholly inaccurate. The extended Drude model however, matches the experimental mobility value exactly and thus values of ρ and $R_\square$ are calculated that are very close (to within $\sim 10\%$) of the experimental values.

In the cases of both Drude and extended Drude model components, the effective electron mass was calculated (according to equation 2.28) as 0.35 m_0. This is slightly higher than
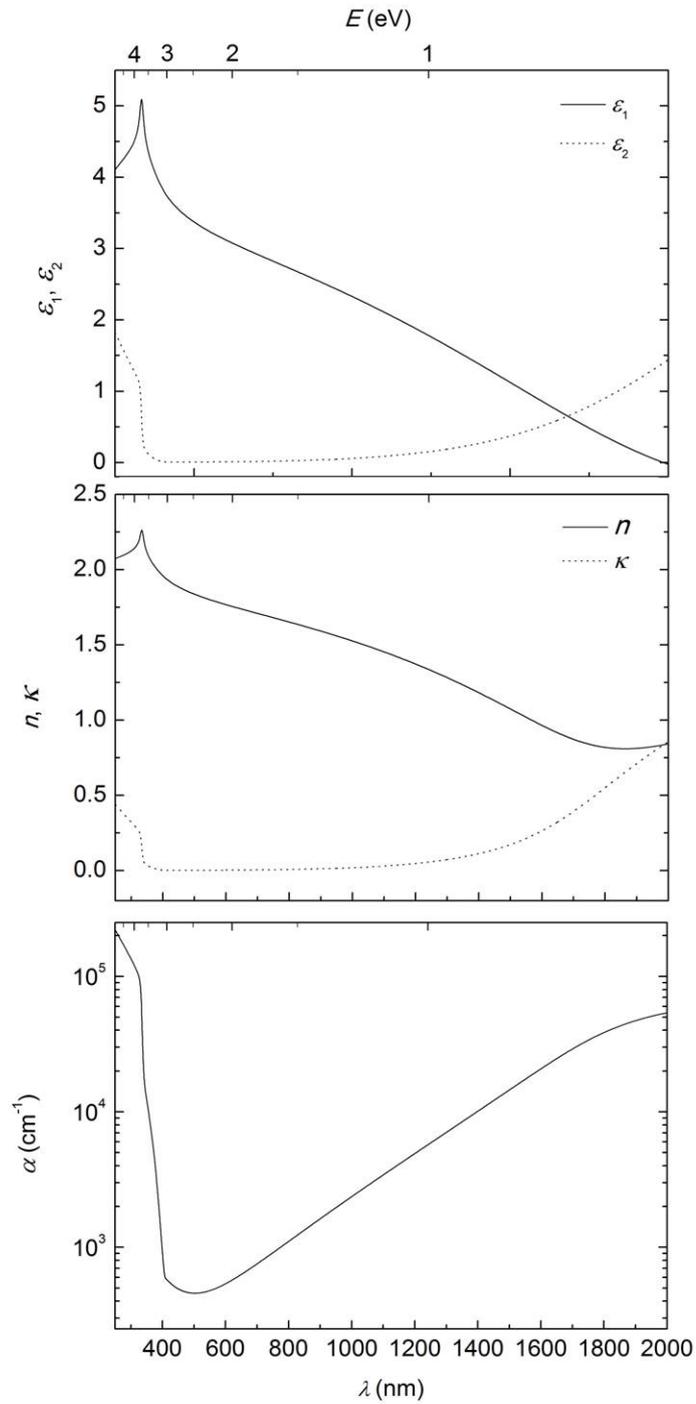
Figure 5.17: Optical behaviour of an AZO film as determined by the model fitting a physical model to its transmittance spectrum: a) Components of complex dielectric permittivity, b) Corresponding n and κ spectra, c)Absorption coefficient.

values of $\sim 0.30\ m_0$ given in the literature [26] but again, this is expected to be due to increased values being predicted for heavily doped films [10]. It was also possible to
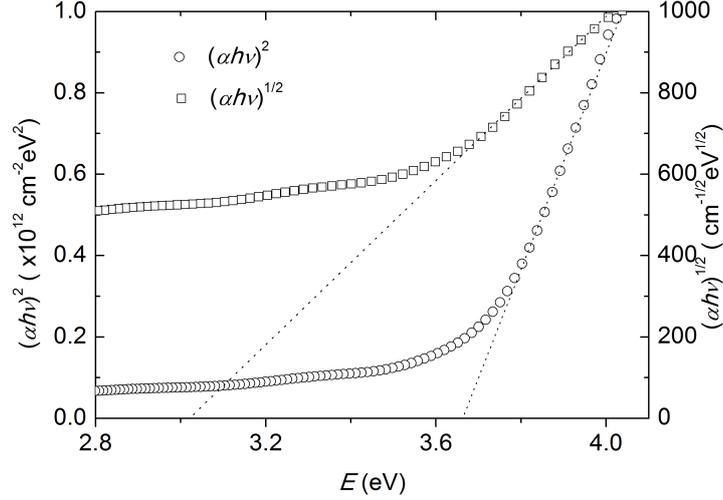
Figure 5.18: Determination of effective direct and indirect band gaps via extrapolation of linear regions of $(\alpha h\nu)^2$ and $(\alpha h\nu)^{1/2}$ plots. Values of $E_d = 3.67 \pm 0.05$ eV and $E_i = 3.02 \pm 0.04$ eV are determined from the plots.

calculate a value for m_e from the Burstein-Moss shift, Δ_{BM}, extracted from the model according to equation 2.54. A value of 0.17 m_0 is in poor agreement with the other values and clearly indicates that the size of the BM shift is much bigger than that expected. In fact, should the shift in the effective direct band gap result solely from a BM shift then a shift of no more than 0.27 eV could be expected. The observed shift is almost double this.

The resultant optical behaviour extracted from the model is shown in figure 5.17. Again, all the expected features are present and the spectra permit the recreation of the transmittance, via the transfer matrix method, for AZO films of different thicknesses. The absorption coefficient, α, over the range 400 - 850 nm is significantly lower than that of the baseline ITO film described in section 5.2. This suggests that thicker films of AZO can be deposited while maintaining a good transmittance in order to further reduce resistivity.

Figure 5.18 corroborates the model's value for the effective band gap, $E_d' = 3.72$ eV, by yielding a value of 3.67 ± 0.05 eV from a $(\alpha h\nu)^2$ vs E plot. Also, unlike the case for the baseline ITO film, the extrapolated value of $E_i = 3.02 \pm 0.04$ eV agrees very well with the value of $E_i = 3.02$ eV generated by the model. For the AZO film, the relative contribution to the absorption coefficient from indirect transitions is much higher and therefore the model gives a more reliable set of fitting parameters for its indirect inter-band transition

128
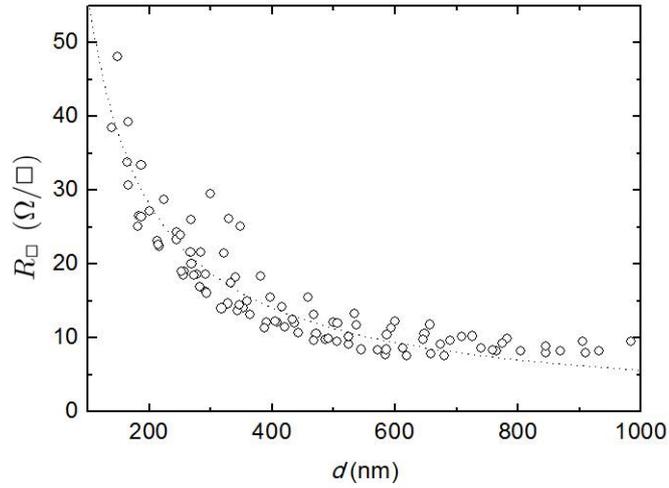
Figure 5.19: The sheet resistance over the wedge shaped AZO sample, as determined by the model, is seen to obey equation 2.63. The line fitted to the data gives a value of $\rho = 5.6 \pm 0.1 \times 10^{-4}$ Ω.cm.
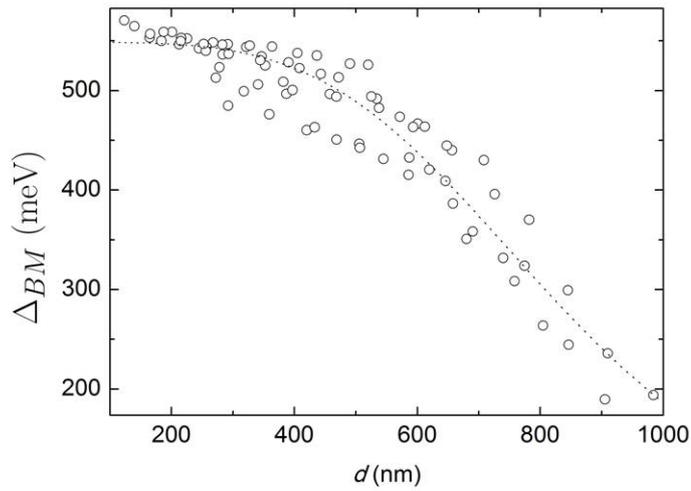
Figure 5.20: The Burstein-Moss shift is shown to decrease as a function of thickness for the AZO wedge sample. At low thickness values the magnitude of the shift is double that predicted by the inter-band transition model. However, as the thickness increases the size of the shift decreases towards the predicted value.

component.

The model was further tested by using it to fit 81 consecutive transmittance spectra taken at 1 cm intervals over a wedge shaped ZnO:Al sample deposited under the optimum conditions from a single mixed composition (ZnO:Al$_2$O$_3$ (2% wt.)) ceramic target and with the substrate rotation turned off. As for the In$_2$SnO$_3$ wedge, the resultant thickness profile (not shown) was smooth and continuous, with no anomalous spikes, indicating that the model has a good degree of self consistency.

The carrier concentration and electron mobility across the wedge remained approximately constant at values of $n_e = 3.4 \pm 0.5 \times 10^{20}$ cm^{-3} and $\mu_e = 32 \pm 5$ cm^{2}V^{-1}s^{-1} respectively. This gave rise to the expected relationship between $R_\square$ and d (stated by equation 2.63) as shown in figure 5.19. Note that, unlike in the case of the In$_2$O$_3$:Sn wedge, there was no obvious correlation between values of μ_e and thickness. However, figure 5.20 shows that there is a significant correlation between Δ_{BM} and thickness.

At thicknesses below 500 nm the BM shift remains artificially high, as previously discussed for AZO, but as the thickness increases beyond 500 nm values for Δ_{BM} are seen to decrease towards the expected value. Again, it may be speculated that the extra component of the band gap shift is related to the grain size within the film and that as the film thickness increases, promoting grain growth, the band gap shift is reduced until it reaches the value of $\sim$ 0.2 eV predicted by equation 2.54. Further investigations of the wedge sample (e.g. using XRD or SEM techniques) might be used to verify any such relationship.

The above result reveals the huge advantage that the application of the SP method to wedge shaped samples affords. The determination of such a result using conventional methods would have involved the fabrication of multiple films and proved extremely time consuming. Furthermore, any run to run variation between samples may serve to negate the observed effect. By incorporating all measurements into one sample this run to run variation can be completely removed.

5.4.3 F doped ZnO

While it has been shown that high quality Al doped ZnO films can be fabricated using RF magnetron sputtering, ZnO:Al may not prove to be the best candidate for use as a TCO front contact in CdTe solar cells. This is due to the potential for out-diffusion of

the electrically active group III Al dopant at the processing temperatures used in the case of close space sublimation ($\sim 500°$C), which could lead to detrimental effects on device performance. It has been shown [27] that ZnO films may instead be doped with fluorine via CVD and achieve electrical and optical properties comparable to those of Al doped films.

In this section, a systematic study of the doping of ZnO with F via RF magnetron sputtering is presented. The aim is to discover the limits of doping using the technique and assess the potential for use of ZnO:F films in thin-film solar cells. Furthermore, optical analysis of the effective band gap shifts with respect to doping levels provides further insight into the fundamental properties of the free carriers. Firstly, the effect of hydrogen incorporation in the chamber during sputtering was investigated, following the conclusion, drawn from reactive sputtering of F doped SnO_2 using CHF_3, that the presence of hydrogen is significant to the doping mechanism. Secondly, CHF_3 was used in combination with hydrogen in an attempt to further increase the substitutional doping of oxygen with fluorine.

Effects of growth in an Ar/H$_2$ plasma

The partial pressure of H_2 was varied over the range $0 - 5\%$ and a power of 100 W was maintained throughout, with experiments being performed at substrate temperatures of $250°$C and $350°$C. Figure 5.21 shows that there was a marked influence of H_2 partial pressure on resistivity, it being reduced by several orders of magnitude, with a minimum level of $\sim 5 \times 10^{-2}$ Ω.cm achieved for partial pressures above 3%. This behaviour is considered to result from a reduction of the films leading to an increased concentration of V_o. The most conductive film, sputtered at $250°$C in 3% H_2 had a resistivity of $\rho = 2 \pm 0.2 \times 10^{-2}$ Ω.cm, a carrier density $n_e = 1.6 \pm 0.2 \times 10^{19}$ cm^{-3} and a carrier mobility $\mu_e = 20 \pm 2$ cm^{2}V^{-1}s^{-1}.

It was found that the lower substrate temperature ($250°$C) encouraged the earlier onset of the resistivity decrease. However, a lower limit of resistivity was achieved for films deposited at $350°$C at H_2 partial pressures $> 3\%$, with values typically reduced by $\sim 20\%$ compared to the lower substrate temperature. Overall, compared to the undoped ZnO films, the resistivities of the films grown in H_2 were reduced by at least four orders of magnitude.
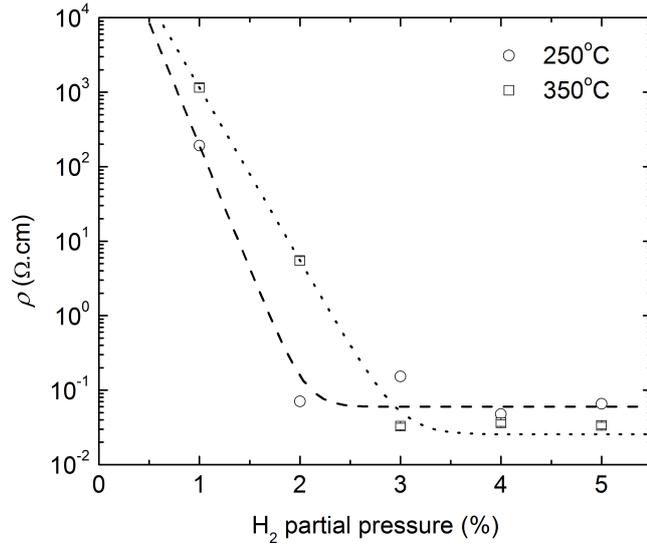
Figure 5.21: The effects of hydrogen incorporation on the resistivity of ZnO films sputtered at 100 W and at substrate temperatures of 250°C and 300°C.

Effects of growth in an Ar/H$_2$/CHF$_3$ plasma

In an attempt to achieve substitutional doping of ZnO with F, trifluoromenthane (CHF$_3$) was used at partial pressures in the range $0-7\%$ in addition to a constant partial pressure of 5% H$_2$. Given the results with hydrogen (previous section) the experiments were continued at 350°C. In order to control any memory or progressive target conditioning effects, all runs were undertaken in order of increasing CHF$_3$ partial pressure. Since cumulative effects were suspected, the CHF$_3$ partial pressure was never decreased during the sequence, and prior to each run the target was pre-sputtered for 10 minutes under the conditions of the subsequent run.

Figure 5.22 (a, b and c) shows the variation of resistivity, carrier concentration and carrier mobility for ZnO films as a function of CHF$_3$ partial pressure in the presence of a 5% partial pressure of H$_2$. Each curve shows a clear dependence on the pressure of CHF$_3$. Inclusion of low concentrations of CHF$_3$ ($< 1\%$) caused a reduction in the resistivity from $\sim 3 \times 10^{-2}$ Ω.cm to $\sim 9 \times 10^{-3}$ Ω.cm. In this range there is a corresponding increase in both carrier concentration and mobility. For concentrations in the range $< 4\%$ a lower base level of resistivity was achieved. In this range, the carrier concentration increased, but the mobility decreased accordingly, leading to the low level of variation in resistivity

132

observed.

For higher concentrations of CHF_3 ($5 - 6\%$) the resistivity increased markedly, this being caused by a simultaneous decrease in both n_e and μ_e as shown in figure 5.22. Further increase in CHF_3 partial pressure to 7% resulted in visible degradation of the films. They appeared mottled, with regions several mm in size appearing as though the film had been etched away. This was attributed to attack of the film by the high concentrations of the fluorine species used. All films represented in figure 5.22 had a thickness of between 90 and 200 nm. A linear decrease was observed in the growth rate as a function of CHF_3 partial presure ranging from 3 nm/min at 0% to 1 nm/min at 6%. It is known, in the case of doped ZnO, that the film thickness can influence the mobility, with thicker films generating higher mobilities [28]. It is assumed in this case that the film thickness does not vary widely enough between films for this effect to dominate over changes observed with respect to the variation of sputtering parameters.

Figure 5.23 (a, b and c) shows the effect that increased RF powers have on the electrical properties of films sputtered under a 4% partial pressure of CHF_3. Initially, as power is increased to 120 W, an increase is observed in both n_e to $8.5 \pm 0.5 \times 10^{19}$ cm^{-3} and μ_e to 26.5 ± 0.5 cm^{2}V^{-1}s^{-1}, resulting in a film with a resistivity of $2.9 \pm 0.1 \times 10^{-3}$ Ω.cm. This was the lowest film resistivity achieved within this work for fluorine doped ZnO. As power increased further, carrier concentrations steadily decreased while a gradual increase in mobility was observed until 200 W where it drops again. Overall, the resistivity of films increased as a function of RF power over the range varied. For films sputtered at 200 W it was possible to manipulate both n_e and μ_e to achieve lower resistivites by decreasing the CHF_3 partial pressure from 4% to between 1 and 3%. All films represented in figure 5.23 have thicknesses between 200 and 300 nm except for the film sputtered at 100 W which has a thickness of $\sim$ 100 nm.

For all doped films it was possible to maintain optical transmittances that are as high as those for undoped films (i.e. $> 80\%$). Again, as for the undoped films, peaks in transmittance spectra coincide with the substrate transmittance indicating that absorption is very low and that any loss in transmittance is due to coherent interference effects.

The success of the model in fitting transmittance data and its ability to extract parameter values comparable to those determined experimentally is now discussed. A further
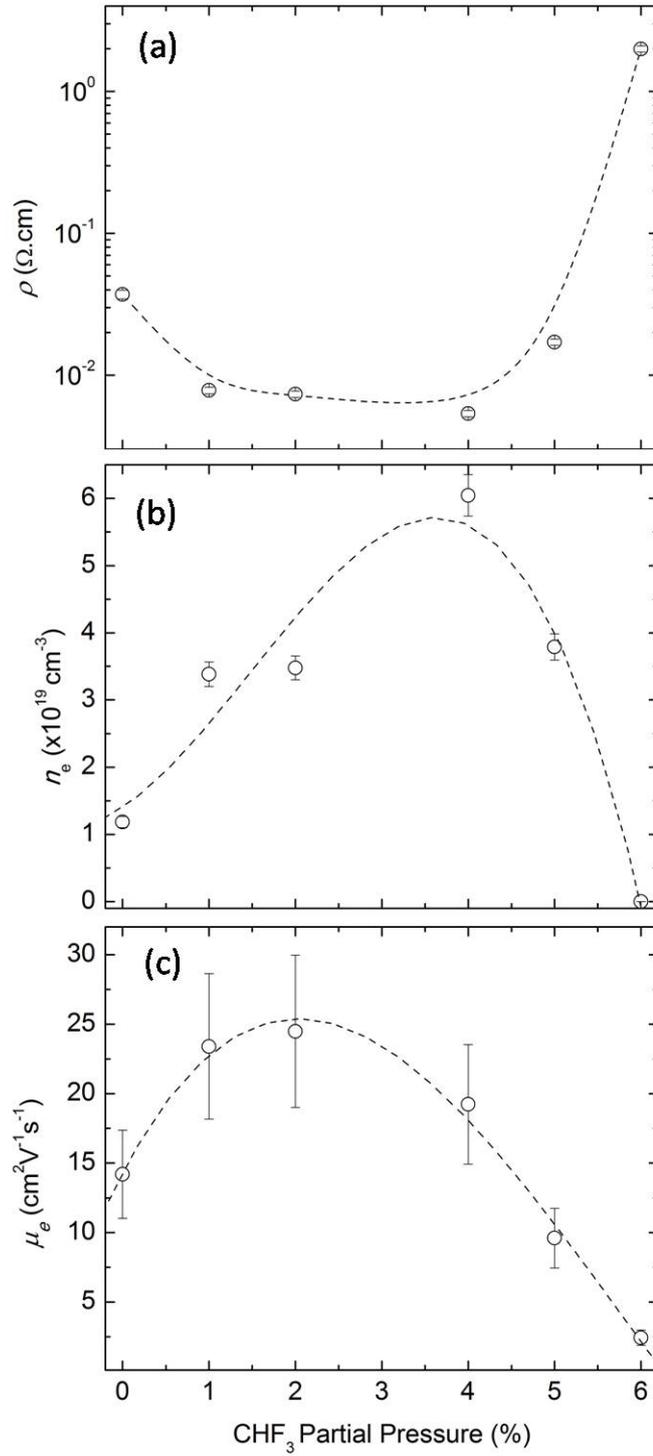
Figure 5.22: The effect of CHF$_3$ incorporation on (a) resistivity (b) carrier concentration and (c) carrier mobility of ZnO:F films sputtered at an RF power of 100 W, a pressure of 5 mTorr (5% H$_2$ + x% CHF$_3$), and at a substrate temperature of 300°C.
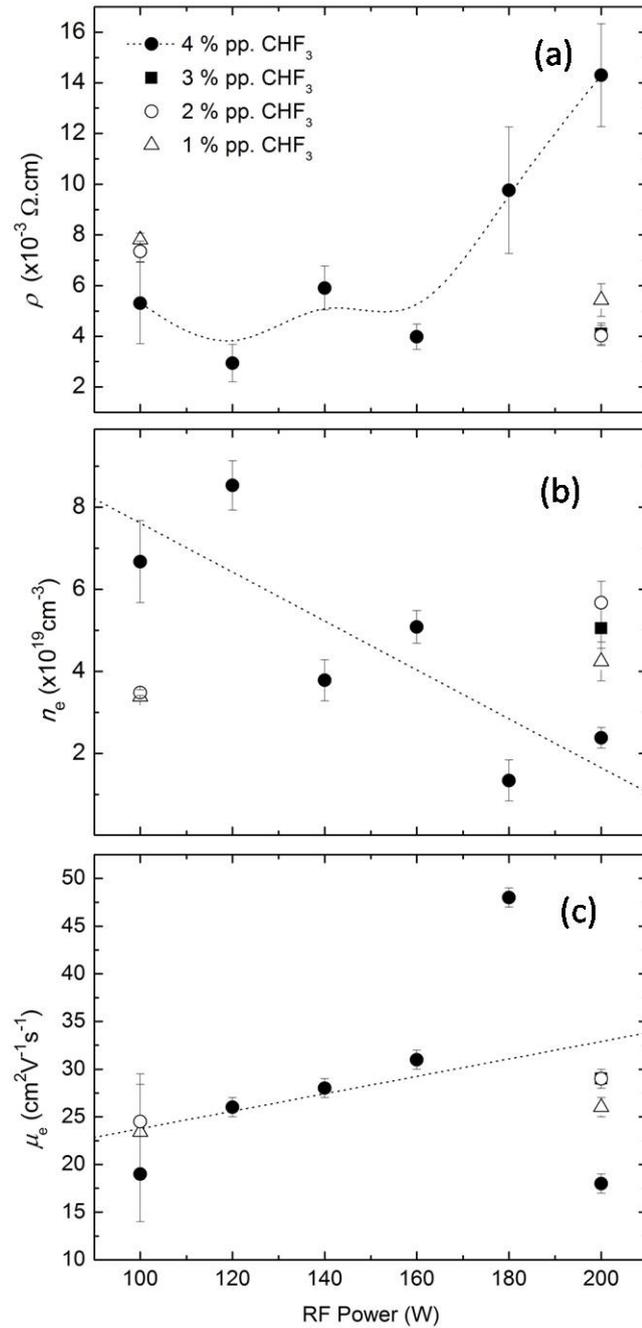
Figure 5.23: The effect of varying RF power on (a) resistivity (b) carrier concentration and (c) carrier mobility of ZnO:F films sputtered at an RF power of 100 W, and at a substrate temperature of 300°C.

Table 5.8: A selection of FZO film parameters determined from both experiment and the modelling of transmittance curves.

CHF$_3$ (%)	d_S (nm)	$n_e^{H\,a}$ ($\times 10^{19}$ cm^{-3})	μ_e^H (cm^{2}V^{-1}s^{-1})	ρ^a ($\times 10^{-3}$ Ω.cm)	Δ_{BM}^{exp} (meV)	Δ_{BM}^{model} (meV)	γ_w (eV)	E_i (eV)	E_p (meV)	d_{SP} (nm)
0	65	1.15	14.2	38.2	75	64	0.49	2.64	3.6	68
1	65	3.14	23.4	8.5	87	82	0.52	2.88	4.4	69
2	115	3.34	24.5	7.6	89	99	0.50	3.06	3.6	119
3	106	3.25	19.8	9.7	94	99	0.52	3.08	4.4	111
4	91	5.83	19.2	5.6	134	138	0.52	3.10	1.8	91
5	95	3.27	9.6	19.9	110	114	0.52	3.06	3.1	104

^{a} Calculated using d_{SP}

discussion is also presented concerning the suitability of the model's assumptions and ways in which they can be improved. Table 5.8 shows the experimental and modelled results for a selection of F doped ZnO films. The experimental and model values for the BM shift, Δ_{BM}, agree typically to within 5%, except for the samples with the lowest carrier concentrations where the error in determining such small shifts in the direct band gap become larger. For all samples, the modelled values of γ_w (i.e. the extent of the Urbach tail) were ~ 0.5 eV.

Values extracted for indirect band gaps were in the range $2.6 - 3.1$ eV and, as for the effective direct band gaps, increased with doping concentration. However, it is not possible to put as much confidence in the accuracy of these values due to the relatively small contribution to ε_2 compared with that for direct transitions.

Comparing the film thicknesses extracted using the Swanepoel method (d_S) and from the SP method (d_{SP}) it is clear that the values agree, although the model values are consistently higher by around 5%. Again, the thickness values extracted by the model may be considered more accurate because all the experimental data points within each spectra are utilised and not just those located at the maxima and minima of the fringes within the low-absorption region according the Swanepoel method.

Figure 5.24 shows an example of a typical fit to a transmittance spectrum for a film deposited in a CHF$_3$ partial pressure of 5%. It is clear that the model achieves an excellent
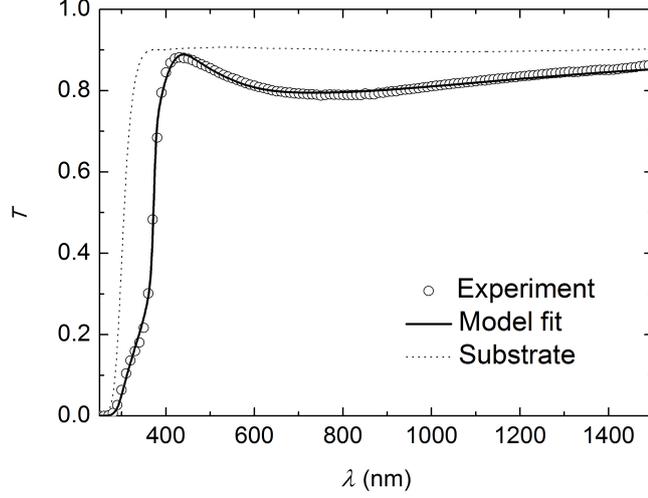
Figure 5.24: Transmittance spectrum for F doped ZnO sample deposited under the following conditions: RF power = 200 W, pressure = 5 mTorr Ar (5% H_2 + 5% CHF_3). An excellent model fit is achieved.

fit to the experimental spectrum, there being a very low MSE value of $\sim 6 \times 10^{-5}$. The corresponding fit parameters for this sample are shown in table 5.9 and the resultant optical properties of the film, as calculated from the fit parameters, are shown in figure 5.25.

The reliability of the model and the validity of its assumptions will now be discussed: Firstly, the model assumes that the increase in the Fermi level (and hence the effective direct band gap) with carrier density is attributed solely to a BM shift (equation 2.54). However, it is apparent that a linear plot of Δ_{BM}^{model} vs $n_e^{2/3}$ (figure 5.26) does not extrapolate through the origin suggesting that there is a component to the increase in E_d that is not due to the BM shift alone. Thus, equation 2.54 can be re-written as

$$E_f = \Delta_{BM} + \Delta_x = \frac{\hbar^2}{2m_e}(3\pi n_e)^{2/3} + \Delta_x \qquad (5.2)$$

where Δ_x is the component of the shift not attributed to a BM effect. It must be noted that because the relationship between Δ_{BM} and $n_e^{2/3}$ is linear over the range shown in figure 5.26, Δ_x must be independent of n_e and must also be constant over the range. Becuase all the films were of similar thicknesses ($\sim 100 - 200$ nm) it is expected that all films within the study had a similar grain size. This is in agreement with the value of Δ_x being constant over the range of n_e observed if the extra shift in the effective grain size is indeed related to grain structure.

Because Δ_{BM} is independent of Δ_x it is still possible to make an estimate for the value

137

of the effective electron mass m_e from the slope of the line in figure 5.26. A value of $m_e = 0.35 \pm 0.3 \ m_0$ was calculated. This value is higher than the value of $m_e = 0.24 \ m_0$ measured for undoped bulk ZnO [29]. Again, this is expected as m_e has been shown to increase as a function of n_e [10] and the value is in accordance with other reported values for doped, polycrystalline ZnO [30, 31]. Note that shifts in the band gap due to the presence of other phases, such as ZnF_2 are unlikely due to the high volatility of fluorides [32].

Table 5.9: Parameter values extracted from model used to fit the transmittance spectrum of F doped ZnO film sputtered in a 4% partial pressure of CHF_3

| Model Component	Parameter	Value
Lorentz Oscillator	A_0 (eV)	40.5
	$\hbar\omega_0$ (eV)	16.3
	$\frac{1}{\tau}$ (eV)	8.59×10^7
Direct Transitions	E_d (eV)	3.20^a
	Δ_{BM} (meV)	113
	D (eV$^{3/2}$)	25.48
	γ_w (eV)	0.52
Indirect Transitions	E_i (eV)	2.74
	E_p (meV)	3.6
	$D^{'}$	0.24
	d (nm)	103.1
	MSE ($\times 10^{-5}$)	6.2
	$\tilde{T}$	0.82
	$\tilde{\alpha}$ (cm^{-1})	2751

[a] Determined from undoped samples
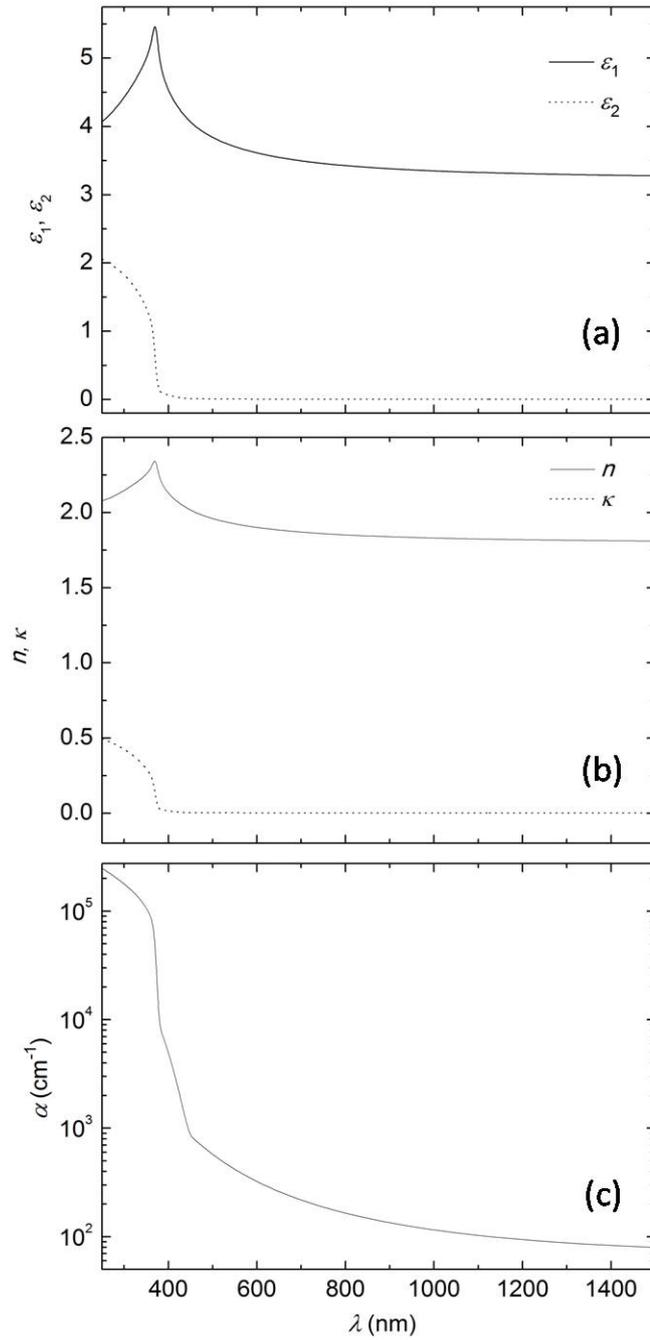
Figure 5.25: Optical behaviour of F doped ZnO film (figure 5.24) as extracted from the model: a) Components of dielectric permittivity, b) corresponding n and κ spectra, c) absorption coefficient.
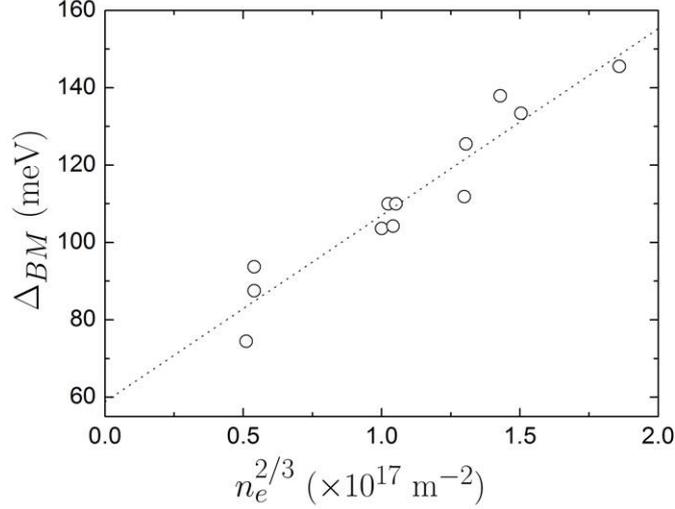
Figure 5.26: Experimental values of BM shift and carrier concentrations determined from the model and van der Pauw measurements respectively, permit the estimation of the effective electron mass in ZnO:F.

Indeed it has been shown that F doped ZnO films deposited by magnetron sputtering generally consist of a single ZnO phase [33]. Secondly, within the experimental range of investigation the use of a Drude component within the model for ZnO was redundant as the carrier concentrations in the films were not high enough to create a discernible change in the dielectric background. Indeed, at the carrier densities observed, plasma frequencies of $\hbar\omega > 0.6$ eV (i.e. below 2 μm) could not have been achieved. Thus, unless the experimental range of measurement or the carrier concentrations of future films is increased it is not necessary to include a Drude component within the model.

5.5   Conclusions

Table 5.10 shows a summary of the best achievable set of opto-electronic properties for each of the TCO materials discussed in sections 5.2-5.4. The best quality films, with respect to the criteria discussed in Chapter 2, section 2.4 were undoubtedly those of In_2O_3:Sn (ITO). In this case, the attainment of high carrier densities (up to 8.9×10^{20} cm^{-3}) in addition to high carrier mobilities ($40-60$ cm^{2}V^{-1}s^{-1}) and transmittances (> 0.82) resulted in typical figures of merit (equation 2.64) well above the desired value of 5×10^{-2} Ω^{-1}, specified for

Table 5.10: A summary of the best opto-electronic properties of the TCO materials reported in this chapter.

Material: dopant	T_{sub} (°C)	n_e (cm^{-3})	μ_e (cm^{2}V^{-1}s^{-1})	ρ (Ω.cm)	E'_d (eV)	$R_\square$ ($\Omega/\square$)	$\tilde{T}$	d (nm)	ϕ (Ω^{-1})
In$_2$O$_3$:Sn	400	8.9×10^{20}	58.4	1.2×10^{-4}	4.20	5.1	0.83	249	8.3
SnO$_2$:F	300	–	–	1.0×10^{-2}	3.89	232.5	0.85	430	0.3
ZnO:V$_O$ [a]	350	1.5×10^{19}	14.2	3.8×10^{-2}	3.2	5.6 k	0.82	68	0.01
ZnO:Al	150	4.3×10^{20}	30.8	4.7×10^{-4}	3.67	9.1	0.84	517	5.2
ZnO:F	350	8.5×10^{19}	26.5	2.9×10^{-3}	3.34	115	0.82	251	0.4
TEC 8 [b]	–	4.1×10^{20}	36.0	4.3×10^{-4}	3.78	8.2	0.69	520	0.8
TEC15 [b]	–	4.6×10^{20}	32.0	4.3×10^{-4}	3.79	13.4	0.79	318 [34]	1.9

[a] Commercial TCO supplied by NSG Pilkington Group. SnO$_2$:F deposited by CVD onto soda-lime glass.

[b] Undoped - the conductivity is usually though to arise from V$_O$.

applicability in thin-film solar cell design. The incorporation of such ITO films as front contact layers in CdTe based solar cells provides an excellent opportunity to establish a working device structure, and this is indeed attempted with some success in Chapter 7.

However, the key objective remains to find a TCO material that possesses equivalent properties to ITO but is not based on In. RF sputtered ZnO:Al (AZO) films, deposited from a standard mixed composition ZnO:Al$_2$O$_3$ (2% wt.) target, show the most promise in meeting this objective. While the best achievable resistivity for these films are nearly four times that of the ITO films, a lower absorption coefficient permits the achievement of low sheet resistances (< 10 $\Omega/\square$), simply by growing thicker films, without generating a significant reduction in the transmittance. Therefore, a figure of merit greater than 5×10^{-2} Ω^{-2} can readily be achieved for sputtered AZO films, making them good candidates for use in CdTe devices. Another advantage of AZO films is that they can be deposited at significantly lower temperatures than ITO. Their use in the development of devices arranged in a substrate configuration (i.e. where the TCO is deposited last) is therefore preferable over ITO, the deposition temperature of which (400°C) is likely to generate a degradation in the resultant device performance. Indeed the use of an AZO based TCO has already been demonstrated in CdTe devices deposited on flexible molybdenum foils
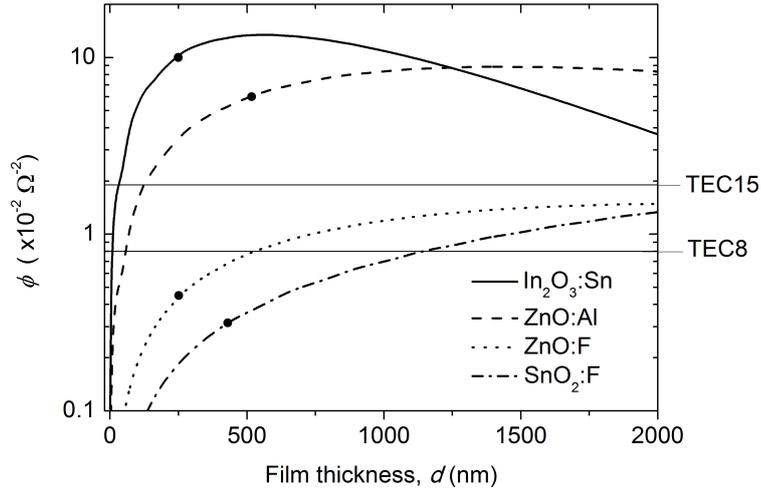
Figure 5.27: The figure of merit as a function of thickness calculated for the best performing TCO material from each section of this chapter. The points are for the best performing films.

[35, 36].

Figure 5.27 shows the figure of merit, ϕ, calculated as a function of film thickness for ITO, FTO, AZO and FZO. The plots were determined by passing the extracted n, κ and α spectra for each material to a model based on a transfer matrix method, and re-calculating $\tilde{T}$ as a function of film thickness, d. The resultant plots were then calculated according to equation 2.64. The horizontal lines in the figure represent the performance limit of two commercial TCOs: TEC8 and TEC15 (Pilkington NSG group): these are commonly used in the industrial manufacture of thin-film PV as well as in lab scale devices. The sputtered ITO and AZO films demonstrate a significant improvement in ϕ compared to the commercial substrates suggesting that superior device efficiencies may be achieved using the sputtered films.

The lowest achievable resistivity limit for reactive sputtering methods was $\sim 3 \times 10^{-3}$ Ω.cm, this being for films of ZnO:F sputtered in H_2 and CHF_3. This value is an order of magnitude higher than that of films sputtered from mixed composition target. Therefore, reactively sputtered films of SnO_2:F and ZnO:F did not meet the TCO criteria set for application in CdTe devices. Furthermore, the use of reactive gases during sputtering generated a considerable reduction in growth rates making deposition from mixed compo-

sition targets preferable. Nonetheless, one important conclusion can be drawn from the work on reactively sputtered films: The presence of hydrogen during sputtering is a key requirement for doping to occur. In cases where no hydrogen was introduced to the system, e.g. sputtering SnO_2 in CF_4, only highly resistive and stoichiometric films were achieved. In general, oxide layers possess a native doping due to the formation of oxygen vacancies within the film. The incorporation of CF_4 during film deposition serves to eliminate this native doping. This result may be applied to the development of highly resistive and transparent 'buffer' layers that are used in CdTe devices, inserted between the TCO and CdS layers, to improve device stability.

Further opportunities to explore the limits of F doping in both SnO_2 and ZnO are likely to lie with co-sputtering techniques; i.e. film deposition that involves the use of two or more targets. In the case of SnO_2:F, sputtering from separate SnO_2 and SnF_2 targets has demonstrated that co-sputtering permits a large range of compositions to be probed. Furthermore the work suggests that the exploration of compositions with lower concentrations of SnF_2, may yield films with significantly lower resistivities. In the case of F doped ZnO, co-sputtering may be achieved through use of both ZnO and ZnF_2 targets. Indeed the merits of using a ZnF_2 target in reactive sputtering experiments has already been demonstrated by Tsai *et.al* [33] for the deposition of high quality ZnO:F films, the properties of which are akin to the AZO films within this work. In both cases (SnO_2:F and ZnO:F), co-sputtering presents a huge opportunity for the rapid combinatorial determination of the optimum sputtering parameters and film compositions required to generate TCO materials that can be used in CdTe based devices. The model of TCO dielectric permittivity and its use in fitting transmittance data provides a key tool for the automated processing of the large amounts of data that will arise from this experimental approach. Also, further investigations via XRD and SEM into the origin of anomalous shifts in the effective direct band gap, strongly suspected to be the result of the grain microstructure, will allow this effect to be incorporated into the model.

To conclude, RF magnetron sputtering has been demonstrated as an excellent deposition technique for the further development of high performance TCO materials. The high degree of control over deposition parameters (pressure, power and substrate temperature) permit significant control over and manipulation of the resultant film properties. The abil-

ity to sputter any material, provided it can be pressed into a ceramic target, gives rise to a significant scope for new TCO materials that avoid the use of In, such as ZnO:Si [37] and TiO$_2$:Nb [38–40]. The technique is also highly comparable with device fabrication procedures, particularly in the case of fully sputtered CdTe solar cells.

The key disadvantages of using RF magnetron sputtering, on the laboratory scale, is the inefficient use of target material and the relatively slow growth rates compared to other competing techniques. However, these problems are easily overcome in the industrial scale-up of thin-film deposition through the use of alternative target geometries and rotating targets [41].

5.6   References

[1] I. Oladeji, L. Chow, C. Ferekides, V. Viswanathan, Z. Zhao. *Sol. Energy Mater. Sol. Cells* **61**, 203 (2000).

[2] K. Barth, R. Enzenroth, W. Sampath. *Conference Record of the Twenty-Ninth IEEE PVSC*, 551–554 (2002).

[3] I. Visoly-Fisher, S. Cohen, D. Cahen, C. Ferekides. *App. Phys. Lett.* **83**, 4924 (2003).

[4] P. Liska, K. Thampi, M. Gratzel, D. Bremaud, D. Rudmann, H. Upadhyaya, A. Tiwari. *App. Phys. Lett.* **88**, 203103 (2006).

[5] T. Gessert, W. Metzger, P. Dippo, S. Asher, R. Dhere, M. Young. *Thin Solid Films* **517**, 2370 (2009).

[6] M. Theiss. *Scout 3.0, Hard and Software for Optical Spectroscopy.* Dr. Bernhard-Klein-Str. 110, 52078 Aachen, Germany (www.mtheiss.com).

[7] H. A. Macleod. *Thin-Film Optical Filters.* Adam Hilger Ltd (1986).

[8] R. Weiher, R. Ley. *J. Appl. Phys.* **37**, 299 (1966).

[9] H. K. Müller. *Phys. Status Solidi* **27**, 723 (1968).

[10] F. Ruske, A. Pflug, V. Sittinger, B. Szyszka, D. Greiner, B. Rech. *Thin Solid Films* **518**, 1289 (2009).

[11] T. Maruyama, K. Tabata. *J. Appl. Phys.* **68**, 4282 (1990).

[12] J. Proscia, R. Gordon. *Thin Solid Films* **214**, 175 (1992).

[13] S. Suh, Z. Zhang, W. Chu, D. Hoffman. *Thin Solid Films* **345**, 240 (1999).

[14] B. Stjerna, E. Olsson, C. Granqvist. *Journal of Applied Physics* **76**, 3797 (1994).

[15] H. M. Schmidt, H. Weller. *Chem. Phys. Lett.* **129**, 615 (1986).

[16] Y. Kayanuma. *Phys. Rev. B* **38**, 9797 (1988).

[17] Y. Wang, N. Herron. *Phys. Rev. B* **42**, 7253 (1990).

[18] M. Krishna, R. Friesner. *J. Chem. Phys.* **95**, 8309 (1991).

[19] A. Tomasulo, M. Ramakrishna. *J. Chem. Phys.* **105**, 3612 (1996).

[20] P. Trwoga, A. Kenyon, C. Pitt. *J. Appl. Phys.* **83**, 3789 (1998).

[21] D. Lide. *CRC andbook of Chemistry and Physics.* CRC Pr I Llc (2003).

[22] A. Gupta, A. Compaan. *App. Phys. Lett.* **85**, 684 (2004).

[23] V. Srikant, D. R. Clarke. *J. Appl. Phys.* **83**, 5447 (1998).

[24] R. Swanepoel. *Journal of Physics E: Scientific Instruments* **16**, 1214 (1983).

[25] R. Swanepoel. *Journal of Physics E: Scientific Instruments* **17**, 896 (1984).

[26] B. Enright, D. Fitzmaurice. *J. Phys. Chem.* **100**, 1027 (1996).

[27] J. Hu, R. Gordon. *Solar Cells* **30**, 437 (1991).

[28] C. Agashe, O. Kluth, J. Hupkes, U. Zastrow, B. Rech, M. Wuttig. *J. Appl. Phys.* **95**, 1911 (2004).

[29] W. S. Baer. *Phys. Rev.* **154**, 785 (1967).

[30] S. Brehme, F. Fenske, W. Fuhs, E. Nebauer, M. Poschenrieder, B. Selle, I. Sieber. *Thin Solid Films* **342**, 167 (1999).

[31] A. Sarkar, S. Ghosh, S. Chaudhuri, A. Pal. *Thin Solid Films* **204**, 255 (1991).

[32] F. Yakuphanoglu, Y. Caglar, S. Ilican, M. Caglar. *Physica B* **394**, 86 (2007).

[33] Y. Tsai, N. Wang, C. Tsai. *Mater. Lett.* **63**, 1621 (2009).

[34] A. Compaan, R. Collins, V. Karpov, D. Giolando. *Fabrication and Physics of CdTe Devices by Sputtering*. Technical report, NREL (2008). www.nrel.gov/docs/fy09osti/45398.pdf - accessed Aug 2011.

[35] I. Matulionis, S. Han, J. Drayton, K. Price, A. Compaan. *MRS Symp. Proc.* **668**, 8 (2001).

[36] J. Drayton, A. Vasko, A. Gupta, A. Compaan. *Conference Record of the Thirty-First IEEE PVSC*, 406–409 (2005).

[37] A. K. Das, P. Misra, L. M. Kukreja. *J. Phys. D: Appl. Phys* **42** (2009).

[38] N. L. H. Hoang, N. Yamada, T. Hitosugi, J. Kasai, S. Nakao, T. Shimada, T. Hasegawa. *Appl. Phys. Exp.* (2008).

[39] N. Yamada, T. Hitosugi, J. Kasai, N. L. H. Hoang, S. Nakao, Y. Hirose, T. Shimada, T. Hasegawa. *Thin Solid Films* **518**, 3101 (2010).

[40] T. Hitosugi, N. Yamada, S. Nakao, Y. Hirose, T. Hasegawa. *Phys. Status Solidi A* **207**, 1529 (2010).

[41] R. Kukla. *Surf. Coat. Tech.* **93**, 1 (1997).

Chapter 6

Device Fabrication and Characterisation

6.1 Introduction

The key objective of the work presented in this chapter was to develop a prototype fully sputtered CdTe solar cell device structure that yielded efficiencies comparable to those deposited via other methods, e.g. close space sublimation CSS [1–3]. Compaan *et al.* have already shown that RFMS is a viable deposition technique for the deposition of CdTe devices that have efficiencies > 14% [4–7]. The use of RFMS has several advantages over other techniques, these include a high degree of control over deposition parameters (i.e. RF power, pressure, substrate temperature, growth rate), excellent reproducibility of film properties over a large series of runs, and the use of lower substrate temperatures. Furthermore, at an experimental scale, the uniformity of films over areas greater than 5×5 cm^2 is superior to that of CSS methods. The technique also provides further scope for combinatorial development and rapid optimisation of device configurations (see section 6.4). Despite these advantages, RFMS is a relatively underused technique for the deposition of the CdTe absorber layer.

In this chapter, section 6.2 presents an assessment of a high number of cell results based on a prototype device structure and a consistent set of processing conditions. Investigations as to how the prototype device structure could be further optimised through the variation of key in-situ and ex-situ processing parameters is then explored in section 6.3. There is

a focus on device characterisation in section 6.3.3, where the results of J-V-T, EBIC and TEM measurements made on a typical device are presented. Finally, some opportunities for future work and the further optimisation of fully sputtered devices are outlined in section 6.4

6.2 Prototype CdTe device baseline performance

6.2.1 Experimental details

Figure 6.1 shows the layer structure of the prototype device design. The fabrication process was as follows: ITO was sputtered from a combined In_2O_3:SnO_2 (10% wt.) target and using the sample deposition parameters described in section 5.2 , i.e. an RF power of 60 W, an Ar pressure of 1 mTorr, and a substrate temperature of 400°C. The resultant films had typical sheet resistances of ~ 6 $\Omega/\square$ for a thickness of 230 nm and integrated transmittances of $\tilde{T} > 85\%$ over the visible range. A high resistivity ($> 10^{-2}$ Ω.cm, 50 nm thick) layer of ZnO was sputtered from a ceramic ZnO target (purity 99.99%, Pi-Kem) at a power of 100 W, a pressure of 5 mTorr and at room temperature. The substrate was then transferred under vacuum to the second chamber, where a 200 nm layer of CdS was deposited at 60 W, under 5 mTorr Ar and at a substrate temperature of 350°C. A 3% partial pressure of CHF_3 was incorporated during growth to improve the quality of the film. According to Romeo *et al.* [3] the decomposition of CHF_3 in the plasma introduces F^- ions that back-sputter the growing CdS film which helps to remove voids within the material and hence increases
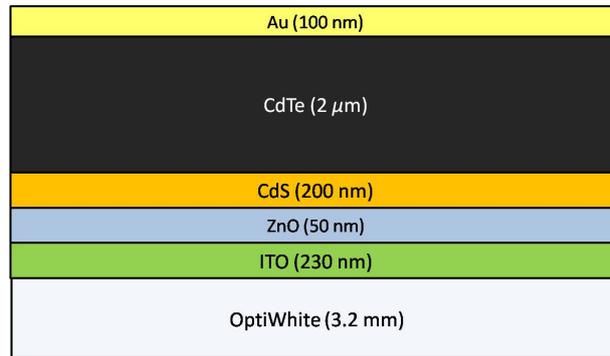

Figure 6.1: Prototype device structure. All layers were deposited by RFMS except the evaporated Au back contact.

the film density.

A 2 μm thick CdTe layer was sputtered from a CdTe target (of purity 99.99 %, AJA) at 70 W, under 5 mTorr of Ar and at a substrate temperature of 350°C. A growth rate of $\sim$ 7.3 nm/min was achieved. The finished 10 $\times$ 10 cm^2 plates were then quartered, and onto each a layer of CdCl$_2$ was evaporated according to the description given in section 4.2.2. Each sample was annealed in a tube furnace for 9 - 11 mins in air at 390°C and contacted. J-V curves were then measured for all 5$\times$5 mm^2 contacts as described in section 4.4.1.

6.2.2 Device results

The distribution of efficiency values from 201 separate 'cells' (i.e. 5 $\times$ 5 mm^2 contacts) is shown in figure 6.2. Three distinct populations of devices were identified and these were attributed to being under-treated, optimised and over-treated by the CdCl$_2$ process. In preliminary experiments the shorter CdCl$_2$ anneal times used ($\sim$ 5 mins) typically led to the low device performance associated with under-treatment. However, for devices annealed in the optimum time window (9 - 11 min) it was often found that some parts of a given 5 $\times$ 5 cm^2 plane were visibly degraded. The cell performance parameters, η, FF, J_{SC} and V_{OC} are given in table 6.1 and selected J-V and EQE curves, that represent the typical

Table 6.1: Average performance characteristics of typical under-treated, over-treated and optimised device populations. The best device performance achieved is also included.

|	Under-treated	Over-treated	Optimised	Best
η (%)	3.1	2.2	9.3	12.4
V_{OC} (V))	0.69	0.77	0.80	0.82
J_{SC} (mA/cm^2)	10.1	6.4	19.6	24.9
FF (%)	43.9	44.6	58.6	61.0
R_s (Ω.cm^2)	23.6	22.1	8.39	7.61
R_{sh} (Ω.cm^2)	641	1113	731	2011
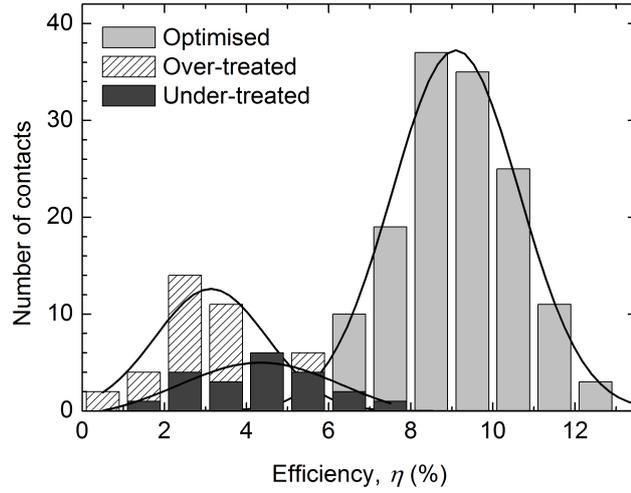
Figure 6.2: Distribution of efficiency of 201 5×5 mm^2 contacts taken from 12 separately processed sample plates. An average efficiency of 8.6 ± 2.2 % was achieved for the group of contacts that received an optimum CdCl$_2$ treatment.

behaviour of each population, are shown in figures 6.3 and 6.4 respectively. The behaviour associated with each population is described below.
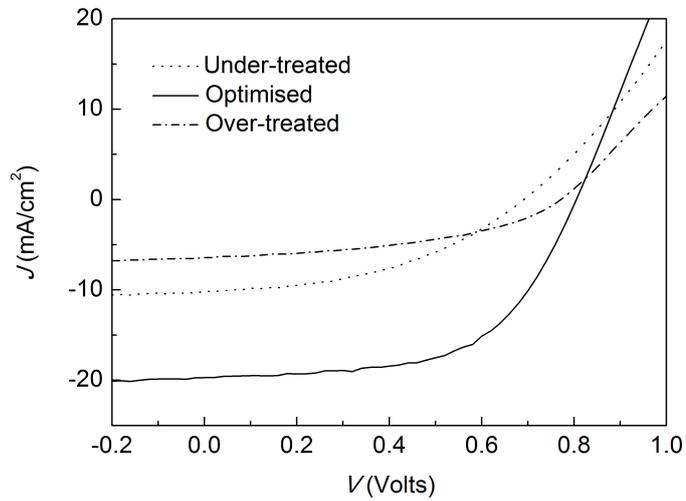

Figure 6.3: $J - V$ curves for under-treated ($\eta = 3.1$ %), optimised ($\eta = 9.34$ %) and over-treated ($\eta = 2.5$ %) devices.
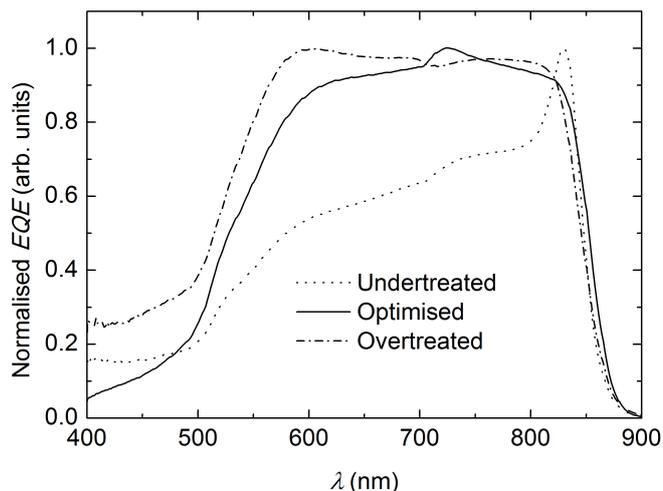
Figure 6.4: The corresponding external quantum efficiency (EQE) of devices from figure 6.3. The curves are normalised in order to allow comparison of their shape. For the under-treated device, the behaviour is characteristic of a buried junction.

Optimised devices:

The main group of cells in the distribution shown in figure 6.2 is for high performing devices that have an average efficiency of $8.6 \pm 2.2\%$. EQE results for a typical cell from this group (see figure 6.4) indicate that the junction is at an optimised position at the CdTe/CdS interface, with a high response over the range 550-800 nm. Poor response in the sub 500 nm range is attributed to the absorption in the CdS, which was 200 nm thick.

The best cell in the group had the following parameter values: $\eta = 12.4\%$, $FF = 61\%$, $J_{SC} = 24.9$ mA.cm^{-2} and $V_{OC} = 0.82$ V. Its high performance was associated with a relatively low series resistance, $R_s = 7.6$ Ω.cm^2, and a high shunt resistance, $R_{sh} = 2011$ Ω.cm^2, leading to good rectification behaviour and a high fill factor.

Over-treated devices:

As mentioned above, over-treatment was clearly identified since there was visible physical degradation of the layer. In particular, the films showed signs of bubbling and exfoliation, and had poor adhesion. Viewing from the glass side revealed discolouration from the more usual black to an orange-grey. The efficiencies ($3.3 \pm 1.3\%$) were correspondingly poor.

Although the shapes of their EQE were comparable to those for optimised cells, their

152

magnitudes were reduced, leading to a reduced J_{SC}. Another factor contributing to the low efficiency of the cells is the series resistance which was typically twice that of the optimised cell population.

Under-treated devices:

Short CdCl$_2$ processing times ($\sim$ 5 mins) gave rise to the J-V and EQE curves shown in figures 6.3 and 6.4. The EQE curve shape is typical for buried junction behaviour, and this is consistent with the depth of chloride diffusion being insufficient to form a junction at the correct position in the CdTe.

The population of under-treated cells shown in figure 6.2 was for cells on the 5×5 cm^2 device plates which were treated for 9 - 11 mins, i.e. the same conditions as for the main series of samples. They were distinguished from optimised contacts on the basis of their low efficiency and/or low FF ($\leq 35\%$), since they were visibly indistinguishable from other parts of the plate. The average efficiency of this population was $4.4 \pm 1.6\%$, the low performance being due to a relatively low FF together with low J_{SC} and V_{OC} values.

Cross sectional SEM

SEM was performed on an FIB-milled cross section of a single cell (contact) that had a performance typical of those within the optimised population ($\eta = 10\%$). Following the preparation of the cross section, according to the methodology described in section 4.4.4, imaging was performed using the secondary electron detector. Figure 6.5a shows the geometry of the cross-section of the thin films of the solar cell, which are clearly visible at "X", even at low magnification. Figure 6.5b shows a $\times 50,000$ magnification image of the same polished cross-section. The complete layer structure shows high contrast and it was possible calculate estimates for the layer thicknesses: CdTe(1.7 ± 0.1 μm)/CdS(100 ± 4 nm)/ZnO(100 ± 10 nm)/ITO(180 ± 10 nm). Furthermore the grain structure of the CdTe is clearly visible and composed mainly of large grains, > 1 μm, but with smaller grains, < 500 nm, located at grain boundary intersections. This indicates that the film has undergone a high degree of re-crystallisation during the post-deposition treatment process, it being known from preliminary investigations that the maximum grain size within as-grown CdTe films does not exceed ~ 200 nm.
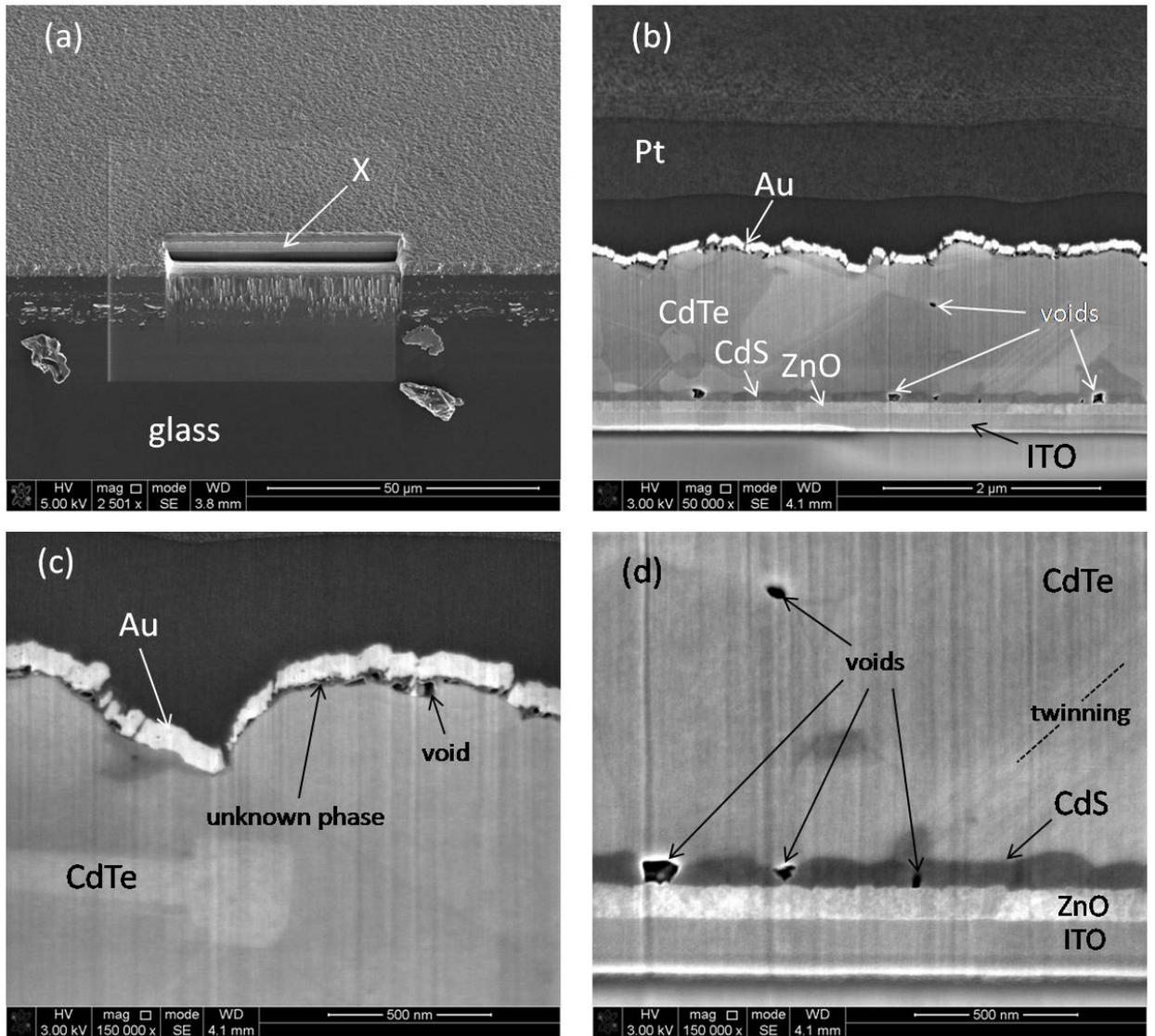
Figure 6.5: SEM imaging of a cross section of a completed device ($\eta = 10$ %). (a) The sample was prepared via cutting and polishing with a focussed ion beam of Ga^+ ions and imaged in secondary electron mode. (b) The full cross-section shows that all layers (i.e. Au/CdTe/CdS/ZnO/ITO) within the layer are distinct and can easily be distinguished from each other. (c) The interface between the Au and CdTe is slightly porous and a change in contrast of the CdTe at the interface indicates some compositional change (e.g. an excess of Te). (d) The CdS layer has a distinct grain structure and voids are clearly present within the layer.

In some of the larger CdTe grains, twin bands are seen (see for example figure 6.5d).

Such defects are common in bulk CdTe [8–10]. While coherent twin boundaries are not strongly electrically active, random grain boundaries orientated such that the photo-current must cross them, might be expected to have a deleterious effect on PV performance [11].

Figure 6.5c shows a high magnification ($\times 150,000$) image of the interface between the back surface of the CdTe and the Au contact. Small voids are clearly observed along this interface. This is unusual, as previously [12] it has been assumed that such voids are a consequence of a nitro-phosphoric (NP) acid etch, commonly used prior to contact CSS deposited CdTe films but not used in the case of these sputtered devices. Furthermore, a very thin dark layer is observable at the interface indicating the presence of some other phase. In the case of NP etched surfaces prepared for contacting, enrichment of Te has been demonstrated. For this material however, the interface phase has not been identified. Further characterisation, via techniques such energy dispersive X-ray analysis (EDX), Auger electron spectroscopy (AES) or X-ray photoemission spectroscopy (XPS), is required to confirm this hypothesis. An alternative hypothesis is that a Cd-O phase may form at the back surface when annealing in air [13].

Another high magnification image, this time of the CdTe/CdS/ZnO interfaces is shown in figure 6.5d. The grain structure of the CdS consists of grains typically $\sim 200 - 400$ nm in width and spanning the thickness of the film. Again, significant re-crystallisation has occurred in this layer following the post-deposition treatment, the grain sizes in as-grown sputtered films being generally too small to determine using SEM. Significant voids are present throughout the CdS layer and are thought to arise from the re-crystallisation process which is likely to involve a densification of the film. Note that while in some cases these voids span the entire width of the CdS layer, at no point along the CdTe/CdS interface does the CdTe layer break through and come into contact with the underlying ZnO layer. Therefore it can be assumed that such voids are passive and do not short the devices. This is consistent with high efficiency CSS devices in which voids within the CdS layer are even more numerous than those that are fully sputtered [12].

6.2.3 Discussion of prototype devices

It has been shown that the all-sputtered prototype device fabrication process is capable of producing excellent device results for the CdTe/CdS/ZnO/ITO/glass structure, with

efficiencies as high as 12.4%. The results presented from this initial sample set provide a baseline from which further optimisation and device design improvements may be made.

It was recognised that the process is particularly sensitive to the $CdCl_2$ annealing step. This can lead to profound differences over a 5×5 cm^2 plate, leading to three separate populations of cell performances as described above. The sensitivity is considered unlikely to be the result from variation in the $CdCl_2$ thickness, since an excess thickness (~ 200 nm) is applied over the entirety of each plate. It is more likely that the differences arise from temperature non-uniformity within the tube furnace (an analytical treatment of the radial temperature distribution in tube furnaces is given in reference [14]).

The response of the CdTe films to $CdCl_2$ treatment is known to take the form of Cl in-diffusion, re-crystallisation and grain growth. Moutinho [15] has demonstrated that such metallurgical changes are accelerated in material having small grains and high strain. Since these are characteristics of as-grown sputtered CdTe films (typical grain size ~ 200 nm), extreme sensitivity to minor temperature variations is expected. Moreover, this degree of sensitivity is neither observed nor expected for CSS deposited material which has a significantly larger grain size [16, 17].

6.3   Further optimisation of prototype design

In the previous section, the initial deposition and post-deposition treatment parameters (e.g. film thicknesses, anneal times) were chosen according to insight given by the literature surrounding such devices (see section 3.3). While these parameters yielded a prototype device that has a good baseline efficiency, it is necessary to optimise each deposition parameter in order to improve the efficiencies further. In this section, the effect of changes in two process parameters are studied. Firstly, the effect of varying the sputtering pressure, in the range 5 - 20 mTorr, on the resultant crystal structure of as-grown CdTe films on glass substrates was investigated using XRD. Secondly the effect of changes in the CdTe sputter pressure and the duration of the $CdCl_2$ post-deposition treatment for completed device structures is investigated. These studies were performed with the aim of improving recrystallisation of the CdTe layer so that all sub-micron grains (see figure 6.5) are consumed by further growth of the surrounding grains and horizontal grain boundaries, which

156

are thought to contribute significantly to recombination [2, 18], are removed.

6.3.1 XRD of as-grown CdTe single films of glass as a function of Ar pressure

Figure 6.6a shows the XRD spectra measured for CdTe films deposited at pressures of 5, 10, 15 and 20 mTorr. Other deposition parameters, i.e. substrate temperature and RF power,
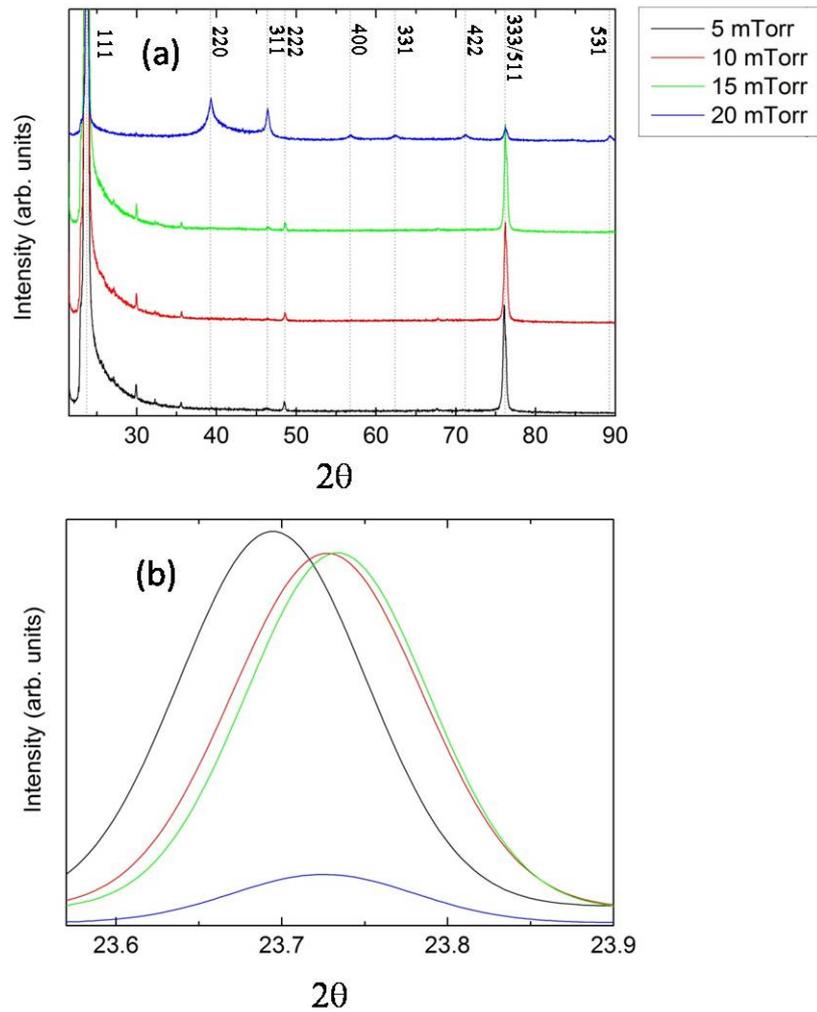

Figure 6.6: X-ray diffraction of as-grown CdTe layers deposited on glass substrates with varying chamber pressures. (a) For all pressures the (111) orientation dominates, however at 20 mTorr a more random orientation was achieved. (b) An increased shift in the (111) peak is observed as a function of increasing pressure corresponding to a reduction in compressive strain.

Table 6.2: Lattice parameter of sputtered CdTe film deposited at pressures in the range $5 - 20$ mTorr. Values of a were calculated from the (111) diffraction peak.

Ar pressure (mTorr)	(111) Peak pos. 2θ (°)	d (Å)	a (Å)
5	23.695	3.755	6.504
10	23.725	3.751	6.496
15	23.734	3.749	6.494
20	23.727	3.750	6.496
ref[a]	23.759	3.745	6.487

[a] Bulk value [19]

were consistent with those used in the initial baseline study. Over the range 5 - 15 mTorr the (111) cubic reflection is dominant indicating that the films have a highly orientated grain structure. Significant (333) Bragg peaks are also observed, the plane being parallel to the (111) plane, but this intensity might be contributed by the overlapping 511 reflection, the (511) plane being the twin orientation presented on a (111) surface when twinning is an inclined close packed plane. At 20 mTorr the structure of the film becomes more randomly orientated with increases in (220) and (221) being observed at the expense of the (111) peak. Nonetheless, the intensities of these peaks are still relatively small compared to the (111) reflection. For all spectra, no other phases were identified other than stochiometric CdTe having the zinc-blende structure.

Figure 6.6b shows how the position and intensities of the (111) peak changes with pressure (a Nelson-Riley plot was not possible in this instance owing to the small number of peaks available). The lattice parameter, a, was calculated for each film according equations 4.12 and 4.13. Table 6.2 shows that the lattice parameters of the sputtered films do not vary significantly as a function of pressure, the biggest change being a decrease from 6.504 Å to 6.496 Å between films sputtered at 5 and 10 mTorr. All films had lattice parameters larger than the bulk powder diffraction value of $a = 6.48$ Å[19], indicating that all the sputtered films are under compressive stress. It is likely that this compressive stress contributes significantly to the high degree of re-crystallisation observed following the post-deposition treatment process, it being shown previously by Moutinho [15] that such stresses have a

significant influence on the nucleation and development of the new CdTe grain structure.

6.3.2   Effects of CdTe sputter pressure and post-deposition treatment time on device results

The growth rate of CdTe on glass as a function of Ar pressure is shown in figure 6.7. This callibration curve was used to ensure that the CdTe thickness in subsequent devices was constant. The duration of the CdTe deposition was changed accordingly to achieve a film thickness of ~ 2 μm. A further four 10 cm^2 samples were fabricated with a layer structure: CdTe (2 μm)/CdS (100 nm)/ZnO (100 nm)/ITO (200 nm), the Ar pressure for the CdTe deposition being varied in the range 5 - 20 mTorr. Each 10 cm^2 sample was then divided into sixteen 2.5 cm^2, twelve of which underwent CdCl$_2$ annealing for times ranging from 10 to 35 mins. The device results for the series, extracted from J-V curves, are shown in figure 6.8. Each point represents an average parameter value over 18 separate 5 mm^2 contacts and the error bars correspond to the standard deviation of this average.

Devices with CdTe layers deposited under 10 mTorr Ar gave rise to the best performances for anneal times $\leq$ 20 mins, the best efficiency of $7.1 \pm 1.1\%$ being observed for a 20 min anneal. At longer anneal times the efficiency decreased steadily due to signifi-
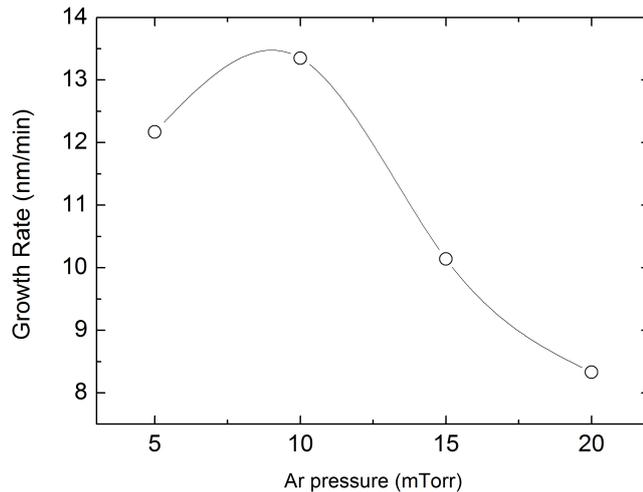

Figure 6.7: The growth rate of CdTe as a function of sputter pressure. The growth rate is maximised at 10 mTorr.
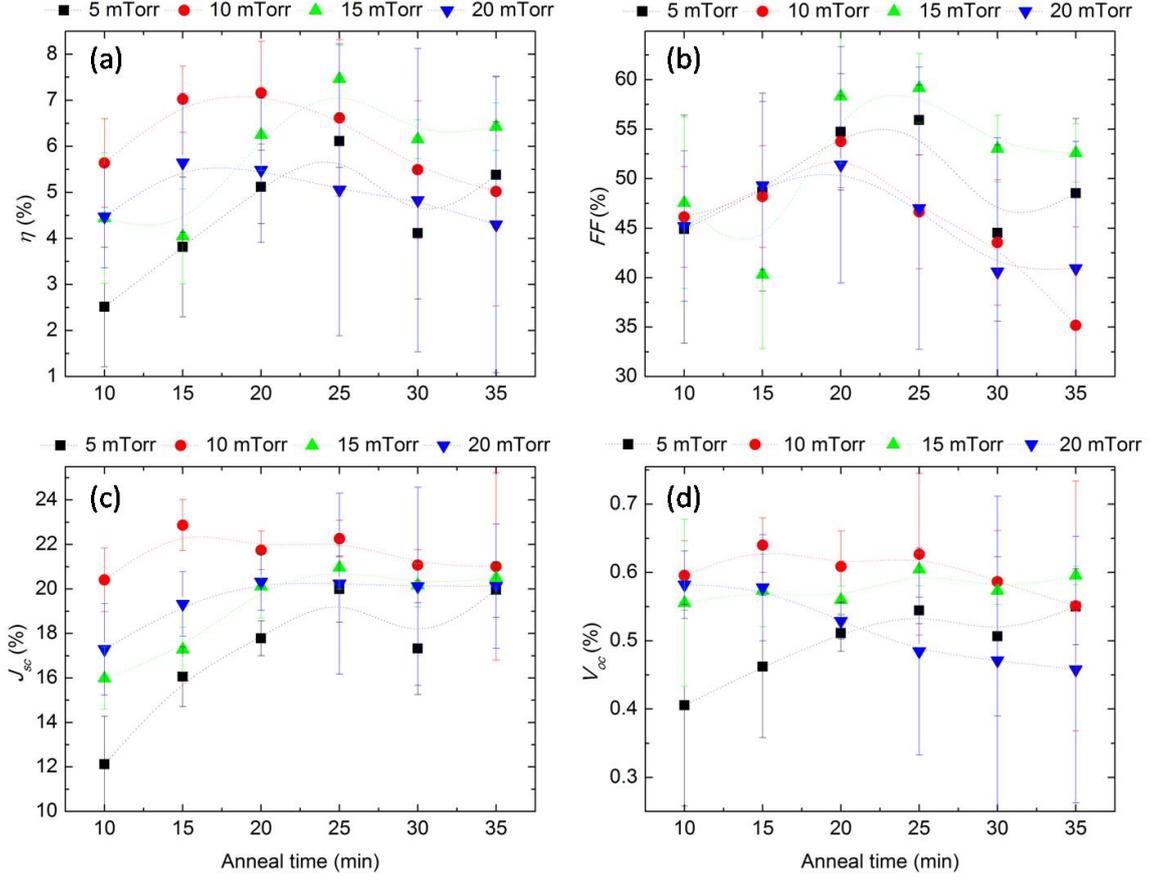
Figure 6.8: Device parameters as a function of both CdCl$_2$ anneal time and sputter pressure. Each point represents the average value taken from a set of 9 5 $\times$ 5 mm^2 contacts on a 2.5 cm^2 sample.

cant reductions in the fill factor, despite maintaining steady values for the J_{SC} and V_{OC}. At longer anneal times, the device with a CdTe film deposited at 15 mTorr achieved the best performances due to improved fill factor values ($> 55\%$). Indeed, the highest quality devices were achieved for CdTe deposited at 15 mTorr and annealed for 25 mins.

The performance for all devices with CdTe films deposited at 5 mTorr were relatively poor (i.e. $\leq 5\%$) over all anneal times. This slightly lower than the results from the original prototype design ($\eta = 8.6 \pm 2.2$) , in which a 5 mTorr deposition pressure was also used. The change in performance between the separate series may be explained by the installation of new ZnO and CdS targets, from which the optimal deposition parameters may have been different. Despite this, the results from the second series show that a 5 mTorr Ar pressure used for the deposition of CdTe is far from optimal and that the use of

higher pressures. i.e. 10 or 15 mTorr, can generate higher device efficiencies.

6.3.3 Further device characterisation

The following subsection is concerned with a deeper investigation of the electrical behaviour of a single contact for a device sputtered under 10 mTorr of Ar and annealed for 20 mins, i.e. one of the best devices from the study described above (see figure 6.8). The contact was investigated using J-V, EQE, J-V-T, C-V, EBIC and TEM techniques. The aim of applying such a wide range of techniques is to build a deeper understanding of the factors that affect the performance of fully sputtered devices. Such an understanding will provide insight into how the devices can be optimised further.

EQE and J-V

Figure 6.9a shows the EQE curve measured for the contact. Again, due to difficulties in callibrating the intensity of the spectra to absolute values, the magnitude of the EQE signal cannot be compared to other devices and is measured on an arbitrary scale. The shape of the curve however is indicative of device performance. The 'top-hat' shape of the EQE curve is indicative of a fully formed junction at the CdTe/CdS interface. A comparison of the EQE curve with that of an optimised device from the previous prototype study (section 6.2) shows that there is an increased response at wavelengths below the CdS band gap (i.e
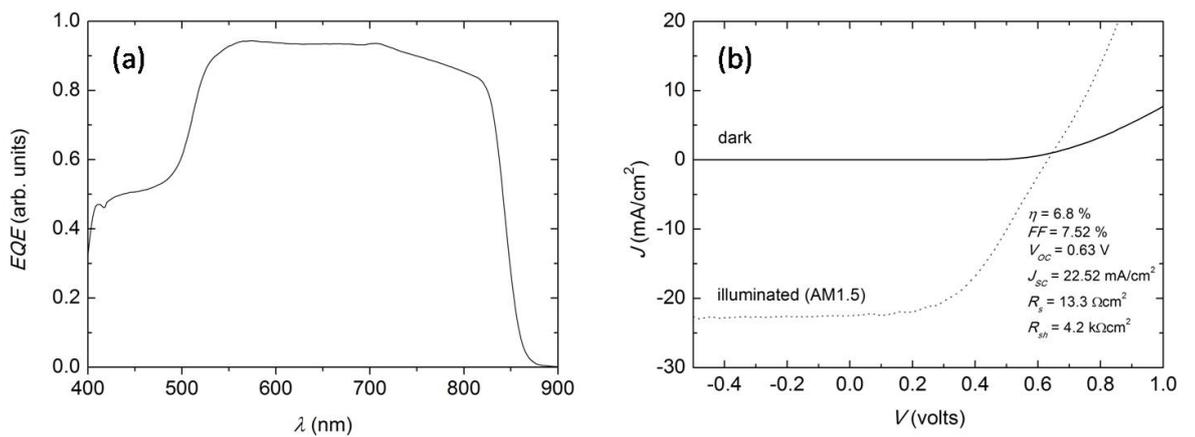

Figure 6.9: EQE and J-V curves for a typical device ($\eta = 6.8\%$) sputtered in a 10 mTorr Ar pressure and treated for 20 mins.

$\lambda < 500$ nm) for this device. This is expected as the CdS in the second set of devices was thinned from 200 to 100 nm. The effect of CdS thickness and the potential for improving device performance, due to an improved blue response, is explored in detail in Chapter 7.

The dark and illuminated J-V curves are shown in figure 6.9b. The working device parameters were extracted from the illuminated data and were: $\eta = 6.8\%$, $FF = 47.52\%$, $V_{OC} = 0.63$ V, $J_{SC} = 22.52$ mA/cm^{-2}. There are some key differences between these values and those extracted for the optimised cells in the prototype study. Clearly, the efficiency of the device is lower and this was generally true for all devices within the second study. This reduction in efficiency was a consequence of both lower FF and V_{OC} values. It is believed that the decrease in FF was caused by an increase, by almost $\times 2$, in the series resistance, R_s, from ~ 7 Ωcm^2 to ~ 13 Ωcm^2. The result was to make the slope of the J-V curve at positive bias more shallow and reduce the 'squareness' of the full J-V response. This increase in the series resistance is attributed solely to changes in the ITO layer. While the same deposition conditions were used for the ITO layer in both device series, it is common for the resultant sheet resistance to increase on a run to run basis. This increase is caused by a drift in the calibration of the chamber's pressure gauge. It is difficult to determine the exact cause of the reduction in V_{OC} but it is most likely due to non-optimised CdCl$_2$ treatment conditions. While, the efficiency of the devices were optimised with respect to treatment time it is expected that the variation in treatment temperature is important for further optimisation.

Compaan has demonstrated [7] that it possible to achieve devices with efficiencies greater then 14% using an all-sputtered process. Compared to the device parameters reported above, Compaan's devices have significantly higher V_{OC}s (> 800 mV) and fill factors ($> 70\%$). The J$_{SC}$s however are similar, having values of ~ 23 mA/cm^{-2}.

Dark J-V-T and C-V characteristics

To determine the nature of the electrical transport mechanism across the junction of the device dark J-V measurements were made as a function of temperature over the range 120 - 330 K. Figure 6.10 shows the forward bias results of the study with the current plotted on a log scale. The diode ideality factor of, A, and the reverse recombination current, I_0, can be estimated for each dark J-V curve making the following approximation to the Shockley

equation (equation 3.9),

$$I = I_0 \left[\exp\left(\frac{qV}{Ak_BT} \right) - 1 \right] \approx I_0 \exp\left(\frac{qV}{Ak_BT} \right) \tag{6.1}$$

Note that this equation is expressed in terms of the current I not the current density J. The use of I is simply a consequence of the experimental set-up. Equation 6.1 can be re-written as

$$\ln I = \ln I_0 + \frac{qV}{Ak_BT} \tag{6.2}$$

Therefore, it was possible to extract values of A from the gradients of the linear parts of the J-V curves and I_0 from the points at which the curves intercepted the x-axis at $V = 0$. The resultant plots of A and I_0 as a function of $1000/T$ are shown in figure 6.11. Both plots indicate that there are two distinct regions in temperature where the behaviour transport mechanisms are different. At temperatures > 250 K the ideality factor has a value of $A \sim 1.6$ and remains temperature independent up to 330 K. This behaviour, and also the result that $lnJ_0 \propto 1/T$ over this region, is indicative of recombination in the depletion region of the device due to traps located, in energy, at the centre of the CdTe band gap (i.e. $\sim E_d/2$) [20, 21]. For this behaviour, known as Shockley-Read-Hall (SRH) recombination [22, 23], the reverse saturation current may be expressed as

$$I_0 = I_{00} \exp \frac{\Delta E}{Ak_BT} \tag{6.3}$$

where I_{00} as a constant and ΔE is the activation energy which is related to the built in potential, V_{bi}, according to

$$A\Delta E = V_{bi} \tag{6.4}$$

By considering the gradient of the log plot of I_0 versus $1000/T$. A value of $\Delta E = 0.713$ eV was extracted and from this a value of $V_{bi} = 1.14$ eV was calculated. This value is similar to, but slightly smaller than, the value of $V_{bi} = 1.2$ eV deduced from the difference between CdS and CdTe work functions [24]. At temperatures below 250 K the value of A varies linearly with respect to $1/T$, increasing with decreasing temperature. This behaviour is indicative of current transport that is dominated by multi-step tunnelling through the depletion region via a uniform distribution of trap states [25]. Similar J-V-T behaviour is observed by Das and Miller [26] who report a value of $A\Delta E = 1.18$ eV.
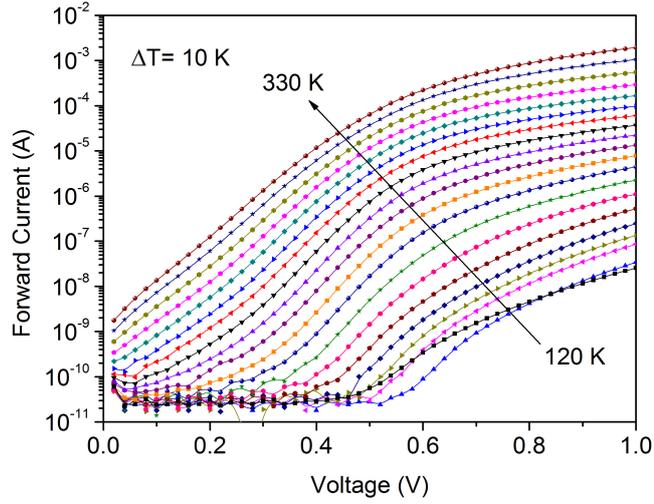
Figure 6.10: Dark I-V-T characteristics of a device with efficiency $\eta = 7$ %.
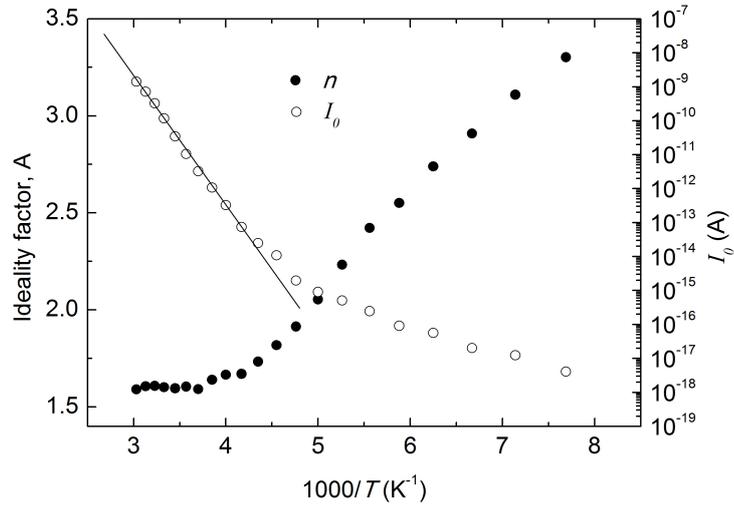
Figure 6.11: The characteristics of the diode quality factor A and reverse saturation current I_0 as a function of $1000/T$, as derived from the data in figure 6.10

Figure 6.12a shows a capacitance-voltage (C-V) curve measured for the contact at a frequency of 150 kHz. The shape of the curve shows a typical response for a p-n junction except for an additional feature in the region of 0.5 - 0.6 V. This extra bump in the C-V curve may be explained by an additional capacitance associated with a second junction located at the Au/CdTe interface [27]. From this it is immediately established that despite the device having a well-behaved J-V curve, the contact between the CdTe and Au is

164
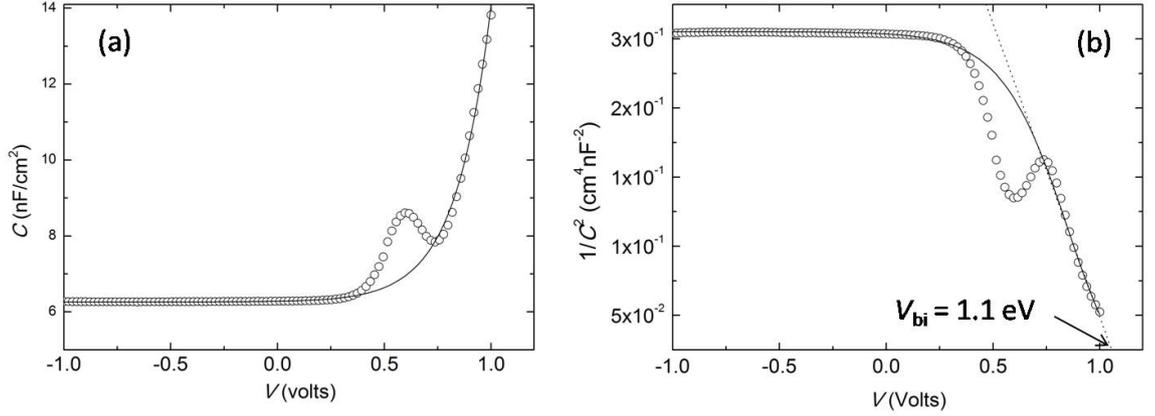
Figure 6.12: Plots of (a) C vs V and (b) $1/C^2$ vs V for data taken at room temperature and a frequency of 150 kHz.

non-ohmic. The corresponding $1/C^2$ vs V plot is shown in 6.12b. At reverse bias the flat plateau indicates that the CdTe layer is fully depleted (i.e. the junction is as wide as the film is thick). The solid line in the figure shows the expected response of the junction minus the effect of the back contact capacitance. It is possible to estimate a value for the dopant concentration of the CdTe film of $N_A \sim 4 \times 10^{14}$ cm^{-3} according to equation 3.8. This value is consistent with that reported by Sites [28, 29] and Ringel [30] for CdTe solar cells. Furthermore an independent value of $V_{bi} = 1.11$ eV can be estimated from the extrapolation of the line to the V axis of the graph. This value agrees with other reported values that were calculated using the same method [26, 31].

EBIC

EBIC measurements were performed on the same contact on which the previous electrical measurement were made. Figure 6.13a shows a secondary electron image of the cell cross section prepared by the FIB method. Figure 6.13b shows the same image but with the EBIC signal superimposed. The bright band of signal indicates the location of the cell's depletion region in which e-h pairs are generated following the excitation from the incident electron beam. It is clear that the location of the depletion region is deep within the CdTe layer and not at the CdTe/CdS interface which suggests that the cell's EQE and J-V spectra should conform to that expected for a buried junction, i.e. a strong peak in
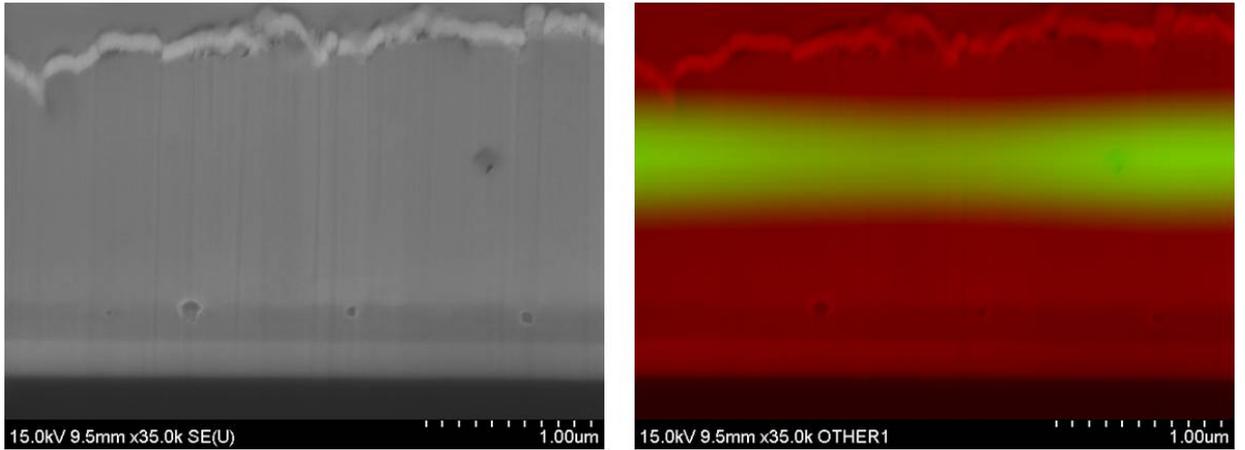
Figure 6.13: FIB prepared cross-sections of a $\eta = 7$ % contact. (a) Secondary electron image, (b) Superimposed EBIC signal on SE image.

EQE close to the CdTe band gap but a reduced response at wavelengths below 700 nm (for example see the under-treated device response in figure 6.4) and a much reduced J_{SC}. However, this is clearly contrary to actual EQE and J-V measurements (figure 6.9).

The location of the active junction must therefore vary over the area of a single 5 mm × 5 mm contact. The overall performance of the device must result from a mixture of fully formed (i.e. at the CdTe/CdS interface) and buried junction behaviour. This would explain the observed 'good' EQE and J-V responses but also explain reductions in the device V_{OC} compared to the best contacts of the previous study. Localised regions in which the junction is buried suggests that the post-deposition treatment conditions are not optimal and that the devices are partially under-treated.

TEM

From the same contact a cross-section was prepared for TEM imaging using the FIB and Omniprobe system (described in section 4.4.4). Figure 6.14a shows the full cross-section and again, as in figure 6.5, the layer structure is distinctly visible. Estimates made for each of the layer thicknesses were: CdTe (1.7±0.1 μm)/CdS (106±8 nm)/ZnO (120±5 nm)/ITO (240 ± 10 nm). Again, the CdTe film is seen to be composed of two distinct populations of grains, one possessing a grain size in the range 0.5 - 1 μm and the other < 500nm. Furthermore, the larger grains are generally located towards the back surface of the film while the smaller grains are located towards the CdTe/CdS interface. This suggests that,

166
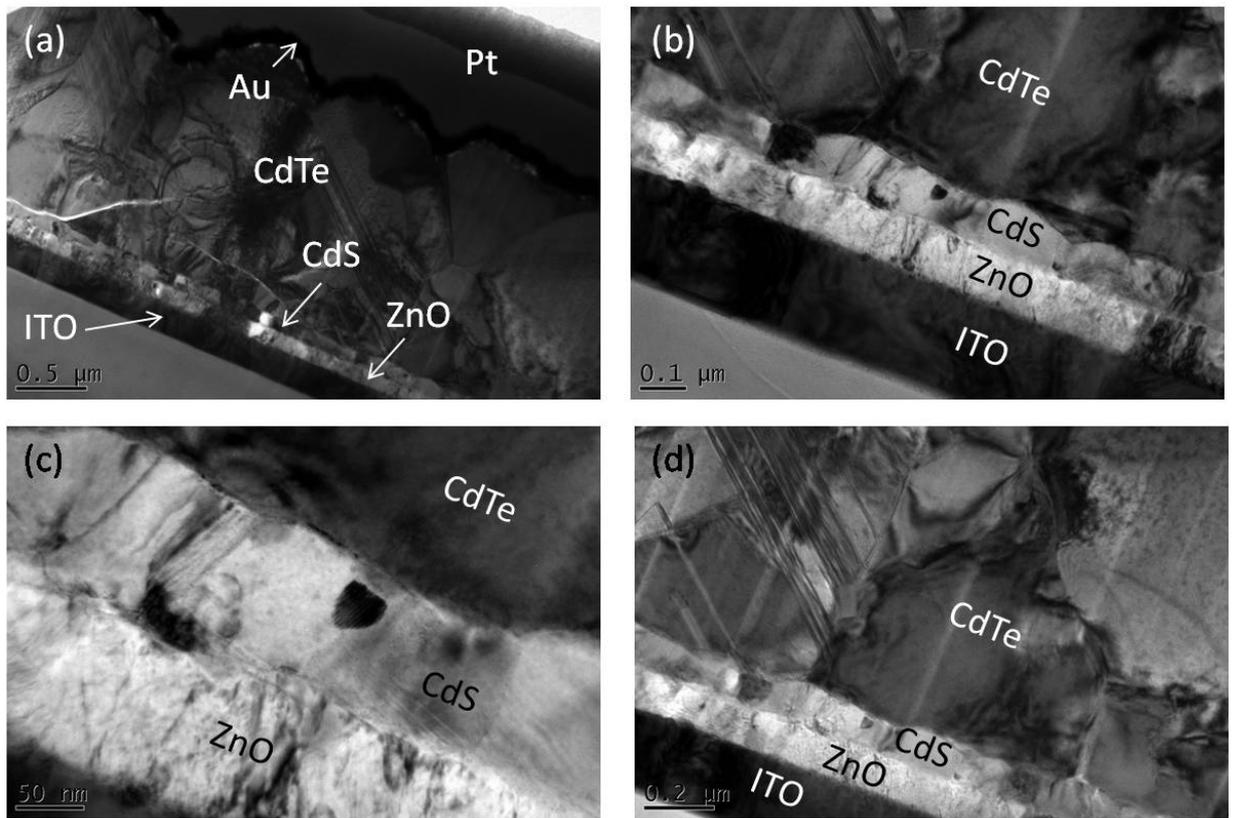
Figure 6.14: Transmission electron microscope images of the same $\eta = 7$ % device contact shown in figure 6.13. (a) shows the full cross-section and (b) highlights the re-crystallisation of the CdS layer. (c) shows a high magnification image of the ZnO/CdS and CdS/CdTe interfaces. (d) shows an example of twinning within CdTe grains.

as previously stated, the post-deposition treatment is non-optimal. In the case of optimal treatment, further re-crystallisation and thus larger grain sizes, more comparable with the entire width of the film, are to be expected.

The re-crystallisation appears to propagate from the back surface towards the CdTe/CdS interface. It is widely believed that during recrystallisation doping occurs within the CdTe grains through the formation of Cl-V_{Cd} complexes [32, 33]. Therefore, in this case it is expected that the doping concentration is higher towards the back surface than the front. It may therefore be speculated that there is a p-p$^+$ junction formed between low and high doped regions within the CdTe film (i.e. a buried junction) in agreement with the EBIC measurements. Note that cracks and bend extinction contours within the CdTe film shown in figure 6.14a are likely to be a feature of the sample preparation method and not of

167

recrystallisation. Similarly the bright bands orientated normal to the interface are likely to be thickness artefacts remaining from FIB thinning.

Figure 6.14b and c show a higher magnification images of the CdTe/CdS/ZnO/ITO interfaces. Again, any variation in the diffraction contrast due to grain structure is not observed in the ITO and ZnO layers indicating that the grains are very small ($<$ 50 nm). The upper surfaces of the CdS is rougher that the lower and undulates with a periodicity of $100 - 200$ nm. Indeed, the film is made up of grains that are of this size in width and which span the whole film (i.e. $\sim$ 100 nm) in height. Figure 6.14d shows a higher magnification image of the CdTe layer. Regions of strong diffraction contrast are associated with orientation, e.g. between grains and at twin boundaries. In this sample the grain boundaries appear to be particularly disrupted, with the complex contrast arising from residual strain or perhaps dislocations decorating the boundaries. Recently it has been demonstrated that for sputtered CdTe solar cells it is the grain boundaries rather than the twins that make a deleterious contribution to device performance [11].

6.4   Conclusion and future Work

A fully sputtered CdTe solar cell fabrication process has been established that generates devices with an average efficiency of $8.6 \pm 2.2\%$ and a maximum efficiency of 12.4% which is comparable to the current record for such devices of 14.5% [4]. The use of RF sputtering enables excellent uniformity to be achieved over a 10 cm^2 area and provides high reproducibility for a set of consecutive runs. The technique also affords a high degree of control over growth rates and the resultant layer thicknesses, particularly in comparison to close space sublimation (CSS) which is commonly used in the deposition of CdTe layer for such devices. The prototype design of the fully sputtered device provides a good platform from which a further optimisation of the device efficiency can be achieved.

The spread of device performance for the repeated fabrication of the prototype structure, and the identification of three separate populations (under-treated, over-treated and optimised) of performance, is attributed solely to variations in the CdCl$_2$ post-deposition treatment. The key limitation of the treatment, which is highly sensitive to changes in temperature, is the temperature non-uniformity of approximately $\pm10°$C over a 2.5 cm^2

sample associated with the use of a tube furnace [14]. Further optimisation of the post-treatment parameters, i.e. anneal temperature and time, will therefore be difficult unless the uniformity of the treatment can be improved. This improvement may be achieved through use of a different heating geometry, e.g. a large muffle furnace instead of a tube furnace, in which the temperature gradient across the sample is uniform.

A further suggestion for a change to post-deposition treatment would be to eliminate the use of $CdCl_2$ altogether. Romeo *et.al* [34, 35] have shown that it is possible to achieve device efficiencies upwards of 15% without $CdCl_2$ and instead through the use of a Cl containing gas (a freon) during annealing. The potential for such a treatment is highly significant as it is likely to reduce the sensitivity to temperature. Furthermore it eliminates the need for $CdCl_2$, which is highly toxic. However, the freon process does involve the use of a high flow of a chloro/fluorocarbon (CFC) gas, the manufacture of which are being phased out due to their contribution to ozone depletion [36]. The volume of gas used may be greatly reduced by incorporating a small partial pressure during sputter deposition and the decomposition of the gas within the plasma during film growth may be expected to generate a uniform distribution of Cl within the CdTe layer. The subsequent anneal (at atmospheric pressure) is likely to generate a similar recrystallisation within the film. Also, the uniform distribution of Cl is likely to ensure that the doping level throughout the film is constant and the device junction forms at the CdTe/CdS interface instead of being buried within the CdTe layer. This route should be investigated experimentally.

The investigation, via XRD, into the crystallographic structure of as-grown CdTe films deposited on glass substrates shows that the lattice parameter, a, of the sputtered material is increased relative to that of bulk and powder samples and indicates compressional strain within the film. It is believed that such strains are responsible for the high degree of recrystallisation observed following post-deposition treatment, whereby the grain size of the CdTe film increases from < 50 nm to as much as 1 μm. The variation of the Ar pressure, in the range 5 - 20 mTorr, used for the deposition of CdTe is not thought to have a significant impact on the level of strain within the layer but it is shown that the best device performances are achieved when a 10 - 15 mTorr pressure is used.

Another route to improved device performance, other than changes to the post deposition treatment, must include investigations into the effect of each of the constituent layer

thicknesses. In particular, it is likely that changes to the ZnO and CdS layers will generate considerable changes in both the electrical and optical response of the devices. Whether these changes have a positive or negative effect on device performance needs to be established. Chapter 7 describes a method for the calculation of the theoretical optical gains that may be achieved by manipulating the ZnO and CdS layer thicknesses. Inevitably however, a full understanding of the effect that ZnO and CdS thickness has on device performance will come from the fabrication and characterisation of real devices. Such a study, involving the making of many samples, could potentially be very time consuming and risks being distorted by inconsistencies in the processing of each individual sample. A solution to this is the design of combinatorial experiments in which the size of the sample set can be greatly reduced. Figure 6.15 shows the thickness profiles of ZnO and CdS films over the surface of a 10 cm^2 substrate that arise when the rotation is turned off during growth.

A wide distribution of film thicknesses, in the range 10-100 nm for ZnO and 20-200 nm for CdS, mean that the incorporation of such wedge shaped profiles into a 10 cm^2 sample will permit the resultant device performance as a function of both ZnO and CdS thickness. Figure 6.16 shows the potential ZnO/CdS combinations that may be achieved, over a 10 cm^2 area, by overlapping the two profiles. Such an experiment would reduce the size of the experiment to the growth of a single sample, thus eliminating any discrepancies in
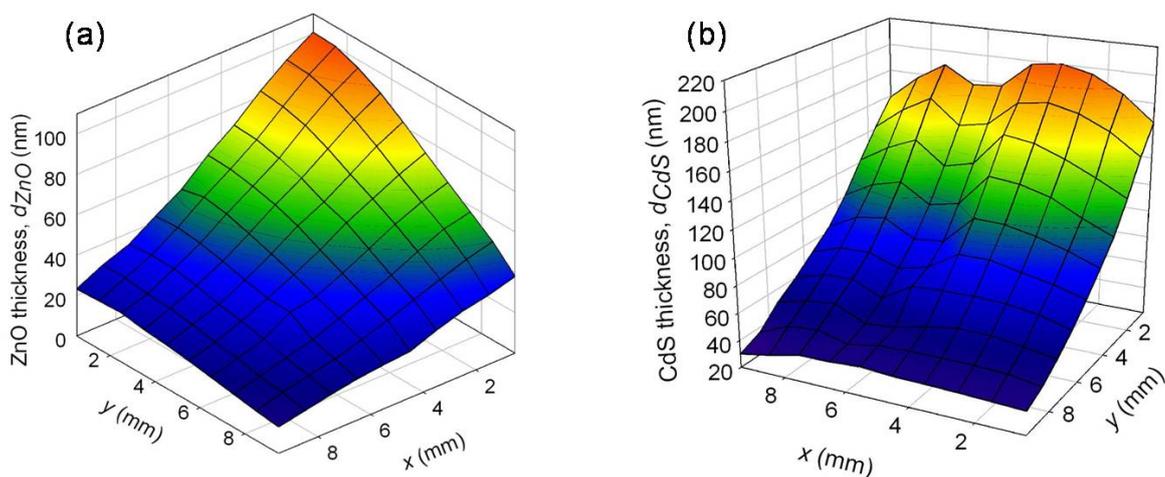
Figure 6.15: Thickness profiles of as-deposited layers of (a) ZnO and (b) CdS on glass substrates (deposited with no substrate rotation). The profiles were determined according to optical method described in Chapter 7.
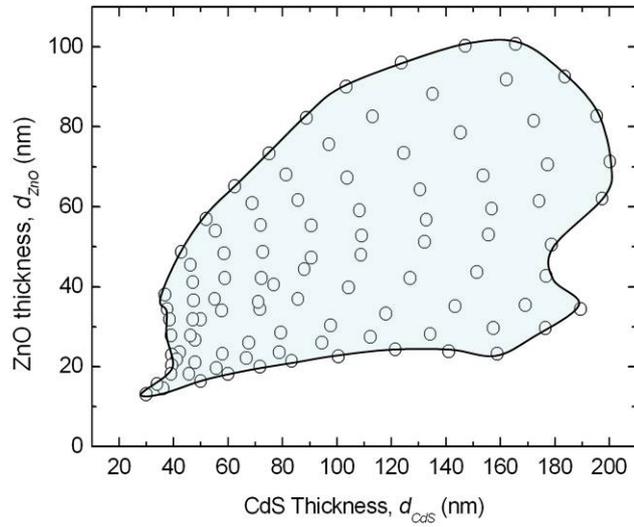
Figure 6.16: Potential range of ZnO/CdS thickness combinations achievable by overlaying the two profiles shown in figure 6.15.
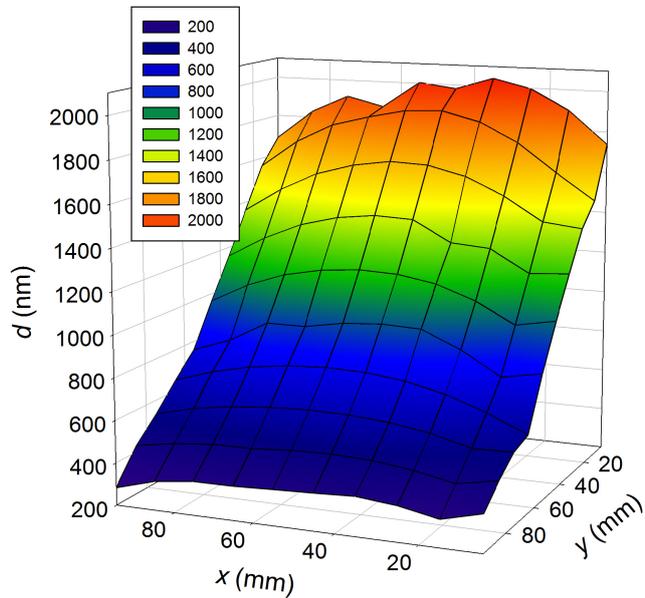
Figure 6.17: Thickness profile of an as-grown CdTe film on glass, determined by the automated SP method (see section 4.3.2).

the results associated with run to run consistancies within a multi-sample set. Note that this combinatorial approach depends critically on the uniformity of the post-deposition treatment.

A similar combinatorial method could be implemented to investigate the effect of the CdTe film thickness on device performance. Figure 6.17 shows that by turning the sub-

strate rotation off during CdTe depostition, a wide spread of thicknesses (0.3 - 2 μm) are achievable within a single sample. Such an experiment would be of particular interest to determine the minimum CdTe thickness that can be used while maintaining good device performance. This could potentially improve the sustainability of CdTe solar cells with respect to the current scarcity of tellurium.

6.5 References

[1] K. Durose, P. Edwards, D. Halliday. *Journal of Crystal Growth* **197**, 733 (1999).

[2] K. Durose, D. Boyle, A. Abken, C. J. Ottley, P. Nollet, S. Degrave, M. Burgelman, R. Wendt, J. Beier, D. Bonnet. *Physica Status Solidi B: Basic Research* **229**, 1055 (2002).

[3] N. Romeo, A. Bosio, V. Canevari, A. Podestà. *Solar Energy* **100**, 795 (2004).

[4] A. Gupta, A. Compaan. *Applied Physics Letters* **85**, 684 (2004).

[5] A. Compaan, A. Gupta, S. Lee, S. Wang, J. Drayton. *Solar Energy* **77**, 815 (2004).

[6] A. Gupta, V. Parikh, A. Compaan. *Solar Energy Materials and Solar Cells* **90**, 2263 (2006).

[7] V. Plotnikov, C. A. *Mater. Res. Soc. Symp. Proc.* **1012**, 431 (2007).

[8] K. Durose, G. J. Russell, J. Woods. *J. Cryst. Growth* **72**, 85 (1985).

[9] K. Durose, G. J. Russell. *J. Cryst. Growth* **101**, 246 (1990).

[10] K. Durose, A. J. W. Yates, A. Szczerbakow, J. Domagala, Z. Golacki, K. Swiatek. *J. Phys. D. App. Phys.* **35**, 1997 (2002).

[11] M. M. Nowell, M. A. Scarpulla, A. D. Compaan, X. Liu, P. N. R., D. Kwon, K. A. Wieland. *IEEE PVSEC 2011* (2011).

[12] J. Major, L. Bowen, K. Durose Article in Press in *Prog.Photovoltaics*, (2011), doi: 10.1002/pip.1164.

[13] D. W. Niles, D. Water, D. Rose. *App. Surf. Sci.* **136**, 221 (1998).

[14] A. Szczerbakow, K. Durose. *Prog. Cryst. Growth Ch.* **51**, 81 (2005).

[15] H. R. Moutinho, M. M. Al-Jassim, D. H. Levi, P. C. Dippo, L. Kamerski. *J. Vac. Sci. Technol. A* **16**, 1251 (1997).

[16] J. Major, Y. Proskuryakov, K. Durose, S. Green. *Thin Solid Films* **515**, 5828 (2007).

[17] J. D. Major. *CdTe Solar Cells: Growth Phenomena and Device Performance.* Ph.D. thesis, Durham University (2008).

[18] R. W. Birkmire, E. Eser. *Ann. Rev. Mater. Sci.* **27**, 625 (1997).

[19] N. K. Abrikosov, V. B. Banikina, L. V. Poretskaya, L. E. Shelimova, E. V. Skudnova. *Semiconducting II-VI, IV-VI and, V-VI Compounds.* Plenum, New York (1969).

[20] K. M. Mitchell. *Evaluation of the CdS-CdTe Heterojunction Solar Cell.* Garland Publishing Inc., New York (1979).

[21] M. K. Al Turkestani. Ph.D. thesis, Durham University (2010).

[22] W. Shockley, W. T. Read. *Phys. Rev.* **87**, 835 (1952).

[23] R. N. Hall. *Phys. Rev.* **87**, 387 (1952).

[24] K. W. Mitchell, A. L. Fahrenbruch, R. H. Bube. *J. Appl. Phys.* **48**, 4365 (1977).

[25] A. R. Riben, D. L. Feucht. *Int. J. Electron.* **20**, 583 (1966).

[26] S. K. Das, G. C. Morris. *Sol. Energy Mater. Sol. Cells* **305**, 305 (1993).

[27] A. Niemegeers, M. Brurgelman. *J. Appl. Phys.* **81**, 2881 (1997).

[28] J. Sites. Technical report, NREL (1999). SR-520-26315.

[29] C. R. Corwine, A. O. Pudov, M. Gloeckler, S. H. Demtsu, J. Sites. *Sol. Energy Mater. Sol. Cells* **82**, 481 (2004).

[30] S. A. Ringel, A. W. Smith, M. H. MacDoughal, A. Rohatgi. *J. Appl. Phys.* **70**, 881 (1991).

[31] P. Burgelman, P. Nollet, S. Degrave. *App. Phys. A* **69**, 149 (1999).

[32] K. J. Price. *Mater. Res. Soc Symp. Proc.* **668**, H1.7.1 (2001).

[33] M. Emziane, K. Durose, N. Romeo, A. Bosio, D. Halliday. *Thin Solid Films* **480**, 377 (2005).

[34] S. Mazzamuto, L. Vaillant, A. Bosio, N. Romeo, N. Armani, G. Salviati. *Thin Solid Films* 7079–7083 (2008).

[35] L. Vaillant, N. Armani, L. Nasi, G. Salviati, A. Bosio, S. Mazzamuto, N. Romeo. *Thin Solid Films* **516**, 7075 (2008).

[36] *Handbook for the Montreal Protocol on Substances that Deplete the Ozone Layer* (2006, 7th Ed.).
http://ozone.unep.org/Publications/MP␣Handbook/. Accessed Aug 2011.

Chapter 7

Optical Modelling of Multi-layer Structures

7.1 Introduction

In general, the development of thin-film PV device structures is progressed by an empirical approach. Any new ideas, such as the inclusion of an additional layer or processing step, are usually tested by the experimental variation of a single parameter (e.g. film thickness or substrate temperature) and involves the fabrication of large sample sets in order to determine the optimum result. While such an approach can be very successful, it can also be extremely time consuming. To increase the speed with which optimum device structures are realised, some form of modelling is required to predict the most promising configurations. It is also important that the results from subsequent experiments are fed back to the initial model in order to refine its ability to make accurate predictions.

A model that contains a complete theoretical understanding of the combined electrical, optical and chemical interactions between each of the layers within a finished device structure may prove impossible to achieve and by no means is this attempted here. Instead, this chapter focuses solely on the development of a model for the optical response of multi-layer structures based upon on the experimentally determined optical properties (namely n and κ) of each of the constituent layers. The key objective of the model is the maximisation of the integrated transmittance, $\tilde{T}$, calculated at the final interface of any multi-layer structure. For the case of a CdTe solar cell this interface is always that between

the CdS window and CdTe absorber layers.

Section 7.2 describes all of the necessary theory required to build such a model for multi-layer structures on soda-lime glass substrates and section 7.3 describes the experimental details regarding film deposition, the optical analysis performed on single films and the implementation of the multi-layer model. Section 7.4 presents the results of optical analysis performed on single films and 7.5 describes several scenarios in which the subsequent multi-layer model is tested. In section 7.6 the multi-layer model is used to determine the optimum CdTe device structure that maximises the amount of light transmitted into the CdTe absorber layer.

7.2 Optical theory of multi-layer assemblies

To predict the transmittance of a multi-layer stack of thin films a detailed knowledge of the interaction between incident light waves and each of the interfaces within the structure is required. Here, a summary of the key elements of such a theory is presented but for a full treatment the reader is referred to texts by *Macleod* [1] and *Heavens* [2].

In an isotropic medium, the electric field associated with a light wave propagating in the direction $\hat{\mathbf{x}}$ may be defined according to the following complex solution to Maxwell's equations

$$
\begin{aligned}
\mathbf{E} &= \mathcal{E}\exp[i\omega(t - x/v)]\hat{\mathbf{x}} \\
&= \mathcal{E}\exp[i(\omega t - \frac{2\pi\tilde{n}}{\lambda}x)]\hat{\mathbf{x}}
\end{aligned}
\tag{7.1}
$$

where $\mathcal{E}$ is the amplitude of the field, v is the speed of the wave in the medium, ω is the angular frequency of the wave (defined by $\omega = 2\pi\nu = 2\pi c/\lambda$) and $\tilde{n}$ is the complex refractive index of the medium, as defined in Chapter 2. A similar expression may also be derived for the magnetic field, $\mathbf{H}$, associated with such a wave. A further consideration of Maxwell's equations permits the relationship between the field vectors to be defined by

$$
\mathbf{H} = \mathcal{A}(\hat{\mathbf{x}} \times \mathbf{E})
\tag{7.2}
$$

where $\mathcal{A}$ is the *optical admittance* of the medium and is defined as

$$
\mathcal{A} = \frac{H}{E} = \tilde{n}\mathcal{Y}
\tag{7.3}
$$

where $\mathcal{Y} = 2.6544 \times 10^{-3} \ \Omega^{-1}$ is the admittance of free space. It shall be shown that the transmittance of a multi-layer structure can be calculated from the knowledge of $\mathcal{A}$ for each film within the structure.

An important consideration is the flow of energy associated with a propagating light wave and this can be defined by the Poynting vector [3]

$$\mathbf{P} = \mathbf{E} \times \mathbf{H} \tag{7.4}$$

where $\mathbf{P}$ represents the energy flow per unit area per second. The average energy flow, in the direction $\hat{\mathbf{x}}$ may then be written as

$$
\begin{aligned}
\bar{\mathbf{P}} &= \frac{1}{2}\Re(\mathbf{E} \times \mathbf{H}^*) \\
&= \frac{1}{2}\Re(\mathcal{A})EE^*\hat{\mathbf{x}}
\end{aligned} \tag{7.5}
$$

and the related scalar quantity, i.e. the magnitude of $\bar{\mathbf{P}}$, is known simply as the intensity of the wave

$$I = \frac{1}{2}\Re(\mathcal{A})EE^* \tag{7.6}$$

This definition of intensity is very useful and the consideration of the reflected and transmitted intensities of a wave on encountering an interface between two different media is the basis from which the transmittance of a full stack can be formulated.

Consider a beam of light propagating, at normal incidence, from a medium with optical admittance $\mathcal{A}_0$ into a medium with a different optical admittance $\mathcal{A}_1$. By applying the boundary condition that the tangential components of both the electric and magnetic vectors are continuous across the interface, the Fresnel reflection (r) and transmission (t) coefficients can be calculated as

$$r = \frac{\mathcal{A}_0 - \mathcal{A}_1}{\mathcal{A}_0 + \mathcal{A}_1} \tag{7.7}$$

$$t = \frac{2\mathcal{A}_0}{\mathcal{A}_0 + \mathcal{A}_1} \tag{7.8}$$

A further consideration of the net intensity of the beam on either sides of the interface in terms of the incident beam I_i, reflected beam I_r and transmitted beam I_t permits the definition of the reflectance R and transmittance T associated with the interface as

$$R = \frac{I_r}{I_i} = rr^* = \left(\frac{\mathcal{A}_0 - \mathcal{A}_1}{\mathcal{A}_0 + \mathcal{A}_1}\right)\left(\frac{\mathcal{A}_0 - \mathcal{A}_1}{\mathcal{A}_0 + \mathcal{A}_1}\right)^* \tag{7.9}$$

$$T = \frac{I_t}{I_i} = \frac{\Re(\mathcal{A}_1)}{\Re(\mathcal{A}_0)} tt^* = \frac{\Re(\mathcal{A}_0)\Re(\mathcal{A}_1)}{(\mathcal{A}_0 + \mathcal{A}_1)(\mathcal{A}_0 + \mathcal{A}_1)^*} \qquad (7.10)$$

The above expressions for T and R must now be extended to describe the interaction of an incident light beam with a thin-film. The term 'thin-film' typically describes a layer of material of thickness d which is smaller than the coherence length of the light. The calculation of R and T must therefore include the treatment of a second interface and the coherent interference effects that arise from successive reflections within the film. Figure 7.1 shows the two interfaces defined by a and b respectively. The relationship between the electric and magnetic field vectors at interfaces a and b can be expressed in matrix notation according to

$$\begin{bmatrix} E_a \\ H_a \end{bmatrix} = \begin{bmatrix} cos\delta & (isin\delta)/\mathcal{A}_1 \\ i\mathcal{A}sin\delta & cos\delta \end{bmatrix} \begin{bmatrix} E_b \\ H_b \end{bmatrix} \qquad (7.11)$$

where the parameter δ represents the difference in phase in the resultant beam between the two interfaces and is expressed as

$$\delta = \frac{2\pi\tilde{n}d}{\lambda} \qquad (7.12)$$

For a full derivation of the result given by equation 7.11, see ref [1], pp.32-34. The treatment of the thin-film described above can be reduced to the original single boundary problem if
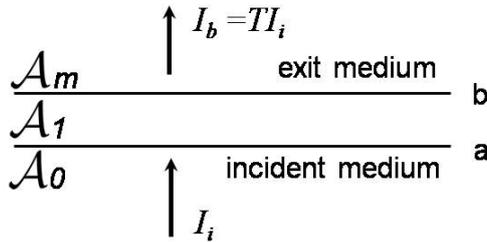

Figure 7.1: Terms used in describing transmittance through a thin film.
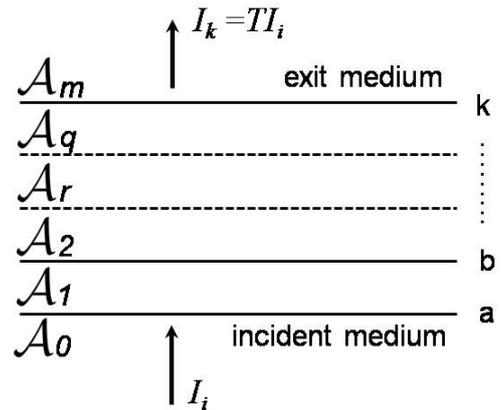
Figure 7.2: Transmittance through an assembly of q thin films

the assembly is re-defined in terms of a single optical admittance

$$Y = \frac{H_a}{E_a} \tag{7.13}$$

Then the reflectance R of the assembly can be re-expressed according to equations 7.9 and 7.10 by substituting $\mathcal{A}_1$ with Y. Furthermore, equation 7.11 can be re-written as

$$E_a \begin{bmatrix} 1 \\ Y \end{bmatrix} = \begin{bmatrix} cos\delta & (isin\delta)/\mathcal{A}_1 \\ i\mathcal{A}sin\delta & cos\delta \end{bmatrix} \begin{bmatrix} 1 \\ \mathcal{A}_m \end{bmatrix} E_b = \begin{bmatrix} B \\ C \end{bmatrix} E_b \tag{7.14}$$

where the assembly is defined by the characteristic matrix

$$\begin{bmatrix} B \\ C \end{bmatrix} \tag{7.15}$$

and clearly $Y = C/B$. The above result for a single thin-film can immediately be extended for a multi-layer structure consisting of q films, see figure 7.2, simply by describing the characteristic matrix as the product of matrices associated with each of the films, i.e.

$$\begin{bmatrix} B \\ C \end{bmatrix} = \left(\prod_{r=1}^{q} \begin{bmatrix} cos\delta_r & (isin\delta_r)/\mathcal{A}_r \\ i\mathcal{A}sin\delta_r & cos\delta_r \end{bmatrix} \right) \begin{bmatrix} 1 \\ \mathcal{A}_m \end{bmatrix} \tag{7.16}$$

where the subscript r denotes the film number and increases in order from 1 to q. The resultant reflectance of such an assembly can then be written as

$$\begin{aligned} R &= \left(\frac{\mathcal{A}_0 - Y}{\mathcal{A}_0 + Y} \right) \left(\frac{\mathcal{A}_0 - Y}{\mathcal{A}_0 + Y} \right)^* \\ &= \left(\frac{\mathcal{A}_0 B - C}{\mathcal{A}_0 B + C} \right) \left(\frac{\mathcal{A}_0 B - C}{\mathcal{A}_0 B + C} \right)^* \end{aligned} \tag{7.17}$$

The calculation of T involves a consideration of the intensity of the incident and exit beams. Firstly, consider the intensity of the exit beam that passes through the final interface, k, into the exit medium.

$$I_k = \frac{1}{2} \Re(\mathcal{A}_m) E_k E_k^* \tag{7.18}$$

This can be related to the intensity that passes through the first interface, a, according to

$$I_a = \frac{1}{2} E_a H_a^* = \frac{1}{2} \Re(BC^*) E_k E_k^* \tag{7.19}$$

180

and the incident intensity of the beam, prior to its entrance into the assembly, can be expressed as

$$I_i = \frac{I_a}{1 - R} = \frac{\Re(BC^*)E_k E_k^*}{2(1 - R)} \tag{7.20}$$

From equation 7.18 $(1 - R)$ can be written as

$$
\begin{aligned}
(1 - R) &= \frac{2\mathcal{A}_0(BC^* + B^*C)}{(\mathcal{A}_0 B + C)(\mathcal{A}_0 B + C)^*} \\
&= \frac{4\mathcal{A}_0 \Re(BC^*)}{(\mathcal{A}_0 B + C)(\mathcal{A}_0 B + C)^*}
\end{aligned} \tag{7.21}
$$

and so an expression for T can be obtained according to

$$T = \frac{I_k}{I_i} = \frac{4\mathcal{A}_0 \Re(\mathcal{A}_m)}{(\mathcal{A}_0 B + C)(\mathcal{A}_0 B + C)^*} \tag{7.22}$$

A final consideration must be made in the case of an incident medium that is non-infinite. This is clearly necessary as all real structures must be deposited on some relatively thick, yet finite substrate. This introduces another interface at the start of the assembly but because of the relative thickness of a typical substrate compared to a thin-film, any reflected component can be calculated without the need to consider the coherent interference from other interfaces. The above expressions for R and T in the case of a finite, non-absorbing substrate can therefore be augmented to read

$$R = \left(\frac{\mathcal{A}_0 - \mathcal{A}_s}{\mathcal{A}_0 + \mathcal{A}_s}\right)^2 \cdot \left(\frac{\mathcal{A}_s - Y}{\mathcal{A}_s + Y}\right)\left(\frac{\mathcal{A}_s - Y}{\mathcal{A}_s + Y}\right)^* \tag{7.23}$$

$$T = \frac{4\mathcal{A}_0 \mathcal{A}_s}{(\mathcal{A}_0 + \mathcal{A}_s)^2} \cdot \frac{4\mathcal{A}_0 \Re(\mathcal{A}_m)}{(\mathcal{A}_0 B + C)(\mathcal{A}_0 B + C)^*} \tag{7.24}$$

where the subscripts $\mathcal{A}_0$ and $\mathcal{A}_s$ now denote the optical admittances of air and the substrate respectively. This final expression for T describes the key parameter, the calculation of which will be the objective of the multi-layer model.

7.3 Methodology

7.3.1 Film deposition

Table 7.1 shows the RF magnetron sputtering deposition parameters for all the films investigated within this chapter. Successive deposition onto the same substrate of ITO, ZnO,

Table 7.1: Sputtering parameters for all films presented within this chapter

Film	T_{sub} (°C)	Power (W)	Ar Pressure (mTorr)
In_2O_3:Sn	400	60	1
ZnO	50	100	5
CdS	350	60	5 (+ 3% CHF_3)
CdTe	350	70	5
TiO_2	room temp.	300	5
SiO_2	room temp.	300	5

CdS and CdTe films constitute a full CdTe device structure. An undoped, highly resistive, ZnO films is incorporated between the ITO front contact and CdS window layer. The reasons for the use of such a layer, commonly referred to as a HRT (highly resistive and transparent) or simply 'buffer' layers, are still widely debated [4–7] but it is generally observed to permit the reduction of the CdS layer thickness while maintaining a stable V_{OC} and limiting the effect of pin-holes in the CdS layer.

A 5% partial pressure of CHF_3 was incorporated during the growth of CdS films. This was not an attempt to dope the CdS (as demonstrated for SnO_2 films in Chapter 5) but was used since CHF_3 has been shown to improve the resultant density of the film [7] and reduce to formation of pin-holes through to the underlying ZnO/ITO layers. All targets were pre-sputtered, for a minimum of 10 minutes prior to deposition in order to remove any dust or contaminants that had fallen onto the target surface during the intervening time between runs. Again, low-Fe soda-lime glass substrates (Pilkington OptiWhite^{TM}) were used throughout and were cleaned prior to deposition using a series of nylon brush scrubs and DI water/isopropanol rinses and finally a 10 min in-situ plasma etch.

7.3.2   Optical methods

The extraction of the optical characteristics, namely the dispersion properties, of single films was achieved via two distinct methods; one involving the fitting of data generated from ellipsometry measurements (SE), and the other based on the fitting of transmittance spectra determined via spectrophotometry (SP). Throughout discussions within this chap-

ter these two methods will be referred to as SE and SP respectively. The reader is referred to Chapter 4, section 4.3.2 for a full description of each method.

For both methods, effort was taken to ensure that the lowest MSE values were achieved while implementing the simplest possible model in each case. In general, it was always possible to achieve lower MSE values by adding more oscillators, but this increased the likelihood that the resultant fitted parameter set was non-unique and that the model did not represent a real physical system. Typically, a model was deemed to be reliable if an MSE value of $< 1 \times 10^{-3}$ was achieved although this was not always possible.

For theoretical multi-layer structures, transmittance spectra were calculated by implementing the theory described in section 7.2 within a FORTRAN90 program (see appendix B. The inputs of this program were composed of the relevant $n(\lambda)$ and $\kappa(\lambda)$ data, as extracted via the SE method, and the thickness of each of the films within the structure. The fitting of experimental transmittance curves, recorded from real multi-layer samples, was achieved using the SCOUT software and permitted the measurement of each of the constituent film thicknesses.

7.4 Extraction of dispersion data from single films

The analyses of ellipsometric and spectrophotometric spectra via the two methods is now presented for the films listed in table 7.1 and a library of optical behaviour, namely n and κ, for the materials is established.

Figure 7.3 a and b show the spectra of Ψ and Δ determined by ellipsometry for a bare glass substrate. The spectra are very simple and can be fitted easily with a B-spline model. While this model has no physical basis, the development and use of a model based upon the physical properties of bulk amorphous materials (i.e. glasses) was considered unnecessary to fit such a simple spectrum. The extracted n and k spectra and corresponding fit of the model to a transmittance spectrum are shown in figures 7.3 c and d. The analysis shows that there is some low level absorption ($\kappa \sim 0.1 \times 10^{-5}$) at wavelengths $\lambda > 600$ nm. However this absorption can be considered negligible and a non-absorbing substrate approximation can be maintained for use in the multi-layer model.

Figure 7.4 a and b show the spectra of Ψ and Δ determined for a thin-film of In_2O_3:Sn
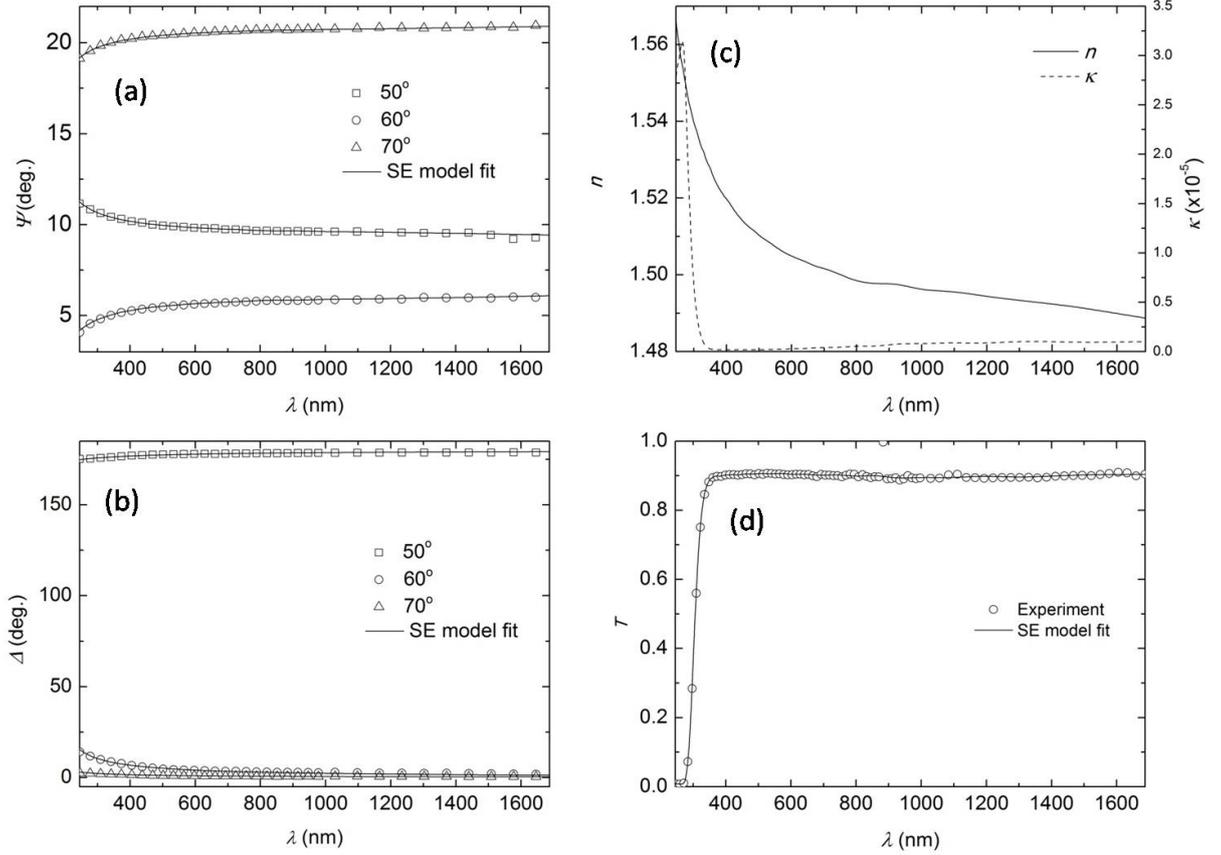
Figure 7.3: Ellipsometry of uncoated OptiWhite substrate (3.2 mm thick). (a) and (b) show the ellipsometric spectra of Ψ and Δ determined from the measurement and the corresponding fits achieved by the CompleteEASE$^{\text{TM}}$ (VASE) software according to a simple B-spline fit. (c) shows the dispersion of n and κ extracted from the software and (d) shows the fit to a transmittance spectra.

(ITO). An ellipsometric model based upon a single Lorentz oscillator and a Drude component identical to those described in Chapter 2 was used to fit the spectra. In this case however, it was not possible using the CompleEASE software to build into the model a component that adequately described the behaviour in the vicinity of the band gap. Nonetheless, figure 7.4 c shows that the model achieved a good fit to the transmittance spectra which is comparable to the fit achieved using the SP model. Accordingly, the resultant n and κ spectra from the separate SE and SP analyses differ only at wavelengths below 400 nm. Both methods permit the reliable determination of the material's optical properties over the range of wavelengths of interest in device design (400-850 nm). Furthermore,

table 7.2 shows that the electrical properties extracted from the Drude components from each of the methods agree very well, both with each other and experimentally determined values. This adds an extra degree of confidence to both approaches.

Figure 7.5 a and b shows the ellipsometric spectra obtained for an undoped ZnO film. A fit to the data was achieved using a "PSEMI-M0" model [8] based on the work of *Johs et. al* [9]. Within the CompleteEASE software no details of the functional form of this model are given and it is defined solely by a set of parameters. Of these parameters, the energy E_0, represents the critical point at which the onset of absorption occurs and clearly
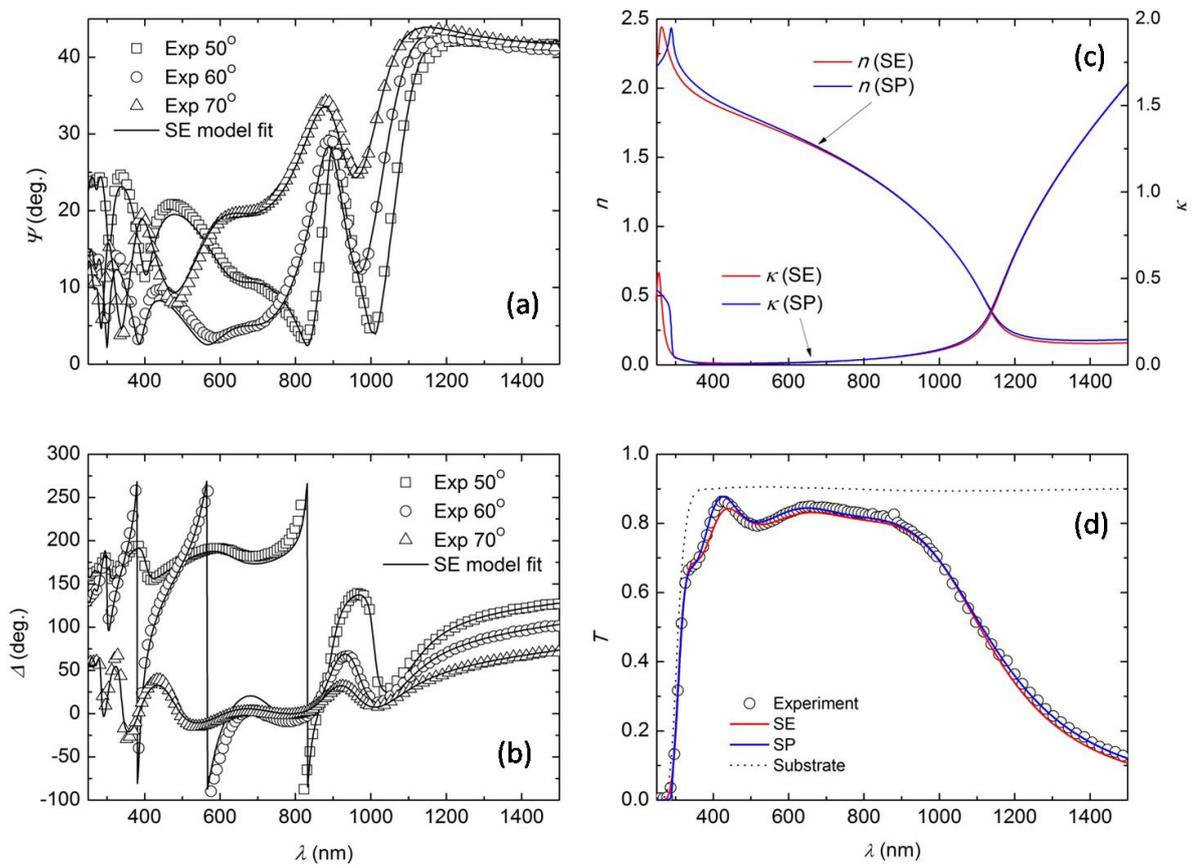
Figure 7.4: Ellipsometry of ITO film (115 nm) on OptiWhite glass substrate: (a) and (b) show the ellipsometric spectra and the corresponding fits achieved using the software. (c) A comparison is made between n and κ dispersion determined by both the standard model for dielectric permittivity (discussed in detail in Chapters 2 and 5) and the CompleteEASE software. (d) The corresponding model fits to an experimental transmittance spectra.

Table 7.2: A comparison between electrical properties of the ITO baseline sample determined by experiment and the SE and SP fits.

	Experiment	SE	SP
d (nm)	220 [a]	237	230
n_e ($\times 10^{21}$ cm^{-3})	1.20 [b]	1.3	1.2
μ_e (cm^{2}V^{-1}s^{-1})	43.0 [c]	42.4	40.0
ρ (Ω.cm)	1.21	1.17	1.23
m_e^*	–	0.4	0.4
E_G (eV)	–	–	4.27

[a] Surface profilometry measurement

[b] van der Pauw measurement

[c] Hall measurement

represents the direct band gap E_d of the material. In this way a band gap of $E_d = 3.33$ eV was determined by the ellipsometric fit. This value is significantly higher (+0.14 eV) than the value of 3.19 eV determined both by the SP fit and $(\alpha h\nu)^2$ vs E plots. Nonetheless, both SE and SP methods determine very similar n and κ spectra and both provide good fits to the transmittance spectrum (figure 7.5 d). However, the SE fit appears to be better because it accounts for the slight kink in the spectrum just after the onset of the band edge. Both fitting approaches also agree on a value of 101 nm for the film's thickness.

A single PSEMI-M0 model was also used to fit the ellipsometric spectra of a CdS film (figure 7.6 a, b). Again, a the value for the direct band gap extracted from this model (2.50 eV) is higher than that determined by the SP fit (2.41 eV) - the latter involved a single Lorentz oscillator and an inter-band transition component. It is believed that the SP model achieves a more accurate value as it is closer to that reported previously for polycrystalline CdS by others [10, 11]. While the shape of the n and κ spectra extracted from both SE and SP fits are similar, there is an obvious shift between the values of n over the range with the values determined by the SE fit being around 0.1 higher. Furthermore, the shapes of both n and κ from both fits are significantly different at wavelengths below the band gap of the material ($\lambda < 450$ nm). Despite these differences, the resultant fits to the transmittance spectrum for the film are almost identical for both methods, and also
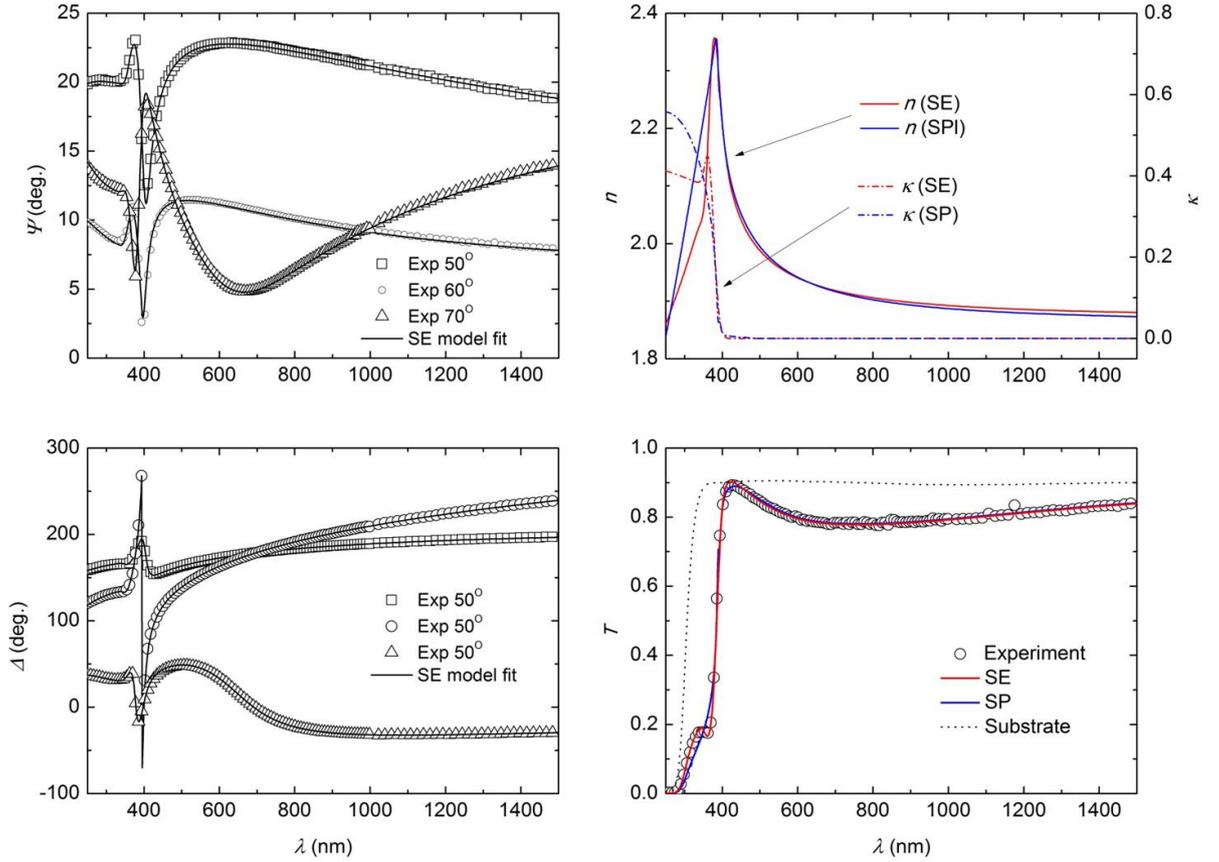
Figure 7.5: Ellipsometry of a ZnO film on OptiWhite glass substrate. n and κ spectra extracted from both the standard model and the CompleteEASE software are in good agreement except in the region $\lambda < 400$ nm. A comparison of fittings to a transmittance spectra show that the SE method provides a more accurate fit in this region.

a film thickness of ~ 220 nm is determined in both cases which is in excellent agreement with profilometry measurements made on the film.

Figure 7.7 a and b shows the ellipsometric spectra of a relatively thick (~ 1.5 μm) CdTe film. The spectra are fitted according to two separate PSEMI-M0 oscillators located at different energies within range measured. The first was located at $E_1 = 1.51$ eV and corresponded to the material's direct band gap and the other was located at $E_2 = 3.08$ eV. The resultant shapes and the positions of the critical points within the n and κ spectra determined by the SE fit are similar to those previously determined by others for sputtered CdTe films [12]. A comparison between the n and κ spectra determined by both
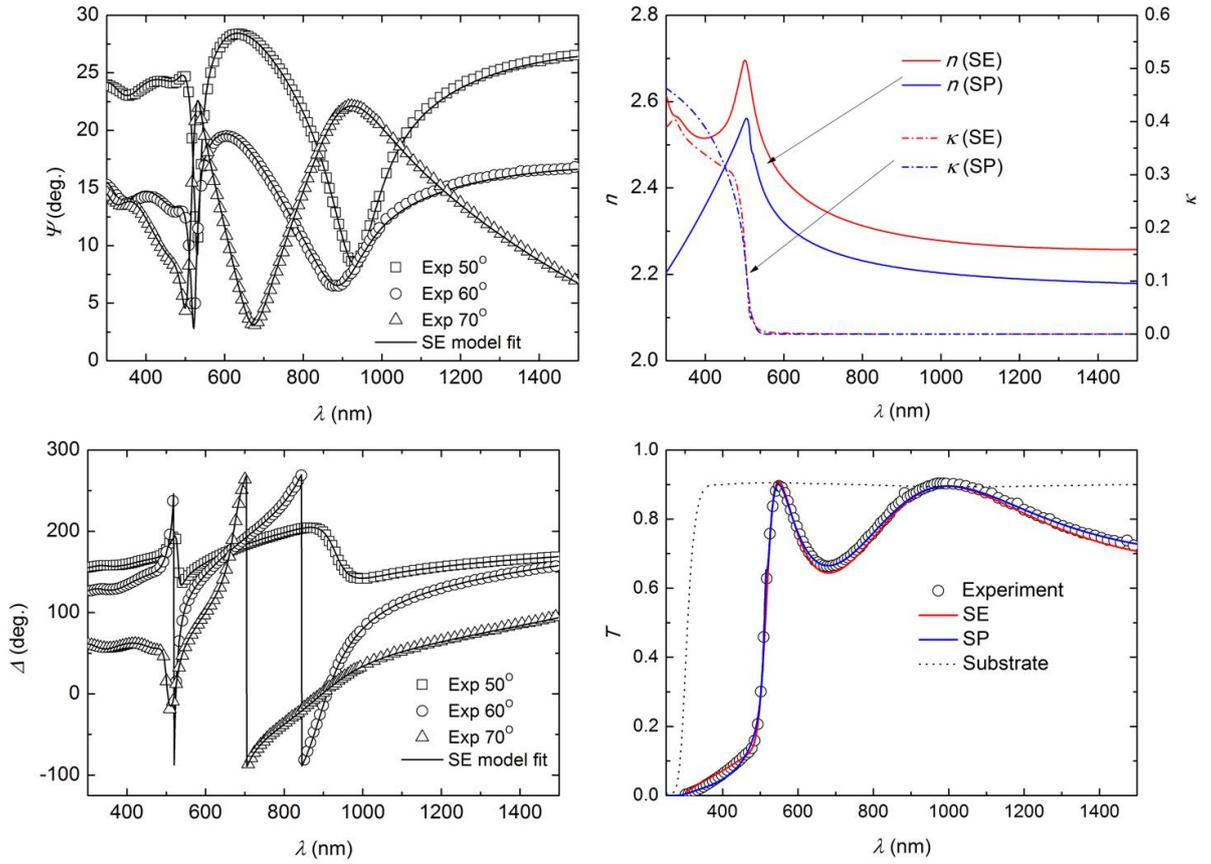
Figure 7.6: Ellipsometry of a CdS film on OptiWhite glass substrate. A significant difference is observed in $n(\lambda)$ extracted from both SE and SP fits. Nonetheless both sets of extracted n and κ spectra give rise to good fits to the film's transmittance spectra.

the ellipsometric and photometric approaches, figure 7.7 c, shows a marked difference at wavelengths $\lambda < 900$ nm. The SP model is incapable of modelling the effect of the second resonance (E_2) because the transmittance measurement does not record a signal below the band gap (E_1). The ellipsometry measurement on the other hand records a signal in this region to which a fit can be made. Therefore, despite both sets of n and κ being able to generate reliable fits to the transmittance spectra of the CdTe film (figure 7.7 d) only the spectra from the SE fit can be trusted when used within a multi-layer model within which the range of wavelengths of interest are below 900 nm.

Further to the decision to disregard the n and κ spectra determined by the SP method for CdTe, all other spectra achieved via this method were excluded from further multi-layer
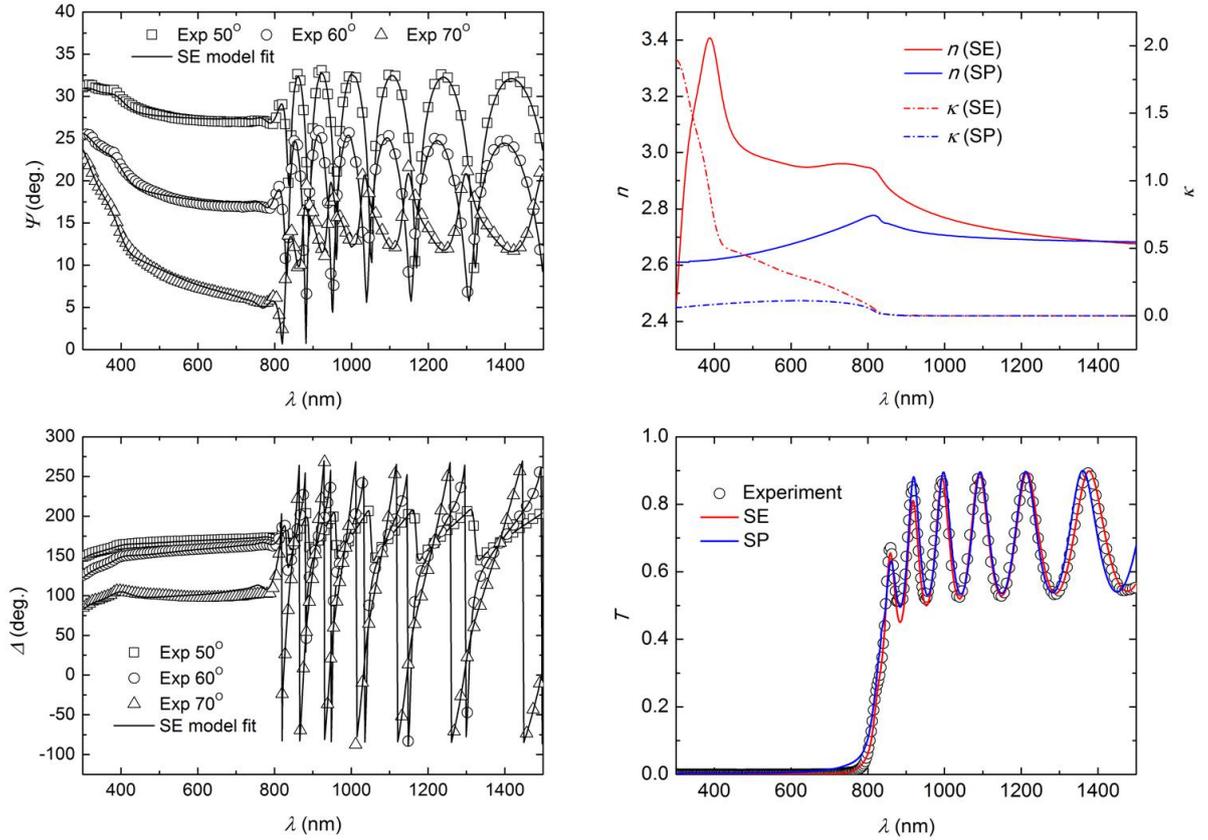
Figure 7.7: Ellipsometry of CdTe film ($\sim$ 1.5 μm) on OptiWhite glass substrate. In this case, over the full measurement range, the extracted n and κ spectra from the SE method is far more reliable than that extracted from a single transmittance spectra using the SP method for dielectric permittivity (see text).

modelling and only the SE results were incorporated. This was done in order to maintain a sense of consistency within the multi-layer models and not to confuse the analysis by combining n and κ spectra from one method with the other.

7.5 Multi-layer test structures

In this section, the theory in section 7.2 is applied to a series of multi-layer test structures. The first two of these structures that are investigated are those of a narrow band-pass filter and an anti-reflection (AR) coating, both of which are based on multi-layer assemblies of alternating high/low refractive index dielectric materials, namely TiO_2 and SiO_2. The third investigation tests the multi-layer model's ability to predict the transmittance of a real

CdS/ZnO/ITO/glass structure. The objective of these test structures is to demonstrate the efficacy of the multi-layer model in predicting the transmittance spectra of real structures. Furthemore, the potential role that such AR coatings might have in improving device efficiency is discussed.

7.5.1 Narrow band filter

A Bragg reflector typically consists of a multi-layer assembly of high/low refractive index films, each of quarter wavelength thickness ($\lambda_0/4$), that generates a high reflectance, R, over a particular wavelength range centred around λ_0. The high reflectance arises because all reflected beams from all interfaces within the structure recombine constructively at the front surface. Such structures are common components within laser spectroscopy and optical waveguides. The multi-layer model was used to determine the optical response of an assembly, based upon original work by *Brand et al.* [13–15], consisting of two TiO_2/SiO_2 Bragg reflectors separated by a relatively thick TiO_2 layer. Such a structure yields a typical reflectance spectrum of a single Bragg reflector but with a very narrow peak of high transmittance located within the high reflectance region. This structure has potential applications as a narrow band pass filter and for the generation of terahertz radiation [16–18].

The n and κ spectra for TiO_2 were determined by applying the SP model fitting procedure to a single film of the material. In the case of SiO_2 however, it was not possible to determine n and κ in this manner due to the inability to distinguish the layer from the glass substrate (a consequence of their similarly matched refractive indices). Instead, the refractive index n for SiO_2 were adopted from previous ellipsometry analysis performed by *Jellison* [19] and it was assumed that the extinction coefficient was zero over the range of wavelengths modelled. Both sets of n and κ were then fed to the multi-layer model which was used to calculate the theoretical transmittance of a structure, on a standard OptiWhite glass substrate, consisting of four repetitions of a TiO_2(95 nm)/SiO_2(153 nm) bi-layer, a 190 nm thick TiO_2 spacer layer and finally four repetitions of a SiO_2(153 nm)/TiO_2(95 nm) bi-layer (i.e. the inverse of the initial bi-layer stack). The resultant theoretical transmittance spectrum generated by the multi-layer model is shown in figure 7.8 (blue line). The model predicts that the structure generates a narrow peak (9.6 nm FWHM) in the
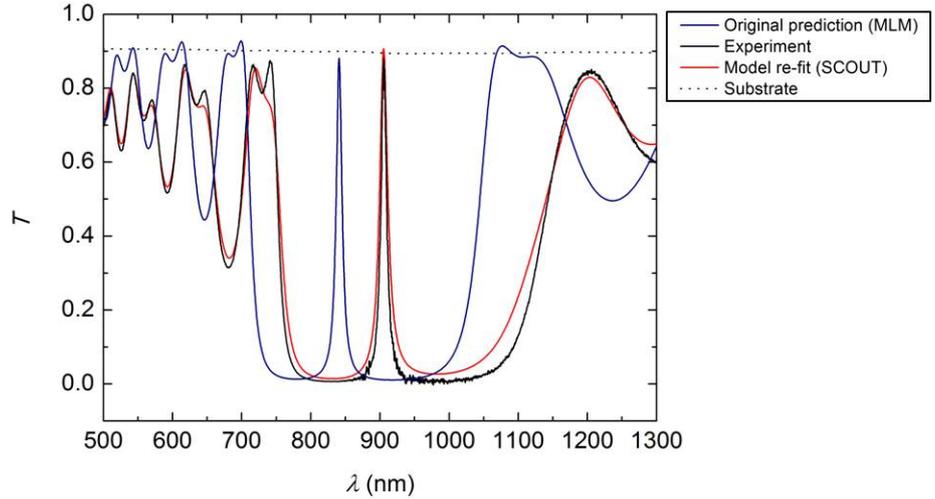
Figure 7.8: Transmittance spectrum for the predicted 17 layer stack structure (blue line) and the corresponding experimental transmittance (black line) of the real structure deposited via RF magnetron sputtering. A shift in the predicted position of the transmittance peak is a result of errors within the initial calibration of growth rates for the TiO_2 and SiO_2. An excellent model fit to the experimental transmittance spectrum is achieved using the SCOUT software, especially considering the complexity of the structure. The corresponding results from the fit are shown in table 7.3.

transmittance spectrum at a wavelength of 840.9 nm.

RF magnetron sputtering was used to deposit the modelled structure following the calibration of growth rates from separate TiO_2 and SiO_2 targets (99.99% purity, PI-KEM) according to profilometry measurements on single films. At RF powers of 300 W, a chamber pressure of 5 mTorr Ar and for a substrate held at room temperature the growth rates of TiO_2 and SiO_2 films were 2.2 ± 0.2 nm/min and 2.7 ± 0.2 nm/min respectively. The sputtering system, which is computer controlled, was then programmed to fabricate the structure. Note that while it was possible to alternately open and close shutters attached to each of the targets and therefore simply run both targets continuously throughout the deposition, RF power was only applied to one magnetron at a time in order to preserve the lifetime of the targets.

Figure 7.8 also shows the resultant experimental transmittance spectrum of the sput-

Table 7.3: 17 layer TiO_2/SiO_2 structure. Film thicknesses were extracted from fitting the multi-layer model to the measured transmittance spectrum.

Layer	Material	d (nm)
17	TiO_2	48.9
16	SiO_2	159.9
15	TiO_2	100.4
14	SiO_2	162.9
13	TiO_2	103.5
12	SiO_2	164.7
11	TiO_2	106.8
10	SiO_2	169.4
9	TiO_2	210.5
8	SiO_2	153.9
7	TiO_2	101.9
9	SiO_2	157.9
5	TiO_2	105.3
4	SiO_2	159.9
3	TiO_2	107.0
2	SiO_2	163.8
1	TiO_2	109.5
0	OptiWhite	4 mm

tered assembly. Clearly, there is a significant shift in the predicted position of the narrow transmittance peak which is found at a wavelength of 905.5 nm). It is believed that this is due to having made errors in the calculation of the growth rates of each material. The SCOUT software was used to re-fit the transmittance spectra to the experimental data and determine the true thicknesses of each layer within the sputtered sample. These results are shown in table 7.3 and are confirmed via direct measurement of the individual layers through cross-sectional SEM imaging, shown in figure 7.9, achieved using a focussed ion beam system located at Durham University. Overall, the average thicknesses of the TiO_2
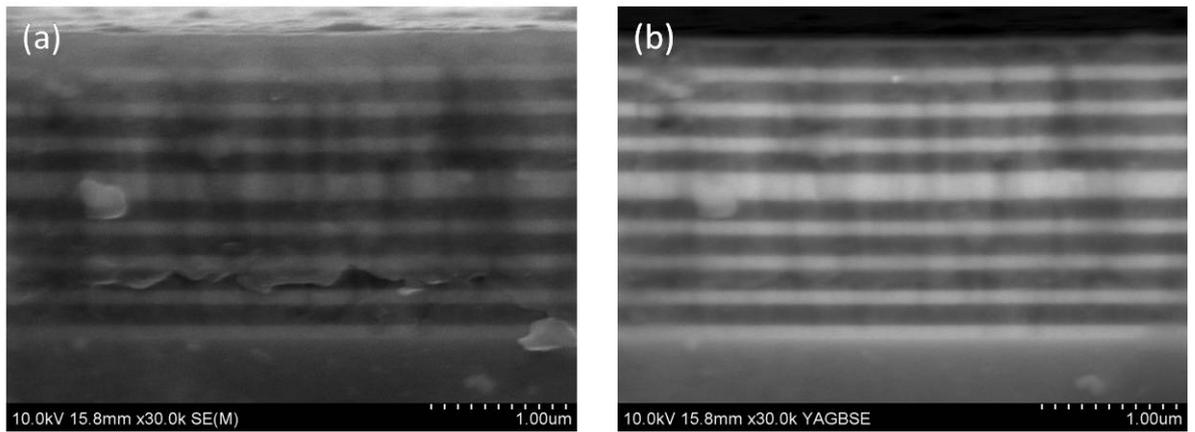
Figure 7.9: Scanning electron microscopy was performed on cross sections of the 17 layer TiO_2/SiO_2 structure. a) Secondary electon image. b) Backscattered electron image. The sample was prepared using a focussed ion beam.

and SiO_2 layers excluding the thick TiO_2 spacer layer) were 105 ± 5 nm and 162 ± 5 nm respectively suggesting that in both cases the measured growth rates were lower than those used in the actual growth run. Despite this, the consistency between the thickness of each of the alternate layers was very good indicating that the automated deposition control of the equipment is reliable.

It must be noted from the backscattered SEM image (figure 7.9 b) that the final layer of TiO_2 (top of image) is incomplete. This was the result of a processing error at the termination of the growth run. Remarkably, the SCOUT software was used produce a good fit to the transmittance spectrum of this 17 layer structure and the thickness of the final layer was estimated at 48.9 nm (Table 7.3) which is in clear agreement with the microscopy. The SCOUT software has therefore proven itself to be a reliable tool for extracting the individual layer thicknesses of complicated multi-layer assemblies from a relatively simple transmittance measurement.

A more precise relationship between predicted and experimental results for such structures could be achieved through a more accurate calibration of the growth rate for each of the deposited materials. This might be achieved through use of ellipsometry, a technique which has been demonstrated as an accurate measure of film thickness to the nearest ± 1 nm, unlike the relatively crude profilometry measurement which can only determine thickness to the nearest ± 10 nm.

Table 7.4: Optimum designs for 2 layer and 4 layer TiO_2 and SiO_2 anti-reflection coatings on OptiWhite substrates.

2 layer			4 layer		
Layer	Material	d (nm)	Layer	Material	d (nm)
2	SiO_2	123	4	SiO_2	94
1	TiO_2	9	3	TiO_2	127
			2	SiO_2	31
			1	TiO_2	17

7.5.2   Anti-reflection (AR) coating

The combined use of TiO_2 and SiO_2 films is also relevant to the design of anti-reflection coatings reflection coatings [20–22]. Such structures are relatively simple compared to the previous example and consist typically of only one or two repeated bi-layer TiO_2/SiO_2 structures. They also present an immediate opportunity to further improve the transmittance of a CdTe solar cell structure and in the case of a completed superstrate device, can be deposited directly onto the back surface of the glass substrate.

The multi-layer model was re-configured to calculate the optical transmittance of a two-layer and a four-layer TiO_2/SiO_2 anti reflective coating. In both scenarios, the integrated transmittance was calculated for every possible thickness configuration by varying the thickness of each film by 1 nm increments over the ranges 0 - 200 nm. The results were then analysed to find the configuration that generated the maximum value of $\tilde{T}$. These optimum configurations are shown in table 7.4 and the corresponding predicted transmittance curves, relative to the glass substrate, are shown in figure 7.10. The optimum two layer structure indicates that there is potential for an increase in $\tilde{T}$ of ~ 0.015, relative to the transmittance of a bare glass substrate, and for the optimum four layer structure, an increase of 0.03.

No experimental sample was fabricated based on the optimised AR coating designs generated the multi-layer model. However, the ability of the deposition technique in creating samples based on such designs, provided that an adequate calibration of growth rate is made, is demonstrated in the previous example.
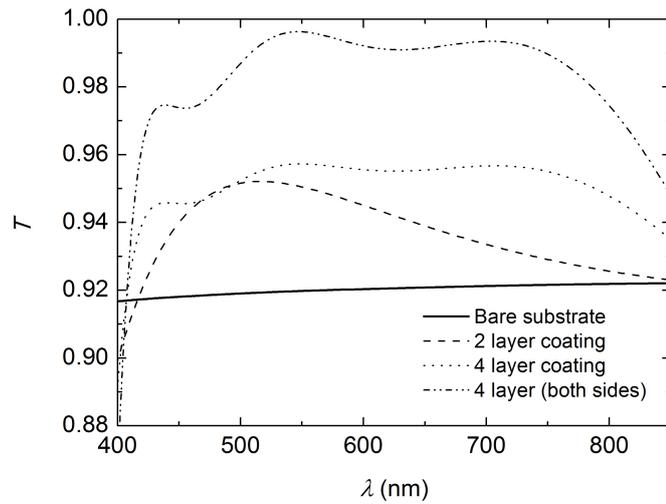
Figure 7.10: The multi-layer model was used to design an optimized anti-reflection coating for the OptiWhite substrate. The figure shows the potential gains in transmittance for both a 2 layer and 4 layer coating (see table 7.4). In the case of the 4 layer structure a maximum gain in $\tilde{T}$ of $+0.03$ is predicted relative to the transmittance of a bare glass substrate.
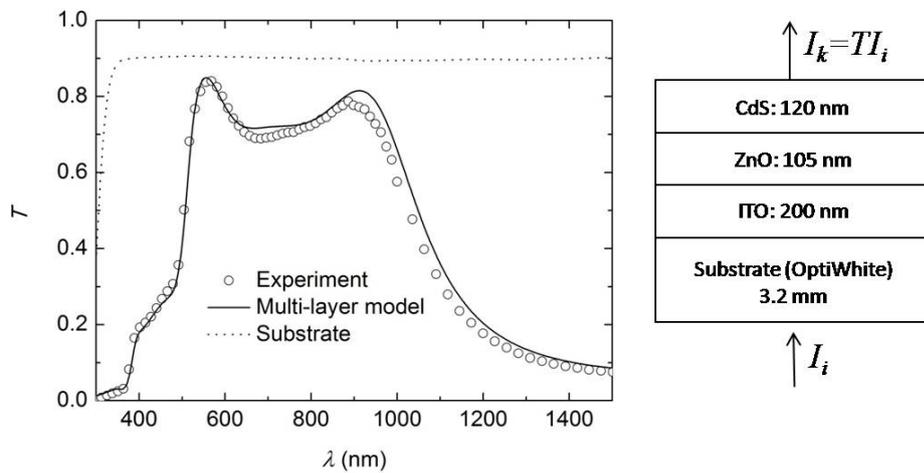
Figure 7.11: Testing of the multi-layer model's ability to predict the transmittance of a real stack structure. A good fit is achieved indicating the reliability of the model.

7.5.3　Test structure for a CdTe based device

Further testing of the multi-layer model was performed by comparing the experimental transmittance of a real CdS/ZnO/ITO sample to that predicted by the model following the incorporation of the n and κ spectra extracted via the SE method (section 7.3). Figure 7.11 shows the experimental transmittance measured for the assembly of CdS(120 nm)/ZnO(105 nm)/ITO(200 nm) films on an OptiWhite glass substrate (3.2 mm). Note that, no CdTe layer was deposited onto the structure as this would have prevented the measurement, via spectrophotometry, of any signal at wavelengths below the CdTe band gap. To account for this within the program an exit medium optical admittance of $\mathcal{A}_m = 1$ (i.e air) was used within equation 7.16. The subsequent output from the multi-layer model (represented by the solid line) shows a good fit to the experimental spectrum. The fit is particularly good at wavelengths in the vicinity of and below the CdS band gap. This is important because any optimisation of the stack's transmittance is likely to result from changes to this region of the spectrum (due to thinning of the CdS layer).

7.6　Optical modelling of CdTe solar cells

The demonstrated ability of the multi-layer model to predict the transmittance spectra of real structures justifies its use in the theoretical optical optimisation of a complete as-grown CdTe device. The objective of such an investigation is to identify device assemblies that show improved optical performance relative to the current fully sputtered prototype design (Chapter 6). It is hoped that these improved designs will correspond immediately with an improvement of completed device performance (i.e. conversion efficiency).

　　Following the incorporation of CdTe into the model as an exit medium, the effect of varying the thicknesses of the ITO, ZnO, CdS layers on the integrated transmittance $\tilde{T}$ was investigated. The thickness of the layers were varied in the ranges (80-100 nm), (25-200 nm) and (25-200 nm) respectively. The minimum values of these ranges correspond to the limit in which such structures are likely to yield working devices following post deposition processes (i.e. annealing/contacting). All results were compared to a baseline structure: CdS(200 nm)/ZnO(100 nm)/ITO(230 nm). This baseline structure is comparable to that of the real prototype devices that yielded typical conversion efficiencies of $\sim 8\%$ on average
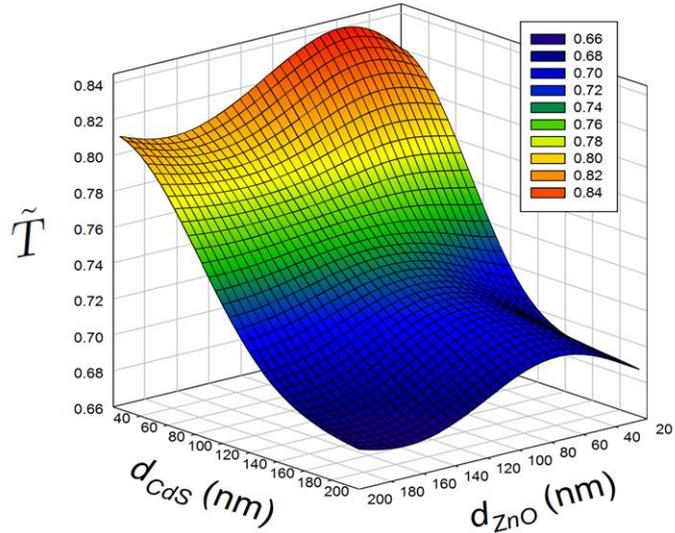
Figure 7.12: The effect of the variation in both CdS and ZnO layer thickness on the resultant fractional transmittance, $\tilde{T}$, into the CdTe layer. A constant ITO thickness of 230 nm was maintained.

and maximum efficiencies upwards of 12% (see Chapter 6).

In general, the investigation found that small changes in the thickness of CdS and ZnO had a greater influence on $\tilde{T}$ than changing the ITO thickness. This is demonstrated by comparing the baseline structures A and B shown in table 7.5, in which the CdS and ZnO layers are thinned, resulting in an increase in $\tilde{T}$ of +14.3%. Thinning the ITO (C) caused a further +3.8% increase in the transmittance. Further reduction in the CdS and ZnO thickness(D and E) allowed for further gains. This is explored further in figure 7.12, in

Table 7.5: A selection of modelled device configurations and their predicted increase in transmittance.

	d_{ITO} (nm)	d_{ZnO} (nm)	d_{CdS} (m)	$\tilde{T}$ (300-850 nm)	% change[a]
A	230	100	200	0.70	-
B	230	50	50	0.80	+14.3
C	115	50	50	0.84	+20.0
D	115	50	25	0.86	+22.9
E	80	25	25	0.87	+24.3

[a]Relative to current baseline structure, A

which the ITO thickness is fixed at 115 nm and $\tilde{T}$ is shown as a function of both the CdS and ZnO thicknesses. It is seen in the figure that changing the CdS thickness for a fixed ZnO thickness has a greater effect than for vice-versa. For example, for a constant 50 nm thickness of ZnO, reduction of the CdS from 200 to 50 nm increased $\tilde{T}$ from 0.69 to 0.84. The dominance of CdS thinning on $\tilde{T}$ is due to the fact that as the film becomes thinner the absorption at wavelengths below its band gap ($\lambda < 500$ nm) becomes less pronounced. This is demonstrated in figure 7.13 by the progression of $\tilde{T}$ in configurations A $\rightarrow$ C $\rightarrow$ E. A maximum increase in $\tilde{T}$, relative to the baseline structure, from 0.7 to 0.87 ($+24.3\%$) is predicted for the device structure E - CdS(25 nm)/ ZnO(25 nm)/ITO(80 nm).

It must be emphasised at this point that while the results of this investigation are promising in terms of optimising the optical performance of CdTe solar cells, they account for the optical performance *only*. The electrical impact of changing the layer thicknesses is not accounted for and indeed, the potential gains predicted by the optical optimisation may be completely negated by the resultant effects on the electrical performance of the device. Furthermore, the spectra n and κ for each material incorporated into the multi-layer model were extracted from as-grown layers. Therefore, the effect of post growth treatments, which typically induces a significant change in the morphological structure in the films as well as inter-diffusion between the layers, is not accounted for. Nonetheless the use of the multi-layer model provides an indication that device performance can be improved by optimising the optical response of the constituent layers. Further experiments, whereby real devices are fabricated, are required to confirm the predictions of the multi-layer model.

The theoretical change in the transmittance of a CdTe device structure on application of a four layer AR coating, as predicted by the multi-layer model, is shown in figure 7.14 and is of clear benefit at all wavelengths within the range. If the assumption is made that any increase in $\tilde{T}$ will be directly proportional to the increase in the photo current generated within such a device then the incorporation of a four layer AR coating could potentially increase device efficiency by an extra 0.5%. This is extremely significant, particularly for high efficiency devices that approach the current world record limit of 16.5% [23].
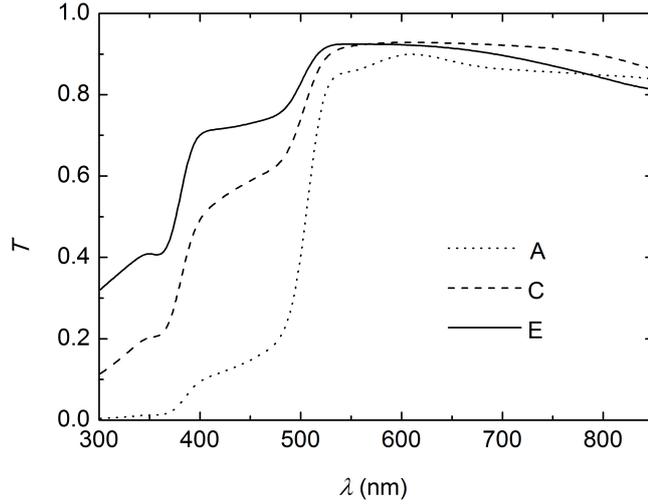
Figure 7.13: Significant gains in transmittance, relative to the baseline structure 'A' are observed at wavelengths below 450 nm as the ZnO and CdS films are thinned to thicknesses below 50 nm. Details for spectra A, C and E are given in table 7.5
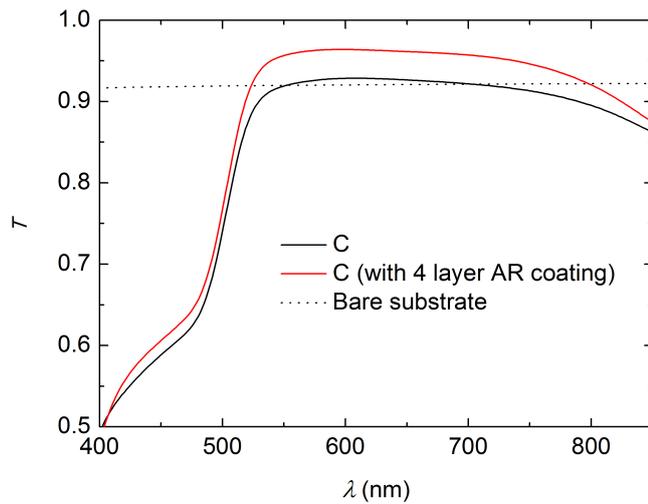
Figure 7.14: The transmittance of the device structure 'C' (see table 7.5) is shown with and without the optimised 4 layer AR coating.

7.7 Conclusions

The two methods, SE and SP, used to extract dispersion data from optical spectra of single films have been demonstrated as being reliable for oxide materials (ITO and ZnO) that have band gaps > 3 eV. However, it was found that the SP method was able to predict

more accurate values for the band gaps for these materials and that those extracted from the SE method were, in general, higher than expected. For films of ITO, both methods extracted very similar values of parameters ω_p, n_e and μ_e according to the use of Drude components. In the case of CdS and CdTe films, the SE method proved to be capable of extracting n and κ at energies above the band gap. This was particularly so in the case of CdTe. The SP method however was unable to predict the behaviour at energies far beyond the band gap where the absorption coefficient became too high for a sufficient transmittance signal to be detected.

A model to predict the optical response of an assembly of thin films has been developed that accurately predicts the experimental transmittance of real structures deposited via RF magnetron sputtering. The model predicts a potential gain upwards of 20% in the integrated transmittance, $\tilde{T}$, over the range 400-850 nm following the optimisation of a baseline device structure. The largest component of this gain arises from the thinning of the CdS layer to a thickness below 50 nm. Validation of this predicted gain is yet to be demonstrated through the fabrication of optimised structures.

Overall, the model provides an excellent starting point for further improvements to the device efficiency of current fully sputtered structures, however further development is required for several reasons: Firstly, the model only predicts the response of as-grown materials. The effects of further processing, namely the CdCl$_2$ activation step, must be incorporated into the model before it can be used to predict the optical response of a 'working' CdTe solar cell. During such processing, the films within the assembly are likely to undergo morphological changes that will inevitably generate a deviation to the predicted optical response. Therefore, the effect of the treatment on both the individual layers and completed structures must be determined by ellipsometry and fed back into the model. Secondly, the effect of voiding within the constituent layers must be considered - it being shown that, for CdS and CdTe in particular, a significant fraction of sputtered films are composed of voids [24]. The model may be adjusted to account for such voiding effects on the resultant transmittance by incorporating a simple Bruggemann model [25]. Finally, the determination of an empirical relationship between the optical and electrical properties of the resultant device structures is desirable, i.e. is there a direct proportionality between the transmittance and the generated photo-current? Such knowledge would help set physically

sensible limits to the minimum thickness of layers within the model.

The model is used to design a four layer anti-reflection coating for glass that could potentially increase the transmittance into a device structure by 0.03. Such an increase, although apparently small, my act to increase the efficiency of a working device by $\sim 0.5\%$, which could prove extremely significant for high efficiency devices. While the fabrication of such an AR coating is not achieved within this work, the demonstrated reliability of RF magnetron sputtering in creating such structures is extremely promising.

7.8 References

[1] H. A. Macleod. *Thin-Film Optical Filters*. Adam Hilger Ltd (1986).

[2] O. S. Heavens. *Optical Properties of Thin Solid Films*. Dover (1965).

[3] I. S. Grant, W. R. Phillips. *Electromagnetism*. Wiley (1990).

[4] I. Visoly-Fisher, S. Cohen, D. Cahen, C. Ferekides. *App. Phys. Lett.* **83**, 4924 (2003).

[5] C. S. Ferekides, R. Mamazza, U. Balasubramanian, D. L. Morel. *Thin Solid Films* **480**, 224 (2005).

[6] Y. Roussillon, D. Giolando, V. Karpov, D. Shvydka, A. Compaan. *Applied Physics Letters* **85**, 3617 (2004).

[7] A. Bosio, N. Romeo, S. Mazzamuto, V. Canevari. *Prog. Cryst. Growth. Ch.* **52**, 247 (2006).

[8] T. Tiwald. *Wollam Co. News* **7**, 6 (2006).

[9] B. Johs, C. Herzinger, J. Dinan, A. Cornfeld, J. Benson. *Thin Solid Films* **313**, 137 (1998).

[10] A. Oliva, O. Solıs-Canto, R. Castro-Rodrıguez, P. Quintana. *Thin Solid Films* **391**, 28 (2001).

[11] A. Oliva, R. Castro-Rodrıguez, O. Solıs-Canto, V. Sosa, P. Quintana, J. Peña. *Applied Surface Science* **205**, 56 (2003).

[12] J. Li, N. Podraza, R. Collins. *Phys. Stat. Sol. A* **205**, 901 (2008).

[13] S. Brand, R. A. Abram, M. A. Kaliteevski. *J. Appl. Phys.* **106**, 113109 (2009).

[14] S. Brand, R. A. Abram, M. A. Kaliteevski. *Opt. Lett* **35**, 2085 (2010).

[15] S. Brand, R. A. Abram, M. A. Kaliteevski. *J. Phys. D: Appl. Phys* **43**, 145104 (2010).

[16] R. Gehlhaar, M. Swoboda, M. Sudzius, M. Hoffmann, H. Frob, V. G. Lyssenko, K. Leo. *App. Phys. B* **86**, 413 (2007).

[17] N. Kim, J. Shin, E. Sim, C. W. Lee, D. Yee, M. Y. Yong, M. Jeon, Y. Jang, K. H. Park. *Opt. Express* **17**, 13851 (2009).

[18] T. Kitada, F. Tanaka, T. Takahashi, K. Morita, T. Isu. *App. Phys. Lett.* **95**, 111106 (2009).

[19] G. E. Jellison Jr. *Thin Solid Films* **206**, 294 (1991).

[20] C. Martinet, V. Paillard, A. Gagnaire, J. Joseph. *Journal of Non-Crystalline Solids* **216**, 77 (1997).

[21] S. Jeong, J. Kim, B. Kim, S. Shim, B. Lee. *Vacuum* **76**, 507 (2004).

[22] M. Kuo, D. Poxson, Y. Kim, F. Mont, J. Kim, E. Schubert, S. Lin. *Optics Letters* **33**, 2527 (2008).

[23] X. Wu, J. C. Keane, R. G. Dhere, C. DeHart, D. S. Albin, A. Dudam, T. A. Gessert, S. Asher, D. H. Levi, P. Sheldon. *Proc. of 17th European PVSEC*, 995 (2001).

[24] A. D. Compaan, R. W. Collins, V. G. Karpov. Fabrication and Physics of CdTe Devices by Sputtering. Technical report, NREL (2009).

[25] D. A. G. Bruggemann. *Ann. Phys* **24**, 636 (1935).

Chapter 8

Conclusions

8.1 Summary of conclusions

This thesis has demonstrated the applicability of RF magnetron sputtering for the development of CdTe PV. In particular, the exploration of several doping routes to a number of TCO materials, namely In_2O_3:Sn, SnO_2:F, ZnO:Al and ZnO:F, has shown that there is a wide scope for further design and optimisation of these materials using RFMS. Also, the development of a fully-sputtered CdTe device platform has yielded efficiencies upwards of 12%, comparable to other such devices reported in the literature [1, 2].

Models for the dielectric permittivity of all of the materials described in this work have been developed and successfully used to extract key film parameters - e.g. n and κ, direct band gap, thickness, carrier concentration and mobility - from data recorded via spectrophotometry and ellipsometry. The potential for rapid screening and analysis of combinatorial samples via these non-destructive optical methods shows promise for the further development of materials for CdTe devices, particularly TCOs. Furthermore, the use of extracted optical data in the development of a theoretical multi-layer model demonstrates the potential optical gains that may be achieved through the further optimisation of device design.

Chapter 5 describes several doping routes for the aforementioned TCO materials: films of In_2O_3:Sn (ITO) and ZnO:Al (AZO) were achieved by sputtering from compound ceramic targets while films of SnO_2F (FTO) and ZnO:F (FZO) were deposited by reactive sputtering from targets of SnO_2 and ZnO respectively while incorporating small partial pressures

of CF_4, CHF_3 and H_2. A further co-sputtering route to FTO, involving the simultaneous sputtering from ceramic SnO_2 and ZnF_2 targets, was also explored.

It was established that of all the TCO materials investigated In_2O_3:Sn (ITO) had the best opto-electric properties with respect to the criteria specified for thin-film PV (see section 2.4). Films of ITO sputtered from a ceramic mixed composition target (In_2O_3:SnO_2 (10% wt.)) at an RF power of 60 W, under 1 mTorr of Ar, and at a substrate temperature of 400°C possessed a resistivity of $\rho = 1.2 \times 10^{-4}$ Ω.cm. This value, corresponding to an electron carrier density and mobility of $n_e = 8.9 \times 10^{20}$ cm^{-3} and $\mu_e = 58.4$ $cm^2V^{-1}s^{-1}$ respectively, is comparable to the lowest resistivity values reported in the literature [3, 4] (see table 2.2). The films had an integrated absorption coefficient (see equation 2.62) of $\tilde{\alpha} \sim 3500$ cm^{-1} over the range $400-850$ nm which corresponded to an optical transmittance of $\tilde{T} \approx 0.83$ for films of thickness $d \approx 250$ nm. The figure of merit (see equation 2.64) for these films was therefore calculated at $\phi \sim 8 \times 10^{-2}$ Ω^{-2} which is higher than that of commercially available TCOs such as Pilkington NSG's TEC15 (CVD deposited SnO_2:F) which has a figure of merit of $\phi = 1.9 \times 10^{-2}$ Ω^{-2}. ITO films were consequently incorporated into fully-sputtered devices in Chapter 7 in order to establish a reproducible prototype structure.

Sputtering of ZnO:Al (AZO) from a mixed ZnO:Al_2O_3 (2% wt.) target yielded a minimum resistivity value of $\rho = 4.7 \times 10^{-4}$ Ω.cm when deposited under the conditions - 50 W, 0.5 mTorr Ar and $T_{sub} = 150$°C. Values of $n_e = 4.3 \times 10^{20}$ cm^{-3} and $\mu_e = 30.8$ $cm^2V^{-1}s^{-1}$ were measured for this film. These values are comparable to those reported elsewhere for RFMS deposited ZnO:Al [5]. The electrical properties of the best AZO films were inferior to those for ITO, with n_e and μ_e values for AZO being typically half those measured for ITO. However, the absorption coefficient for AZO was significantly lower, $\tilde{\alpha} \sim 1400$ cm^{-1} meaning that for film thicknesses above 500 nm a figure of merit of $\phi > 5 \times 10^{-2}$ Ω.cm, i.e comparable to that of ITO, could be achieved.

Attempts to dope ZnO with fluorine via reactive sputtering using partial pressures of H_2 and CHF_3 achieved a significant reduction in resistivity, by a factor $> 10^5$, relative to un-doped films. The incorporation of H_2 during growth was key to this reduction, and acted to promote the level of F doping within the films. The minimum level of resistivity, $\rho = 2.9 \times 10^{-3}$ Ω.cm, achieved using deposition parameters of 100 W, 5 mTorr total

pressure, 5% H_2 partial pressure, 4% CHF_3 partial pressure and a substrate temperature of 300°C. This resistivity value is comparable to those reported by Yoon [6] and Ku [7] for sputtered FZO films. However, it has been demonstrated by Tsai [8] that lower resistivities, of the order $\sim 5 \times 10^{-4}$ Ω.cm, are achievable using sputtering. Films with such resistivities are the target of future work (see section 8.2) and are necessary before FZO films can be incorporated as front contact layers into fully-sputtered CdTe devices.

A similar reactive doping route, i.e involving a partial pressure of CHF_3, was investigated for SnO_2 (FTO) sputtered from a ceramic SnO_2 target was also investigated. It was not possible to reach resistivity values below $\sim 10^{-2}$ Ω.cm. This minimum limit to the resistivity is almost four times higher than the lowest reported resistivity values for films reactively sputtered in partial pressures of CF_4 [9]. Furthermore, it was shown in this work that the incorporation of CF_4 served to significantly increase the resistivity of FTO films (to beyond measurable limits).

It is believed that further reductions in the resistivity of SnO_2:F (FTO) films is more likely to be achieved via non-reactive gas methods. For example, Geoffroy [10] has shown that sputtering from a mixed composition SnO_2:SnF_2 target can yield a minimum resistivity of 5×10^{-4}, i.e comparable to ITO. Attempts, within this work, to explore this particular doping route were hampered by the large disparity in growth rates between SnO_2 and SnF_2 which caused the mixed target to become rapidly depleted of SnF_2. However, preliminary experiments that involved the co-sputtering of SnO_2 and SnF_2 from separate ceramic targets showed more promise, with a significant decrease in ρ observed as the difference between the relative growth rates from the SnO_2 and SnF_2 was increased. For such a co-sputtering approach, there is also potential for the generation of combinatorial samples, in which a doping gradient can be introduced. This will permit the rapid optimisation of film deposition without the need to creation large sample sets.

For ITO and AZO films, where the doping level was sufficient, it was possible to extract electrical properties from simple transmittance spectra using a model for the dielectric permittivity that included an extended Drude component. Values extracted for n_e and μ_e from the spectra were shown to agree to within 10% of the values extracted from van der Pauw and Hall measurements. Such a method for extracting electrical properties is advantageous as it is non-destructive and in the case of combinatorial samples, which

cannot be measured using conventional electrical methods, can be used to generate 3D plot of the change in electrical properties as a function of position across a sample.

The modelling of the effect of direct inter-band transitions on the dielectric permittivity also permitted the effective band gaps, E_d, and Burstein-Moss shifts, Δ_{BM}, for highly doped films to be extracted. However, it was generally observed that the corresponding carrier densities, n_e, extracted from values of Δ_{BM} did not correspond directly with those values extracted from the Drude component of the model. Through an investigation of the change in Δ_{BM} as a function of thickness in a wedge profile of AZO with a constant n_e, it was observed that at thicknesses < 100 nm the size of Δ_{BM} was bigger than expected but decreased towards the expected value as the film thickness increased. It is therefore speculated that there is some other component to the observed shift in band gap that arises, e.g. due to a quantum confinement effect that occurs in films with the small (i.e. < 50 nm) grain structure associated with thinner layers. Further structural characterisation of the films is required, e.g. by X-ray diffraction or atomic force microscopy, to confirm this micro-structural development.

In Chapter 6 the results from a prototype fully-sputtered device design were reported. The device structure was CdTe ($\sim 2\mu$m)/CdS (100 nm)/ZnO (100 nm)/ITO (180 nm)/glass. Over a consistent series, involving the fabrication and measurement of over two hundred 5 mm $\times$ 5 mm device contacts, three distinct populations were identified according to their performance. These separate populations, identified as being *under-treated*, *optimized* and *over-treated*, arose as a result of a non-uniform temperature distribution within annealing apparatus (a tube furnace) during the post-deposition CdCl$_2$ treatment process. Under-treated devices were characterised by their low J_{SC}, FF and V_{OC} values and by EQE measurements that indicated buried-junction behaviour. Over-treated devices showed visible signs of degradation (i.e blistering and de-lamination) and when measured showed significant reductions in the J$_{SC}$. For the optimised population an average efficiency of $9.3 \pm 2.2\%$, and a maximum of 12.5%, was achieved. Such efficiencies are comparable to the record fully-sputtered device efficiency of 14.5% [1]. Therefore, provided the issue of treatment non-uniformity can be overcome, the prototype design provides an excellent platform from which further gains in efficiency may be achieved.

An example of the necessary materials development from the present work is the ef-

fect upon devices of changing the sputtering conditions used for the CdTe absorber layer. Varying the Ar pressure in the range $5 - 20$ mTorr on the structure of as-deposited CdTe films showed that for pressures of 5, 10 and 15 mTorr the films were highly orientated in the cubic (111) direction. A CdTe film deposited at 20 mTorr showed a significant reduction in the intensity of the (111) peak and a more randomised crystal structure. For all layers the lattice parameter, a, was higher than that reported for bulk CdTe [11] indicating that some degree of lateral strain is present in the sputtered films. It is believed that this strain helps to promote the extensive recrystallisation and grain growth during post-deposition treatment [12]. Further studies into the combined effect of CdTe deposition pressure and post-depostion treatment anneal times indicate that the best device performance is achieved for pressures between $10 - 15$ mTorr and for anneal times of 20 mins, at $390°$C.

Further electrical and structural characterisation of the devices gave some important insights into their behaviour and properties. J-V-T analysis of a 7% efficient device showed that in the temperature range > 250 K the device ideality factor remained constant at a value of $A \sim 1.6$ and that there was an inverse proportional relationship between the log of the reverse saturation current J_0 and the temperature. This behaviour indicates that, over this range in temperature, the current transport behaviour across the junction of the device was dominated by Shockley-Read-Hall (SRH) recombination, the result of a population of mid-gap (i.e. $E_d/2$) trap states within the CdTe layer. This transport mechanism has also been shown to dominate in CSS deposited CdTe [13, 14]. Further analysis of this behaviour permitted a value for the built in potential of $V_{bi} = 1.14$ eV to be estimated which is in accordance with values reported by other groups [15]. This value was corroborated by a value of $V_{bi} = 1.11$ eV extracted from C-V measurements. C-V analysis also showed that the CdTe layer, under reverse bias, was fully depleted and that the layer had a net carrier concentration of $N_A \sim 10^{14}$ cm^{-3} which is typical for CSS-grown CdTe devices [16, 17]. Furthermore, an anomalous "bump" in the C-V curve suggests the presence of a secondary junction within the device. Such a junction may be the result of a CdTe/ZnO interface (i.e through pin-holes or non-uniformities in the CdS layer) or, more likely, a CdTe/Au interface located at the back surface of the CdTe.

EBIC measurements, performed on a cross-section of the same 7% device, showed the

electrically active region of the cell as being located ~ 0.8 μm away from the CdTe/CdS interface and ~ 0.5 μm away from the back surface of the CdTe layer. This suggests that, over this particular region of measurement, the post-deposition treatment has been insufficient to promote the full formation of an n-p junction at the CdTe/CdS interface and instead a p-p$^+$ homo-junction has formed within the CdTe layer. The expected EQE response of this device would be that of a buried junction however this is not consistent with what is measured, the EQE showing a normal response for an optimised device. It is speculated that due to the non-uniformity of the CdCl$_2$ treatment procedure a variation in the location of the junction may be expected oven over a 5mm × 5mm sized contact. An alternative explanation could be that a buried homo-junction exists over the entire contact area is not so deeply buried as to effect the EQE shape.

TEM performed on cross-sections from the same device shows that the extent of re-crystallisation within the CdTe layer is extensive with grain sizes increasing from < 100 nm to > 1 μm during CdCl$_2$ treatment. Variation in the diffraction contrast within the TEM images identifies defect structures such as twins and grain boundaries, the latter of which are generally considered to contribute the most significantly to performance losses. It is believed that the reduction of in-plane orientated grain boundaries, through further recrystallisation may improve device quality.

Having demonstrated that competitive devices could be fabricated by an all-sputtered method, Chapter 7 explores the extent to which the optical design of the TCO, HRT and CdS layers may contribute to further increased efficiencies. The methodological framework for this was also established. The applicability of the dielectric permittivity models presented for TCOs in Chapter 2 was demonstrated for other semiconductor materials, namely undoped (intrinsic) ZnO, CdS, CdTe, SiO$_2$ and TiO$_2$. Two optical methods for the extraction of n and κ, based on separate measurements via spectrophotometry (SP) and spectroscopic ellipsometry (SE), are presented and it was shown that both methods are capable of reliably extracting the optical parameters. The SE method however, is more advantageous for the characterisation of CdTe as it can extract information at wavelengths below the gap whereas the SP method cannot. A library of n and κ data for each of the above named materials was developed and used in a multi-layer transmittance model which was developed in this work. It was written in FORTRAN and is based on a transfer matrix

method [18].

The multi-layer model was tested through its application to several test structures. Its ability to reproduce the transmittance spectra of a 17 layer TiO_2/SiO_2 narrow band filter and an air/CdS/ZnO/ITO/glass cell test structure, was demonstrated with a high degree of agreement between theoretical and experimental spectra. The model was therefore used to predict the fraction of incident light transmitted to a CdTe absorber layer through a CdS/ZnO/ITO/glass structure, i.e. a fully-sputtered CdTe device. Furthermore, the model was used to predict the optical gains associated with changes to each of the component layer thicknesses. It was shown that changes in the thickness of the ZnO and CdS were more significant that changes to the ITO thickness and that an increase in $\tilde{T}$ upwards of 20% may be achieved by thinning the CdS layer to around 50 nm. Such an increase would be extremely significant for a real device with a corresponding increase in J_{SC} expected. Modelling the effect of a 4-layer TiO_2/SiO_2 anti-reflection coating, applied to the front surface of the glass substrate, showed that there is a potential gain of $\sim 2\%$ in $\tilde{T}$ for CdTe devices. It was therefore demonstrated that optimisation of the HRT and CdS layers had greater potential for improving efficiency than did an AR coating.

While the multi-layer model was successful at predicting the optical response of as-deposited devices, the potential effects that post-deposition treatment may have on the resultant optical properties of the constituent layers were not incorporated into the model. For the time being therefore, it is not possible to directly predict the exact optimised structure of a fully-sputtered CdTe solar cell and a full ellipsometric analysis of the effects of post-deposition treatment shall be required before this is can be achieved. Nevertheless, the method offers significant design insight in its present-form.

8.2   Suggestions for further work

The work presented in Chapters 5, 6 and 7 now gives rise to several potential routes for further investigations. These are categorised below according to their relation to TCO design, the fully-sputtered prototype device structure and the multi-layer optical model:

8.2.1 Transparent conducting oxides

- **Development of a combinatorial approach to TCO improvement**: Co-sputtering from separate ceramic oxide targets while maintaining a fixed substrate (i.e rotation off) will generate combinatorial samples that contain a continuum of doping concentrations. It is hoped that the rapid, non-destructive analysis of these samples via the optical methods developed in this work will determine the optimum deposition parameters required to achieve TCOs with sufficiently high figures of merit (i.e $> 5 \times 10^{-2}$ Ω^{-2}) that enable them to be incorporated into CdTe device designs. Suggestions for such experiments include sputtering from ZnO-ZnF$_2$ targets, to achieve improved ZnO:F films and from TiO$_2$-Nb$_2$O$_3$ targets, to achieve TiO$_2$:Nb films [19, 20]. TCOs based on TiO$_2$ are of particular interest because of the material's relatively high refractive index > 2.6. This could lead to the development of AR coatings that are also conductive.

- **Investigations into the effects of film structure on shifts in the band gap**: It is hoped that further investigations into the grain structures of sputtered TCOs my determine a relationship between grain size and shifts in the band gap. The incorporation of such a relationship into the existing inter-band transition components of the dielectric permittivity model may resolve the inconsistencies observed between Drude and inter-band component values for n_e. Furthermore, such a model may be used to infer grain sizes in subsequent TCO films from simple spectrophotometry measurements.

8.2.2 Fully-Sputtered devices

- **Improving the uniformity of the post-deposition treatment**: Future studies that investigate the effects of systematic changes to the constituent layers of fully-sputtered devices require a significant improvement to the uniformity of the current CdCl$_2$ treatment. The use of a muffle (box) furnace, the size of which greatly exceeds that of samples, is likely to significantly reduce any temperature gradient over a sample surface. This is important due to the large temperature sensitivity associated with the CdCl$_2$ annealing process.

- **Development of a CdCl$_2$-free post-deposition treatment**: The use of chlorine containing freon gases has been demonstrated by Romeo *et. al* [21] as achieving excellent device results, i.e. $> 15\%$. The incorporation of small partial pressures of such gases during the sputter deposition of CdTe films may introduce Cl to the as-deposited films. Subsequent annealing of devices, without CdCl$_2$, may lead to similar activation effects.

- **Application of combinatorial methods for device optimisation**: The introduction of wedge shaped films of ZnO, CdS and CdTe into devices may prove an effective way of rapidly optimising device design. It is recognised that a uniform post-deposition treatment is a key requirement for such studies.

8.2.3   Optical modelling

- **Investigating the optical effects of post-deposition treatment**: An understanding of the changes in the optical properties of TCO, CdS and CdTe is required for the optical response of real devices to be completely modelled. Spectroscopic ellipsometry might be used to make a full analysis, i.e. the extraction of n and κ data for each of the constituent layers within treated devices. The incorporation of such an analysis into the multi-layer model will strengthen its ability to predict the optical response of real, completed devices.

It is anticipated that these suggestions will lead to the development of sustainable TCO alternatives to ITO and improvements in photovoltaic conversion efficiency of CdTe based devices.

8.3   References

[1] A. Gupta, A. Compaan. *Applied Physics Letters* **85**, 684 (2004).

[2] A. Gupta, V. Parikh, A. Compaan. *Solar Energy Materials and Solar Cells* **90**, 2263 (2006).

[3] Y. Shigesato, S. Takaki, T. Haranoh. *J. Appl. Phys.* **71**, 3356 (1992).

[4] R. N. Joshi, V. P. Singh, J. c. McClure. *Thin Solid Films* **257**, 32 (1995).

[5] K. H. Kim, K. C. Park, D. Y. Ma. *J. Appl. Phys.* **81**, 7764 (1997).

[6] H. Yoon, K. Lee, T. Lee, B. Cheong, D. Choi, D. Kim, W. Kim. *Sol. Energy Mater. Sol. Cells* **92**, 1366 (2008).

[7] D. Ku, Y. Kim, K. Lee, T. Lee, B. Cheong, T. Seong, W. Kim. *Journal of electroceramics* **23**, 415 (2009).

[8] Y. Tsai, N. Wang, C. Tsai. *Materials Letters* **63**, 1621 (2009).

[9] B. Stjerna, E. Olsson, C. Granqvist. *Journal of Applied Physics* **76**, 3797 (1994).

[10] C. Geoffroy, G. Campet, F. Menil, J. Portier, J. Salardenne, G. Couturier. *Active and Passive Elec. Comp.* **14**, 111 (1991).

[11] N. K. Abrikosov, V. B. Banikina, L. V. Poretskaya, L. E. Shelimova, E. V. Skudnova. *Semiconducting II-VI, IV-VI and, V-VI compounds.* Plenum, New York (1969).

[12] H. Moutinho, M. Al-Jassim, F. Abulfotuh, D. Levi, P. Dippo, R. Dhere, L. Kazmerski. *Proc. 26th IEEE PVSC*, volume 26, 431–434. Citeseer (1997).

[13] S. S. Hegedus, B. McCandless. *Sol. Energy Mater. Sol. Cells* **88**, 75 (2005).

[14] M. K. Al Turkestani. Ph.D. thesis, Durham University (2010).

[15] S. K. Das, G. C. Morris. *Sol. Energy Mater. Sol. Cells* **305**, 305 (1993).

[16] C. R. Corwine, A. O. Pudov, M. Gloeckler, S. H. Demtsu, J. Sites. *Sol. Energy Mater. Sol. Cells* **82**, 481 (2004).

[17] S. A. Ringel, A. W. Smith, M. H. MacDoughal, A. Rohatgi. *J. Appl. Phys.* **70**, 881 (1991).

[18] H. A. Macleod. *Thin-Film Optical Filters*. Adam Hilger Ltd (1986).

[19] Y. Sato, H. Akizuki, T. Kamiyama, Y. Shigesato. *Thin Solid Films* **516**, 5758 (2008).

[20] N. Yamada, T. Hitosugi, J. Kasai, N. L. H. Hoang, S. Nakao, Y. Hirose, T. Shimada, T. Hasegawa. *Thin Solid Films* **518**, 3101 (2010).

[21] S. Mazzamuto, L. Vaillant, A. Bosio, N. Romeo, N. Armani, G. Salviati. *Thin Solid Films* 7079 (2008).

Appendix A

List of Publications

- R. E. Treharne and K. Durose. Alternative doping routes to fluorine doped SnO_2 using RF magnetron sputtering, PVSAT-5, Glyndwr University, (2009)

- R. E. Treharne and K. Durose. Fluorine doped Zinc Oxide thin-films, PVSAT-6, Southampton University, (2010)

- B. L. Williams, R. E. Treharne and K. Durose. All sputtered CdTe/CdS solar cells, PVSAT-6, Southampton University, (2010)

- R. E. Treharne and K. Durose. Florine dope ZnO films by RF magentron sputtering, Article in press in *Thin Solid Films*, (2011), doi:10.1016/j.tsf.2010.12.126

- R. E. Treharne and K. Durose. Optical modelling of fluorine doped ZnO. Article in press in *Thin Solid Films*, (2011), doi:10.1016/j.tsf.2011.04.155

- R. E. Treharne, A. Seymour-Pierce, K. Durose, K. Hutchings, S. Roncallo, and D. Lane. Optical design and fabrication of fully sputtered CdTe/CdS solar cells, *JPCS* **286**, 012038 (2011)

Appendix B

FORTRAN95 Code

```fortran
PROGRAM MLM
-------------------------------------------------------------------------
! MULTI-LAYER MODEL - 26/08/11 - By Robert E. Treharne

! This program outputs the transmittance spectrum measured at the
! CdTe/CdS interface for an ITO/ZnO/CdS stack on an OptiWhite
! soda-lime glass substrate.
! The output file records the integrated transmittance over the
! range 400 - 850 nm as a function of CdS and ZnO thickness.
-------------------------------------------------------------------------
! DEFINE VARIABLES.

IMPLICIT NONE

        COMPLEX :: delta, j, B, C, N0
        REAL :: Y = (2.6544e-3), pi, Ta, Tb, Tc, Tint=0
        INTEGER :: i,k,e,w,q
        COMPLEX, DIMENSION (2,2) :: M, M1
        COMPLEX, DIMENSION (2,600) :: R
        REAL, DIMENSION (11,600) :: data
    REAL, DIMENSION (1,3) :: d
        COMPLEX, ALLOCATABLE, DIMENSION(:) :: N
    REAL, ALLOCATABLE, DIMENSION(:) :: lambda, T
        INTEGER :: status, nvals=0, l

! DEFINE j AS UNIT IMAGINARY NUMBER.
    j = (0,1)

! DEFINE PI.
    pi=2*ACOS(0.0)

! DETERMINE HOW MANY ENTRIES (nvals) ARE IN THE OPTICAL LIBRARY FILE
'primary.dat'.
        OPEN (UNIT=1, FILE='Primary.dat',
STATUS='OLD',ACTION='READ',IOSTAT=status)
            DO
                READ (1,*,IOSTAT=status)
                IF (status /=0) EXIT
                nvals=nvals+1
        END DO

! RE-READ FILE AND ALLOCATE ALL DATA TO ARRAY 'data'.
                REWIND (UNIT=1)
                        READ (1,*, IOSTAT=status) data

        CLOSE (UNIT=1) !Close file, 'primary'

! SET LENGTH OF ARRAYS 'lambda' and 'T' TO EQUAL nvals.
                ALLOCATE (lambda(nvals))
        ALLOCATE (T(nvals))
```

```fortran
!INPUT OPTICAL DATA INTO INPUT/EXIT MEDIUM MATRIX
        DO i =1,nvals
                lambda(i) = data(1,i)
            R(1,i) = (1) !THIS MATRIX ELEMENT REPRESENTS THE INPUT MEDIUM, I.E.
AIR.
            R(2,i) = (data(10,i)-(j*data(11,i)))*Y   !THIS MATRIX ELEMENT
                                                     !REPRESENTS THE EXIT MEDIUM,

                                                     !I.E. CdTe.
                                                     !`Y` IS ADMITTANCE OF
                                                     !FREE-SPACE

        END DO

! SET THE LENGTH OF TEMPORARY ARRAY `N` as nvals
        ALLOCATE (N(nvals))

! SPECIFY PATH FOR OUTPUT FILE AS `DATA.dat`
        OPEN (UNIT=5, FILE='DATA.dat', STATUS='REPLACE')

! THE FOLLOWING DO LOOPS GENERATE THE OUTPUT DATA


                DO e = 1, 20                    ! VARY CdS THICKNESS IN THE
RANGE 35 - 235 nm
                    d(1,3) = 15 +(10*e)
                DO w = 1, 20                    ! VARY ZnO THICKNESS IN THE
RANGE 35 - 235 nm
                    d(1,2) = 15+(10*w)

                    d(1,1) = 115                ! SET ITO THICKNESS AT 115 nm

                    DO i = 1,283                ! DEFINE UNIT MATRIX
                        M = 0

                        DO k = 1,2
                            M(k,k) = 1
                        END DO

                        DO l = 1,3! CALCULATE TRANSMITTANCE FOR A SINGLE
WAVELENGTH

                        N(i) =
data(4+(2*(l-1)),i)-(j*data(4+((2*l)-1),i))
                        N0 = (data(2,i) - j*data(3,i))*Y

                        ! CALCULATE CHANGE IN PHASE BETWEEN
LAYERS
                        delta = (2*pi*N(i)*d(1,l))/lambda(i)

                        M1(1,1) =  cos(delta)
                        M1(1,2) =  (j*sin(delta))/(N(i)*Y)
                        M1(2,1) =  j*sin(delta)*N(i)*Y
                        M1(2,2) =  cos(delta)

                        M = MATMUL(M,M1) ! MATRIX MULTIPLICATION

                    END DO

                    B = (M(1,1)*R(1,i)) + (M(1,2)*R(2,i))
                    C = (M(2,1)*R(1,i)) + (M(2,2)*R(2,i))
```

```fortran
                                    ! APPLY FINITE SUBSTRATE CORRECTION
                          Ta =
(4*REAL(N0)*REAL(R(2,i)))/(((REAL(N0)*B)+C)*CONJG((REAL(N0)*B)+C))
                              Tb = 1
                              Tc = (4*REAL(data(2,i)))/(REAL(data(2,i))+1)**2
                              T(i) = ((1/Tb)+(1/Tc)-1)**(-1)*Ta


                    END DO

            ! CALCULATED INTEGRATED INTENSITY

            DO i = 1, 283-1
                    Tint = Tint + (lambda(i+1)-lambda(i))*(T(i)+T(i+1))*0.5

            END DO

            Tint = Tint/(lambda(377)-lambda(63))

            Td(1,e) = d(1,3)
            Td(2,e) = Tint

            ! WRITE d(ZnO), d(CdS, and INTEGRATED TRANSMITTANCE TO FILE

            WRITE(5,*) d(1,2),d(1,3), Tint


            END DO
            END DO

! CLOSE OUTPUT FILE

            CLOSE(UNIT=5)



END PROGRAM MLM
```